INSIGHTS INTO THE MECHANISM OF X-RAY INDUCED STRUCTURAL PERTURBATION OF MACROMOLECULES

by Kristin A. Sutton

January 9, 2013

A dissertation submitted to the
Faculty of the Graduate School of
the University at Buffalo, State University of New York
in partial fulfillment of the requirements for the degree of

Doctor of Philosophy

Department of Structural Biology
School of Medicine and Biomedical Sciences
University at Buffalo, The State University of New York and
Hauptman-Woodward Medical Research Institute

I dedicate this dissertation

to my parents who made who I am

and to my husband, Matt who has supported me all the way.

ACKNOWLEDGEMENTS

I'd like to acknowledge the following people who have contributed to my experience as a graduate student. Edward Snell, PhD, my mentor and advisor, who originally took me on as an undergraduate summer student and sparked my interest in X-ray crystallography. After rotating in his lab in my first year of graduate school, his excitement and passion for his work reignited this interest. To my Graduate Committee members Robert Blessing, PhD, Andrew Gulick, PhD, and Joseph Luft- I sincerely appreciate the suggestions, guidance and direction you have given me. I'd also like to thank Jill Szczesek for her help in coordinating with UB and assisting me in the final push. An acknowledgement is also due to the donors to the Stafford Fellowship, which funded my graduate research. I'd like to thank everyone at HWI- PIs, graduate students, post docs, technicians and staff as I've interacted with each person during my time here. Especially the girls in the lab: Robin, Jen, Mary, Wendy, Peggy, Angela, Ellie, Jenn, Jessica and Elizabeth.

To my friends and family- it is with your support that I was able to achieve this accomplishment. My grandparents, aunts, uncles, cousins, the Sutton family, my brother Scott, my parents Dale and Cindy Wunsch- I love you all. Your continued support means the world to me, thank you for always believing in me and pushing me to be my best. Last but not least, Matt- thank you for always believing in me and knowing exactly the right thing to say to make me laugh when I need it.

TABLE OF CONTENTS

DEDICATION……i

ACKNOWLEDGEMENTS……...ii

TABLE OF CONTENTS……iii

LIST OF FIGURES ……vii

LIST OF TABLES……..…..xii

ABBREVIATIONS ……..xv

ABSTRACT ……xix

CHAPTER 1: SUMMARY OF RADIATION DAMAGE IN MACROMOLECULAR CRYSTALLOGRAPHY LITERATURE

1.1 STRUCTURAL BIOLOGY AND X-RAY CRYSTALLOGRAPHY……1

1.2 X-RAY INDUCED DAMAGE……4

1.3 MANIFESTATIONS OF DAMAGE……...13

1.4 IMPLICATIONS OF DAMAGE……..17

1.5 TECHNIQUES TO MONITOR DAMAGE……19

1.6 DISSERTATION AIMS……..…23

CHAPTER 2: INSIGHTS INTO THE MECHANISM OF X-RAY INDUCED DISULFIDE BOND CLEAVAGE IN LYSOZYME

CRYSTALS BASED ON EPR, OPTICAL ABSORPTION AND X-RAY DIFFRACTION STUDIES

2.1 INTRODUCTION……27

2.2 THE RADIATION CHEMISTRY OF DISULFIDE BOND BREAKAGE……..29

2.3 EXPERIMENTALLY TESTING THE MODEL……35

2.4 RESULTS……43

2.5 X-RAY DIFFRACTION DATA AND STRUCTURAL RESULTS……52

2.6 DISCUSSION……...66

2.7 SUMMARY……75

CHAPTER 3: A GENERALIZED MODEL FOR RADIATION DAMAGE OF AMINO ACIDS BASED ON MULTI-TRACK MODEL PREDICTIONS

3.1 INTRODUCTION……76

3.2 EXPERIMENTAL DATA TO TEST THE MODEL……..77

3.3 DEVELOPING THE GENERALIZED MODEL……78

3.4 REDUCTION AND OXIDATION SITES……..…82

3.5 SPECIFIC REACTION SCHEMES FOR AMINO ACIDS……87

3.6 QUANTITATIVE PREDICTIONS BY THE MODEL……101

3.7 AGREEMENT WITH THE MODEL AND EXPERIMENTAL RESULTS..…111

3.8 MODEL PREDICTIONS……...134

3.9 DISCUSSION……135

CHAPTER 4: XYLOSE ISOMERASE: A CASE STUDY FOR X-RAY INDUCED STRUCTURAL PERTURBATIONS IN METALLOPROTEINS

4.1 INTRODUCTION TO XYLOSE ISOMERASE MECHANISM……140

4.2 XYLOSE ISOMERASE MECHANISM……...141

4.3 THE INFLUENCE OF RADIATION CHEMISTRY ON XI STRUCTURE….159

4.4 RESULTS……...164

4.5 DISCUSSION……..……...198

4.6 CONCLUSIONS……..……206

CHAPTER 5: UNDERSTANDING THE EFFECT OF RADIATION ON THE ACTIVE SITE OF METALLOPROTEINS WITH DIFFERENT METAL TARGETS AND SURROUNDING AMINO ACID ENVIRONMENT

5.1 INTRODUCTION……..…207

5.2 THE INFLUENCE OF THE ACTIVE SITE METAL AND THE SURROUNDING AMINO ACID ENVIRONMENT……..208

5.3 EXPERIMENTALLY DETERMINING THE DAMAGE AT METAL SITE….208

5.4 RESULTS……..…….217

5.5 DISCUSSION…..……..267

5.6 CONCLUSION……..……...271

CHAPTER 6: DISCUSSION AND FUTURE WORK

6.1 DISCUSSION…….272

6.2 FUTURE WORK ……...276

REFERENCES AND LITERATURE CITED……279

VITA……286

LIST OF FIGURES

CHAPTER 1

Figure 1.1 Proportion of unchanged, damaged and destroyed molecules as a function of exposure time……..……..…....**7**

CHAPTER 2

Figure 2.1 Key reaction pathways for cleavage of the disulfide bond……...**32**

Figure 2.2 UV-Vis absorption spectra of the disulfide radical anion……..**44**

Figure 2.3 Post X-ray exposure decay of the disulfide peak……..**46**

Figure 2.4 EPR spectra for a lysozyme crystal with increasing dose……**48**

Figure 2.5 Dose response for radical trapping in lysozyme crystals……**50**

Figure 2.6 Isomorphous difference density maps for disulfide bonds……...**56**

Figure 2.7 Isomorphous difference density maps for methionine residues…..…**62**

Figure 2.8 Concentration of one electron reduced disulfide bonds with increased absorbed dose……**64**

CHAPTER 3

Figure 3.1 Generalized scheme for reduction and oxidation of proteins……..…**80**

Figure 3.2 One-electron reduced species resulting at sites with high reduction potentials……..…**83**

Figure 3.3 Partial list of radicals produced by a one-electron oxidation……..…**86**

Figure 3.4 Reductive and oxidative reaction pathways for cystine……...**88**

Figure 3.5 Reductive and oxidative reaction pathways for aspartate……...**90**

Figure 3.6 Reductive and oxidative reaction pathways for tyrosine……..**92**

Figure 3.7 Reductive and oxidative reaction pathways for cysteine…….**94**

Figure 3.8 Reductive and oxidative reaction pathways for methionine……**96**

Figure 3.9 Reductive and oxidative reaction pathways for the peptide bond..…**98**

Figure 3.10 Reductive and oxidative reaction pathways for the solvent……**100**

Figure 3.11 Radical interactions…….....**106**

Figure 3.12 Fo-Fc maps for the disulfide bond in lysozyme…….**113**

Figure 3.13 Fo-Fc maps for methionine in lysozyme……**115**

Figure 3.14 Fo-Fc maps for glutamate in lysozyme……..**117**

Figure 3.15 Fo-Fc maps for aspartate in lysozyme……...**119**

Figure 3.16 Fo-Fc maps for tyrosine in lysozyme……..**121**

Figure 3.17 Fo-Fc maps for glycine in lysozyme……...**123**

Figure 3.18 Fo-Fc maps for methionine in xylose isomerase……..……**127**

Figure 3.19 Fo-Fc maps for gluatmate in xylose isomerase……**129**

Figure 3.20 Fo-Fc maps for aspartate in xylose isomerase……..……**131**

Figure 3.21 Fo-Fc maps for tyrosine in xylose isomerase……**133**

CHAPTER 4

Figure 4.1 Sugar binding……**143**

Figure 4.2 Substrates and inhibitors used in mechanistic studies of XI…….**144**

Figure 4.3 Ring opening……**146**

Figure 4.4 Extension of the linear substrate ……..**149**

Figure 4.5 Isomerization……..…**153**

Figure 4.6 Active site of XI highlighting metal positions……**156**

Figure 4.7 Comparison of diffraction images from the high-resolution region...**165**

Figure 4.8 Average change in B factor with increased absorbed dose……..**171**

Figure 4.9 Relationship between solvent accessibility and change in B factor with increased absorbed dose……**173**

Figure 4.10 Isomorphous difference density map of XI ……**177**

Figure 4.11 Progression of radiation damage with increased absorbed dos…**179**

Figure 4.12 Comparison of the active sites of XI with different absorbed doses……..**182**

Figure 4.13 Comparison of the experimental electron density maps of the active site……...…**184**

Figure 4.14 Comparison of the isomorphous difference density maps of the active site with increased absorbed dose……..…**185**

Figure 4.15 Trajectory of M2……**187**

Figure 4.16 Metal site occupancies……..**190**

Figure 4.17 Isomorphous difference density maps for residues involved in XI mechanism……**196**

CHAPTER 5

Figure 5.1 Active site of XI containing cadmium……**226**

Figure 5.2 Active site of XI containing manganese……**228**

Figure 5.3 Active site of XI containing cobalt……..**230**

Figure 5.4 Active site of XI containing copper……**232**

Figure 5.5 Active site of XI containing zinc……..…**234**

Figure 5.6 Active site comparison of metal replaced XI structures……**245**

Figure 5.7 Influence of increased absorbed dose on active site position of metal atoms and amino acid side chains……....**247**

Figure 5.8 Fluorescence scan of XI crystal containing manganese……**249**

Figure 5.9 Isomorphous difference density map for SOD…….**255**

Figure 5.10 Progression of SOD disulfide bond breakage……...**258**

Figure 5.11 SOD active site……...**260**

Figure 5.12 Influence of dose on radiation induced damage in the active site of SOD……**261**

Figure 5.13 Comparison of SOD structure with PDB ID 1Q0E……**265**

Figure 5.14 Comparison of absorbed doses for metal replaced crystals……...**269**

LIST OF TABLES

CHAPTER 2

Table 2.1 Crystal dimensions and dose points used for EPR measurements….**39**

Table 2.2 Crystallographic data collection and refinement statistics…….**54**

Table 2.3 Solvent accessibility…….**59**

Table 2.4 Parameters used to fit plot of one-electron reduced disulfides…….**65**

CHAPTER 3

Table 3.1 Radiation induced reaction yields and probability for amino acids....**104**

Table 3.2 Percentage of reside damage to lysozyme expected from absorbed doses of 0.07 and 1.05 MGy……..**110**

Table 3.3 Percentage of reside damage to xylose isomerase expected from absorbed doses of 0.35 and 5.60 MGy……..…**125**

CHAPTER 4

Table 4.1 Data collection dose scheme……...**162**

Table 4.2 Global indicators of radiation damage……**167**

Table 4.3 Specific damage statistics……**169**

Table 4.4 Effect of increased dose on side chain position……**175**

Table 4.5 Isomorphous difference density peaks……..……**188**

Table 4.6 Metal coordinates and B factors……..**192**

Table 4.7 Bond distances for metal atoms……..**194**

CHAPTER 5

Table 5.1 Crystallization conditions for metal replaced XI crystals……..…**211**

Table 5.2 Data collection strategy……**213**

Table 5.3 Resolution and absorbed dose……**214**

Table 5.4 Data processing statistics for metal replaced XI……..…**219**

Table 5.5 Isomorphous difference map peaks for metal replaced XI structures……...**221**

Table 5.6 Approximate comparable absorbed doses for metal replaced XI…..**223**

Table 5.7 Metal properties for XI containing one position for M2……**236**

Table 5.8 Metal properties for XI containing cadmium……..…**237**

Table 5.9 Metal properties for M1 in XI containing three positions for M2……...**238**

Table 5.10 Metal properties for M2 in XI containing three positions for M2……...**239**

Table 5.11 Metal properties that may influence the position of M2……**243**

Table 5.12 Data collection statistics for SOD……..…**251**

Table 5.13 Isomorphous difference map peaks for SOD……..**253**

Table 5.14 Disulfide bond lengths for SOD……..…**257**

Table 5.15 Metal properties and bond lengths for SOD……**263**

Table 5.16 Photoelectric cross section for elements used……**268**

ABBREVIATIONS

Å	angstrom
APS	Advanced Photon Source
CCD	charged coupled device
Cd	cadmium
CEWL	chicken egg white lysozyme
Co	cobalt
Cu	copper
DNA	deoxyribonucleic acid
DNTB	5,5’-dithio-bis-2-nitrobenzoic acid
DMFG	3-deoxy-C3-fluoro-methylene-D-glucose
EDO	ethylene glycol
EDTA	Ethylenediaminetetraacetic acid
EPR	electron paramagnetic resonance
GHz	gigahertz
Gy	gray
HEPES	4-(2-Hydroxyethyl)piperazine-1-ethanesulfonic acid
HWI	Hauptman-Woodward Medical Research Institute

I	intensity
K	kelvin
k_b	back reaction rate constant
keV	kiloelectron volt
k_f	forward rate constant
kGy	kilogray
k_r	radicalization rate constant
M	molar
mA	milliampere
MAD	multiple anomalous dispersion
MES	2-(N-morpholino)ethanesulfonic acid
Mg	magnesium
Mn	manganese
MGy	megagray
MHC	major histocompatibility complex
mT	millitesla
µg	microgram

µL	microliter
µm	micrometer
mg	milligram
mL	milliliter
mM	millimolar
MME	monomethyl ether
MR	molecular replacement
Ni	nickel
nM	nanometer
NMR	nuclear magnetic resonance
NaCl	sodium chloride
PDB	protein data bank
PEG	polyethylene glycol
ph	photons
RMSD	root mean squared displacement
RSH	sulfhydryl group
RSSR	disulfide bond

s	second
S	rate of change of unit cell volume
$SS^{\bullet-}$	disulfide radical anion
$SS(H)^{\bullet}$	protonated disulfide radical
SSRL	Stanford Synchrotron Radiation Laboratory
σ	sigma
SOD	superoxide dismutase
TGP	5-thio-α-D-glucose
UV	ultraviolet
XANES	X-ray absorption near edge spectroscopy
XI	xylose isomerase
Zn	zinc

ABSTRACT

This dissertation focuses on the structural changes induced by X-rays during macromolecular crystallographic data collection. This damage cannot be prevented and often leads to degradation in the data quality, which can affect the resulting structure and thus the biological interpretation. The aim of this research was to understand the radiation chemistry of the damage process. This includes the protein components most susceptible to damage, the disulfide bond and metal atoms. By providing some insight into the mechanism for disulfide bond cleavage and the role the active site metal and its surrounding environment plays in the extent of the damage that occurs we have proposed an initial, generalized model for radiation damage. The results indicate that this multi-track process is due to the overlap of two one-electron reductions or two one-electron oxidations. A reaction scheme for the most susceptible residues (cystine, cysteine, methionine, aspartate, glutamate and tyrosine) is provided with experimental evidence of the predicted damage from crystallographic data collected on lysozyme and xylose isomerase.

1. Introduction

1.1 *Structural Biology and X-ray crystallography*

Structural biology concerns the molecular structure and from that the mechanism of biological molecules. These range in size from ~0.3 nm for small peptides to ~30 nm for complex biological machinery such as the ribosome. These cannot be seen through an optical microscope; they are smaller than the wavelength of light, so a variety of biophysical techniques are employed. These techniques include electron microscopy, nuclear magnetic resonance (NMR) spectroscopy and X-ray crystallography. X-ray crystallography is the predominant technique, representing ~88% of the ~81,000 protein structures deposited to date in the Protein Data Bank (PDB) (Berman *et al.*, 2000). X-ray crystallography, as its name implies, employs X-rays to probe structural arrangement at the atomic level. These X-rays have a wavelength on the order of 0.1 nm (~1Å), an order of magnitude comparable to inter-atomic bond distances.

It is hard to overstate the importance of crystallography in structural biology. Some 13 Nobel Prizes have been awarded in its biological application. These include the discovery that enzymes could be crystallized (Inglis *et al.*, 2006, Gizatullin *et al.*, 2006, Northrop, 1946), the first structures of globular proteins (Kendrew, 1962, Perutz, 1962), the double helical structure of DNA (Crick, 1962, Harding, 2006, Wilkins, 1962), the three-dimensional structure of a photosynthetic reaction center (Deisenhofer, 1988, Huber, 1988, Michel, 1988), potassium channels (Agre, 2003, MacKinnon, 2003), the molecular basis of eukaryotic transcription (Campbell, Foster*, et al.*, 2006) and the

structure and function of the ribosome (Yonath, 2009, Ramakrishnan, 2009, Steitz, 2009) as examples.

X-ray crystallography is a key technique but the X-rays that provide structural information also induce radiation chemistry that can cause damage to the biological macromolecules making up the crystals. The introduction of third generation synchrotron sources has provided high brilliance monochromatic X-rays and an increase in the detail that can be seen, but at the same time they raise the significance of these radiation damage effects. As the X-rays interact with the crystal (containing the macromolecule, solvent within the crystal and any surrounding solution) free radicals are generated that propagate and cause structural changes. Both global and site-specific damage effects are observed (Gonzalez & Nave, 1994, Ravelli & McSweeney, 2000a, Murray & Garman, 2002, Muller *et al.*, 2002, Kmetko *et al.*, 2006, Weik *et al.*, 2000a, Burmeister, 2000b, Leiros *et al.*, 2001). Global radiation damage effects include increases in mosaicity, B factor, unit cell parameters, background noise and a decrease in intensity of reflections. Specific damage effects include the photoreduction of active-site metal atoms, disulfide bond breakage, decarboxylation of acidic side chains, carbon-sulfur bond cleavage in methionine residues and the loss of the hydroxyl group on tyrosine residues. Global damage effects are seen during the data collection process, while specific effects only become apparent in the refined structure.

Radiation damage occurs through interactions of X-rays with the crystal or the solvent depositing enough energy to break bonds. The energy is deposited through the photoelectric effect, where the energy of the photon ejects a lower shell electron from the atom forming free radicals, primarily hydroxyl and free electron radicals. This process is dose dependent and cannot be prevented. The free radicals can be formed in either the solvent (indirect effect) or the protein (direct effect). They then propagate through the sample causing further (secondary) damage. Secondary damage is time and temperature dependent and is limited by the diffusion of the damaging radicals. Cooling the sample to 100 K reduces the mobility of the radicals, reducing the secondary damage.

Both global and specific damage can be mitigated through the use of cryocooling at cryogenic temperatures (typically 100 K but sometimes as low as 4 K). Cooling the crystal to temperatures at or below 100 K reduces the mobility of the damaging hydroxyl radicals; a longer total X-ray exposure can be tolerated. Cryocooling prolongs crystal lifetime in the beam, but it does not eliminate the damage as the free electrons are still mobile. Methods for cryocooling have become well established, with over 90% of crystallographers collecting X-ray diffraction data at or around 100 K (Garman & Owen, 2006).

While we can mitigate radiation damage through cryocooling, the structural perturbations can still be significant. Some proteins are very radiation sensitive, for

example there are many proteins containing a metal redox center where excess electrons may cause photoreduction. Similarly there are residues that will be chemically sensitive to electron free radical attack. In the metal situation, case studies show a change in oxidation state (Carugo & Djinovic Carugo, 2005, Yano *et al.*, 2005) while sensitivity is seen through decarboxylation of glutamate and aspartate residues (Weik *et al.*, 2000a). These are discussed in detail in Section 1.3. This type of damage, if not identified, could easily lead to misinterpretation of a macromolecule's biological mechanism.

1.2 X-ray induced damage

1.2.1 Interaction of X-rays with the sample.

Protein crystals are composed of 30-70% solvent (Matthews, 1968). Crystals are typically mounted in a loop, surrounded by aqueous mother liquor, and vitrified for cryogenic data collection. An incident X-ray photon can pass completely through the sample in the loop, be diffracted, or be absorbed. At an energy of 12.7 keV, only 2% of the X-rays interact with the sample, with the rest hitting the beam stop. Of the 2% seen by the crystal, 8% interact via elastic and coherent Thomson scattering (Murray *et al.*, 2005) giving rise to X-ray diffraction. The rest interact via Compton scattering (8%) and via the photoelectric effect (84%). The energy absorbed through the photoelectric effect gives rise to hydroxyl radicals and hydrated electrons as mentioned above but also, protons, hydrogen radicals and molecular hydrogen (von Sonntag, 1994). These radicals have a short path length, are energetically unstable and react very quickly.

These radicals are able to diffuse through the crystal, causing further chemical reactions that perturb the molecules in the crystal lattice and damage the intermolecular contacts, which stabilize the lattice. With increased X-ray exposure, radical formation and propagation increases. Radiation damage is proportional to the number of radicals produced (from the energy absorbed in the crystal), rather than number of photons absorbed (Gonzalez & Nave, 1994).

1.2.2 Models of the damage process

Blake and Phillips conducted the first radiation damage study on crystals of sperm whale myoglobin at room temperature (Blake, 1962). They measured the same set of reflections seven times as a function of X-ray exposure time. Intensities decayed with time (corresponding to dose). Reflections were grouped according to their diffraction angle θ and average intensities in each group for each set of measurements were divided by the initial measurements. The resulting ratios were plotted as a function of $\sin^2\theta$. The decay of reflection intensity with resolution is given by

$$I=I_o\exp(-B \sin^2\theta/\lambda^2) \qquad [1]$$

where I is the measured intensity, I_0 the incident intensity and B, the mean square atomic displacement factor, that takes into account positional disorder and atom themal motion. Blake et al. (1962) noticed that as dose increased the data no longer fit this equation. They proposed that the proteins in the crystal became damaged and that the crystal could be modeled with three components after irradiation: (i) A_1, an undamaged fraction, contributing to diffraction at all angles; (ii) A_2, a highly disordered fraction, which only contributes to the diffraction at low angles and (iii) $1-(A_1+A_2)$, an amorphous

fraction, which does not contribute to the diffraction at all. Their model allowed two pathways to the destroyed amorphous state, an indirect pathway via the highly disordered part and a direct pathway from undamaged to destroyed. The proportion of these components was fit to the experimental data resulting in the graph shown in Figure 1.1.

$$I(t)/I_O = A_1 + A_2 \exp(-B_2 \sin^2\theta/\lambda^2) \quad [2]$$

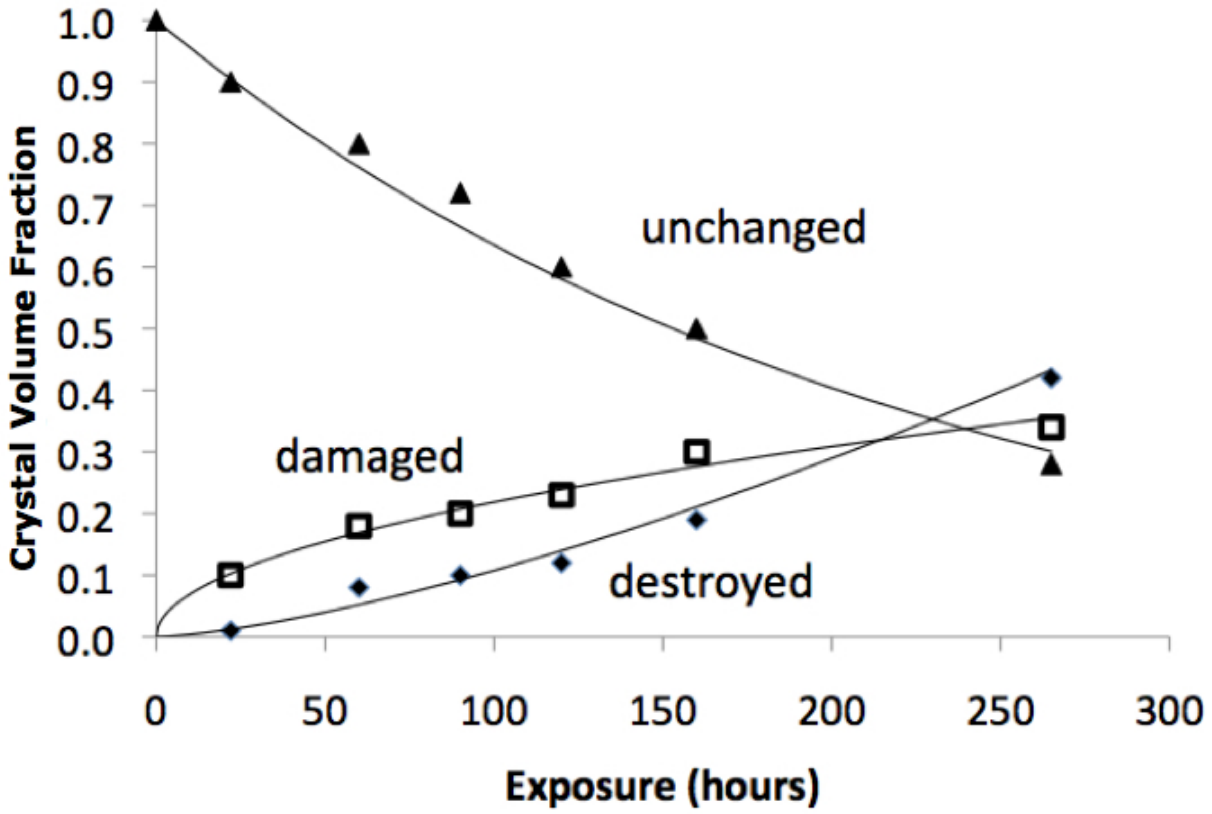

Figure 1.1: Proportion of unchanged (A_1), damaged (A_2) and destroyed ($1-(A_1+A_2)$) molecules as a function of exposure time. (Figure redrawn from Blake & Phillips 1962).

The dose was calibrated by photobleaching a radiation sensitive sheet. Using this dose calibration and the results shown in Figure 1.1 they were able to determine that each 8 keV X-ray photon was capable of disrupting 70 molecules and disordering 90 more, for doses up to about 20 Mrad.

Knowing that radiation damage was a problem, Haas and Rossman (1970) collected data at low-temperature (less than -60°C) on lactate dehydrogenase and two heavy atom derivatives. The crystals were prepared for cooling by dialysis against a sucrose-ammonium sulfate solution. They were plunged into liquid nitrogen for initial cryopreservation and held cold in a gaseous nitrogen stream. The decay in reflection intensity as a function of time was reduced ten-fold compared to crystals studied at 25°C. The cooling process did not seriously damage the crystal and the derivatives retained reasonable isomorphism with the native structure in the cooled state.

Using data collected from glycogen phosphorylase A, Fletterick et al. (1976) proposed a modified model for radiation damage, equation [3], that assumed a sequential process, the protein (A_1) becoming damaged (A_2) and then destroyed (A_3) with rate constants k_1 and k_2.

$$A_1 \xrightarrow{k_1} A_2 \xrightarrow{k_2} A_3 \qquad [3]$$

In this case direct transitions from the undamaged state (A_1) to amorphous destroyed (A_3) were no longer allowed. Building on these two models Hendrickson (1976) derived

an analytical expression for radiation damage which included rate constants for all possible paths.

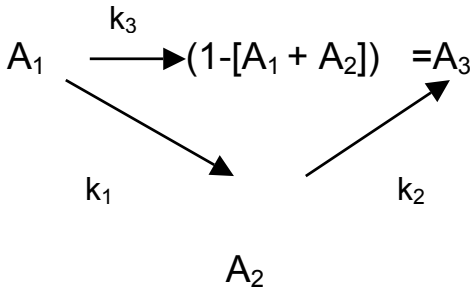

[4]

All three models explained the experimental data well at moderate dose with k_3=0, but none explained the data at very high dose. Sygusch et al. (1988) added a dose dependent component, A_1', between the damaged and undamaged state that conformationally resembles the undamaged state.

$$A_1 \xrightarrow{k_0} A_1' \xrightarrow{k_1} A_2 \xrightarrow{k_2} A_3 \qquad [5]$$

The transition from A_1 to A_1' is zero order, independent of concentration of protein, and irradiation beyond a certain time will convert the undamaged fraction (A_1) into the dose dependent fraction (A_1'). This model explained the intensity decay of reflections over the complete dose ranges studied.

1.2.3 Mitigating damage

There have been several methodologies developed to mitigate the damage that occurs during data collection. These include cryoprotection, the use of scavengers, multiple

crystal methods and combinations of all three. Cryoprotection makes use of both nitrogen (Garman, 1999, Teng & Moffat, 2000, Garman & Doublie, 2003, Kmetko *et al.*, 2006, Owen *et al.*, 2006a, Ravelli & Garman, 2006, Garman & Nave, 2009) and helium (Meents *et al.*, 2007, Teng & Moffat, 2002, Weik *et al.*, 2001, Chinte *et al.*, 2007, Meents *et al.*, 2010, Weik & Colletier, 2010) at temperatures typically of 100 K and close to 4 K respectively. Scavengers, also known as radioprotectants, chemically neutralize free radicals that are formed (Murray & Garman, 2002, Kauffmann *et al.*, 2006, Beitlich *et al.*, 2007, Southworth-Davies & Garman, 2007, Macedo *et al.*, 2009, Nowak *et al.*, 2009). Multiple crystal methods extract undamaged data from complete data sets and merge this to construct a complete undamaged set of data (Berglund *et al.*, 2002, Matsui *et al.*, 2002, Adam *et al.*, 2004). Each of these techniques (with the exception of the multiple crystal strategy) can prolong crystal lifetime in the beam but does not completely prevent radiation damage.

General cryocooling techniques were introduced for biological crystal samples by Hope (1988). Combined with the development of effective cooling systems (1987) and the use of loops for crystal mounting (Hough & Hasnain, 2003) the practice grew. Crystals are protected either with cryoprotectants already present in their growth conditions or by the addition of suitable cryoprotectants. They are then looped out of solution and cooled either by rapidly plunging in a cryogenic fluid (typically liquid nitrogen, but sometimes propane or helium) or by placing directly in a gaseous nitrogen or helium stream that is also used to maintain the crystals at cryogenic temperature during data collection. Cryocooling mitigates radiation damage but it has also enabled effective sample

manipulation and eliminated time-consuming capillary mounting. It is now the predominant protocol in current structural data collection (Garman & Doublie, 2003).

More recently, cryocooling techniques have been combined with the use of chemical scavengers that attempt to neutralize ionized groups formed by primary or secondary ionizations (Murray & Garman, 2002). Most of these scavengers, possess a ring like structure, allowing radicals to delocalize over multiple sites within the scavenger. Murray & Garman (2002) noted that ascorbate directly or indirectly scavenged the disulfide radical species in experiments on lysozyme crystals. Other studies have supported the protective effects of ascorbate (Southworth-Davies & Garman, 2007, Holton, 2007, Barker *et al.*, 2009) providing an optimal range of 0.3-1.0 M concentration for increased dose tolerance. Kauffmann et al. investigated the protective effect of three soluble scavengers: nicotinic acid, 5,5'-dithio-bis-2-nitrobenzoic acid (DNTB) and oxidized glutathione. DNTB provided an increase of five times the native crystal lifetime for lysozyme crystals, and while nicotinic acid did not increase crystal lifetime, it did reduce the specific damage to disulfide bond Cys64-Cys80. Both DNTB and nicotinic acid reduced the specific damage to disulfide bonds in thaumatin (Kauffmann *et al.*, 2006).

1.2.4 Dose, dose rate and energy

Studies have been carried out on the dependence of damage on dose, dose rate and energy. In terms of dose and dose rate a study of two MHC class I complexes and a viral polymerase, found that global radiation damage was proportional to the total

absorbed dose, not the dose rate (Sliz *et al.*, 2003). However, a dose-rate dependent increase in unit cell parameters was observed for crystals of holoferritin, which was attributed to sample heating (Ravelli *et al.*, 2002). Leiros et al. (2006) found the dose rate had no clear effect on global damage, but was a factor in specific damage. Increased dose rate resulted in increased radiation damage at sensitive sites, such as sulfur atoms. Similarly, a 10% lifetime decrease for a 10-fold increase in dose-rate was observed for crystals of apoferritin (Owen 2006). A more pronounced dose-rate effect was observed for crystals of holoferritin in the same study, with a 10% lifetime decrease for a 3-fold increase in dose rate. It is not clear if effects are general or sample specific.

The X-ray photoabsorption cross section of an atom is dependent on incident photon energy. X-ray crystallographic studies show that the energy at which data are collected has little or no overall effect on radiation damage (Gonzalez 1994, Weiss 2005). An energy range of 6.5 to 33 keV studied for lysozyme crystals with the same absorbed dose, confirmed this (Shimizu 2007).

The absorbed dose depends on incident flux, crystal size and crystal composition and can be calculated using the program *RADDOSE* (Murray 2004, Panthikar 2009), which takes these parameters into account.

1.3 Manifestations of damage

Radiation damage can be seen in both the initial data collection (global effects) and in the resulting structure (specific effects).

1.3.1. Global indicators

Global indicators of damage are seen in the X-ray data with scattering power gradually decreasing as a function of dose. This reduces the overall signal to noise (and therefore resolution) as X-rays scattered coherently (in the reflections) become incoherently scattered and increase the background. The agreement between symmetry related reflections will fall and the R_{merge}[1] will therefore increase. Other indicators of radiation damage include increasing crystal mosaicity, an increasing overall B factor, and unit cell volume increase (Ravelli *et al.*, 2002).

R_{merge} is a statistic used to indicate the quality of the X-ray data. It reflects the consistency of a dataset by comparing multiple observations of the reflection (related by symmetry). R_{merge}[1] is often reported as an average percentage for the dataset, in

$$R_{merge} = \frac{\sum_{h}\sum_{j=1}^{N}\left|F_M(h)\right| - F_j(h)\right|}{N\sum_{h}F_M(h)}$$

1

addition to the percentage for the high resolution shell. An increase in R_{merge} indicates the related reflections differ in their intensities and the total diffracted intensity has decreased.

The crystal mosaicity is an indication of the long-range order within the crystal; it describes the angular extent of any Bragg reflection and is a convolution of the crystal quality with instrument geometrical and spectral parameters. Lower mosaicity indicates a more ordered crystal and can result in a higher signal-to-noise, while increasing mosaicity spreads the reflections thereby reducing signal-to-noise, decreasing precision in intensity measurements and in the worst cases can lead to reflection overlap.

The B factor (also known as the temperature factor or the atomic displacement parameter) is a measure of how much an atom oscillates or vibrates about its centroid in the model. A reduction in X-ray scattering leads to an increased B factor. An increase in the Wilson B factor indicates the average position of the atoms in the protein is more mobile or uncertain. This can be an indication of radiation damage. However, since it is an average, the increase in Wilson B factor from one data set to the next is not expected to be large. After building and refining the model, it is possible to analyze the B factor for each residue.

The rate of change *(S)* of unit cell volume with accumulated dose ($S=\Delta V/\Delta$dose) is noted in radiation damage studies and has been suggested as a metric for radiation damage (Ravelli & McSweeney, 2000a, Ravelli *et al.*, 2002). The increase in *S* may be due to an electrostatic repulsion between the charges that buildup during each X-ray exposure. This effect was observed to be the greatest at temperatures near the glass transition state (155K), where water molecules, hydroxyl radicals and aqueous electrons become more mobile and potential energy is released via unit cell expansion.

These global indicators of damage are determined after the X-ray data collection is complete. For radiation damage studies, multiple data sets are collected to observe the progression of damage. The global damage metrics explained above indicate that a structure is damaged, but do not indicate to what extent.

1.3.2. Specific indicators

Structural studies show specific indicators for radiation damage and provide a clue as to how the process occurs. The oxidation of disulfides and saturation of aromatic side chains were observed in electron density maps of ribonuclease, after 0.1 MGy of absorbed dose (Burley et al. unpublished results, referred to in Helliwell 1988). A similar effect was seen in room temperature data collection of insulin (Helliwell, 1988). Inspection of difference electron density maps ($(F_{damaged}-F_{undamaged})e^{l\alpha}$) showed evidence

of cleavage and oxidation for all disulfide bonds after about 0.20 MGy of absorbed dose. This study suggested using fast data collection methods (i.e. using synchrotron radiation) might decrease the formation and propagation of dislocations or free radicals inducing secondary radiation damage. The intensity of the X-ray beam using synchrotron radiation was able to decrease the amount of time needed to collect a dataset, therefore the crystal would be in the beam for much less time with a more intense source. This led to an increase in achievable resolution. Specific chemical and structural damage to proteins at cryogenic temperatures was studied on proteins that diffract to high resolution (Weik *et al.*, 2000a, Ravelli & McSweeney, 2000a, Burmeister, 2000b, Leiros *et al.*, 2001, Fioravanti *et al.*, 2007). In addition to breakage of the disulfide bonds, there was loss of definition on carboxyl groups of acidic side chains, loss of the hydroxyl groups on tyrosines and carbon-sulfur bond cleavage in methionines. Irradiation can induce change in the oxidation state of a metal ion in the active site of the protein from its native state (Alphey *et al.*, 2003, Carugo & Djinovic Carugo, 2005, Yano *et al.*, 2005). This non-native state of the metal can be misleading in studies of mechanistic properties of a protein (Takeda *et al.*, 2004).

Specific damage occurs in a reproducible order. First disulfide bonds elongate and then break, then glutamates and aspartates are decarboxylated, tyrosine residues lose their hydroxyl group and finally carbon-sulfur bonds in methionine residues are cleaved. For specific damage to be observed, the protein structure has to be at least partially solved and refined. Specific damage occurs before there is any degradation in the diffraction pattern, as the damage may not affect every unit cell in the crystal in the same way.

Analysis of the resulting electron density map will indicate where damage has occurred; at regions with significant difference map peaks.

1.4 Implications of the damage

1.4.1 Failure of Multiple Anomalous Dispersion (MAD) phasing techniques

Multiple Anomalous Dispersion (MAD) is a technique used to determine phases using anomalous scatterers present in the crystal. MAD requires the collection of complete datasets at several wavelengths (typically three), ideally all from the same crystal. Local changes in protein structure with increasing dose results in a lack of isomorphism in the crystal between datasets, which complicates scaling. The decay in reflection intensities can cause the MAD phasing signal to be destroyed, making structure determination fail.

1.4.2 Susceptibility of components in the protein

Radiation damage is directly related to the absorbed dose during the diffraction experiment. The absorbed dose is proportional to the X-ray cross section of the elements making up the sample. For example, the X-ray photo-absorption of sulfur is almost 80 times larger than that for carbon or nitrogen at the energies typically used for X-ray diffraction experiments (Ravelli & McSweeney, 2000a). Sites with high X-ray cross sections, e.g. disulfide bonds, would be expected to be damaged first. Photoabsorption is not the only thing that dominates residue sensitivity. Residues can be reduced or oxidized by aqueous electrons or hydroxyl radicals, respectively.

Hydroxyl radicals are strong oxidizing agents. The order of chemical sensitivity, based upon ease of susceptibility to oxidation by hydroxyl radicals, is : tryptophan > tyrosine > thiols > disulfides ~ aliphatic residues (O'Neill, 2002).

1.4.3 Reduction of metal sites

Metalloproteins contain one or more metal ions; these metals are often found in the active site. Metals also have large X-ray absorption cross-sections, leading to the susceptibility of residues around the metal ions to damage. Enzymes that function to perform a reduction or oxidation reaction have evolved to channel electrons into the active site. Techniques used to mitigate damage, such as scavengers and using short wavelength X-rays, are not efficient enough to preserve the redox intermediates during conventional X-ray data collection. X-ray induced electrons and free radicals are generated during data collection. The metal cofactors can absorb free electrons and change the metals oxidation state, or coordination number. This causes difficulty in determining the intermediate redox states throughout an enzyme mechanism. This was the case for horseradish peroxidase, with unknown intermediates until 2002 when Berglund et al. (2002) employed the multi-crystal data collection approach to track the oxidation state of the heme iron. Using this approach, they solved the structures of the five states of horseradish peroxidase with preserved active site. Yano et al. (2005) observed structural damage to the manganese cluster in photosystem II before damage was detected through the loss of diffractivity. By using X-ray absorption near edge spectroscopy (XANES) they tracked the redox state of the metal and the spectra

showed that the structure changes from a high-valent Mn (III_2, IV_2) to Mn(II) upon irradiation. This study suggested the use of complementary spectroscopic methods to monitor the oxidation state of the metal during X-ray data collection. Belitch (2007) followed this suggestion and collected online spectroscopy data on three different proteins, myoglobin, cytochrome P450cam and chloroperoxidase, which showed very rapid reduction of the heme iron. The dose required for reduction was reached before a full dataset was collected. These studies all show that radiation damage occurs in metalloproteins and alters the redox state of the metal in the active site. This specific damage can affect the structural information subsequently causing a misinterpretation of the enzyme mechanism.

1.5 Techniques to monitor damage

Since there is no technique available to prevent radiation damage, it is important to understand the process of damage and how it might affect an X-ray diffraction experiment and the resulting structure. Biological information is often extracted from these structural models and misinterpretation of that information could be avoided with foreknowledge of the damage process and how it can affect the. There are many complementary techniques that can be used to study the damage process; these include techniques that can be used in parallel with X-ray diffraction. In the work presented here, we have used a combination of X-ray crystallography, online spectroscopy and Electron Paramagnetic Resonance to study the radiation damage process and to develop a model for radiation damage.

1.5.1 X-ray crystallography

X-ray crystallography is a method used to determine the three dimensional arrangement of atoms in a protein crystal. An incident beam of X-rays interacts with the crystal, producing a diffraction pattern. Based on the diffraction patterns obtained from the periodic arrangement of molecules within the crystal, the electron density can be reconstructed. A model is built into the electron density and refined against the data, giving a molecular structure.

X-ray crystallography can be used to monitor damage by collecting consecutive datasets on the same protein crystal (Weik *et al.*, 2000a, Ravelli & McSweeney, 2000a). This allows tracking the progression of damage with dose in a single crystal. Global damage can be assessed through metrics such as unit cell expansion, decrease in reflection intensities and increase in Wilson B factor over the course of the consecutive data collection. Specific damage can be assessed by analysis of changes in electron density, specifically in susceptible regions of the protein. The active site damage can be assessed by changes in bond lengths, metal coordination and occupancy.

1.5.2 UV/Visible microspectrophotometry

UV/Visible microspectrophotometry can be used to probe protein crystals containing metal centers, chromophores or colored substrates and cofactors, as it is sensitive to

their valence structure. This technique measures the intensity of light passing through a sample and compares it to the intensity of the light before it passes through the sample. Absorbed energy excites an electron into an empty higher orbital. The absorbance of energy can be plotted versus wavelength to get an UV/Vis spectrum. This can be applied to metallo-enzymes, photosensitive proteins or proteins containing colored co-factors, substrates or products. This technique is non-destructive, allowing the same crystal to be used for X-ray data collection. By examining the difference spectra of the native protein and the irradiated protein, one can make qualitative conclusions about the redox state of the protein.

Offline microspectrophotometry was used to monitor an absorption peak at 400 nm, indicative of the formation of disulfide radicals, in crystals of acteylcholinesterase (Weik *et al.*, 2002a). By combining the absorption data with the structural data, there was evidence for disulfide elongation and therefore creation of the disulfide radical anion upon X-ray irradiation. This technique can also be used to investigate the protective effect of scavengers (Murray & Garman, 2002) by comparing absorption spectra from before and after exposure to X-rays. Spectroscopy can be used to study intermediates of light, oxygen and voltage sensitive proteins and determine the enzyme's mechanism by causing turnover in the enzyme (Matsui *et al.*, 2002, Takeda *et al.*, 2004, Sato *et al.*, 2004, Adam *et al.*, 2004, Hough *et al.*, 2008), or to track specific active site changes (Dubnovitsky *et al.*, 2005), and of interest to this subject matter, studies of X-ray induced structural modifications (Berglund *et al.*, 2002, Carugo & Djinovic Carugo, 2005, Pearson *et al.*, 2007).

1.5.3. Electron Paramagnetic Resonance (EPR)

EPR is a technique used to study chemical species that have one or more unpaired electrons. It allows for the detection and identification of free radicals and paramagnetic centers. Radicals produce an unpaired spin on the molecule from which the radical is removed. EPR is sensitive enough to detect the free radical species generated by X-ray irradiation. The interaction of an external magnetic field with the electron spin depends on the magnetic moment of the spin, of which two orientations are possible, parallel or anti-parallel to the applied field. This creates distinct energy levels for the unpaired electrons, making it possible for the net absorption of electromagnetic radiation to occur. This is referred to as the resonance condition and takes place when the energy of the microwaves corresponds to the energy difference between the pair of spin states. Unlike X-ray absorption studies, with spectral changes only due to metal site or co-factor changes, EPR provides information for the radiation induced radical formation in the whole protein. EPR studies can be conducted at low doses (in the kGy dose range), irradiating the crystal with minimal surrounding mother liquor and observing the radicals at 4 K in the instrument.

While EPR studies of dry protein or protein in aqueous solution have been conducted for over 50 years, the calculations for radical yields in single protein crystal had not been performed previously. However, there was evidence to support our experimental approach. EPR spectra have shown direct evidence for radiation-induced reductions of quinones and other cofactors in crystals of the photosynthetic reaction center (Utschig

et al., 2008). The quantification of free radical production with dose will aid in the development of a radiation chemistry model for radiation damage in irradiated macromolecules.

1.6 Outline of research

Radiation damage is a dose dependent process, inherent to X-ray crystallography. There are many variables that can affect the radiation damage to a crystal. Techniques such as cryocooling and the use of free radical scavengers can mitigate the process, but primary damage cannot be prevented. The order of damage susceptibility is known: metal targets are the most susceptible to photoreduction, followed by disulfide bond cleavage, decarboxylation of acidic side chains, carbon-sulfur bond cleavage in methionines and loss of the hydroxyl group on tyrosine residues. However, there are still many aspects of the radiation damage process that are yet to be determined; the dose at which disulfide bond cleavage occurs, the influence of the metal and its surrounding amino acid environment on the extent of damage that occurs and the development of a generalized model for radiation damage based on radiation chemistry. This work will provide insight into the mechanism of X-ray induced radiation damage.

The mechanism of X-ray induced cleavage of disulfide bonds in protein crystals has been studied using X-ray crystallography (Weik 2000, Murray & Garman, 2002) and microspectrophotometry (McGeehan 2009, Carpentier 2010). From these studies, it has been proposed that X-rays induce reduction of RSSR (disulfide) groups to reversibly

form disulfide radical anions ($RSSR^{\bullet -}$) and sulfur-sulfur bond is elongated by ~0.7 Å (Weik 2002). A study by Carpentier *et al.* (2010) using Raman spectroscopy and X-ray crystallography to track disulfide bond breakage, suggested the reversible build up of one (or several) intermediate radical states along the disulfide bond breakage pathway. By comparing the Raman spectra with the difference electron density at the sulfur atoms, they also determined the saturation dose for the disulfide radical anion, reaching a maximum concentration at <~5.0 MGy. This study was the first to show the disulfide bond repair facilitated by X-rays. These studies have all been done at doses typically associated with X-ray crystallography (MGy).

In chapter 2, radiation induced mechanism of disulfide bond breakage is studied with the outcome that the process is a result multi-track radiation chemistry. By collecting low dose EPR spectra on single crystals of lysozyme and comparing the data with higher X-ray dose online microspectrophotometry the dose at which disulfide bond breakage occurs as well as the dose at which the disulfide radical saturates are determined. This information provides the basis for a new model for the radiation chemistry of X-ray induced disulfide bond breakage.

Currently, there is no comprehensive model for the radiation damage process. There are many studies that characterize some aspects of the damage, but they are not generalizable for other proteins. Combining information from the multi-track model for disulfide bond cleavage presented in chapter 2 with radiation chemistry results from

other susceptible amino acid residues has allowed the initial development of a general model for radiation damage. This model is presented in chapter 3 and explains the expected structural changes induced in a crystalline protein at cryotemperatures during irradiation.

To extend the general model to metalloproteins in chapter 4, a radiation damage study on a metalloprotein, Xylose Isomerase (XI), is conducted. Discrepancies in the proposed enzymatic mechanism of XI still exist and this study also looked to see if radiation chemistry effects could explain these. By collecting consecutive datasets on substrate free XI, radiation induced changes were seen in the structure of XI. These structural changes showed similarity to some structural changes previously attributed to the mechanism.

Chapter 4 showed that the position of metals in a protein can change during irradiation. In chapter 5, we investigated the role of the active-site metal and its surrounding amino acid environment in the extent of the radiation induced damage. The active-site metal of XI was exchanged with other divalent metal ions and structural studies were carried out as a function of the metal and dose. The protein's active-site environment may play also play a role in the extent of damage that a protein undergoes. This was the basis for a similar study performed on superoxide dismutase, an enzyme that actively scavenges free radicals. The two proteins with significantly different environments are analyzed; XI, with acidic side chains, known to be susceptible to damage and SOD1 with histidine

residues, known to be electron sinks, coordinating the active site metal atoms. The metal and the environment have an influence on the damage seen.

In Chapter 6 the results are linked together and the status of a general radiation chemistry model described along with the additional studies needed to bring that to fruition.

2. Insights into the mechanism of X-ray induced disulfide bond cleavage in lysozyme crystals based on EPR, optical absorption and X-ray diffraction studies

2.1 Introduction

As noted in chapter one, specific structural damage to particular covalent bonds occurs in a reproducible order. First disulfide bridges elongate and then break, second glutamates and aspartates are decarboxylated, third tyrosine residues lose their hydroxyl group and fourth the carbon-sulfur bonds in methionines are cleaved (Weik *et al.*, 2002b, Weik *et al.*, 2000b, Burmeister, 2000a, Ravelli & McSweeney, 2000b). These structural effects occur before global effects are seen, *i.e.* decreasing diffraction intensity, and increasing B factor, R-factors, mosaicity and unit cell volume. Disulfide bond breakage has been studied in detail by Carpentier *et al*. (2010) who combined Raman spectroscopy with X-ray studies of Chicken egg white lysozyme (CEWL) crystals. They proposed a process initiated by a rapid build-up of an anionic radical intermediate that either reverts back to the oxidized state or evolves toward a protonated radical species or cleaved product. Their data strongly suggested an X-ray induced 'repair' mechanism. This was supported by UV microspectrometry studies on the X-ray irradiation of trypsin crystals (McGeehan *et al.*, 2009).

In this chapter radiation chemistry theory combined with X-ray measurements, UV/visible spectroscopy and electron paramagnetic resonance (EPR) are used to develop and test a quantitative model of the radiation damage associated with disulfide bonds. CEWL, a relatively small protein with 129 residues and four disulfide bonds per molecule, is used to test the model. Two of these are intra α-domain disulfide bonds (C6-C127 and C30-C115), one an intra-β-domain disulfide bond (C64-C80) and the final one an inter-αβ-domain disulfide bond (C76-C94). The model presented here is based on physical-chemical properties and therefore its application is not limited to lysozyme. It is proposed as a first step in a comprehensive, predictive model of the radiation induced processes that perturb the native structure of biological macromolecules.

The chapter is based on a paper to be submitted for publication to *Acta Crystallographica* Section D (Sutton, K.A., Black, P., Mercer, K., Garman, E.F., Owen R.L., Snell, E.H. and Bernhard, W.A. (2013)). Advice on the chemical and mathematical model came from Bernhard, the microspectrophotometry work was performed by Garman and Owen. The rest of the work described was performed by, or directly involved the author. The full study, including the model and microspectrophotometry work is presented here; the model is confirmed by the experimental data. The microspectrophotometry provides the link between EPR and the crystallographic analysis.

2.2 The Radiation Chemistry of Disulfide Bond Breakage.

2.2.1 Mechanistic Model

In earlier work on crystals and films of DNA, a mechanistic model was developed in order to describe the dose dependence of radiation products (Swarts *et al.*, 2007b). The model was used to quantitatively connect the yields of product (produced by X-rays of 70 keV) with the yields of the intermediate free radicals trapped by DNA. These products were produced by the direct effect, whereby energy is deposited directly in the DNA. Doses of 10 to 100 kGy were used to detect and quantify products. In this dose range, a bend in the product's dose response curve was difficult to explain using a conventional model based on a linear one-to-one correspondence between radical intermediate and end product. We have developed a new model here that ascribes product formation, in the higher dose range, incorporating the interaction of two separate tracks. A track begins with inelastic Compton scattering, creating a fast electron, a secondary photon of lower energy and a radical cation. The secondary photon and fast electron propagate the track by creating additional fast electrons, photons, electronic excited states, and radical cations. The ejected electrons eventually thermalize creating primarily radical anions. The radical anions, radical cations, and excitations are distributed non-homogeneously, in a branched structure known as a track. As dose increases, the probability of one track overlapping another increases and consequently the probability of any given site being ionized twice also increases. At the energies typically associated with macromolecular crystallography, the photoelectric effect dominates the total X-ray interaction with the crystal (Paithankar & Garman, 2010). The chemical effect is similar to that of Compton scattering, creating a fast

electron, a secondary photon of slightly lower energy (if decay of atom is by fluorescence rather than by Auger electron emission) and a radical cation.

Under the expectation that the role of two ionizations at one site would play an important role in explaining S-S bond damage seen in X-ray crystallographic studies of macromolecular crystals, the model is expanded here to describe these systems. The model implies that the S-S bond in macromolecular crystals at 100 K would not be cleaved as a result of a single one-electron reduction but rather by one-electron reduction followed by protonation, then a second one-electron reduction. Concurrence of these events at the same site, although possible within a single track of ionizing radiation, has a much higher probability when tracks overlap each other. The probability of S-S bond cleavage, therefore, increases when two tracks intersect at the same S-S site.

The key reaction pathways constituting our chemical model for cleavage of the disulfide bond (RSSR) into sulfhydryl groups (RSH + SHR) in the solid state (crystals at ≤ 100 K) are shown in Figure 2.1. In step $\mathbf{1_+}$, one-electron addition yields the radical anion, $SS^{\cdot -}$ with the rate constant k_r. If RSSR is coordinated with a favorable proton donor, then proton transfer gives the neutral radical, SS(H)•, as in step $\mathbf{2_+}$. This is reversible, with the back reaction indicated in Figure 2.1 as step $\mathbf{2_-}$, providing a repair pathway. If a radical cation is generated in the proximity of RS-SR, either by the same track or a second track, deprotonation of that radical cation may result in protonation of $SS^{\cdot -}$: this

is presented as step **3** in Figure 2.1. Unlike $\mathbf{2}_{+}$, step **3** is not reversible. The unpaired electron in $SS^{\cdot -}$ and $SS(H)^{\cdot}$ resides in a three-electron sigma bond (Rao *et al.*, 1983b, Asmus *et al.*, 1977).

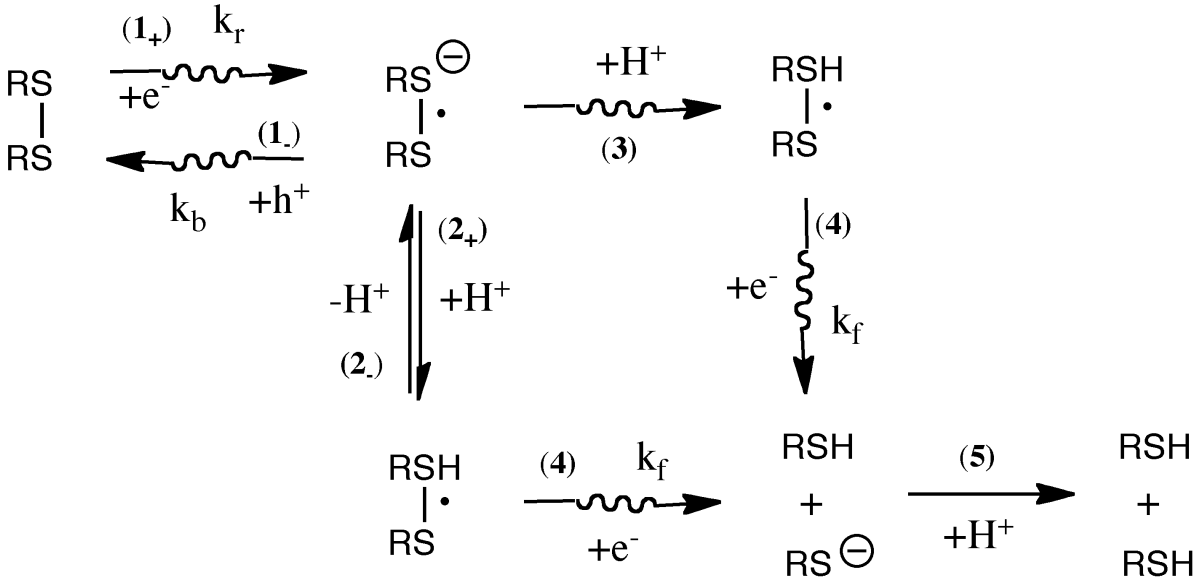

Figure 2.1: Key reaction pathways constituting the proposed chemical model for cleavage of the disulfide bond.

Typically, crystallographic data collection is carried out under cryogenic conditions at a temperature of ~100 K. Helium, which boils at 4 K, can be used to reduce that temperature but even at 4 K the $SS^{\cdot -}$ and $SS(H)^{\cdot}$ radicals will be highly reactive with holes (radical cations designated as H^+) and electrons that are generated by an overlapping track. Reaction with a hole generated by the same, or a second track, takes the radical anion backward to its parent. On the other hand, electron attachment (step **4)** drives $SS(H)^{\cdot}$ forward to the product, **1-** with a rate constant of k_f. The cleavage products, RSH and RS-, can progress via step **5** to give two RSH. Pivotal to SS cleavage is the competition between the back reaction at rate k_b in **1.** and the forward reaction at rate k_f in step **4**.

2.2.2. Mathematical description

A mathematical model can be developed based on the reaction scheme proposed in Figure 2.1 consisting of two first order reactions. In the first, radiation drives a reversible reaction between a parent molecule *M*, and a radical intermediate *R*, and in the second, radiation irreversibly drives the radical *R* to the product *P*.

$$M \underset{k_b}{\overset{k_r}{\rightleftharpoons}} R \xrightarrow{k_f} P \qquad (2.1)$$

In this case *M* is the disulfide bond, RSSR, and *P* is the cleaved disulfide, two RSHs. The radical intermediate, *R*, depends on the path. All of the reactions proposed in Figure 2.1 fall into either radicalization or product formation. The dependence of the

concentration of *M*, *R,* and *P* on dose, *D*, is described by three first order differential equations containing rate constants k_r, k_f, and k_b:

$$\frac{dM(D)}{dD} = -k_r M(D) + k_b R(D) \tag{2.2a}$$

$$\frac{dR(D)}{dD} = k_r M(D) - (k_f + k_b) R(D) \tag{2.2b}$$

$$\frac{dP(D)}{dD} = k_f R(D) \tag{2.2c}$$

This set of coupled equations arises in a number of different fields. The solutions are:

$$M = \frac{M_0(qe^{-mD} + e^{-nD})}{q+1} \tag{2.3a}$$

$$R = \frac{M_0((qm+n)e^{-nD} + (qm-n)e^{-mD})}{(q+1)((m-n)} \tag{2.3b}$$

$$P = M_0 + \frac{M_0(ne^{-mD} - me^{-nD})}{m-n} \tag{2.3c}$$

where M_0 is the concentration of *M* at zero dose and *m*, *n*, *q* (used for compactness) are determined by the three rate constants using

$$n = \frac{2k_r k_f}{(k_r + k_b + k_f) - \sqrt{(k_r + k_b + k_f)^2 - 4k_r k_f}} \quad (2.4a)$$

$$m = \frac{(k_r + k_b + k_f) - \sqrt{(k_r + k_b + k_f)^2 - 4k_r k_f}}{2} \quad (2.4b)$$

$$q = \frac{n - k_r}{k_r - m} \quad (2.4c)$$

Equations 2.2-2.4 describe the dose dependence of the concentrations of *M*, *R,* and *P* using four physically relevant parameters: the rate constants k_r, k_f, k_b, and initial concentration of *M*, M_0.

2.3. Experimentally testing the model

2.3.1. Crystal Preparation

Chicken egg white lysozyme crystals for the Electron Paramagnetic Resonance (EPR) and X-ray crystallographic studies were prepared using protein purchased from Hampton Research (HR7-110, Aliso Viejo, CA) without further purification. Crystals were grown using the hanging drop vapor diffusion method with a protein concentration ranging from 50-75 mg/ml in 0.1 M sodium acetate buffer, pH 4.8. The precipitant, prepared in the same buffer, contained 7.5-15 % (w/v), sodium chloride and 25 % (v/v) ethylene glycol as a cryoprotectant. Drops of 10 µl were setup with a 1:1 protein to precipitant ratio. The crystallization precipitant was also used for reservoir solution. For the UV spectroscopy (microspectrophotometry) studies, similar crystallization conditions were used with the exception that the cryoprotectant was incorporated by soaking

crystals in mother liquor containing 20 % (v/v) glycerol rather than growing the crystals in the presence of ethylene glycol.

2.3.2. Microspectrophotometry

Crystals were mounted in fiber loops, flash-cooled in liquid nitrogen and held at 100 K by an open flow nitrogen stream, and then irradiated at Diamond Light Source beamline I24. An energy of 12.8 keV was used and the beam was defocused to be 50×50 μm^2 with an incident flux of 1.54×10^{12} ph s^{-1} at the sample position. Changes in UV/visible optical absorbance were measured using an *in-situ* microspectrophotometer with a 50 μm diameter probe beam to closely match the X-ray illuminated area. Spectra were collected using mirrored lenses (Bruker, Billerica, MA) mounted in an off-axis geometry with a deuterium halogen light as the light source (Ocean Optics, Dunedin, FL). Absorption was monitored over the wavelength range of 300-800 nm using a Shamrock 303 imaging spectrograph (Andor, Belfast, UK). One spectrum was collected over a continuous 20 s exposure. A second spectrum was collected to further probe saturation effects by subjecting another crystal to a series of 1 s exposures interspersed with a 5 s rest period with the X-ray shutter closed.

2.3.3. Irradiations and EPR

For the EPR studies crystals were harvested directly from the crystallization drop and mounted in 1.0 mm outer diameter quartz glass capillaries tubes (Hampton Research). An approximate measure of crystal dimensions was made for each (+/- 50 μm) using a

stereo microscope. The capillaries contained mother liquor on both sides of the crystal approximately 100 μm away to keep the crystal hydrated. They were then sealed at either end using wax and mounted on a sample stage for the EPR measurements. These were inserted into a Janis liquid helium cryostat in the EPR machine and cooled to a temperature of 4 K in less than 30 seconds. No attempt was made to obtain precise information on alignment of the crystal with respect to the magnetic field. Crystals were irradiated *in situ* with 70 keV X-rays at 4 K using a Varian/Eimac OEG-76H tungsten target tube operated 20 mA, and filtered by a 25 mm aluminum foil. The dose rate at the sample was 0.0125 kGy s^{-1}, determined by calibration with radiochromic film (Niroomand-Rad *et al.*, 1998). Following irradiation, EPR was performed on samples at 4 K. First-derivative EPR-absorption spectra were recorded at Q-band (35.3 GHz) microwave frequency. An upper limit on formation of water ice during sample cooling was obtained by the observation that the EPR signal due to hydrogen atoms was not observed. Ice irradiated at 4 K gives a distinctive 50 mT doublet due to trapped hydrogen atoms (Johnson & Moulton, 1978). Lack of the doublet signal limits the ice content to a few percent of crystal mass and, based on extensive experience with other organics at high concentration, the above cooling procedure created little to no water ice. As the system is closed we cannot absolutely determine if the sample has cooled amorphously or if crystalline ice has formed. However, the EPR signal is largely independent of this (Bednarek *et al.*, 1998) so unlike crystallography, the type of ice formed does not impact our measurements.

Double integration of the EPR spectra gave the number of trapped free radicals by comparison with the signal of a ruby standard mounted on the inside wall of the microwave cavity. A relatively weak quartz signal, produced in the capillary, was subtracted out as described previously (Purkayastha & Bernhard, 2004) and, thereby, isolates the signal from the lysozyme crystal. The number of radicals per crystal mass is the radical concentration *R (D)* used to calculate the chemical yield. A total of three lysozyme crystals were studied; their dimensions, approximate volume and the dose points where spectra were recorded are given in Table 2.1. All crystals were measured to obtain their dimensions. The mass of Crystal 1 was determined by weighing the crystal sealed in the capillary before irradiation, repeating the measurement after irradiation with the capillary cracked to remove any mother liquor, and finally dissolving the crystal and weighing just the dry capillary and wax sealant. The masses of the other two crystals were determined by scaling the known mass of the first to the total free radical concentration at 20 kGy. These masses were validated by comparison with the measured dimensions, Table 2.1.

Table 2.1: Crystal dimensions and dose points used for EPR measurements

	Dimensions (mm)	Volume (mm^3)$^+$	Weight (µg)	Dose points for EPR measurements (kGy)
Crystal 1	0.60 × 0.50 x 0.40	0.12	208	5, 10, 20, 40, 60, 100, 150
Crystal 2	0.50× 0.50 x 0.25	0.06	135*	10, 20, 40, 60, 100
Crystal 3	0.50× 0.50 x 0.40	0.10	185*	20, 40, 100, 200, 300, 400, 500

+Volume is approximate, calculated by assuming a cuboid, which does not take into account crystal shape. *Masses were calculated based on the measured radical yield at 20 kGy exposure as detailed in the results section later.

After accumulating data at 4 K, Crystal 3 was annealed to consecutively higher temperatures (50, 100 and 150 K), held at that temperature for 15 minutes, and then returned to 4 K (where all radicals are trapped) to record the impact of annealing.

Chemical yield is defined as the slope of the dose response at zero dose. In an often-used simple case, the dose response for radicals trapped in the solid is described by:

$$\frac{dR(D)}{dD} = R_{\infty} - kR(D) \tag{2.5}$$

the solution of which is

$$R = R_{\infty}(1 - e^{kD}) \tag{2.6}$$

In order to obtain the expression for the chemical yield, *G*, a Taylor expansion is applied under the condition *kD* <<1.

$$G = kR_{\infty} \tag{2.7}$$

Equations 2.6 and 2.7 are applicable when destruction of the radical only returns it to the parent structure. In other words, there is no forward reaction producing a product and, consequently, there is no depletion of the parent molecule beyond that due to radical formation. Under these conditions *R* reaches saturation at R_{∞}. The units of *R* are mol g^{-1} and the initial slope of the dose response, *R* vs. *D*, is the chemical yield *G* in mol J^{-1}.

Of interest here are the two closely related radicals $SS^{\cdot -}$ and $SS(H)^{\cdot}$ described in §2.1 and shown in Figure 2.1. $SS^{\cdot -}$ and $SS(H)^{\cdot}$ are collectively described by the radical concentration denoted *R(SS)*. The fraction of trapped radicals ascribed to *R(SS)* is *F(SS) = R(SS)/R(tot)*, where *R(tot)* is the concentration of all radicals trapped in the crystal.

The dose response curves were recorded separately for the three crystals described earlier. The yield of all radicals trapped in each crystal, *G(tot)*, was calculated from the initial slope of the curve described by Equation 6. Non-linear least-squares fits were performed using the Graphpad Prism Software (GraphPad Software, LaJolla, CA).

In order to determine *F(SS),* the powder spectrum of $SS^{\cdot -}$ was simulated using published g- and hyperfine coupling tensors reported by Lawrence *et al*. (1999) and the simulated spectrum was used to fit the *R(SS)* component of the EPR spectrum. The use of a powder spectrum assumes a large number of randomly oriented radicals. Simulations were performed using Powder Sim, a program developed in house (Bernhard & Fouse, 1989). While treating the experimental spectrum as a powder spectrum is not strictly correct, it is a reasonable approximation because i) the lysozyme crystal contains 32 magnetically distinct cysteines per unit cell (4 per molecule and 8 molecules per unit cell) and ii) the signal anisotropy was difficult to discern when the crystals were rotated through 180° in 15° steps. Of course (ii) is a direct consequence of (i).

2.3.4. X-ray crystallography

For crystallographic studies, crystals were harvested using a nylon CryoLoop (Hampton Research, Aliso Viejo, CA) and flash cooled in liquid nitrogen. They were shipped to Stanford Synchrotron Radiation Laboratory (SSRL, Palo Alto, CA) where diffraction data were collected at 100 K remotely using a MAR325 CCD detector on beamline 9-2. The synchrotron data were collected at an energy of 12 keV (1.033 Å) and a detector distance of 131.6 mm, and the beam was attenuated by 93.6% giving a flux of 3.8×10^{10} phs^{-1}. Two initial images were recorded 90° apart and used with the *STRATEGY* option of *Blu-Ice* (Gonzalez *et al.*, 2008, McPhillips *et al.*, 2002) to define an appropriate starting angle. A total of 15 datasets over 57.0° were collected using a 2 s exposure and oscillation angle of 1.0°, each data set starting at the same position as the first ensuring that the same area of the crystal was irradiated for each dataset. The crystal was approximately 0.3 × 0.3 × 0.3 mm with the beam (approximating a top hat profile) illuminating an area of 0.2 × 0.2 mm. The absorbed dose was estimated using the program *RADDOSE*, version2 (Murray *et al.*, 2004a, Paithankar *et al.*, 2009b) but not adjusted for fresh regions of the crystal that rotated into the beam (estimated to reduce the calculated absorbed dose by less than 0.2% per °).

The data were integrated with *HKL2000* (Otwinowski & Minor, 1997) and reduced with *SCALA* (Evans, 2006). An initial model was determined by molecular replacement using *MOLREP* (Vagin & Teplyakov) with lysozyme entry 6LYZ from the Protein Data Bank (PDB) as the search target. The resulting model was refined against the data using an iterative process combining *PHENIX* (Adams *et al.*, 2010b) with manual model building

using *COOT* (Emsley *et al.*, 2010). The process continued until there were no positive or negative peaks in the electron density above 5 sigma. Isomorphous difference Fourier maps, Fo_n-Fo_1 were calculated with *PHENIX* (Adams *et al.*, 2010b), using the observed amplitudes from each dataset and the phases derived from the model fitted to the first dataset. This technique is a sensitive way to visualize specific damage (Weik *et al.*, 2000b, Carpentier *et al.*, 2010). The maps were viewed in *CCP4mg* (McNicholas *et al.*, 2011). The solvent accessibility of the cysteine residues involved in the disulfide bonds was calculated using *AREALMOL*, part of the CCP4 package (Winn, 2003).

2.4. Results

2.4.1 Microspectrophotometry

The X-ray induced changes in the optical absorption of lysozyme crystals upon irradiation were monitored using an on-line microspectrophotometer. Increased absorbance at 400 nm has been attributed to the radical species SS•- (Weik *et al.*, 2002b) and this can clearly be seen in the spectral series in Figure 2.2(a) from a continuous 20 s irradiation with a cumulative dose of 5.74 MGy (dose rate 287 kGy s^{-1}). Absorbance at 400 nm increases rapidly before saturating. In Figure 2.2(b) the dose-dependent increase in absorbance at 400nm is plotted. The saturating dose is defined as the point when the absorbance reaches 90% of the maximum, D_{90}. This is the point where fast changes no longer dominate. In this case the D_{90} for lysozyme crystals is 2.7 MGy.

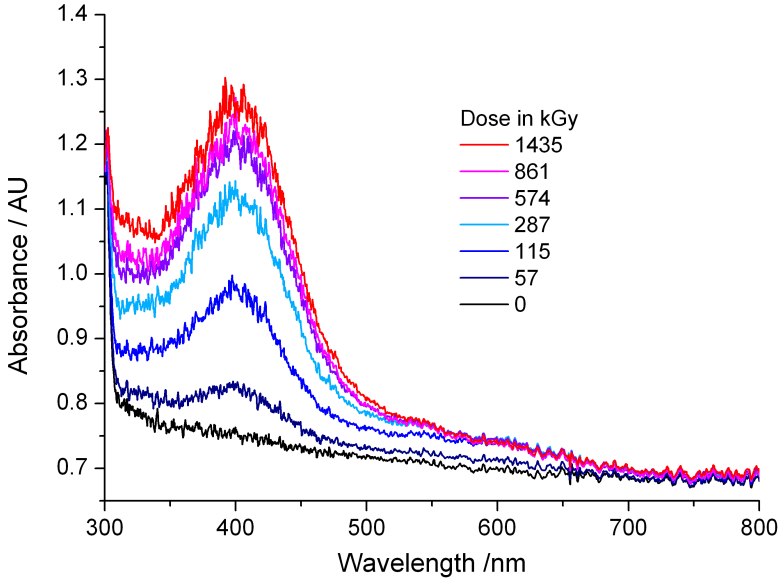

(a)

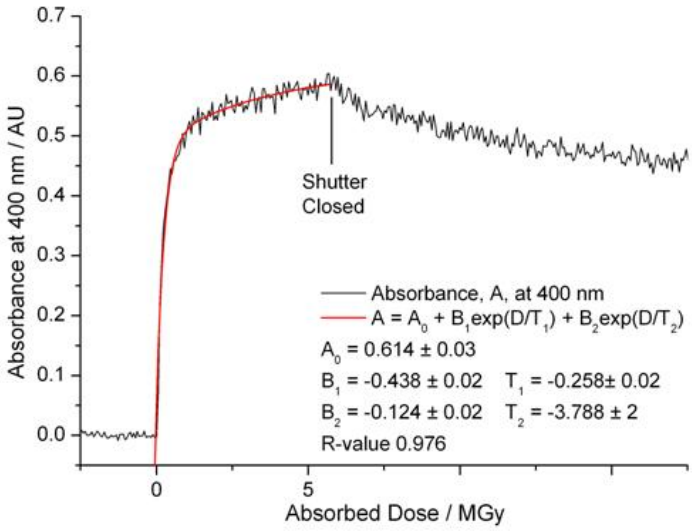

(b)

Figure 2.2: The dose response behaviour of the $SS^{\bullet -}$ radical in a lysozyme crystal observed through UV-Vis absorption spectroscopy. The spectra show (a) the rapid rise in the overall signal due to the increase in radical concentration and (b) the change in SS•- radical signal at 400 nm. The crystal was subjected to a total absorbed dose of ~5 MGy (~ 1 s at 287 kGy per s) before the shutter was closed, with an apparent onset of saturation at 2.7 MGy (see text for details).

The change in absorbance from a series of 1 s exposures interspersed with a 5 s rest period is shown in Figure 2.3(a). Despite a rapid reduction in absorbance when the X-ray shutter was closed for the rest period, saturation at 400 nm was still achieved rapidly with a progressively smaller change in absorption for the same additional absorbed dose. The reduction in absorption seen during the rest period indicates that some fraction of SS•- was lost due to recombination and/or protonation, but the dominating increase over time indicates that some fraction was stable at 100 K. The post-exposure decay of the disulfide peak at 400 nm subsequent to a 20 s continuous X-ray exposure is shown in Figure 2.3(b). The decay follows a double-exponential decay with rate constants of τ_1 and τ_2 equal to 13.1 ± 1.6 s^{-1} and 140.2 ± 20.7 s^{-1} respectively, shown in Figure 2.3(b). This double exponential decay is in agreement with previous observations (Owen *et al.*, 2011, Beitlich *et al.*, 2007).

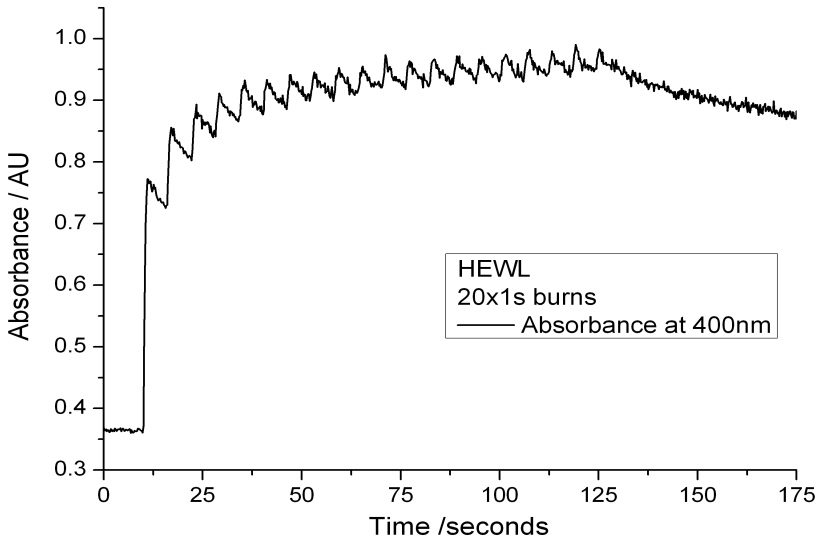

(a)

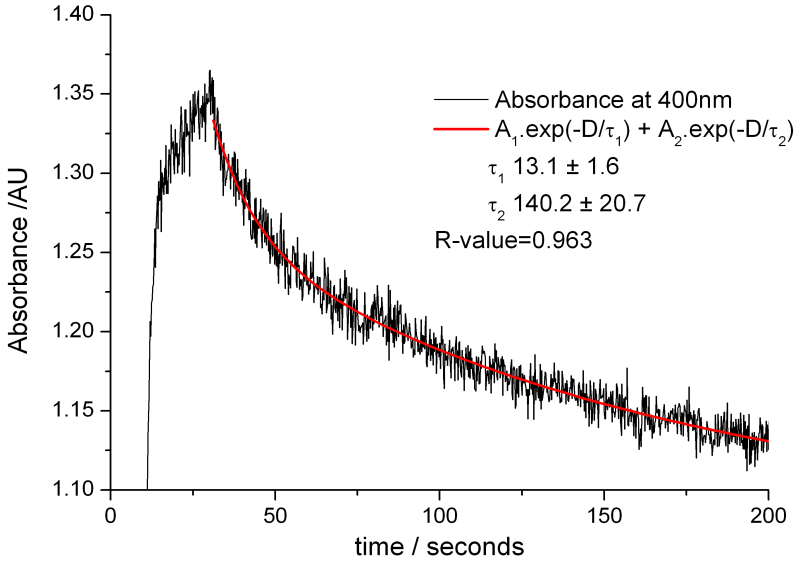

(b)

Figure 2.3: Absorbance spectra for (a) 20 × 1 s burns and (b) a single 20 s burn. The absorbed dose per 1 second exposure was 287 kGy. The cumulative dose over 20 s was thus 5.74 MGy. The multiple burns (a) show a progressively smaller change in absorption for the same absorbed dose, rapid loss of $SS^{\bullet-}$ was observed after each pulse. The single continuous 20 s burn (b) highlights the post-exposure decay of the disulfide peak best described by a two-rate model in agreement with previous observations (Owen et al., 2011, Beitlich et al., 2007).

2.4.2. Irradiations and EPR

Radical trapping in lysozyme crystals at 4 K was quantified using EPR spectroscopy for three different lysozyme crystals, as detailed in Table 2.1. Crystal 1 sampled absorbed doses from 5 to 150 kGy with crystal 2 used to replicate similar doses. Crystal 3 extended the absorbed dose range to a total dose of 500 kGy. Crystal 1 weighed 208 µg and the calculated weights of Crystals 2 and 3 from the total free radical concentration at 20 kGy were 135 µg and 185 µg, respectively. These were compatible with the observed crystal volumes and allowed normalization of the data, enhancing the analysis based on relative changes as a function of dose. One should note however, that the absolute free radical yield is based on the data set from crystal 1 only. The yield of one-electron reduced RSSR, denoted *G(SS)*, was calculated using the R(SS) component of the spectrum.

In Figure 2.4, EPR spectra are shown for four different X-ray doses. At low doses in the EPR experiment, *e.g.*, between 10 kGy and 20 kGy, the spectrum intensity increases linearly with dose. At higher doses, *e.g.*, 200 kGy to 400 kGy, a plateau is reached. The blue traces in Figure 2.4 are simulations of the $RSSH^{\cdot}$ component, which as described above are associated with the low field signal assigned exclusively to $RSSH^{\cdot}$. The double integral of the experimental and calculated spectra gave the radical concentrations, *R(tot)* and *R(SS)* respectively. These concentrations were used in the dose response curves shown in Figure 2.5. The peak from the growing $RSSH^{*}$ component is indicated along with a peak from trace amounts of Mn^{+} known to be present in the experimental cavity of the instrument.

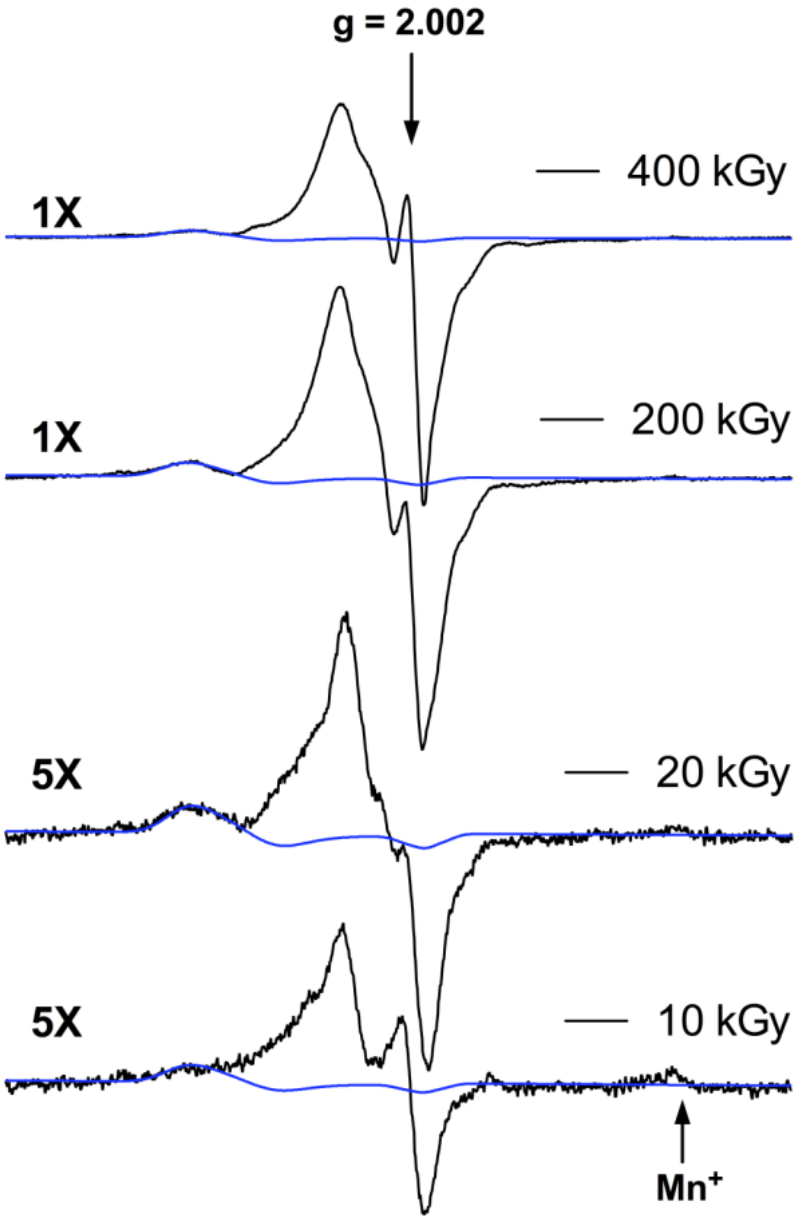

Figure 2.4: Four Q-band EPR spectra spectra (in black) recorded for crystal 3, at 4 K after X-irradiation at 4 K. The first two dose points of 10 and 20 kGy have been scaled by 5x for clarity. The scan width is 40 mT. The orientation of the crystal was not determined. The simulated spectrum of $RSSR^{\cdot-}$ is shown in blue. The sharp peak at g ~2.002 becomes apparent at doses above 100 kGy; it is due to paramagnetic centers trapped in the quartz sample holder. At high field a weak signal is observed in the 10 kGy and 20 kGy spectra (marked with an arrow). This signal is due to trace amounts of Mn^{+}.

In Figure 2.5, the *R(tot)* data are plotted using black symbols referring to the left *y*-axis and the *R(SS)* data are plotted using blue symbols referring to the right *y*-axis. The curves fitting these data are derived from a non-linear least squares fit to Equation 2.6. The fitting parameters for *R(tot)* were *G(tot)* = 281 ± 20 nmolJ^{-1} and *k* = 4.2 ± 0. 6 MGy^{-1}. For *R(SS),* fitting parameters were calculated to be *G(SS)* = 64 ± 5 nmolJ^{-1} and *k* = 17 ± 2 MGy^{-1}. Saturation values for *R(SS)* vs. *R(tot)* are distinctly different, reflecting the differences in dose response properties between the radical species. *R(SS)* saturates ~ 200 kGy at a value of $R(SS)_\infty$ = 3.7 ± 0.5 mmol kg^{-1}, whereas *R(tot)* saturates above 500 kGy at a value of $R(tot)_\infty$ = 66 ± 10 mmol kg^{-1}. This difference is a consequence of the relatively large destruction cross-section (*k*) for the SS centered radicals compared to that of the other radical species trapped in lysozyme.

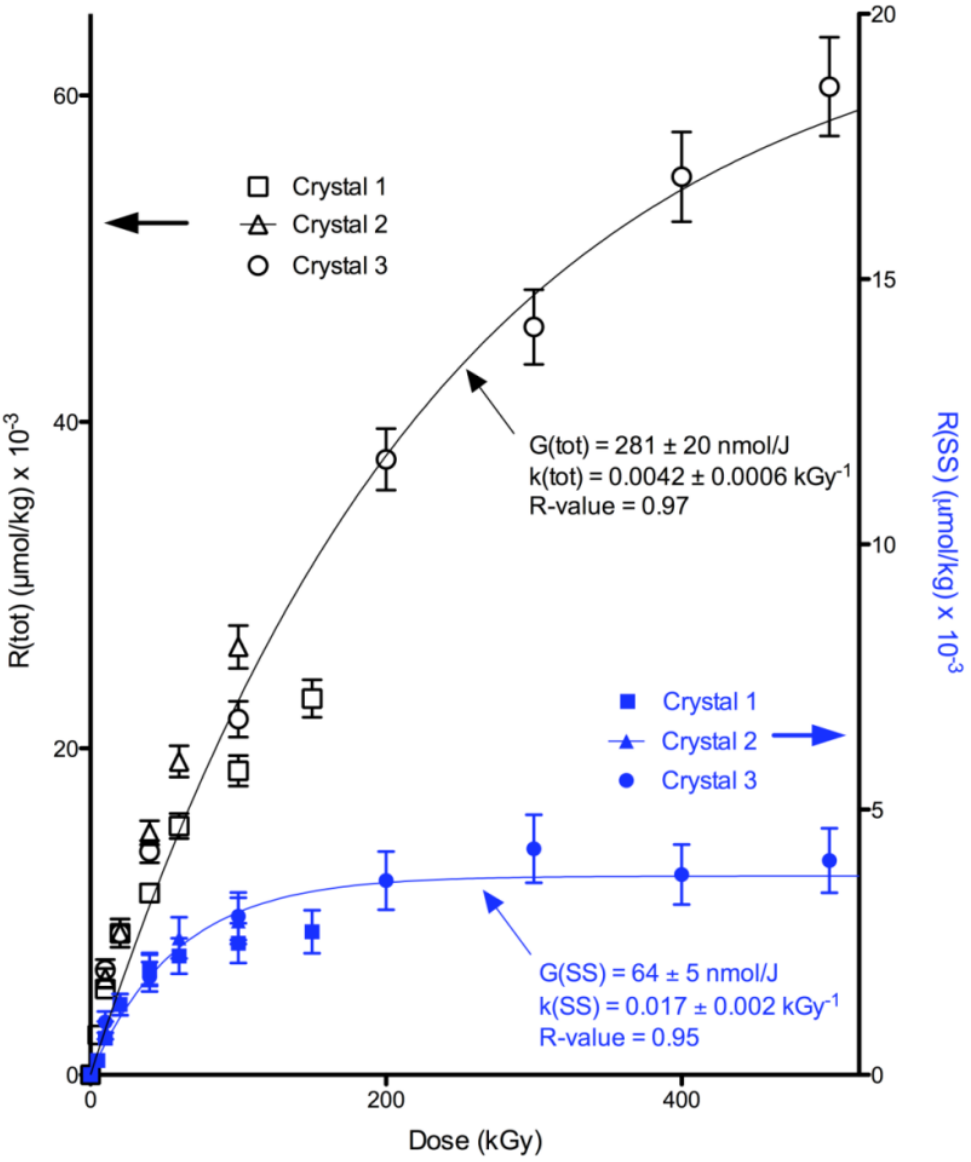

Figure 2.5: The dose response for radical trapping in lysozyme crystals irradiated with 70 keV X-rays at 4 K. Data for the concentration of total trapped radicals, R(tot), is shown for three different crystals using open black symbols (left y-axis). Data for radicals formed by reduction of RSSR, R(SS), are shown using closed blue symbols (right y-axis). See text regarding the normalization of the data using the measured mass of Crystal 1. The curves were obtained by a non-linear least squares fit to Equation 2.2 using the parameters detailed in the figure.

The above values for *G(SS), k*, and $R(SS)_\infty$ are for the sum of all four disulfide bonds in lysozyme. EPR data cannot distinguish between the individual SS sites, however division by 4 (*G(SS)*/4 = 16 nmol J^{-1}) provides an average yield at each site with crystallographic data being used to explore differences between sites in detail.

In terms of Equation 2.1, *M* is the concentration of RSSR and is denoted *M(SS)*. Using a density of 1.17 g cm^{-3}, the concentration of cystine, [RSSR], based on the lysozyme crystal structure was calculated at 229 mmol kg^{-1}. *R* is *R(SS)*, the concentration of SS radicals, and *P* is the concentration of product resulting from cleavage of the S-S bond, which is denoted P(SS*). Since we do not have a direct measure of *P(SS*), $M_0 - M$* is used as a measure of SS*. It is assumed that the decrease in occupancy by one of the two sulfurs in RSSR is equal to *P(SS*)*. The sulfur atom chosen is that whose occupancy is most sensitive to dose, the logic being that loss of occupancy by either of the S atoms forming the SS bond implies that the bond was broken. With respect to product formation, it has been assumed that the rate-limiting step is a one-electron reduction of RS-S(H)R•. Consequently, whether proton transfer is thermally (2_+) or radiation (3) driven, product formation is governed solely by k_f and k_b. Another rate constant to account for reaction 3 could be included however the experimental data suggest that the reaction kinetics are dominated by processes 1_- and 4 (Figure 2.1) and thus that this third rate constant would be marginal.

2.4.2.1. Free radical stability

During the EPR annealing experiments, no spectral changes occurred until reaching a temperature of 130 K. This observation indicates that processes observed at 4 K with EPR can be directly related to experimental crystallographic data collection conditions at 100 K. After reaching a temperature of 130 K, changes in EPR spectral features were observed, but these changes were indicative of thermal evolution of radical species distinct from the disulfide radical anion. The signal from the disulfide radical anion persisted up to temperatures of 190 K.

2.5 X-ray diffraction data and structural results

The statistics for the diffraction data collection at 100 K and the structural refinement results are summarized in Table 2.2. Fifteen consecutive data sets were collected on a single crystal, exposing the same area of the crystal for each data set. The dose per data set was 0.07 MGy with a cumulative dose of 1.05 MGy. Beyond a progressive increase in scaling B factors from 10.67 to 11.32 $Å^2$ there were no systematic trends in the crystallographic statistics as a function of absorbed X-ray dose, and few global indicators of damage are observed. The unit cell dimensions remained approximately constant (variation of <0.5 %) and the average intensity ($I/\sigma(I)$) in the highest resolution shell decreased slightly from 5.0 to 4.7. In terms of structural refinement statistics for each model (R_{work} and R_{free}) there were also no global differences between models independently derived from the different data sets collected as a function of dose.

Structurally, apart from a slight increase in SS bond distance, there were no major differences between data sets.

Table 2.2: Crystallographic data and structural refinement statistics for a lysozyme crystal from which structural X-ray data were collected. The absorbed dose for each data set was 0.07 MGy.

Data sets	15			
Absorbed dose per data set	0.07 MGy			
Total dose	1.05 MGy			
Data collection statistics				
	First data set	Last data set	Mean	Standard deviation
Unit cell parameters (a=b,c Å)	78.77, 38.86	78.76, 36.86	78.76, 37.39	0.004
Wilson B factor $Å^2$	10.67	11.32	11.12	0.163
Structural statistics				
R_{work}/R_{free} (%)	19.09/19.97	19.12/20.30	19.14/20.31	0.128/0.273
SS bond length (Å)				
Cys 6 - Cys 127	2.04	2.05	2.04	0.0051
Cys 30 - Cys 115	2.05	2.09	2.09	0.0139
Cys 64 - Cys 80	2.04	2.05	2.04	0.0046
Cys 76 - Cys 94	2.02	2.04	2.03	0.0077

Fo_n-Fo_1 maps contoured at 3σ for the disulfide bonds at each successive dose are shown in Figure 2.6. Positive density (green) indicates the presence of more electron density than seen in the 0.070 MGy data set while negative density (dark red) indicates a loss in electron density. An inspection of the successive dose electron density maps in the area associated with each disulfide bond showed bond specific effects. The two intra-α-domain disulfides, C6-C127 and C30-115, appeared more sensitive to radicalization with positive density immediately visible in the Fo_2-Fo_1 map at 0.14 MGy absorbed dose. The intra-β-domain disulfide C64-C80 again shows positive electron density in the Fo_2-Fo_1 map with negative density (possibly the start of bond breakage) appearing in the Fo_{11}-Fo_1 map (0.77 MGy). The inter-αβ-domain C76-C94 also shows negative density immediately but the progression as a function of dose is small; finally C76-C94 seems the least susceptible to bond to damage. The solvent surrounding the protein molecule is a potential source of free radicals: the solvent accessibility for the residues associated with each bond is shown in Table 2.3. The residues in the C6-C127 bond are the most solvent accessible of the four disulfide bonds, while C30-C115 has a small accessible area for both Cys-30 and Cys-115 and C64-C80 having a larger area for Cys-64 but no solvent accessible area for Cys-80.

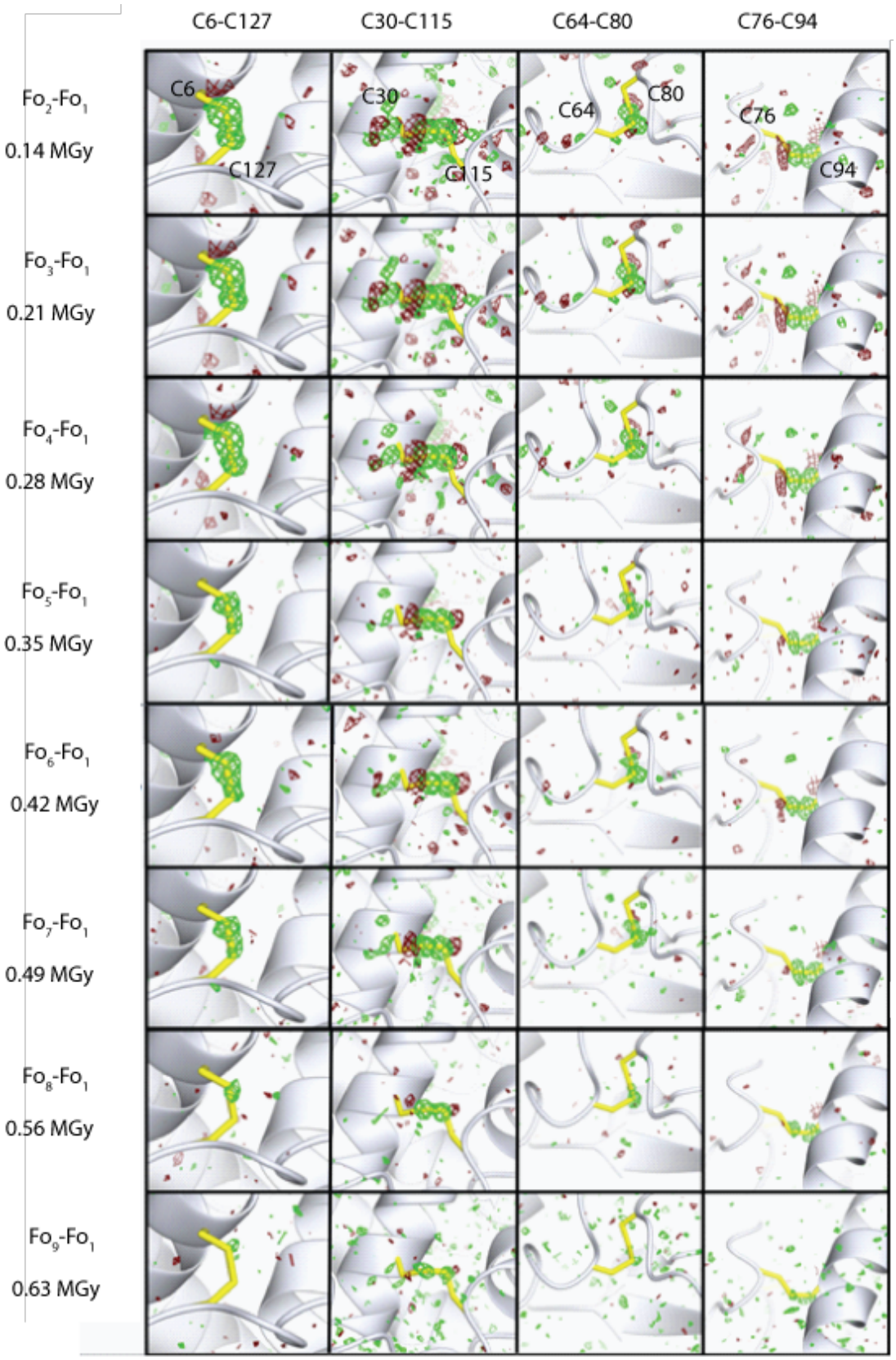
C6-C127
C30-C115
C64-C80
C76-C94
Fo2-Fo1
0.14 MGy
Fo3-Fo1
0.21 MGy
Fo4-Fo1
0.28 MGy
Fo5-Fo1
0.35 MGy
Fo6-Fo1
0.42 MGy
Fo7-Fo1
0.49 MGy
Fo8-Fo1
0.56 MGy
Fo9-Fo1
0.63 MGy
C6
C127
C30
C115
C64
C80
C76
C94

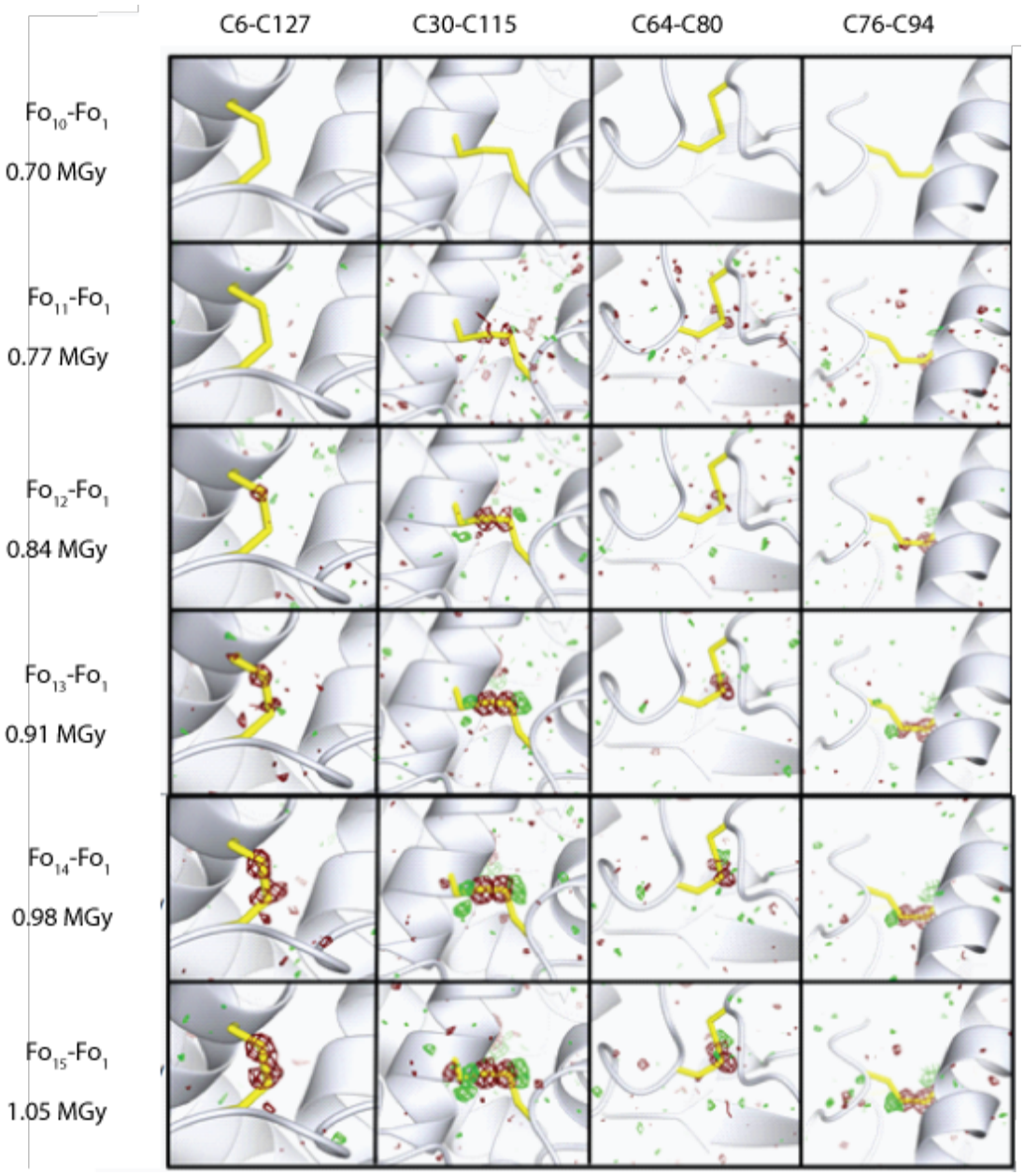

Figure 2.6: Isomorphous difference density maps Fo_n-Fo_1 (where n is the data set number) around the four disulfide bonds present in lysozyme. Disulfide bonds are highlighted in yellow. Maps are contoured at +3σ (green) and -3σ (red). For C6-C127 the top most part of the bond is C6 with the bottom being C127. The remaining bonds are positioned such that the label matches the residue positions in each figure with the first to the left and the second to the right. Note that the dose indicated is the total overall dose.

Positive electron density surrounding the C6-C127 disulfide bond is clearly present in the Fo_2-Fo_1 map (0.14 MGy total absorbed dose); the bond displays evidence of radicalization. A similar result was noted by Carpentier *et al.* (2010) (at a higher absorbed dose than used here) who attributed it to the formation of a weak stabilizing hydrogen bond between the sulfur atom of Cys6 and a water molecule. As dose increases this electron density dissipates with negative density (presumably the initial signs of bond breakage) appearing in the Fo_{12}-Fo_1 map (0.84 MGy). The Fo_n-Fo_1 maps are sensitive to small changes. However, it should be remembered that these maps are based on the difference from the model produced from the first set of structural data. If the bond was already becoming radicalized at 0.07 MGy, then the positive electron density seen is an underestimate since the initial signs of bond breakage would occur earlier. From the crystallographic data alone we cannot determine if this is the case. Sensitivity to radiation damage in the C6-C127 region has been noted in other studies at both cryogenic temperatures (Weik *et al.*, 2000b) and ambient temperature (Kmetko *et al.*, 2006).

Table 2.3: Solvent accessibility for the disulfide residues in lysozyme was calculated using the program AREAIMOL.

Bond	Residue	Solvent Accessibility ($Å^2$)
C6-C127	Cys 6	43.2
	Cys 127	21.8
C30-C115	Cys 30	0.4
	Cys 115	0.1
C64-C80	Cys 64	0.0
	Cys 80	1.3
C76-C94	Cys 76	20.0
	Cys 94	2.4

At C30-C115 there is both evidence of positive density and negative density in the region of the bond. The positive density directly surrounds the bond while the negative density seems to be at either end of the two S atoms making up the bond. This could be interpreted as a radicalization and/or shift in position. As the dose increases, the effect is reversed, which is again indicative of the initial signs associated with bond breakage. This intra-α-domain bond is stabilized by a hydrogen bond between the sulfur atom of Cys30 and the carbonyl oxygen of Gly26.

C64-C80 and C76-C94 appear to be less affected than C6-C127 and C30-C115. In both cases there is initial positive density (presumably radicalization), which shifts with dose to negative density (bond breakage). C76-C94 is the second most solvent accessible disulfide bond in lysozyme (Table 2.3). This bond is also stabilized by a weak hydrogen bond, providing a proton source, between the sulfur atom of Cys94 and a water molecule. An alternate conformation of the rotamer for Cys94 develops with increasing dose. This was not modeled into the structure so as to highlight the development of the alternative conformation via the increase in positive electron density in the Fo_n-Fo_1 maps. While other bonds show the initial evidence of breakage, at the absorbed doses studied, C76-C94 is the only one that shows structural evidence of cleavage and, in the case of Cys94, formation of an alternate conformation.

In addition to the sulfur atoms in the four disulfide bonds, there are also two additional sulfur atoms present in lysozyme, in Met12 and Met105. Both of these have zero solvent accessibility. The Fo_n-Fo_1 maps for these residues are shown in Figure 2.7. In the case of Met12 there is little if any indication of dose related damage. However, there is some evidence for initial damage of the carbon sulfur bond in Met105. Negative density on the sulfur atom is present in the Fo_2-Fo_1 maps onwards to Fo_6-Fo_1 (0.49 MGy). After the sixth dataset, this density is no longer localized on the sulfur atom. While the effect appears marginal, any increased sensitivity of Met105 compared to Met12 may be associated with the close proximity of the C30-C115 disulfide bond and the increased free radicals associated with this.

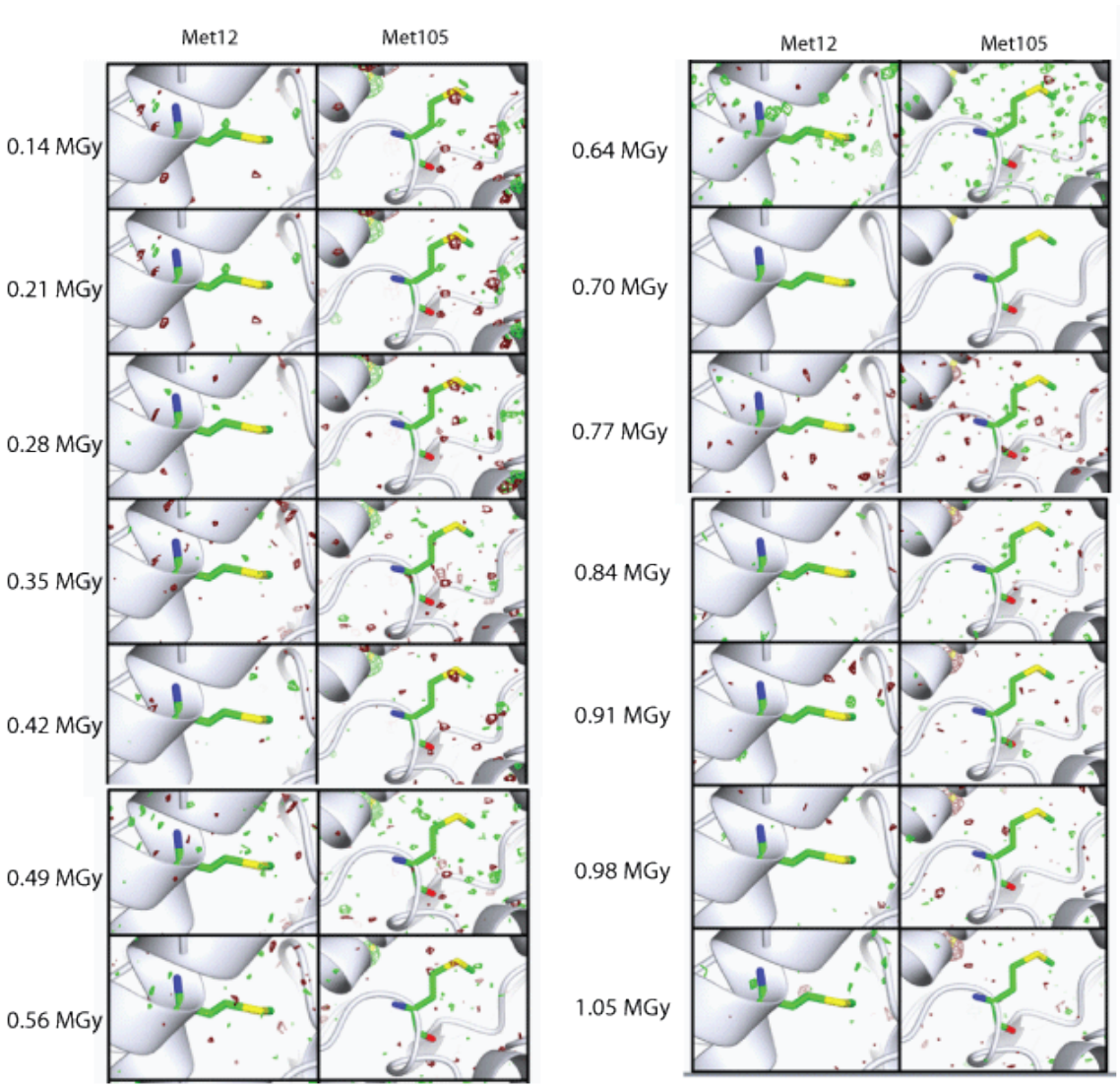

Figure 2.7: Isomorphous difference density maps Fo_n-Fo_1 (where n is the data set number) for residues Met12 and Met105. Maps are contoured at 3σ in green and -3σ in dark red.

The resulting structures and experimental data have been deposited in the PDB as entries 4H8X, 4H8Y, 4H8Z, 4H90, 4H91, 4H92, 4H93, 4H94, 4H9A, 4H9B, 4H9C, 4H9E, 4H9F, 4H9H and 4H9Iwith the absorbed doses starting at 0.07 MGy for 4H8X and incrementing by 0.07 MGy to 1.05 MGy in 4H9I.

2.5.1 Connection between SS cleavage and radical formation

In examination of the EPR results Figure 2.8(a) shows the *R(SS)* data from lysozyme as a function of absorbed dose and *P(SS*)*. Radiation damage to disulfide bonds has been studied by others and Figure 2.8(b) illustrates the extension of our model to data recorded by Petrova *et al.* (2011) on elastase. Comparing the EPR data from lysozyme with that of elastase (or other macromolecules containing disulfide bonds) is justified given that the efficiency of forming the disulfide radical anion, studied by EPR, was found to be the same across 15 different proteins (Rao *et al.*, 1983a). The *R(SS)* and *P(SS*)* data were fitted simultaneously using Equations 2.3b and 2.3c. In the case of elastase, four different non-linear-least-squares fits were carried out from information on the structural derived differences in *P(SS*)* between the four elastase SS sites. Three conditions were imposed on the fits: i) the four highest dose points were excluded because dose saturation of *P(SS*)* is almost certainly a consequence of the detection method and not cessation of product formation; ii) the back reaction rates k_b were constrained to the maximum values detailed in Table 2.4 in order to ensure that the curve for *R(SS)* fits the saturations values in the 100-400 kGy range; and iii) M_0 was fixed at 229.4 mmol kg^{-1}, which is the concentration of SS sites in the lysozyme crystals.

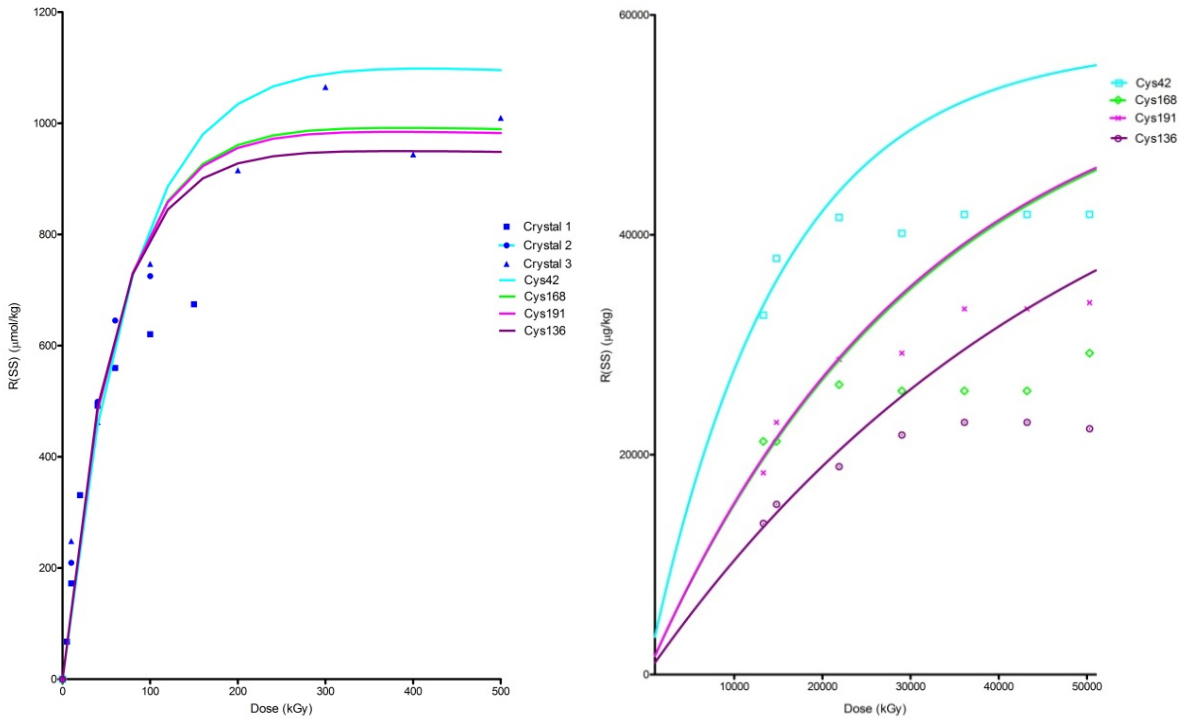

Figure 2.8: The concentration of one one-electron reduced SS at each SS site, R(SS)/4, in crystals of lysozyme (see Figure 2.5) is provided on the left. Loss of electron density at the SS sites in elastase (Petrova 2010) is provided on the right. Curves were obtained by a fit of Equations 2.3b and 2.3c to the data from both the EPR and Petrova et al. (2010) studies combined. Note that the four highest dose points in the Petrova et al. (2010) study were excluded from the fit.

	Elastase			
	Cys42	Cys168	Cys191	Cys136
k_r	0.32	0.32	0.32	0.32
k_f	2.14	1.8	1.26	0.8
k_b	12.7	14	16	17.5
M_o	57348	57348	57348	57348

Table 2.4: Parameters used in fitting the data shown in Figure 2.8. Here k_r, k_f, and k_b, are the rates of primary reduction event (radical production), secondary reduction event (forward reaction), and secondary oxidation of one-electron reduced disulfide radicals (back reaction) respectively. The occupancy refinement provides rate constants for each atom.

Note that P(SS*) grows at the expense of R(SS). Based on the fitted curve in Figure 2.8(b), 1-2 % of the S-S are cleaved at 0.6 MGy. That this is not experimentally observed in elastase reflects the fact that 0.6 MGy is the dose used to collect the first data point to which subsequent points are normalized, and thus it is assumed that no SS cleavage has occurred. Our model predicts this assumption to be false. Also, note that all four curves are approaching saturation at P(SS*) = 229.4 mmol kg^{-1}, the value of $M(SS)_0$. The data points, however, show saturation well below $M(SS)_0$. This suggests that the presumed fraction of intact SS at doses above 20 MGy is too large, *i.e.*, the diffraction due to products cannot be fully distinguished from the diffraction attributable to the remaining undamaged structure.

2.6 Discussion

In this study for the first time microspectrophotometry, EPR with *in situ* X-ray irradiation, and X-ray crystallography have all been combined to study disulfide damage in lysozyme crystals. This has allowed us to sensitively probe radical chemistry at low doses with EPR while the UV microspectrophotometry permitted the investigation to be extended to conditions typical for cryocrystallography studies. Finally, the crystallographic studies allowed us to probe site-specific effects that are averaged in the EPR and spectroscopic analysis.

UV-Vis spectroscopy showed that disulfide radicalization appeared to saturate at an absorbed dose of approximately 2.7 MGy in contrast to a saturating dose of ~0.2 MGy

observed by EPR at much lower dose rates. The observation that saturation occurs in both cases suggests that a multi-track model, product formation due to the interaction of two separate tracks, is a valid model for radiation damage in protein crystals. The disagreement between the optical and EPR saturation dose could be explained by the influence of a number of factors including sources of error in the measurements, or more likely, the physical conditions under which the different experiments were conducted.

The estimation of the absorbed dose and crystal volume is a source of error for both the UV-Vis and EPR measurements. For single crystal work the calculation of absorbed dose is now well determined (Owen *et al.*, 2006b, Paithankar & Garman, 2010, Paithankar *et al.*, 2009a). In the case of EPR the absorbed dose is calculated based on water. Using crystal properties and X-ray cross sections at 70 keV, this underestimates the actual dose received by ~6%: a small error compared with the difference in saturation levels. Crystal volume errors are associated with the accuracy of dimension measurement (+/- 50 μm) and the assumption of a cuboid shape, rather than the tetragonal crystal morphology. In the EPR case, the volume measured was in agreement with the volume calculated from the measured radical yield at 20 kGy. Any errors associated with crystal volume also appear small in comparison to the difference in saturation levels and would be expected to be systematic.

The most likely explanation for the differences in the saturation dose are the different physical conditions of the measurements, i.e. temperature, energy and dose rate.

Considering temperature first, EPR data are obtained at 4 K to maximize the observed signal over noise, while the optical data were recorded at 100 K. The optical data show that ~8 % of the radicals observed immediately following the pulse have decayed in 5 s (reducing the free radical concentration seen in the crystal). According to our model, this decay is assigned primarily to reactions of SS-centered radicals with holes and electrons. Reactions of one-electron reduced disulfide bonds with holes yield parent, while reactions with electrons yield product. Over the time scale of seconds, hole/electron transfer may proceed by tunneling or hopping and, given the photon flux density (10^{12} ph s^{-1} in 50 μm^2), overlapping tracks are involved. At 4 K in the EPR measurements, the tunneling rates would be comparable to those at 100 K but conversely the hopping rates would be effectively zero. This decay is not observed within the dose range of the EPR experiment; therefore, it is likely that this ~8 % reduction in radical signal at 100 K occurs due to hopping yielding parent, rather than product, i.e. a repair process. Experimentally others have not observed a large difference between experiments conducted at 100K and those at lower temperatures. Meents et al. (2007) studied the temperature dependence of holoferritin and insulin crystals, cooling the crystals to 15-90 K with gaseous helium from a liquid helium cryostat. There was a small positive protective effect by collecting data at 15 K versus 90 K. This effect, leading to a decrease in decay of the signal over noise, was greater for holoferritin (23%) than for insulin (6%) possibly due to the pH dependence of radiation chemistry and the crystallization conditions, pH 11 of insulin and ferritin at pH 7. However, at 15 K rather than 4 K, hopping still takes place. It is possible to conduct

the optical measurements closer to liquid helium conditions but for practical purposes nitrogen gas stream temperature control at 100 K is a standard in the field.

While the type of ice does not greatly influence the free radical signal, the behavior of ice at 4 K and at 100 K could have an effect. Johnson and Moulton (1978) noted that the temperature at which ice is irradiated has a significant effect on the free radical yield of both OH^- and HO_2 radicals. Annealing and re-cooling of samples showed that radicals formed at low temperature can reversibly evolve at higher temperatures and that samples irradiated at 4 K vs. 77 K exhibit a higher free radical yield. EPR peaks in ice for both OH^- and HO_2 radicals were found at g = 2.08 and g = 2.05 (Johnson & Moulton, 1978), which places them outside of the maximum g value of our simulated disulfide radical, 2.02. However, due to the broad line width of both radicals in question, their presence may have an influence on the integral analysis results of the disulfide radical anion EPR signal. In this context, it is possible contributions to the EPR signals due to ice radical species may result in an overestimation of the free radical yield of SS•, due to influence of ice radical signals. This would not have a deleterious effect on the identification of the EPR disulfide signal, since the g values of ice radicals are too large to directly interfere with SS• features. In comparison, for spectrophotometry data, the signal being followed is specific to disulfide radical formation and is not influenced by OH^- and HO_2 radicals. The contribution from the tails of ice radical signals may explain some of the discrepancy between the saturation values for the microspectrophotometry and the EPR results.

The microspectrophotometry data were recorded at an incident X-ray energy of 12.8 keV whereas the irradiation of the sample studied by EPR was with 70 keV X-rays. X-ray crystallographic studies show that energy has little overall effect on radiation damage when absorbed dose is used as the metric (Gonzalez *et al.*, 1994, Weiss *et al.*, 2005) even over as wide a range as 6.5 to 33 keV (Shimizu *et al.*, 2007). Other studies covering 3 MGy to 26 MGy of cumulative absorbed dose on lysozyme indicate a small but consistent energy dependence in the rate of specific damage (Homer *et al.*, 2011). Homer *et al.* reported lower disulfide bridge damage for 9 keV incident X-rays than for 14 keV X-rays (1 electron per $Å^3$ per MGy). While absorbed dose calculations take into account X-ray cross sections at different energies, this effect may be magnified in the 12.8 keV and 70 keV range used for the collection of the experimental data. The disulfide bonds in the crystal used in the EPR study, if subjected to 70 keV X-rays, would be more likely to be damaged at a higher rate, and thus saturation would occur at a lower dose point than at the lower energies used for the microspectrophotometry and X-ray crystallography measurements. However, this effect, if present, is unlikely to be large enough to explain the difference in saturation values observed in our study.

Dose rate differences between the microspectrophotometry and EPR data were significant, a 23,000 fold difference. It has been known for some time that free radical yields in a variety of systems are dependent on the dose rate of the incident radiation. An early study utilizing Fricke dosimetry discovered that production of certain radiation products decreased with increasing intensity of energetic electron pulses (Thomas & Hart, 1962). This provided early evidence that single-radical chemistry was not an

appropriate model for systems with high dose rates. An earlier study observed a similar effect when tracking the radiation-dependent decolorization of methylene blue (Hutchinson, 1958). This study concluded that decolorization, a radiation dependent reaction, decreased in samples receiving the same dose at an increased dose rate. This effect can be explained through an increase in recombination of electrons and electron holes formed in the target, step 2. in Figure 2.1. Higher dose rates would produce holes and electrons in closer proximity, increasing the recombination (or repair) rate and as a result, decreasing the stabilization of free radicals compared to lower dose rates. Since the dose rate in microspectrophotometry experiments is over four orders of magnitude higher compared to EPR studies, it is very likely that differences in dose rate are a major, if not dominant source of the change in disulfide free radical yield observed.

Crystallographically, dose rate has no clear effect at the macroscopic level, but has been shown to be a factor in specific radiation damage. Increased dose rate results in small, but measurabley increased damage at radiation sensitive sites (Se and S atoms) (Leiros *et al.*, 2006). Leiros et al. (2006) studied maltooligosyltrehalose trehalohydrolase and trypsin with 10 fold and 24 fold dose rate differences respectively. When monitoring global damage in the form of the loss of diffraction intensity, Owen et al. (2006b) observed a similar effect, seeing a 10% lifetime decrease for a 10-fold increase in dose rate for apoferritin. The addition of a metal atom within the protein (iron in holoferritin) produced a more pronounced effect, yielding a 10% lifetime decrease for a 3-fold increase in dose rate. This appears to be the reverse to our observation of a decreased

saturation dose with a lower dose rate, although the effects are small compared to the role played by the total absorbed dose. We note that the difference in dose rates used for our experiments is so large that caution must be taken in any comparison.

While technically possible to increase the dose rate for the EPR studies, it is practically unfeasible given the scale of the EPR equipment. Reducing the dose rate in the microspectrophotometry experiment is also possible through attenuation, but again faces a practical limit in terms of the duration of beamtime requirements. Additional studies will need to be carried out on a laboratory source with microspectrophotometry capability. It is possible that the combination of dose rate and temperature play a role in explaining the differences.

In addition to temperature, energy, and dose rate, another influence on the radiation chemistry is the oxygen or O_2 effect. Oxygen can both sensitize and protect molecules from free radical damage, depending on the environment and the specific type of damage considered. Chan and Bielski (1973) measured the decay rate of the absorption peak due to one-electron reduced disulfide as a function of molecular oxygen concentration. They found that decay rates increased from 3.22×10^4 to 1.63×10^5 s^{-1} with oxygen concentration increasing from 2.08×10^{-5} to 1.25×10^{-4} M respectively. This led to the conclusion that O_2 oxidizes disulfide radical anions, resulting in reduced yields. This was also observed by Barton and Packer (1970) in which they explored the pH dependence of the O_2 effect. In EPR studies, samples are held under vacuum in an environment where oxygen and nitrogen are excluded to

prevent the formation of nitrogen or oxygen ice at liquid helium temperatures. The microspectrophotometry experiments are performed on lysozyme crystals within a nitrogen stream, where there is more possibility of access to oxygen. It is likely that this effect only has a marginal influence as permeability of oxygen will be limited and the concentration in the stream, if any, will be low.

The cause of different saturation levels will have to be determined by further experiments and this work suggests a number of them. However, despite these differences, our model appears consistent. It fits well across a range of X-ray doses explaining both the lysozyme data from 5 kGy to 1.05 MGy (EPR and crystallographic studies) and that of Petrova et al. (2011) on elastase spanning 1.2 MGy to 67 MGy. We differ in our interpretation of the processes underlying the elastase observations, but only in terms of the development of our multiple-track model, which was not available to the authors of the elastase study. At even the smallest absorbed dose in this range (5 kGy), our EPR measurements indicate complete dose saturation of one-electron reduced disulfide bonds within the protein. In addition, our model predicts that the initial reduction of disulfide bridges would not result in the scission of the bond. The disulfide scission observed by Petrova et al. (2011) is likely to be due to two one-electron reduction events at the disulfide bonds of elastase. Unlike the Petrova et al. (2011), our lysozyme study did not show large scale rigid body structural changes or significant elongation of disulfide bonds. This is not surprising, given that the dose range of our studies ends before those of Petrova et al. (2011) start; our results are not inconsistent with their observations. They see the formation of alternate conformations for cysteines

that are water accessible. At the absorbed doses we have used, only the Cys94 of the C76-C94 disulfide bond forms an alternate conformation. Of the two cysteines making up this bond Cys94 has the lower water accessibility but Cys76 does not show evidence of developing different conformations. We speculate that the production of a rotomer cysteine is an indication that cysteine is the major and perhaps only product (P in equation 2.1). The highest water accessible disulfide bond, C6-C127 shows no evidence of developing any alternate conformation in our study. It would appear that structural perturbation due to ongoing radiation chemistry is both dose and environment specific.

An important aspect of the experimental results presented here is the observation of radical formation even at 5 kGy, the lowest dose used. Radiation studies based upon X-ray crystallographic data require careful evaluation; the experimental method observes structural changes that are inherent to the method. The starting structure is determined with the application of X-rays, whose effects cause the very mechanism that is being studied. Our results indicate that even at the lowest doses used for structural investigations, disulfide bonds are already radicalized. Extra electron density is present, which if not taken into account, could give misleading results when trying to quantitatively assess damage observed from difference map techniques. Practically, there are few ways to avoid this. One solution may be to use neutron diffraction to provide an unbiased baseline structure, but no radiation damage studies have made use of this approach to date. Our model allows us to understand the nature of disulfide bond loss in lysozyme crystals, and can potentially be extended to predict the labiality of

each amino acid side chain within a protein. More work is required to empirically test our protein damage model, in which other local factors should also be considered, such as solvent accessibility and proximity of other amino acid side chains, all of which are a consequence of secondary antiary protein structure.

2.7 Summary

Understanding radical destruction as well as formation is key to understanding the radiation induced changes that impact X-ray diffraction data. A multi-track model involving both formation and destruction of free radicals explains X-ray induced disulfide bond damage. It fits UV, EPR and both low and high dose crystallographic data. Multi-track considerations offer the first step in a comprehensive model of radiation damage that could potentially lead to a combined computational and experimental approach identifying when damage is likely to be present and the ability to recover the native unperturbed structure. In the next chapters this model is extended showing the theoretical implications of multi-track processes and further experimental evidence that supports them. Intriguingly, a successful model of the damage process would not only allow treatment of new structural information but, in cases where absorbed dose has been recorded, allow remediation of previously deposited structural data.

3. A Generalized Model for Radiation Damage of Amino Acids Based on Multi-Track Model Predictions

3.1 Introduction

In chapter 2, radiation damage was studied at the disulfide bond level and determined to fit a multi-track model where free radical formation and recombination processes take place. Multi-track radiation chemistry is associated with large doses (such as those used for X-ray crystallography), and it is well studied, but not for proteins. Therefore, given the confirmed presence of a multi-track process in Chapter 2, a general model for radiation damage to specific amino acids is proposed in this chapter based on the available literature. This model has been tested empirically.

Structural studies of radiation damage in macromolecules have noted residue specific effects, residue lability appears to occur in the order: cystine > glutamate ~ aspartate > tyrosine > cysteine > methionine (Burmeister, 2000b, Ravelli & McSweeney, 2000a, Weik *et al.*, 2000a). The chemical process for the damage is specific to the amino acids' chemistry; examples include cleavage of disulfide bonds in lysozyme, and decarboxylation of acidic side chains in acteylcholinesterase. These damage effects are induced by the interaction of free radicals within the crystal. Deposition of energy by X-ray photons causes ionization and other excitation events. During the ionization process, an electron loss center is formed along with a secondary electron with several kiloelectron volts of energy. The secondary electron is typically ejected from an inner

shell of an atom. The secondary electrons induce further excitation and ionization (~500) events throughout the crystal, resulting in the formation of free radical species (Burmeister, 2000b). These excitation and ionization events can occur either directly in the macromolecule (a direct event) or within the solvent (indirect event). The primary direct events, through direct ionization of the macromolecules within the crystal, cannot be prevented. The secondary events are limited by diffusion and can be mitigated through the use of cryocooling and radical scavengers.

The model presented here was developed principally by collaborators at Rochester, Bernhard and Black in discussions with Snell in Buffalo and based on the results described in Chapter 2. The authors' role was in collecting the data that demonstrated outcomes of the model and the analysis of those outcomes. The results have the potential to explain the damage to specific amino acids both qualitatively and quantitatively.

3.2 Experimental data to test the model

X-ray crystallographic data was collected on lysozyme as described in Chapter 2 and used for the studies presented here. It was supplemented with Xylose isomerase (XI) data (described in the next chapter), to extend results to a higher dose regime to test predictions from the model. The lysozyme diffraction data was collected on a single crystal in 15 consecutive datasets to 1.2 Å resolution with each data set having a dose of 0.07 MGy and a total cumulative dose of 1.05 MGy. XI from *Streptomyces rubiginosus* was obtained from Genencor (Palo Alto, CA). The protein buffer contained 50 mM sodium phosphate, pH 7.7; 100 mM sodium chloride and 0.02 % (w/v) sodium

azide. The protein was crystallized using the hanging drop vapor diffusion crystallization method. A total of 5 µL of protein at a concentration of 100 mg/ml was added to a 5 µL drop of precipitant solution containing 8% (v/v) 2-propanol (as a precipitant), 25 % (v/v) ethylene glycol (as a cryoprotectant), 50 mM HEPES, pH 7.0 and 50 mM magnesium chloride. The crystals were flash cooled at 100 K directly in the cryostream for data collection. Seven medium resolution (1.2 Å) datasets were collected with a partial high resolution 10 degree swathe collected after each medium resolution dataset. Each data set had an absorbed dose of 0.8 MGy (an order of magnitude greater than the lysozyme case). The details of the XI data collection can be found in the next chapter.

3.3 Developing the generalized model

A generalized model begins with a qualitative question, what are the radiation induced intermediates and expected end products? A generalized reaction scheme to answer this question is presented in Figure 3.1 based on the specific reaction scheme presented in Chapter 2. Ionizing radiation deposits energy via ionizations and excitations. In polar condensed matter, in this case protein crystals, damage due to excitations is expected to be negligible (Spinks, 1990). A single ionization creates two free radicals, one due to electron-loss (a hole) and one due to electron gain. Starting with a neutral molecule M, one-electron reduction gives a radical anion (reaction r1) and subsequent protonation (r2) converts it to a neutral radical. Both species, $M^{\bullet -}$ and $M(+H)^{\bullet}$, are referred to as one-electron reduced sites. If a second track creates an ionization in the vicinity of a pre-existing electron-gain site, a second one-electron reduction (r3) may occur. The result is a two-electron reduction product P_{re}. The

second track may also generate a hole that adds to the electron-gain site, reaction r4, giving a back reaction that regenerates M, Figure 3.1(a). Oxidation gives a radical cation (reaction o1) and subsequent deprotonation (o2) converts it to a neutral radical. Both species, $M^{\bullet+}$ and $M(-H)^{\bullet}$, are referred to as holes or one-electron oxidation sites. If a second track creates an ionization event in the vicinity of a pre-existing hole, a second one-electron oxidation (o3) may occur. The result is a two-electron oxidation product P_{ox}. The second track may also generate an electron that adds to the hole, reaction o4, giving a back reaction that regenerates, Figure 3.1(b). Proton transfer accompanies nearly all of the reactions that carry the initial radical ions forward to stable end products. These are thermodynamically driven by two factors: i) the change in effective pKa when an electron is either added or removed and ii) the proton donating and accepting ability of the immediate environment. Also, protons released by ionizing radiation will add to neighboring sites, before or after electron addition. In either case, (Purkayastha *et al.*, 2007)proton adding before or after, at least two overlapping traps would be required to push the two one-electron reduction reactions forward to product.

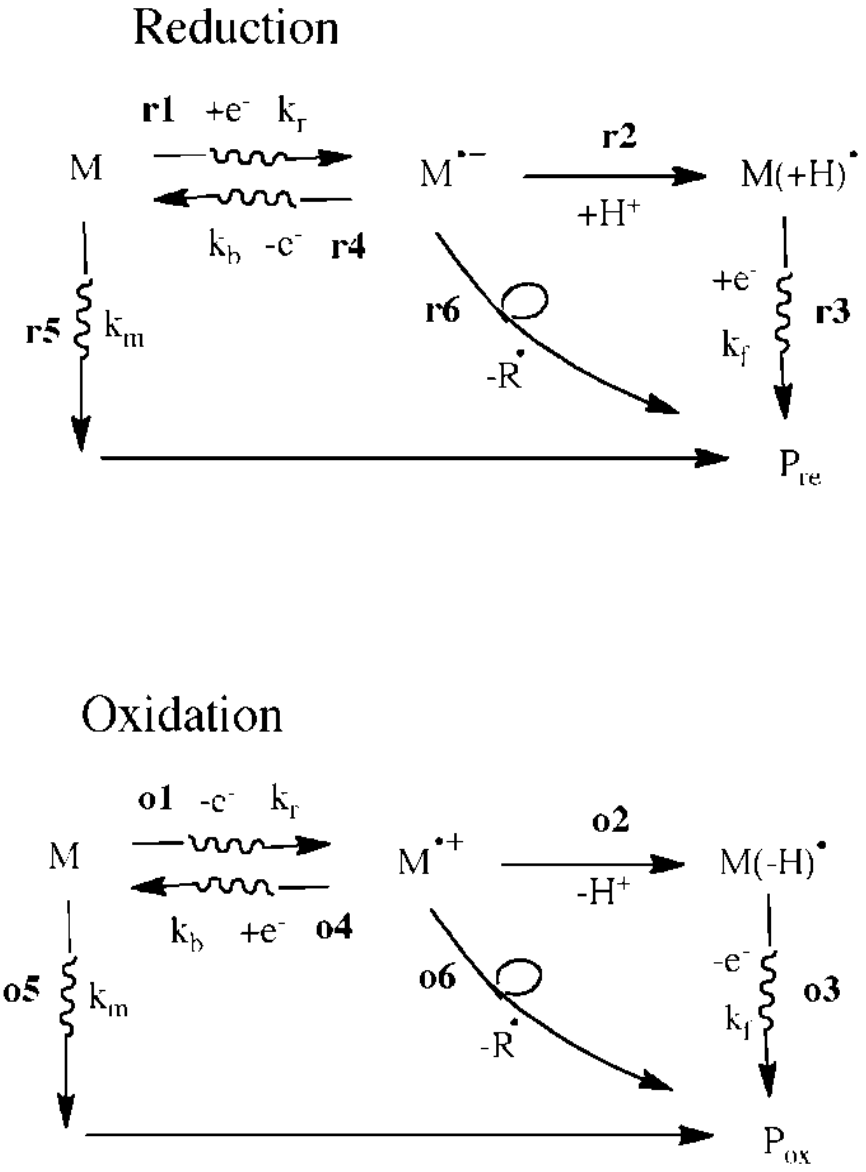

Figure 3.1: Generalized scheme for reactions initiated by reduction and oxidation of protein component M to yield the reduced product P_{re} and the oxidized product P_{ox}.

The majority of damage that can be detected by X-ray crystallography (as an increase or decrease in electron density or even a visible structural change) will occur by either two serial one-electron reductions or two serial one-electron oxidations. For these pathways, the dose dependent rate of product formation depends on k_r (the radical formation rate), k_f (the rate by which the radical goes forward to product rate), and k_b (the rate by which the radical goes back to parent). It is important to note that these rates depend on absorbed radiation dose, not time.

Two other pathways are included for completeness. One is the molecular pathway, reactions r5 and o5; these entail two-electron reduction and two-electron oxidation, respectively. They occur within a spur (cluster) of ionizations such that an intermediate radical cannot be trapped. Products formed in this way are called molecular products (Sharma, 2011, Swarts *et al.*, 2007a, Purkayastha *et al.*, 2007) and are by definition not free radicals. The molecular reaction proceeds at a rate k_m. The other is a unimolecular rearrangement of the radical intermediate creating a radical plus a non-radical fragment, reactions r6 and o6. This type of reaction is relatively rare for organic molecules in the solid state at low temperatures.

Below, these two general schemes are applied to specific protein residues. In doing so, the reaction label given in the general scheme is used to label the reaction for specific residues. For example, reaction 2.o3, refers to Scheme 2 and reaction o3 in Figure 3.1.

3.4 Reduction and oxidation sites.

3.4.1 One-electron reduction sites

It is known from EPR studies that sulfhydryls (Cys, Met), carboxylates (Glu, Asp), and aromatics (His, Phe, Trp, Tyr) are favorable sites for one-electron reduction(Black & Swarts, Matsuki, 1981, Krivokapic *et al.*, 2010, Sevilla, 1979a, b). Other one-electron reduction sites, although less favorable, are the peptide bond, Gln, Asn, and Arg. Note that out of the peptide bond and 20 residues, only 11 residues will compete effectively for capture of an electron (Cys, Met, Glu, Asp, His, Phe, Trp, Tyr, Gln, Asn and Arg) (Zhou & Nelson, 2010). Figure 3.2 illustrates one-electron reduction sites associated with amino acids.

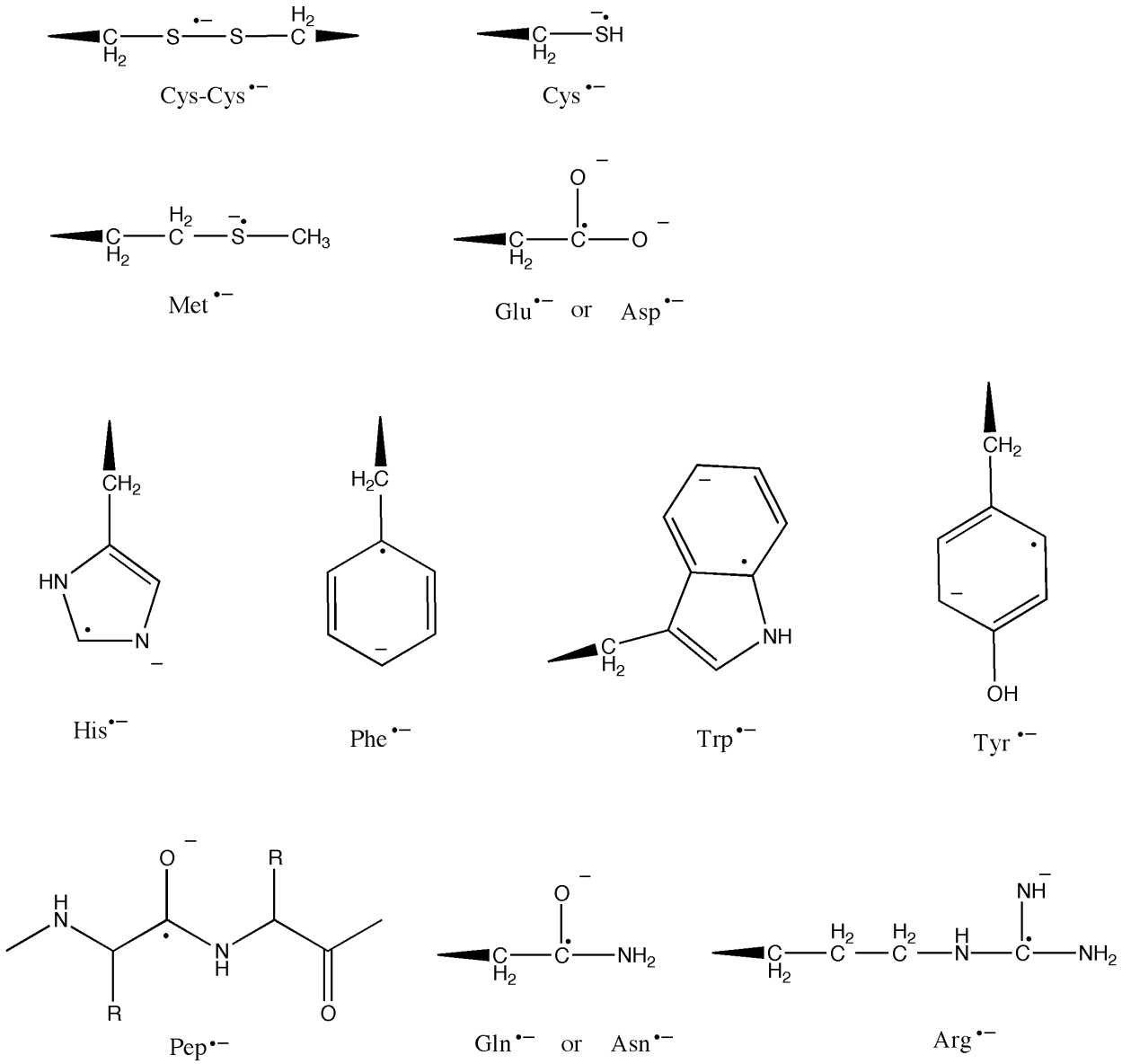

Figure 3.2: One-electron reduction is specific, occurring at sites with relatively high reduction potential.

3.4.2 One-electron oxidation sites

Based on the Bragg rule (Harding, 2006) all of the protein constituents will be ionized with a relative probability that depends on the total number of electrons making up the constituent. Initially all of the residues and every peptide bond will sustain ionization with a probability governed by its electron number. Transfer of the hole from its initial site of formation to other sites is limited primarily by two types of reactions: i) deprotonation resulting in the net loss of H and ii) electron return. Deprotonation from carbon is generally irreversible and from nitrogen or oxygen is reversible; both are possible for the peptide bond, Pep(N-H) and Pep(C-H), as shown. Electron return restores the parent structure (back reaction o4 in Figure 3.1). Only four sites are not expected to deprotonate: cystine, Met, Glu, and Asp.

There will be a preference for hole trapping at the sites of lowest oxidation potential, most noteworthy are Tyr, Cys, Trp, His, Met. Of particular interest are the neutral radicals produced from Glu, Asp, and the peptide bond, as X-ray induced damage has been observed for these. All 20 residues, all peptide bonds, the amino terminus, and carboxyl terminus are potential hole traps. Furthermore, the larger residues contain more than one site capable of trapping a hole; for example, lysine can trap a hole by loss of a hydrogen atom from any of its four carbons. Figure 3.3 shows a partial list of radicals produced by one-electron oxidation.

A major difference between hole trapping and excess-electron trapping is that the latter is significantly more specific than the former. While a residue like Tyr has a significant

thermodynamic advantage for hole trapping, it must compete with a plethora of other sites. In contrast, cystine and cysteine have only a hand full of other sites to compete with for electron addition.

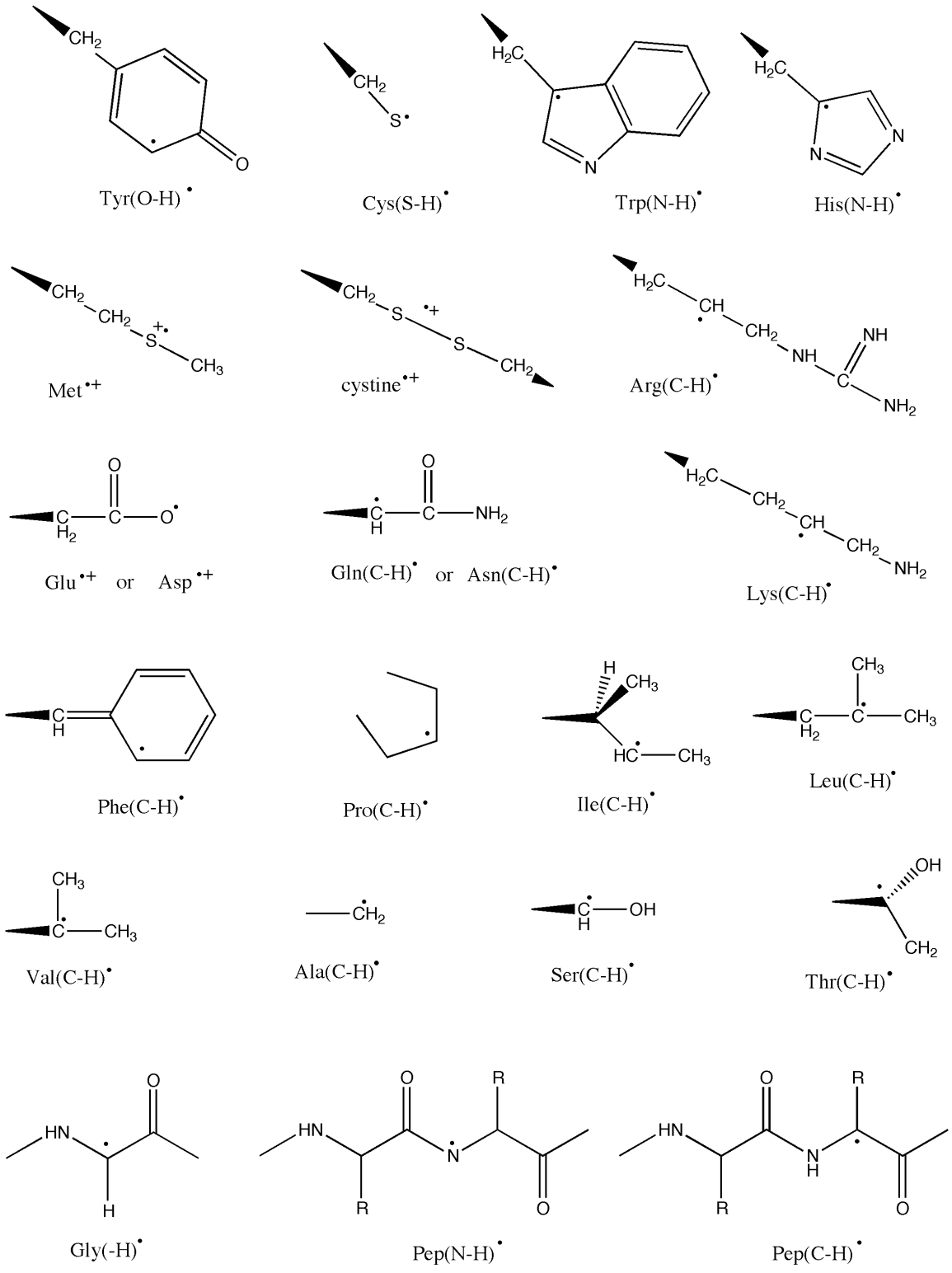

Figure 3.3: A partial list of radicals produced by one-electron oxidation. Initial ionization is non-specific, occurring at every site in the protein.

3.5 Specific reaction schemes for amino acids

3.5.1 Cystine

Disulfide bond cleavage is due to a reductive pathway initiated by electron addition to RSSR (reaction 1.r1) giving the radical anion ($RSSR^{\bullet -}$) (Chapter 2). Subsequent proton transfer (1.r2) followed by a second electron addition (1.r3) results in SS bond cleavage. Subsequent protonation of RS- completes formation of two Cys from one cystine. SS bond cleavage is due to two one-electron reductions spawned by two separate tracks. The first track creates a radical anion and a second overlapping track adds another electron. The second track may also remove an electron (equivalent to adding a hole) via reaction 1.r4, regenerating the native structure. The reaction goes forward via 1.r3 and backward via 1.r4. Disulfides are not only good electron traps, they are also good hole traps; i.e., they are easily one-electron oxidized. Reaction 1.o1 gives the radical cation ($RSSR^{\bullet +}$) but a second one-electron oxidation (1.o3) is thermodynamically unfavorable. In this case, an overlapping second track will strongly favor the back reaction 1.o4 over the forward reaction 1.o3. By this reasoning it is likely that reduction, not oxidation, accounts for cleavage of the SS bond. The scheme is illustrated in Figure 3.4.

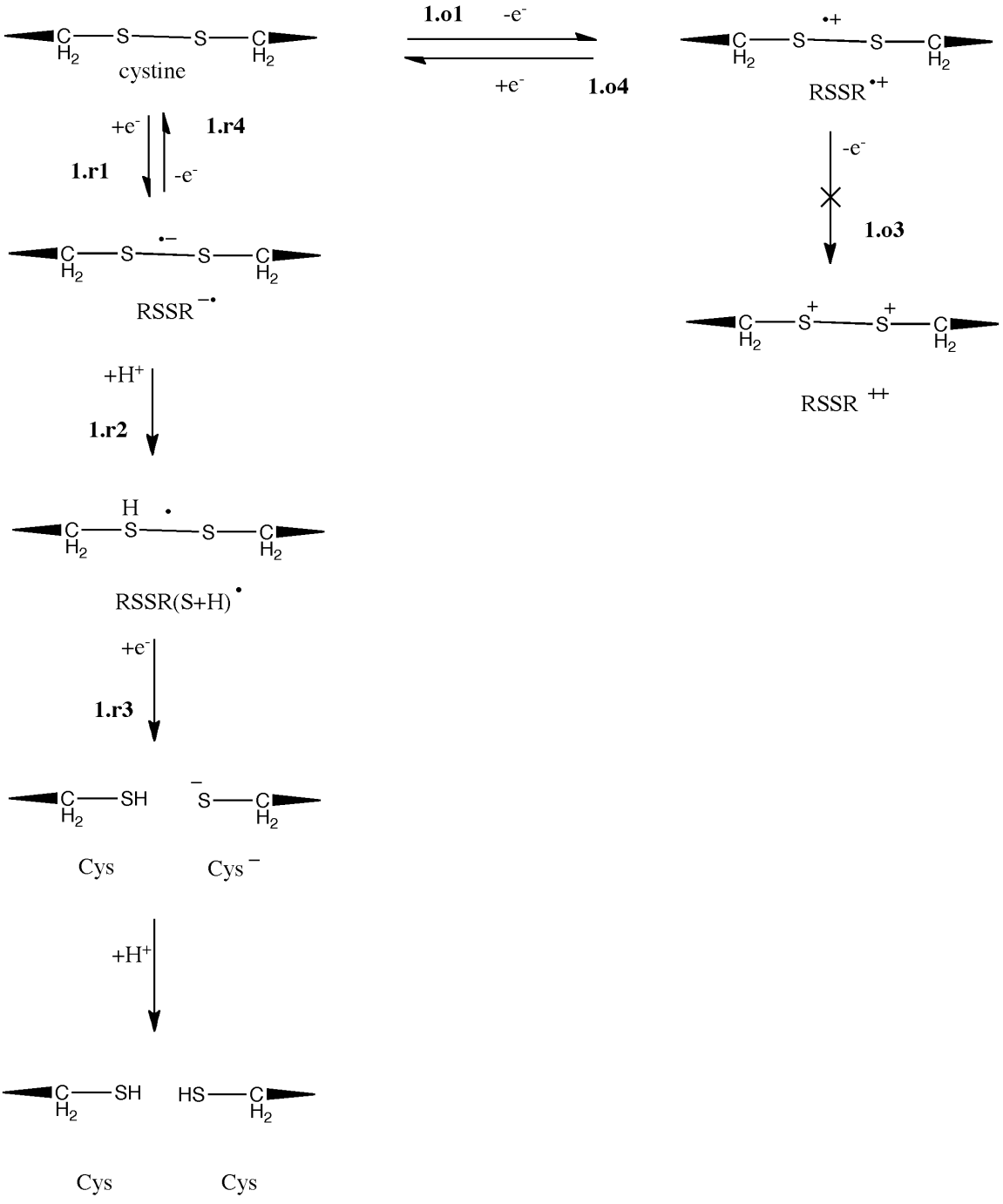

Figure 3.4: Scheme 1. Reductive and oxidative reaction pathways for cystine. The reaction numbers are keyed to Figure 3.1. The 1 in reaction 1.r3 refers to Scheme 1 and the r3 refers to reaction r3 of Figure 3.1.

Protonation of one-electron reduced RSSR, RSH, and $RSCH_3$ results in a type of radical that is in itself a good electron trap. Thus, at higher doses, a second one-electron reduction is likely. When this happens, strong covalent bonds break: the S-S and S-C bond, respectively. This results in the loss of electron density at these sites.

3.5.2 Aspartate and Glutamate

Electron capture by the carboxyl group (2.r1) and its subsequent protonation (2.r2) is well documented by EPR (Box, 1998). Recombination with holes (2.r4) is more likely to occur than further reduction (2.r3).

One-electron oxidation (2.o1) results in a highly unstable oxyl radical that is not observed by EPR, even at 4 K. A unimolecular reaction (2.o6) gives rise to a neutral carbon centered radical (-CH2•) plus CO_2. Also favorable will be the one-electron reduction of $-CH_2^{\bullet\bullet}$ (2.o3)$^{\bullet}$ to give a carbanion, which upon protonation gives –CH3. Thereby, one-electron reduction of aspartate gives alanine plus carbon dioxide. This is shown in Figure 3.5.

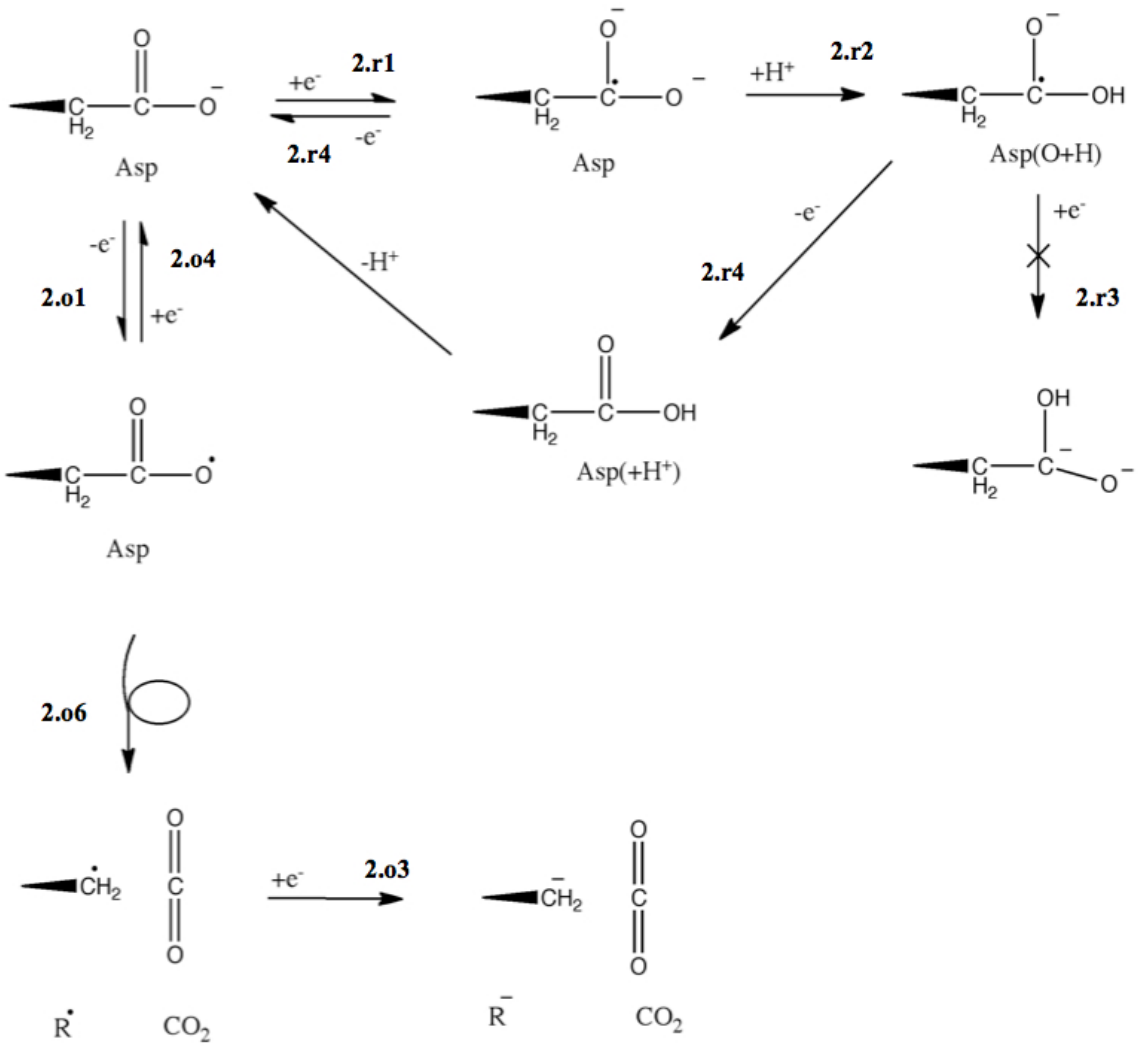

Figure 3.5: Scheme 2. Reductive and oxidative reaction pathways for aspartate. The corresponding reactions are just as likely for glutamate. The reaction numbers are keyed to Figure 3.1, as explained in Scheme 1.

3.5.3 Tyrosine

One-electron oxidation (3.o1) of Tyr is thermodynamically favorable, particularly if it is coupled with proton transfer (3.o2) (Sevilla, 1979a). The resulting neutral radical Tyr(O-H)$^{\bullet}$, if one-electron oxidized (3.o3), will give a carbocation that may react with a neighboring water to give alanine plus 1,4-benzoquinone. In using this pathway to explain the structural data showing a loss of the OH group, a reorientation of the benzoquinone such that the oxygen is repositioned is required while leaving the cleavage of the CH_2- phenol bond undetected. A more tenable explanation for "loss" of the –OH group is through the reduction pathway. One-electron reduction (3.r1) followed by protonation (3.r2) has been observed by EPR (Black & Bernhard, 2011). A second one-electron reduction (3.r3) followed by protonation would produce dihydro-Tyrosine. This partial saturation of the phenol ring will pucker the ring and a shift in the position of the –OH group is likely. Neither by oxidation or reduction is there a reasonable mechanism for cleaving the >C-OH bond.

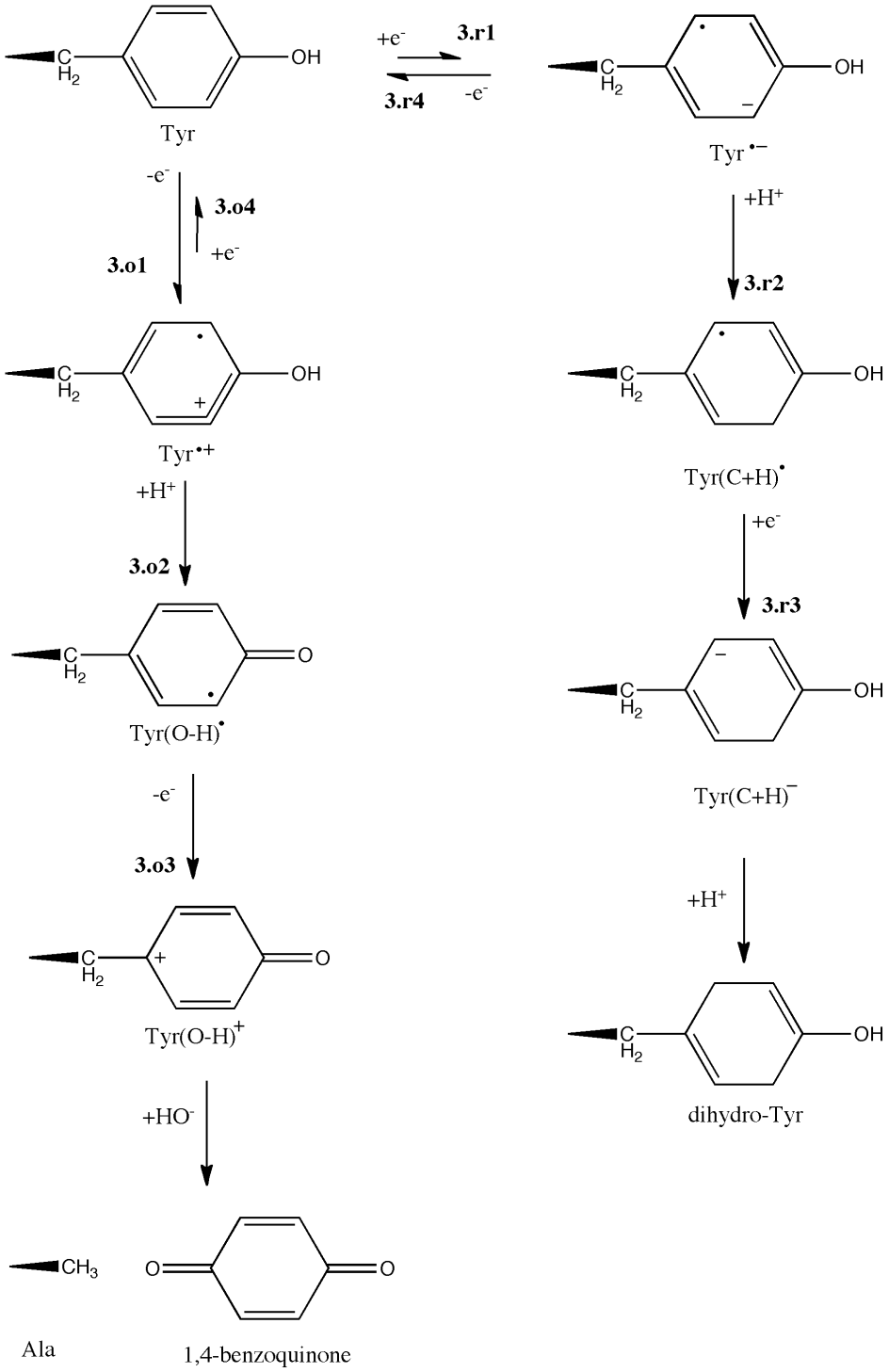

Figure 3.6: Scheme 3. Reductive and oxidative reaction pathways for tyrosine. The reaction numbers are keyed to Figure 3.1, as explained in Scheme 1.

3.5.4 Cysteine

As in cystine, the oxidative pathway is not expected to lead to cleavage of non-hydrogen covalent bonds while the reductive pathway is. One-electron reduction followed by protonation (4.r1 and 4.r2) gives Cys(S+H)$^{\bullet}$. It is an unstable intermediate can undergo unimolecular rearrangement (4.r6) resulting in cleavage of the S-C bond to yield SH$^{\bullet}$ and alanine. Given that one-electron reduction of SH$^{\bullet}$ is highly favorable, as is protonation of SH^{-}, the stable end products of alanine and SH_2 are predicted. If one-electron of Cys(S+H)$^{\bullet}$ occurs prior to the rearrangement, *i.e.* 4.r3 competes with 4.r6, then subsequent proton addition results in the same two end products. This process is illustrated in Figure 3.7.

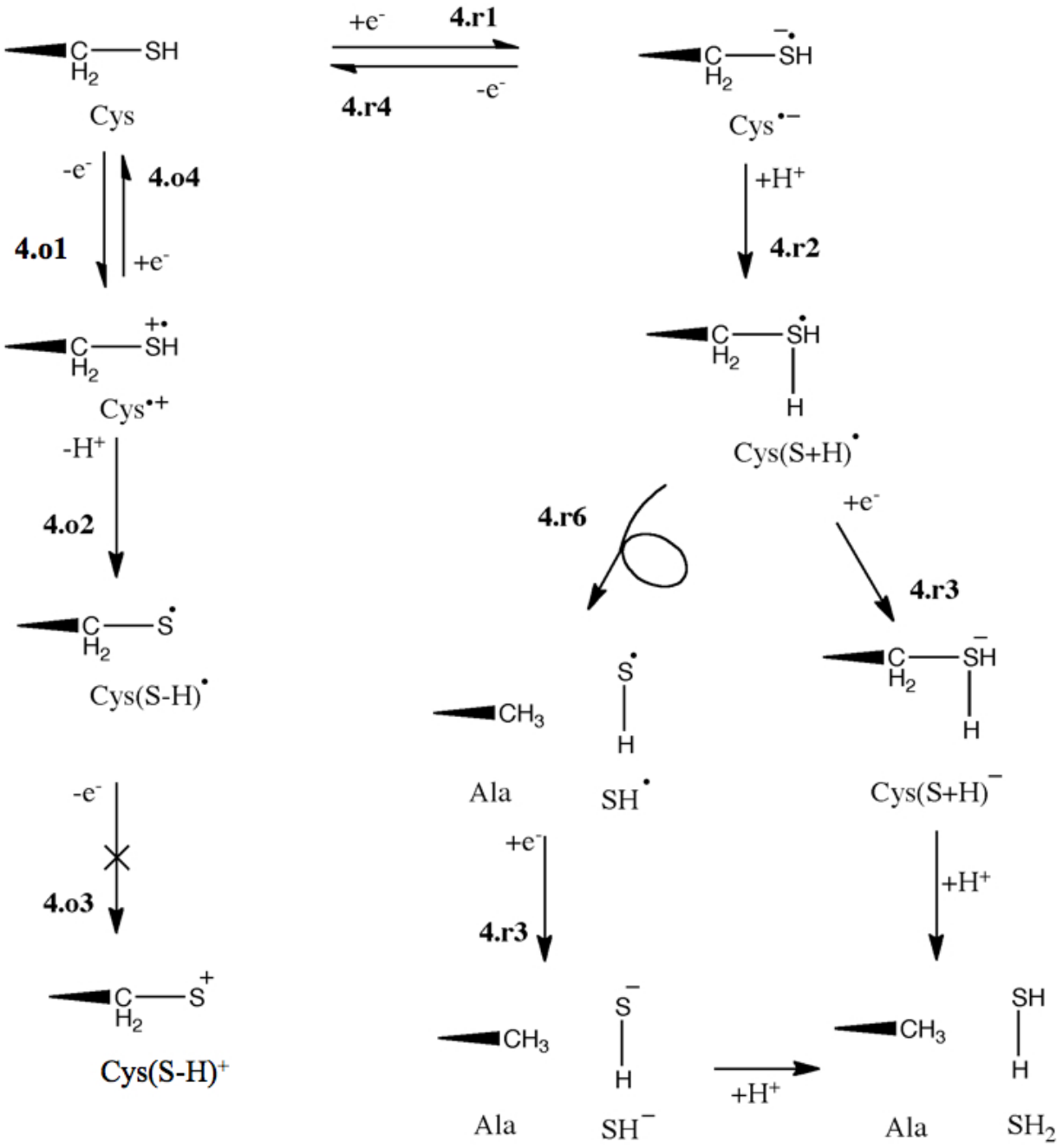

Figure 3.7: Scheme 4. Reductive and oxidative reaction pathways for cysteine. The reaction numbers are keyed to Figure 3.1, as explained in Scheme 1.

3.5.5 Methionine

The reactions stemming from Met follow the same pathways as Cys with just two differences. The unimolecular rearrangement (4.r6 in Scheme 4) is less likely and the final products are predicted to be methane plus a $–CH_2CH_2SH$ residue and/or methanethiol plus a $–CH_2CH_3$ residue.

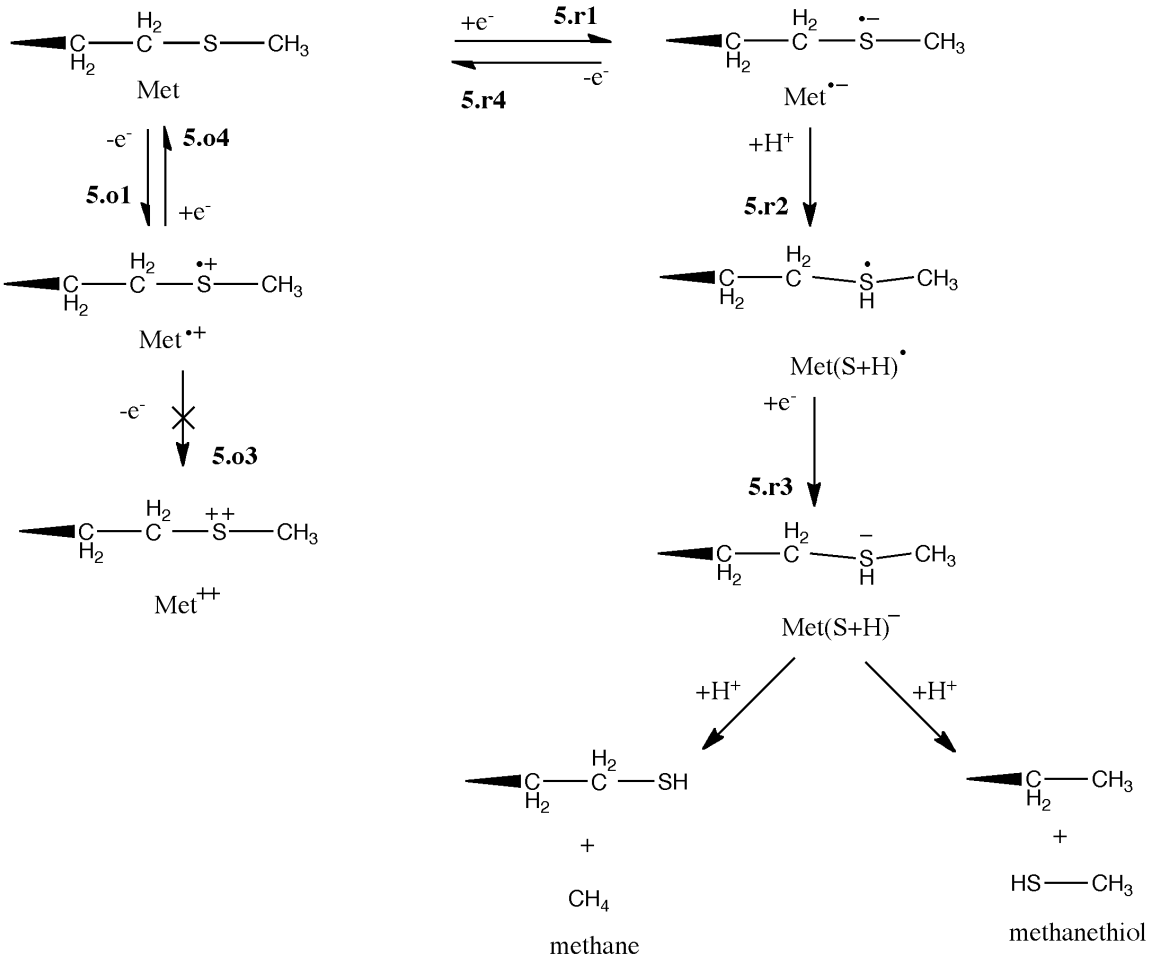

Figure 3.8: Scheme 5. Reductive and oxidative reaction pathways for methionine. The reaction numbers are keyed to Figure 3.1, as explained in Scheme 1.

3.5.6 The Peptide bond

The polypeptide structure of the protein backbone is predicted to be unique in its resistance to damage against the direct effects of ionizing radiation. A prominent feature of Scheme 6 (Figure 3.9) is that, for both the reductive and oxidative side of Scheme 6, recombination of holes with excess electrons dominates. The back reactions, 6.o4a, 6.o4b, and 6.r4 are all expected to be favorable. Furthermore, the forward reactions 6.o1-6.o2-6.o3b and 6.r1-6.r2-6.r3 terminate in a partial saturation of the peptide bond, but do not break the backbone.

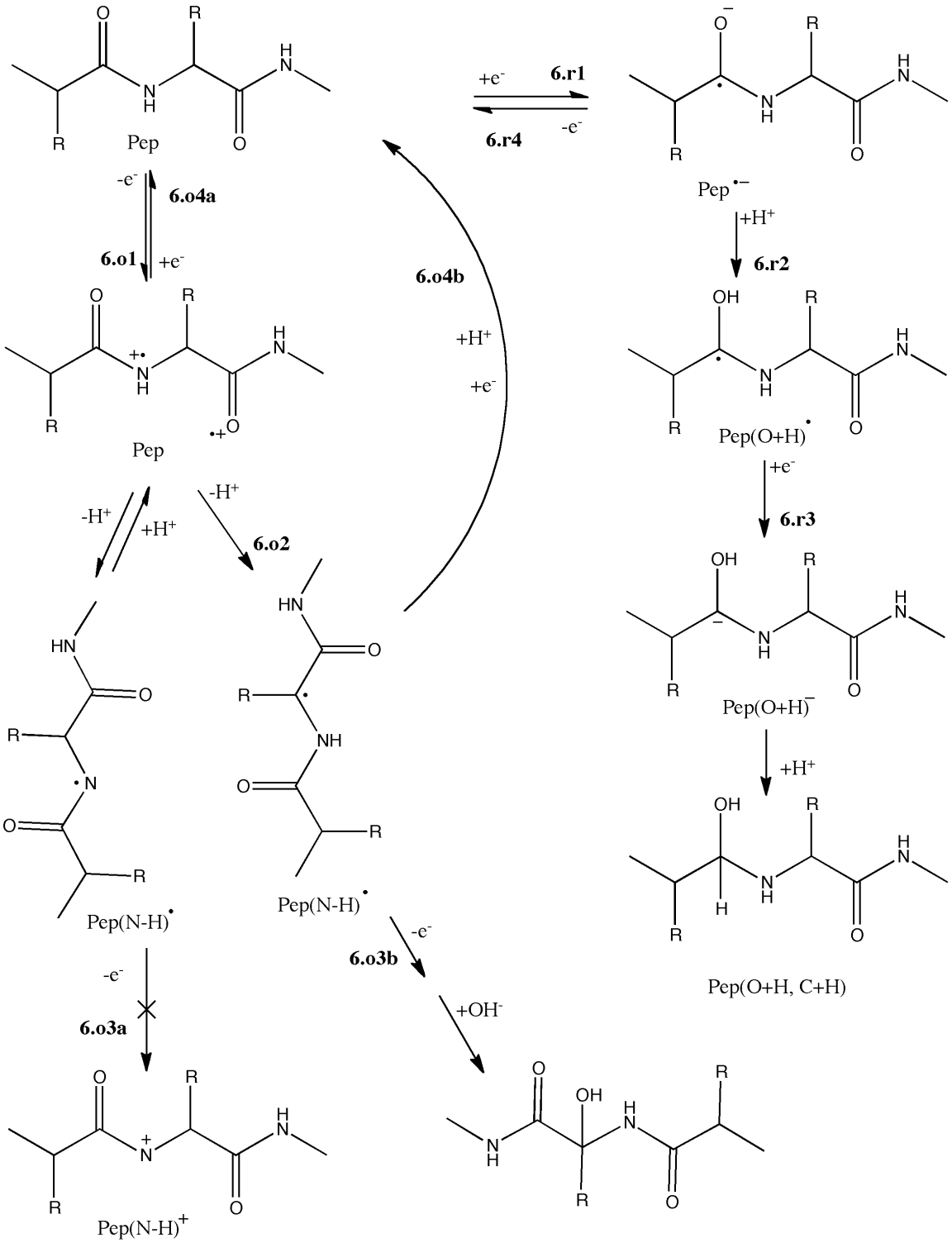

Figure 3.9: Scheme 6. Reductive and oxidative reaction pathways for the peptide bond. The reaction numbers are keyed to Figure 3.1, as explained in Scheme 1.

3.5.7 Solvent

Between 27 and 65% of a protein sample is made up of solvent, predominately water (Matthews, 1968). The reaction scheme proposed for water, scheme 7, is shown in Figure 3.10.

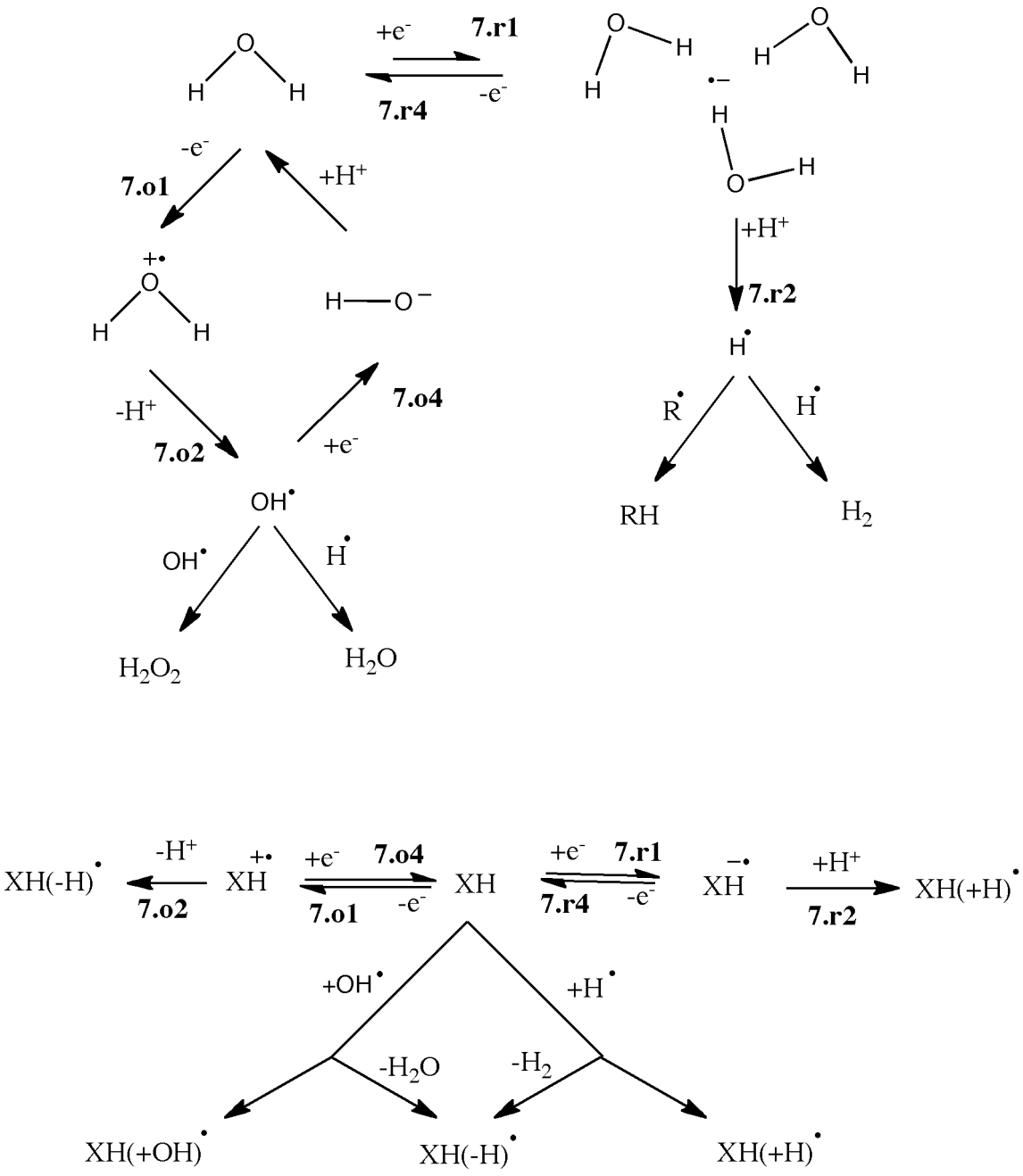

Figure 3.10: Scheme 7. Reductive and oxidative reaction pathways for the solvent, consisting of water and a protectant labelled XH. The reaction numbers are keyed to Figure 1, as explained in Scheme 1.

3.6 Quantitative Predictions by the Model

3.6.1 Theory

In chapter 2, we solved the 3 coupled first order equations that describe the reaction scheme shown in Figure 3.1 under the simplifying assumption that reactions r5 and r6 could be neglected. The simplified reaction sequence is

$$M(D) \underset{k_b}{\overset{k_r}{\rightleftarrows}} R(D) \xrightarrow{k_f} P(D)$$

where concentrations of the starting molecule M, intermediate radical R, and final product P depend on dose D. The dependence of M, R, and P on dose, D, is described by three first order differential equations containing rate constants k_r, k_f, and k_b:

$$\frac{dM(D)}{dD} = -k_r M(D) + k_b R(D) \tag{3.1a}$$

$$\frac{dR(D)}{dD} = k_r M(D) - (k_f + k_b) R(D) \tag{3.1b}$$

$$\frac{dP(D)}{dD} = k_f R(D) \tag{3.1c}$$

The solution to Equations 3.1a, 3.1b, and 3.1c is:

$$M = \frac{M_0(qe^{-mD} + e^{-nD})}{q+1} \tag{3.2a}$$

$$R = \frac{M_0((qm+n)e^{-nD} + (qm-n)e^{-mD})}{(q+1)((m-n)} \tag{3.2b}$$

$$P = M_0 + \frac{M_0(ne^{-mD} - me^{-nD})}{m-n} \tag{3.2c}$$

where M_0 is M at zero dose and m, n, q (used for compactness) are determined by the three rate constants using

$$n = \frac{2k_r k_f}{(k_r + k_b + k_f) - \sqrt{(k_r + k_b + k_f)^2 - 4k_r k_f}} \quad (3.3a)$$

$$m = \frac{(k_r + k_b + k_f) - \sqrt{(k_r + k_b + k_f)^2 - 4k_r k_f}}{2} \quad (3.3b)$$

$$q = \frac{n - k_r}{k_r - m} \quad (3.3c)$$

Equations 3.1-3.3 describe the dose dependence of M, R, and P using four physically relevant parameters: k_r, k_f, k_b, and M_0. Coupled with rate constants defined by each scheme this model has the potential of quantitatively predicting the onset and growth of damage at specific constituents in a protein crystal.

3.6.2 Experimental Determination of Yield

The rate constants k_r, k_f, and k_b have yet to be defined for all the amino acids. However, the experimental determination of yield is irrespective of the exact radiation damage process giving that yield, therefore experimental results can be used to develop the model of the process. In Table 3.1, the individual amino acids are listed together with the reaction yield, G, determined by Hatano *et al.* (Hatano, 1962). G values are typically given as the number of particular species produced per 1 Joule of energy. As the data in Table 3.1 was derived from determining the point where 63% of the amino acid was destroyed the G values represent a qualitative rather than quantitative measure. To overcome this, the yield is converted to a probability by normalizing to the sum of G values. The probability[2] is also presented as a measure of double oxidation or double

reduction (the square of the probability representing the chances of two radicals interacting, see section 3.6.2). The G values were determined for the individual amino acids in solution by gamma ray irradiation. The type of irradiation is unimportant in this case, but the radiation chemistry of a cryocooled crystal will differ from a solution due to the immobilization of OH radicals. An argument can be made that this should be a systematic effect on the actual G value, but not the relative probability. Similarly, these G values are for individual amino acids. They do not take into account effects that adjacent residues may influence over the overall process. Despite these two significant flaws, with the absence of better data, they provide an initial indication of the sensitivity of individual residues and can be used to a first approximation.

Table 3.1: Reaction yield and probability for amino acids present in macromolecular samples. G-value is the basic unit of radiation chemical yield. G = 1 indicates that one entity (e.g., one free radical of a given type) is formed or destroyed for each 100 eV of energy absorbed by the medium.

Amino Acid	Weight	G	Probability	Probability[2]
Alanine[1]	71.0788	0.84	0.02	0.001
Arginine	156.1876	2.33	0.07	0.005
Asparginine[2]	114.1039			
Aspartic Acid	115.0886	1.00	0.03	0.001
Cysteine	103.1448	1.26	0.04	0.001
Glutamic Acid	129.1155	2.33	0.07	0.005
Glutamine[2]	128.1308			
Glycine	57.0520	1.13	0.03	0.001
Histidine	137.1412	2.49	0.07	0.005
Isoleucine	113.1595	2.13	0.06	0.004
Leucine	113.1595	2.69	0.08	0.006
Lysine	128.1742	2.09	0.06	0.004
Methionine	131.1986	3.79	0.11	0.012
Phenylalanine	147.1766	2.69	0.08	0.006
Proline	97.1167	0.62	0.02	0.000
Serine	87.0782	2.24	0.07	0.004
Threonine	101.1051	3.03	0.09	0.008
Tryptophan	186.2133	1.21	0.04	0.001
Tyrosine	163.176	0.55	0.02	0.000
Valine	99.1326	2.02	0.06	0.003

[1]Concentration dependent, value at approximately 0.5 M, decreases markedly below that described by (Rodgers, 1968)

[2]No experimental data was provided for this residue.

3.6.3 Quantitative prediction

Radical interactions cause two one-electron reductions or two one-electron oxidations, Figure 3.11. We can consider this in combination with the schemes presented above, the experimental yield in Table 3.1, and a prediction of the structural consequences, to determine what would be crystallographically observable.

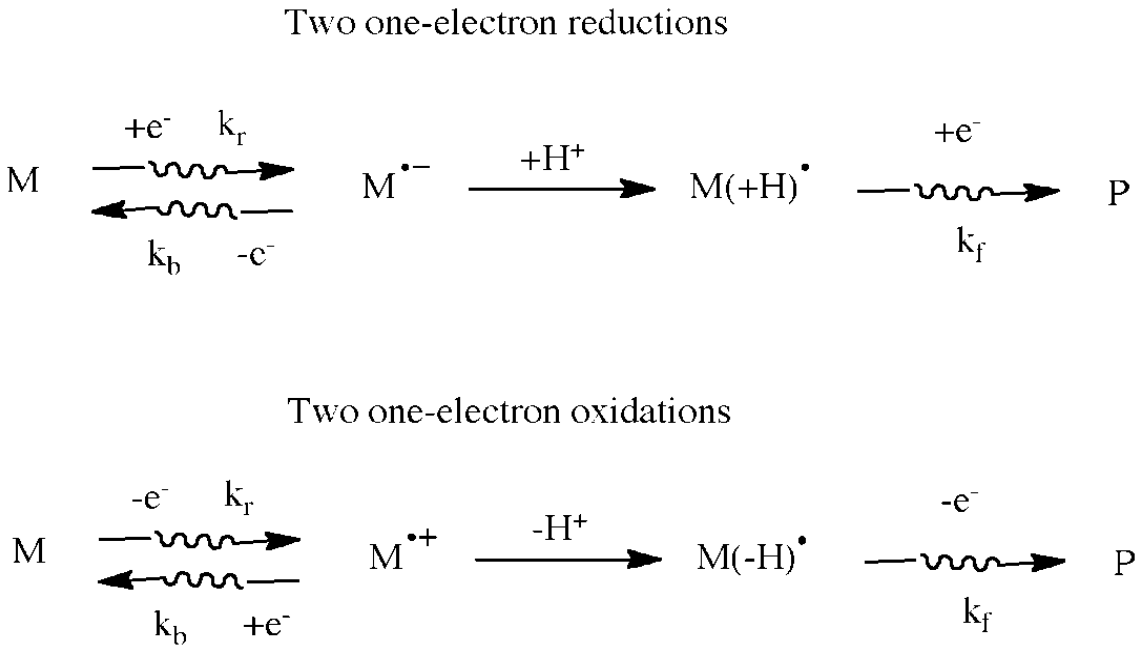

Figure 3.11: Radical interactions are either two one-electron reductions or two one-electron oxidations.

3.6.3.1 One-electron reduction

The products produced by one-electron reduction can be estimated from Chapter 2 (Sutton et al., 2013). The total free radical production was measured as 281 $nmolJ^{-1}$. Assuming that the total radical production by one-electron reduction is equal to that by one-electron oxidation then the radical production by one-electron reduction, G(1ER), is ~140 $nmolJ^{-1}$. The $G(SS^{\bullet-})$ was 60 $nmolJ^{-1}$ so the yield of all other one-electron reduction radicals, seen in Figure 3.2, is $G(1ER)-G(SS^{\bullet-})$, or 80 $nmolJ^{-1}$. It is unlikely that these products would be easily discernible by X-ray crystallography given that only small changes in bond length (~ 0.1 Å) would result around the site of electron gain. The radical concentration will dose saturate between ~50 kGy and ~500 kGy. The saturation concentration is <0.2%; in effect this introduces one defect per 500 undamaged sites. Even using small molecule crystallography with <0.1 Å, these structural changes would not be detectable. One-electron reduction is not observable through X-ray crystallography.

3.6.3.2 Two one-electron reductions

Two one-electron reductions can cleave non-hydrogen covalent bonds, examples including cystine to cysteine, cysteine to SH_2 and methionine to methanethiol. These are detectable crystallographically with significant structural differences resulting as described in earlier chapters. Another effect will be the ring saturation of aromatics, *e.g.* tyrosine. Using estimates from EPR data on lysozyme (Sutton et al., 2013), we can calculate the dose response curves for these products.

From above, the yield of all other one-electron reduction radicals is 80 $nmolJ^{-1}$. The probability of one-electron reduction of H_2O is 0.08 accounting for 6.4 $nmolJ^{-1}$. For the sulfur containing residues, the probability for one-electron reduction of Cys is 0.04 yielding 3.2 $nmolJ^{-1}$ and for Met the probability is 0.11 yielding 8.8 $nmolJ^{-1}$. The probability of a one-electron reduction for Asp and Glu is 0.07, yielding 5.6 $nmolJ^{-1}$ and for Tyr the probability is 0.02, yielding 1.6 $nmolJ^{-1}$. The probability of a one-electron reduction for cystine is not available. Given that cystine has two sulfurs, it is safe to assume that the likelihood of being one-electron reduced is at least twice that of a Cys residue. We can estimate that the probability of a one-electron reduction of cystine as ~0.08, yielding 6.4 $nmolJ^{-1}$.

The yield for two one-electron oxidations can be calculated from the square of one-electron oxidations given the probability of radical interaction. This gives a yield of 0.08 $nmolJ^{-1}$ for Cys, 0.96 $nmolJ^{-1}$ for Met, 0.04 $nmolJ^{-1}$ for Asp and Glu, 0.03 $nmolJ^{-1}$ for Tyr and 0.51 $nmolJ^{-1}$ for cystine.

Of all of the protein components, Tyr has the smallest reduction potential of 930 EmV^{-1} at pH 7, therefore it is easiest to oxidize. After one-electron oxidation it will deprotonate to give a radical that in itself is also a decent hole trap. Double oxidation, at high dose, will not break any strong covalent bonds but it will result in the formation of new double bonds that should cause significant reorientation of the benzoxyl group. Because the benzoxyl remains attached, the reorientation of the keto oxygen (previously OH) should be larger than other atoms, in what used to be a phenol. It would appear as though the

OH was lost (observable in the structure) although mechanistically, it is very hard to conceive of a way to cleave the C-OH bond with ionizing radiation. The explanation for the observed loss of the hydroxyl group in crystallographic data is unknown.

Dose is given in Gy, which is equivalent to 1 JKg^{-1}. The lysozyme crystal used for the crystallographic data shown in this chapter was 0.3 × 0.3 × 0.3 mm giving a volume of 0.027 mm^3. Using a density of 1.17 g cm^{-3} the mass of the crystal under study is approximately 31.6 µg or $3.16x10^{-5}$ g. The dose per data set was 0.07 MGy equating to 2.2 J per data set. In terms of two one-electron oxidized Asp, Glu and Tyr, a dose of 2.2 J should result in 0.09 nmol of oxidized Asp and Glu, and 0.07 nmol of Tyr. Within a single lysozyme molecule there are 7 Asp, 2 Glu, and 3 Tyr per 129 residues. The crystal volume is 0.27 mm^{-3} with a density of 1.17 gcm^{-3} and mass of 14.31 kDa equating to $3.16x10^{-5}$ g and 2.2 nmol of protein. Asp makes up 5.6% of this, Glu 1.8%, Tyr 3.42%, Met 1.6% and Cys 6.2%, or $1.77x10^{-6}$ g, $5.69x10^{-7}$ g,$1.08x10^{-6}$ g, $5.05x10^{-7}$ g and $1.96x10^{-6}$ respectively. Therefore within the crystal there is 15.45 nmol of Asp, 4.41 nmol of Glu, 6.62 nmol of Tyr, 3.39 nmol of Met and 16.19 nmol of Cys, Table 3.2. The two one-electron oxidation is distributed over these, dividing the effect by 7, 2, 3, 2 and 8 respectively. One data set would damage 1.03% of the Asp, 19.54% of Glu, 1.06% of Tyr, 62% of Met and 1.73% of the Cys residues. For final data set, with an absorbed dose of 1.05 MGy, damage would be expected in 15.38% of the Asp residues, 100% of the Glu residues 15.95% of the Tyr residues, 100 % of the Met residues and 26% of the Cys residues. At a level of 25% of the residue damaged, radical damage to the Glu, Met and Cys residues would be expected to be observed crystallographically.

Table 3.2: Concentration of residues in the lysozyme crystal with the corresponding percentage expected to be damaged at absorbed doses of 0.07 MGy and 1.05 MGy.

Residue	concentration in crystal (nmol)	% expected to be damaged	
		0.07 MGy	1.05 MGy
Asp	15.45	1.03%	15.38%
Glu	4.41	19.54%	100.00%
Tyr	6.62	1.06%	15.95%
Met	3.39	62.00%	100.00%
Cys	16.19	1.73%	26.00%

3.6.3.3 One-electron oxidation

The key concepts are quite similar for the one-electron oxidized sites but the impact is not nearly as specific. This is because every peptide bond is a good hole trap. Some residues, Tyr and Glu for example, are also good hole traps, but the concentration of the competing backbone sites (peptide bonds) will typically be ~100X greater. Thus, the backbone protects the residues from oxidation. One-electron oxidation produces the hydroxyl radical with a probability of 0.08. The one-electron oxidation yield can also be estimated as ½ G(total radical) equating to 140 $nmolJ^{-1}$. Therefore the yield of hydroxyl radicals is 0.08x147=11.76 nmol/J for all water in lysozyme. These are immobile at 100 K and serve to collect additional holes and electrons. The yield of oxidized Asp and Glu can be estimated from Figure 3.6. For Asp and Glu, oxidation of the whole residue is 0.24 $nmolJ^{-1}$ and 0.30 $nmolJ^{-1}$ respectively. For the CO_2 group it is 0.18 $nmolJ^{-1}$

3.7 Agreement with the model and experimental results.

The model is based on a multi-track radiation damage process. The experimental G values provide predictions of when we would expect to see damage occurring, and the model explains why that process occurs. Support for the model comes from a study of lysozyme, in particular the damage to disulfide bonds. However, the radiation damage process and the radiation chemistry behind it are well known for amino acids in general. The model can be tested looking at the lysozyme results and extended to the second protein, XI, studied in detail in later chapters.

3.7.1 Lysozyme

Based on the above model and the dose received by the lysozyme crystal (0.07-1.05 MGy) the damage from two one-electron reductions causing cystine to cysteine, cysteine to SH_2 and methionine to CH_3SH should be visible in the electron density map. Similarly ring saturation of aromatics, *e.g.* tyrosine, and decarboxylation of acidic side chains should be observable.

3.7.1.1 Cystine

Electron density in the form of Fo-Fc maps is shown for cystine, Cys6-Cys127, in Figure 3.12. Based on Scheme 1, an increase in positive density first at the disulfide bond due to the electron addition to give $RSSR^{\bullet-}$ (1.r1) is expected. Upon the second electron addition an increase in negative density between the sulfur atoms indicating cleavage of the disulfide bond (1.r3) is expected. Positive density near the sulfur atoms and negative density between the sulfur atoms was observed. This illustrates the first electron addition and second electron addition, respectively, supporting the model predictions. Similar density peaks were observed for the dose 0.07-1.05 MGy indicating that there is a mixture of one-electron reduced and two one-electron reduced species in the crystal.

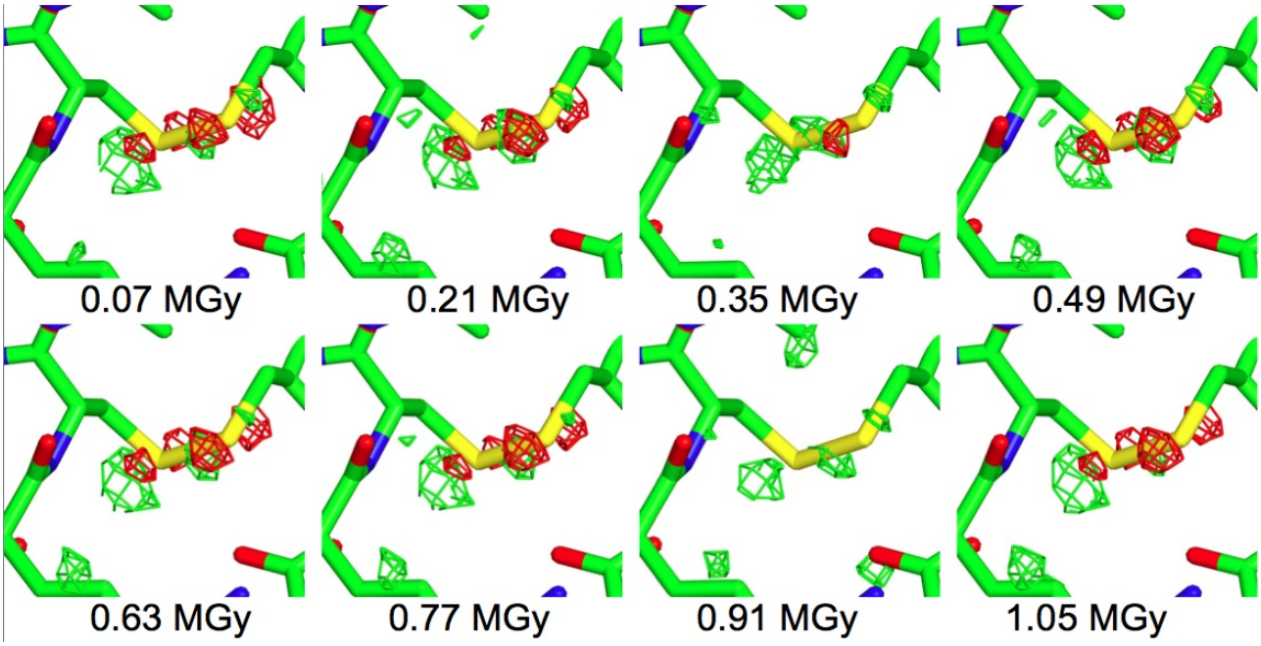

Figure 3.12: Fo-Fc maps of the disulfide bond Cys6-Cys127 in lysozyme contoured at +/- 3 sigma at dose points ranging from 0.07 MGy to 1.05 MGy. Increase in positive density (green) illustrates radicalization and negative density (red) illustrates elongation and cleavage of the bond.

3.7.1.2 Methionine

Electron density in the form of Fo-Fc maps is shown for methionine (Met12), in Figure 3.13. Based on the model and G values evidence of radical accumulation near the sulfur atom of methionine due to the one-electron addition to form Met•- (Scheme 5, 5.r1), would be expected. With an increased in absorbed dose, the addition of a hydrogen atom (5.r2) and another electron (5.r3) leads to cleavage of the carbon-sulfur bond in methionine, which should be observeable via negative density surrounding the sulfur atom. Positive density is indeed seen on the sulfur atom at 0.35 MGy and 0.91 MGy suggesting that an SH• is formed however, this density is not observed in each of the datasets. The radical yield estimates suggest that 62% of the methionine residues will be two one-electron reduced in the first dataset and 100% reduced in the second dataset. This is obviously not the case here with the expectation of bond cleavage. Since the radical yields were calculated using solutions at room temperature (Hatano, 1962), methionine may react with the hydroxyl radical in those experiments, while it is trapped at the conditions explored here. The damage expected is likely significantly over estimated.

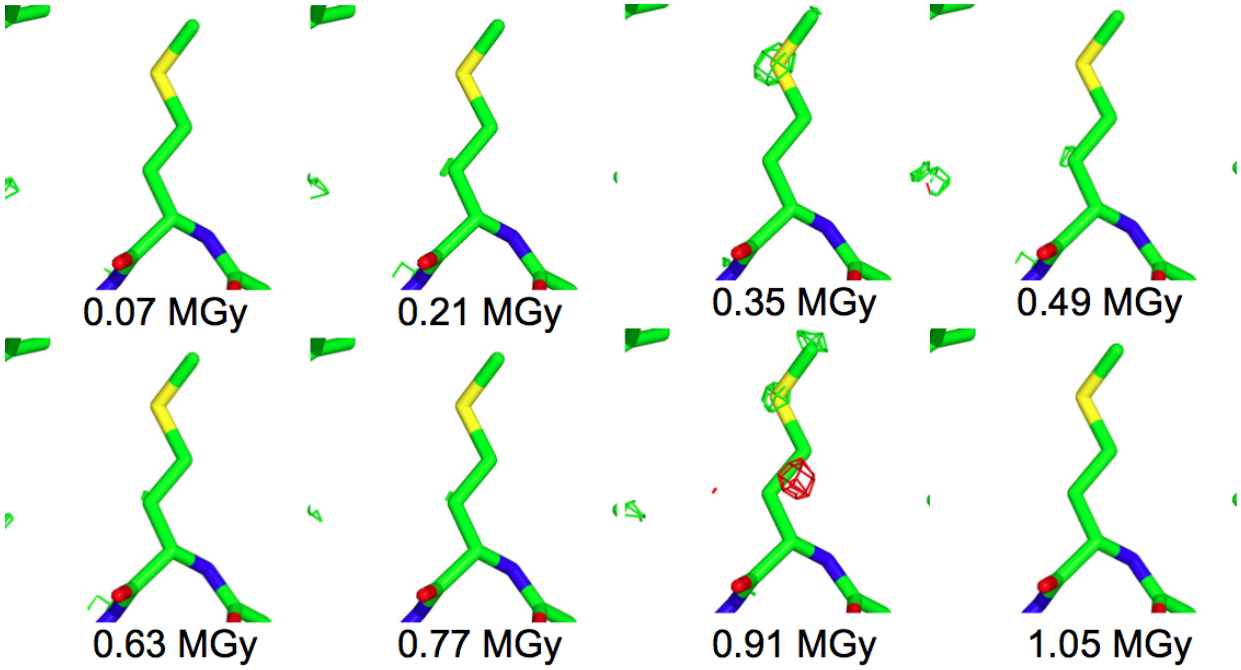

Figure 3.13: Fo-Fc maps of Met12 in lysozyme contoured at +/- 3 sigma at dose points ranging from 0.07 MGy to 1.05 MGy. Radicalization of the carbon sulfur bond in the 0.35 and 0.91 MGy datasets is illustrated by the positive density peak (green mesh) on the sulfur atom (shown in yellow).

3.7.1.3 Glutamate

For both Glu and Asp residues evidence of the formation of a carbon-centered radical on the carboxyl group of the residue (Scheme 2, 2.r1), or evidence of decarboxylation (2.o6) is predicted. If decarboxylation were occurring, negative density surrounding the oxygen atoms of the carboxyl group should be present. In Figure 3.14, no evidence of the carbon-centered radical is present. There is a negative density peak adjacent to one of the oxygen atoms of the carboxyl group. This may suggest that decarboxylation of this residue will occur with a greater absorbed dose. The radical yield estimations for glutamate predict that 19.56% of the two glutamate residues will be two one-electron reduced in the first dataset (0.07 MGy) and 100% by the sixth dataset (0.63 MGy). This is not seen. Again this may be due to the estimates of yield used, which may differ based on the estimates calculation at room temperature and the cryogenic conditions used for crystallographic data collection.

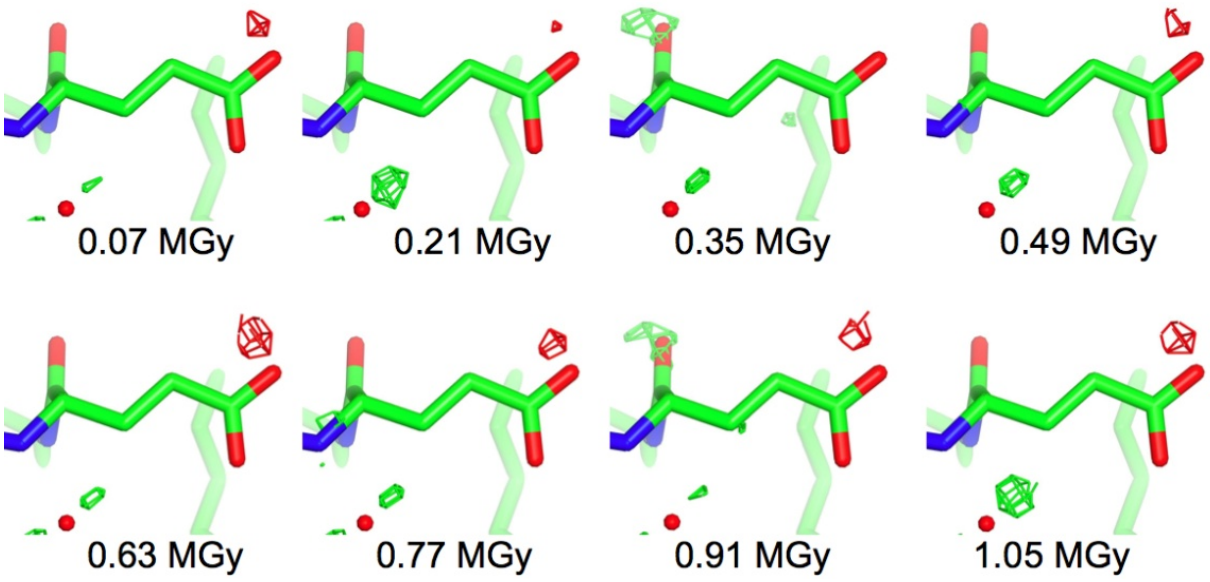

Figure 3.14: Fo-Fc maps of Glu7 in lysozyme contoured at +/- 3 sigma at dose points ranging from 0.07 MGy to 1.05 MGy illustrating the increase in the negative electron density peak near the carboxyl group of glutamate. This may indicate the initial radical damage to cause decarboxylation at a higher absorbed dose.

3.7.1.4 Aspartate

The Asp residue shown in Figure 3.15 illustrates both effects predicted by the model; formation of the carbon-centered radical (Scheme 2, 2r.1) and decarboxylation (2.o6). The positive density peak between the two oxygen atoms provides evidence for the formation of the carbon-centered radical and the negative density located on the oxygen atom provides evidence for decarboxylation. The estimations of radical yield suggest 1% of the Asp residues will be two one-electron reduced by the collection of the first dataset (0.07 MGy) and 15.38% by the last dataset (1.05 MGy). There are no major changes in the difference electron density as a function of dose, but we observe the effects predicted by Scheme 2, the formation of the carbon-centered radical and decarboxylation at the appropriate locations.

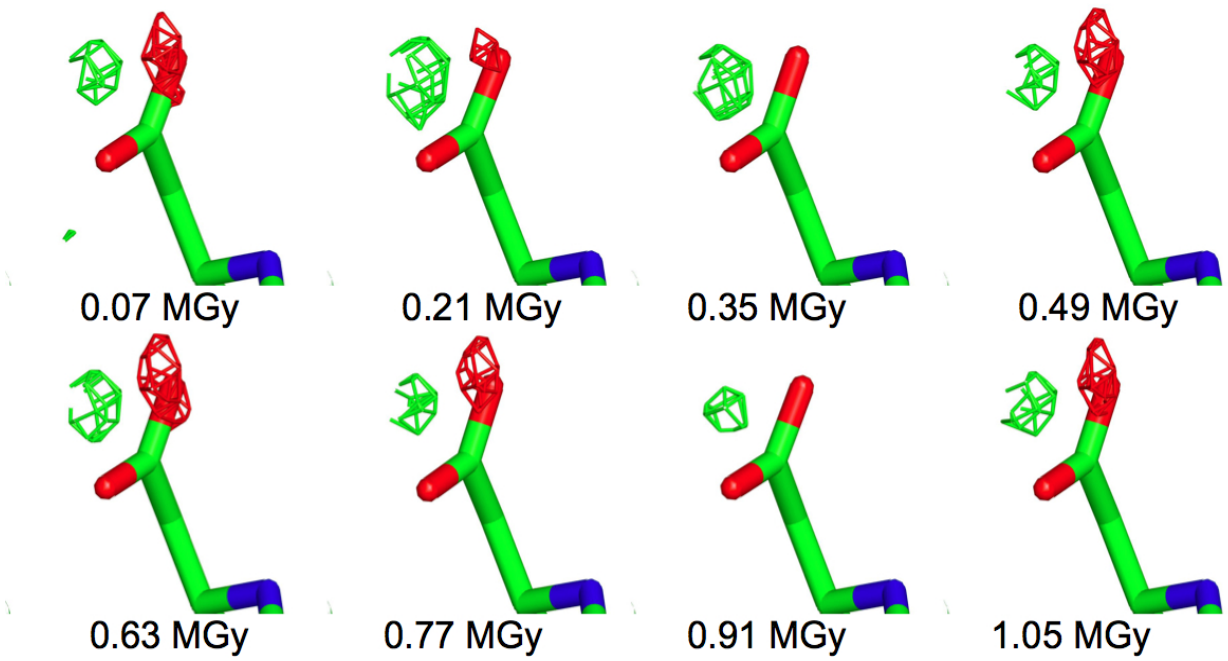

Figure 3.15: Fo-Fc maps of Asp52 in lysozyme contoured at +/- 3 sigma at dose points ranging from 0.07 MGy to 1.05 MGy. An increase in absorbed dose does not appear to increase the apparent damage. Negative density on one oxygen atom of the carboxyl group suggests decarboxylation may occur at higher doses than the doses employed for this study.

3.7.1.5 Tyrosine

The one-electron oxidation of tyrosine coupled with proton transfer is observed in Figure 3.16. Tyrosine can either be reduced or oxidized (Scheme 3). The radical yield estimation suggests 1.06% of Tyr will be two one-electron reduced or oxidized in the first dataset (0.07 MGy) and 15.95% will be affected by the last dataset (1.05 MGy). Since only a small percentage of Tyr would be affected, one would expect little structural evidence for the process. However, a positive electron density peak is seen adjacent to the Tyr ring suggesting saturation of that carbon atom. This is possibly a combination of the neutral radical, Tyr(O-H)$^{\bullet}$, due to the one-electron oxidation (Scheme 3, 3.o1) and a proton transfer (3.o2).

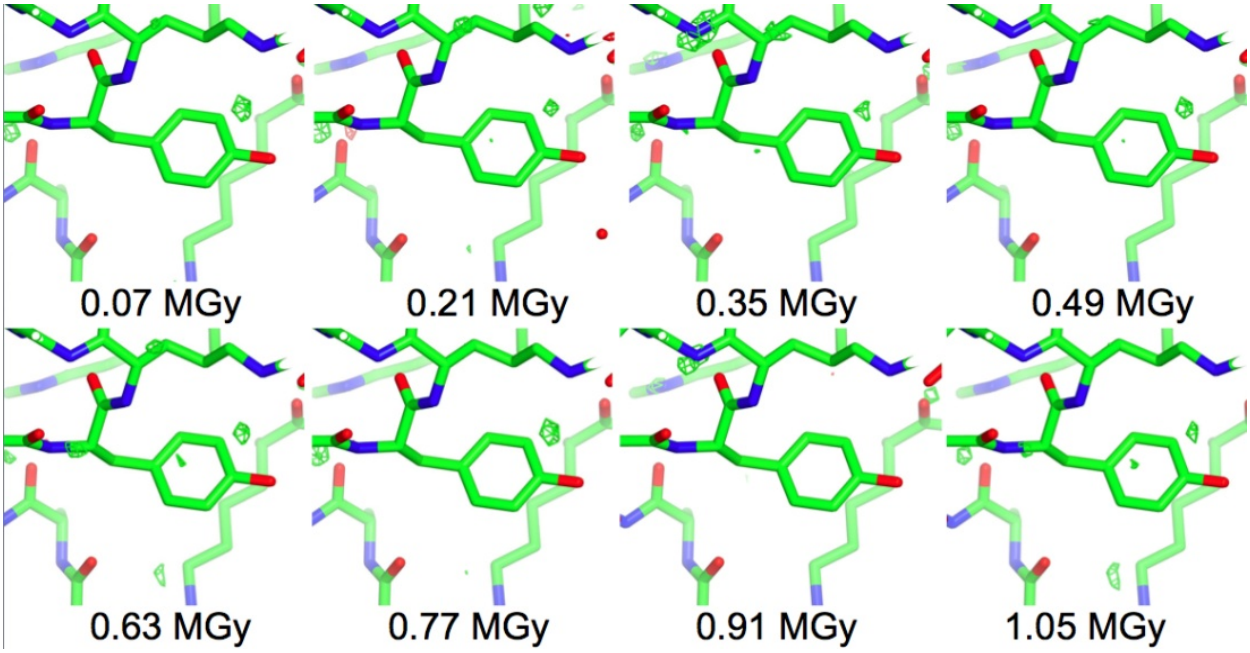

Figure 3.16: Fo-Fc maps of Tyr20 in lysozyme contoured at +/- 3 sigma at dose points ranging from 0.07 MGy to 1.05 MGy illustrating a small positive electron density peak inside the tyrosine ring and a small positive electron density peak outside the ring, suggesting saturation of one of the ring carbons.

3.7.1.6 Contol residue- glycine

As a control glycine was also studied, Figure 3.17. Glycine does not have a side chain, i.e. no X-ray labile groups to be damaged and, partly as a consequence of this, the G-value is one of the lowest for all the amino acids (0.03). At a difference map density level of +/- 3 sigma, no positive or negative density peaks are in close proximity to the residue, indicating no evidence of radiation damage.

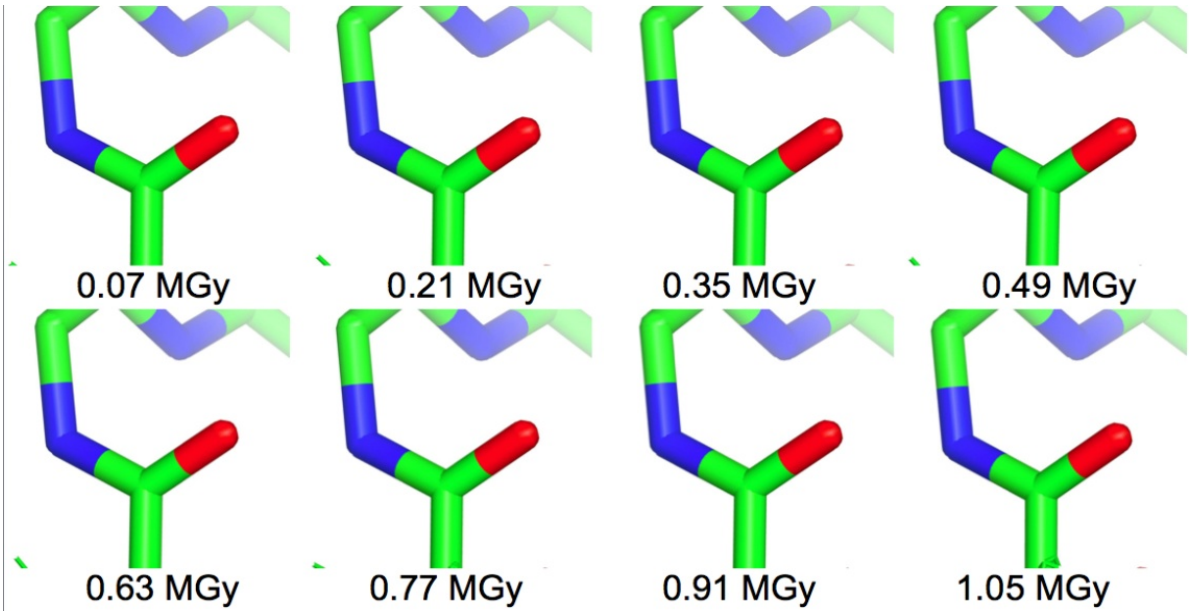

Figure 3.17: Fo-Fc maps of Gly125 in lysozyme contoured at +/- 3 sigma at dose points ranging from 0.07 MGy to 1.05 MGy. Glycine is not expected to show signs of radiation damage. It is shown as a control, no positive or negative density peaks are observed above 3 sigma.

3.7.2. Xylose Isomerase

XI is a larger protein that lysozyme (43 kDa versus 14 kDa) and contains no disulfide bridges. For the estimations of radical yield, we used the total yield of radicals determined for lysozyme, 140 $nmolJ^{-1}$, as an order of magnitude estimation. The XI crystal used for the crystallographic data shown in this chapter was $0.3 \times 0.3 \times 0.3$ mm giving a volume of 0.027 mm^3. Using a density of 1.17 g cm^{-3} the mass was calculated at ~31.6 µg or $3.16x10^{-5}$ g. The dose per data set was 0.8 MGy equating to 36 J per data set. Within a single XI molecule there are 37 Asp, 28 Glu, 9 Tyr, 7 Met and 1 Cys per 386 residues. The crystal volume is 0.27 mm^{-3} with a density of 1.17 gcm^{-3} and mass of 43 kDa equating to $3.16x10^{-5}$ g and 2.2 nmol of protein. Asp makes up 34.4% of this, Glu 28.8%, Tyr 11.4%, Met 1.8% and Cys 0.3%, or $1.09x10^{-5}$ g, $9.08x10^{-6}$ g, $3.60x10^{-6}$ g, $5.69x10^{-7}$ g and $9.48x10^{-8}$ g respectively. Therefore, within the crystal there is 81.66 nmol of Asp, 61.80 nmol of Glu, 19.86 nmol of Tyr, 3.82 nmol of Met and 0.78 nmol of Cys. The two one-electron oxidation is distributed over these, dividing the effect by 37, 28, 9, 7 and 1 respectively. One data set would damage 1.70% of the Asp, 12.21% of Glu, 3.10% of Tyr, 100% of Met and 100% of the Cys residues. By the 7^{th} data set, damage would be expected to occur in 25.56% of the Asp residues, 100% of the Glu residues 46.69% of the Tyr residues, 100 % of the Met residues and 100% of the Cys residues. Using the same 25% of the residue damaged as used for the lysozyme case, radical damage should be visible on the Asp, Glu, Tyr and Met residues and possibly the Cys residues.

Table 3.3: Concentration of residues in the XI crystal with the corresponding percentage expected to be damaged at absorbed doses of 0.35 MGy and 5.60 MGy.

Residue	concentration in crystal (nmol)	% expected to be damaged	
		0.35 MGy	5.60 MGy
Asp	81.66	1.70%	25.56%
Glu	61.80	12.21%	100.00%
Tyr	19.86	3.10%	46.69%
Met	3.82	100.00%	100.00%
Cys	0.78	100.00%	100.00%

3.7.2.1 Methionine

The model predicts cleavage of the carbon-sulfur bond in methionine with increased absorbed dose. In Figure 3.18 there is no evidence of this cleavage. However, there is an increase in the positive density surrounding the residue, suggesting that radicalization has occurred. Radical accumulation near the sulfur atom of methionine is expected due to the one-electron addition to form Met•- (Scheme 5, 5.r1). An increase in absorbed dose, the addition of a hydrogen atom (5.r2) and another electron (5.r3) should result in cleavage of the carbon-sulfur bond in methionine, indicated via negative density surrounding the sulfur atom. In this case positive density is seen on the carbon atom bound to sulfur, which increases with increased absorbed dose. The radical yield estimates suggest that 100% of the methionine residues will be two one-electron reduced in the first dataset; this is not observed. Again, a possibility is that the yields calculated from the room temperature solutions may not be appropriate for cryocrystallography.

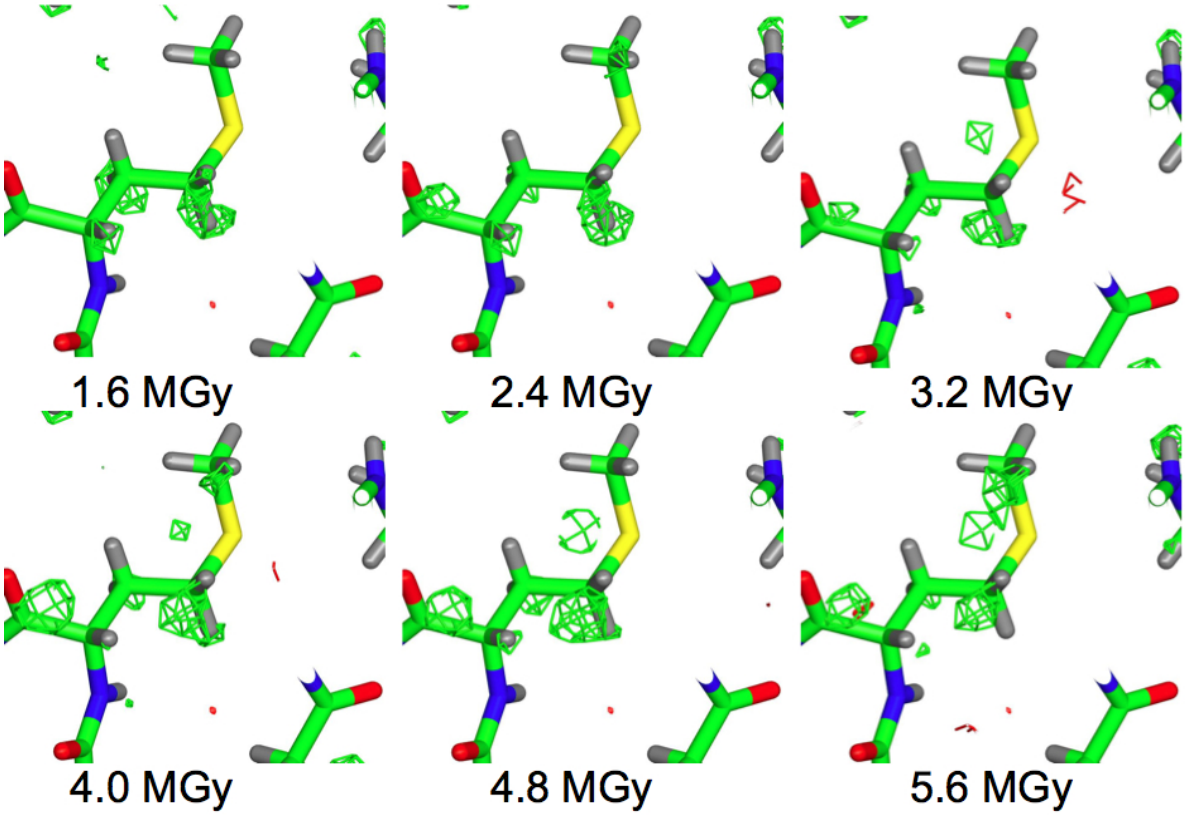

Figure 3.18: Fo-Fc maps of Met222 in XI contoured at +/- 3 sigma at dose points ranging from 1.6 MGy to 5.6 MGy illustrating an increase in positive density accumulating around the residue suggesting radicalization of the residue.

3.7.2.2 Glutamate

For Glu residues, the formation of a carbon-centered radical on the carboxyl group of the residue (Scheme 2, 2.r1), or evidence of decarboxylation (2.o6) is expected. If decarboxylation were occurring, then negative density surrounding the oxygen atoms of the carboxyl group would be present. In Figure 3.19, no evidence of the carbon-centered radical is present. However, there is an increase in positive electron density with increase absorbed dose located on the hydrogen atoms of the residue. This may suggest the addition of one-electron to these sites. The radical yield estimations for glutamate predict that 12.21% of the glutamate residues will be two one-electron reduced in the first dataset (0.35 MGy) and 100% by the fifth dataset (4.10 MGy). This is not what we observe. The difference density does not change with increased absorbed dose.

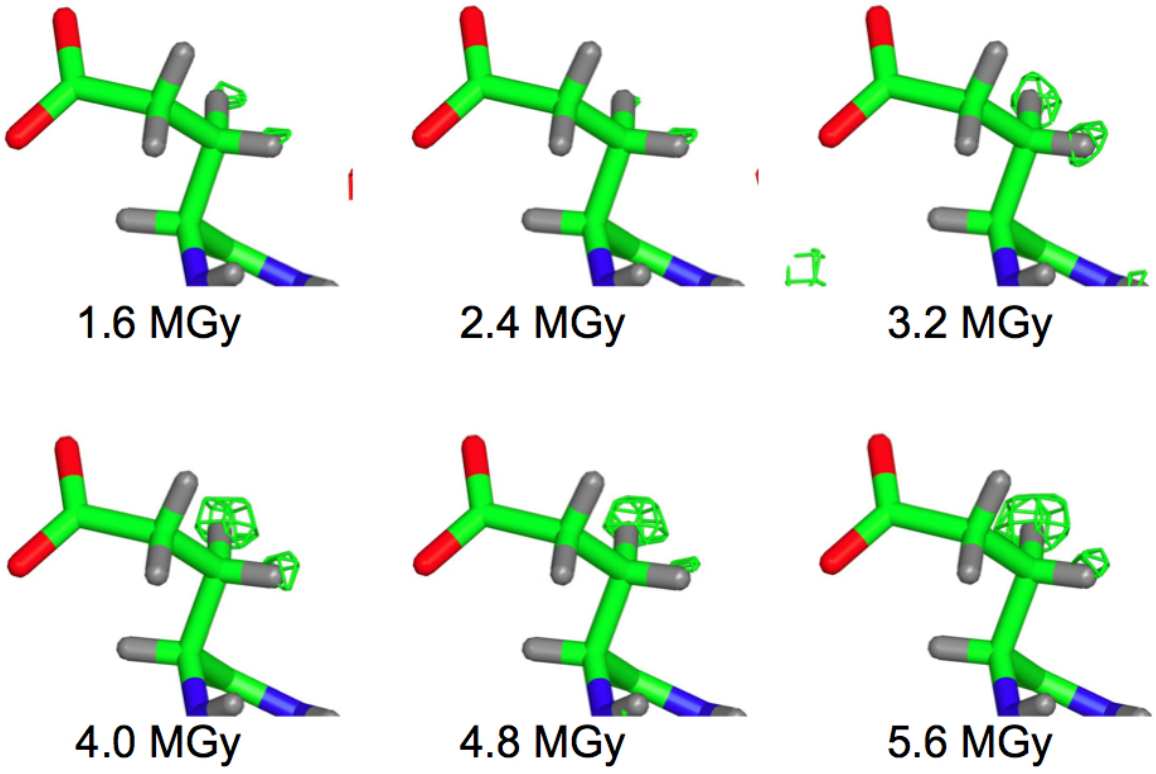

Figure 3.19: Fo-Fc maps of Glu372 in XI contoured at +/- 3 sigma at dose points ranging from 1.6 MGy to 5.6 MGy illustrating an increase in positive density accumulating on the hydrogen atoms. We would expect to see an increase in negative density surrounding the carboxyl group. This may occur with a higher absorbed dose.

3.7.2.3 Aspartate

The Asp residue shown in Figure 3.20 partially illustrates the effects predicted by the model. There is evidence of decarboxylation (2.o6) in the negative difference density shown on the carboxyl group. However, there is no evidence for the formation of the carbon-centered radical (Scheme 2, 2r.1). An increase in positive density surrounding the hydrogen atoms is observed after an absorbed dose of 4.0 MGy. This is similar to what was seen for Glu. There is also some evidence of decarboxylation in the 3.2 and 4.0 MGy data. It is not clear why the negative density for the carboxyl oxygen is not present in the 4.8 and 5.6 MGy data. The estimations of radical yield suggest 1.7% of the Asp residues will be two one-electron reduced by the collection of the first dataset (0.35 MGy) and 25.56% by the last dataset (5.84 MGy).

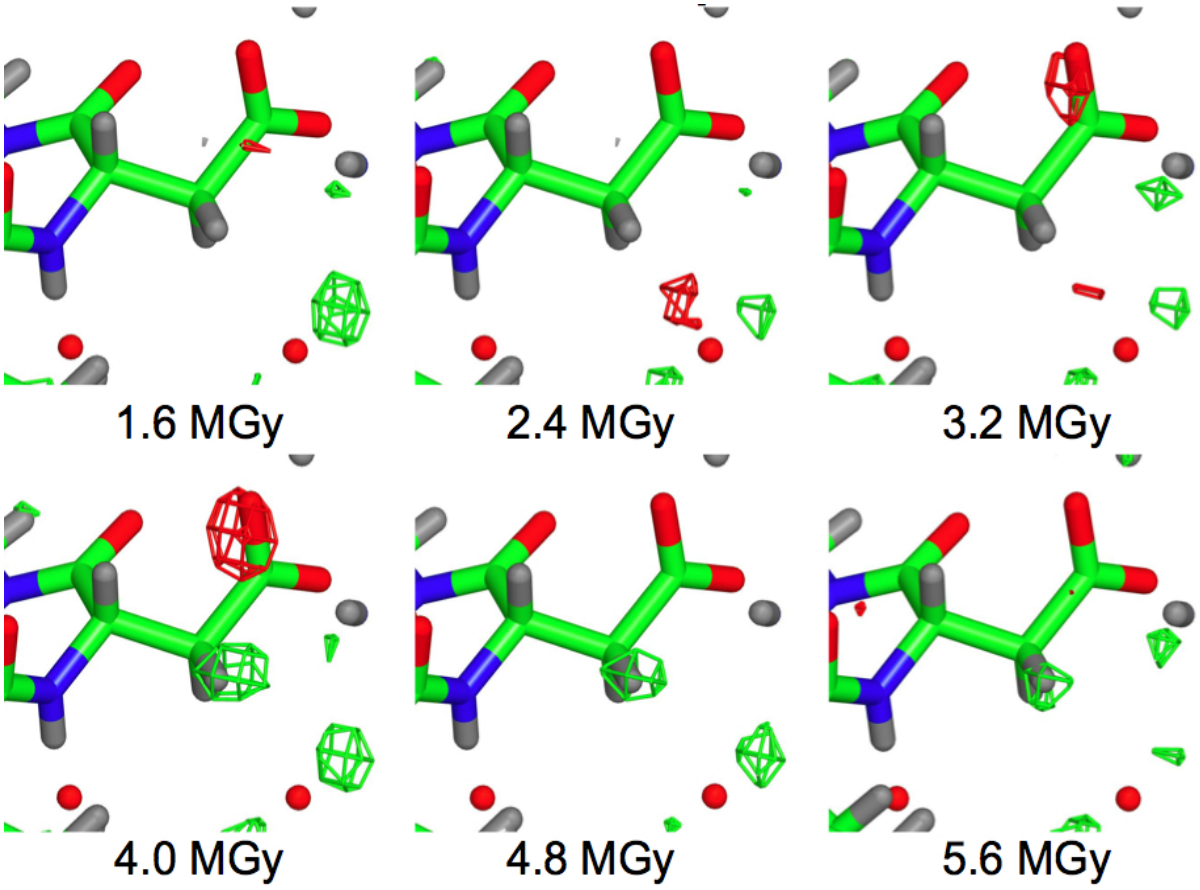

Figure 3.20: Fo-Fc maps of Asp55 in XI contoured at +/- 3 sigma at dose points ranging from 1.6 MGy to 5.6 MGy illustrating an increase in negative density accumulating around one of the oxygen atoms in the carboxyl groups.

3.7.2.4 Tyrosine

The one-electron oxidation of tyrosine coupled with proton transfer is observed in Figure 3.21. Tyrosine can either be reduced or oxidized (Scheme 3). Similar to Tyr in lysozyme, Tyr in XI experiences an increase in positive electron density on the hydrogen atoms bound to the ring carbon atoms, suggesting saturation of these carbons as suggested by the model. The radical yield estimation suggests 3.10% of Tyr will be two one-electron reduced or oxidized in the first dataset (0.35 MGy) and 46.69% will be affected by the last dataset (5.84 MGy). We observe positive electron density peak adjacent to the ring suggesting saturation of that carbon atom, as predicted by the model.

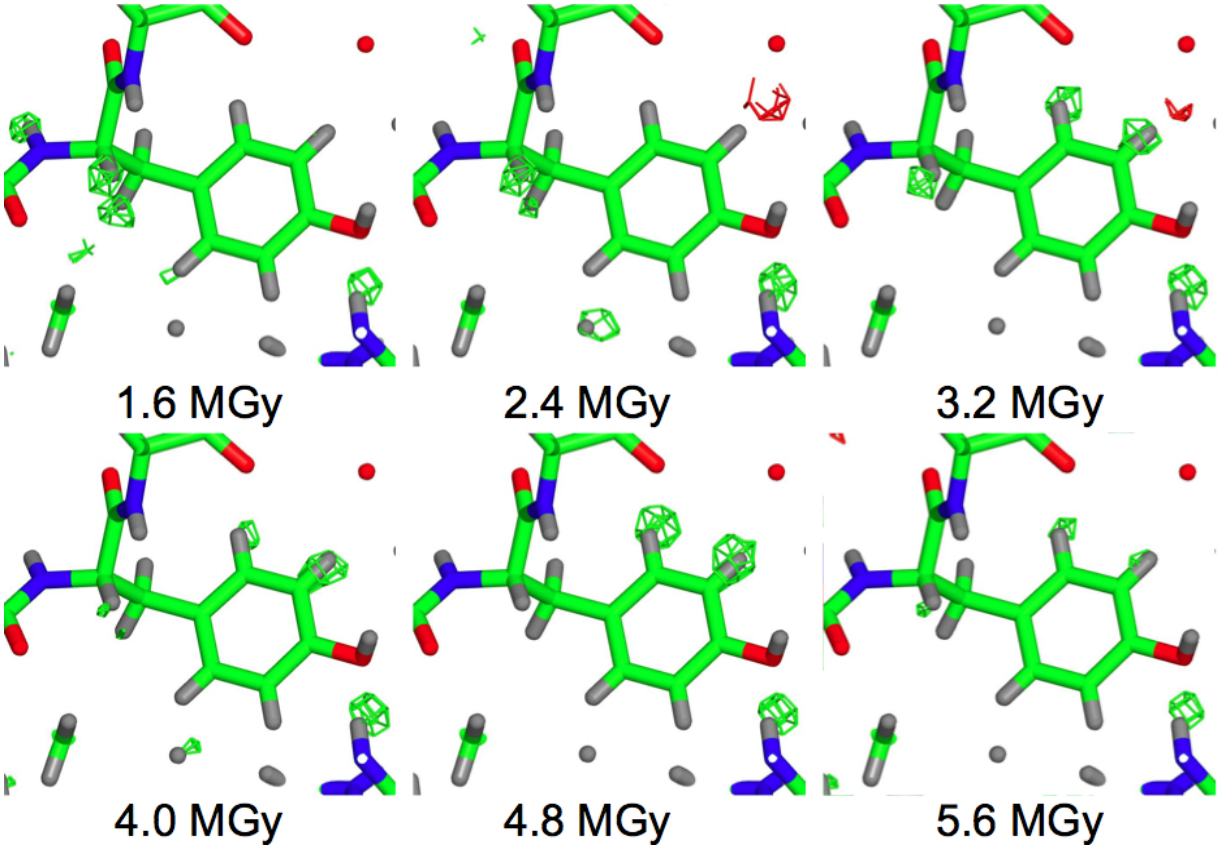

Figure 3.21: Fo-Fc maps of Tyr in XI contoured at +/- 3 sigma at dose points ranging from 1.6 MGy to 5.6 MGy illustrating an increase in positive density accumulating around the hydroden atoms on the ring carbons suggesting saturation of these carbons as suggested by the model.

3.8 Model Predictions

The model appears to be valid for some residues but does not explain all the observations either due to the lack of appropriate G values or a general failure of the model. The model also allows a number of predictions to be made about influences on the damage seen.

3.8.1 Temperature

Firstly at 100K, the reduction in radiation damage seen is due to the immobilisation of OH• and the reduced range of electrons after addition. There is no effect on tunnelling (short range hole/electron transfer) and little effect on spur reactions (localized ion-pair generation controlled by kinetics and not thermodynamics). Low temperatures can affect proton transfer rates and thereby k_b versus k_f.

3.8.2. Dose rate

The multi-track model suggests that dose rate will be a parameter in radiation protection. It comes into play when the time between coincident tracks is on same time scale as the forward and backward reactions. These are time-dependent rates, not to be confused with the dose-dependent rates, k_b and k_f. The backward rate, k_b, will depend on hole/electron transfer rates: 10^{12} to 10^{10} s^{-1} while the forward rate will depend on proton transfer rates: 10^{12} s^{-1}. Obviously, temperature comes into play here with hole transfer rates being greatly reduced, if not eliminated, at 100K.

3.8.3. X-ray energy

At higher linear energy transfer (LET) (absorption) there is more clustering of radical formation and a higher probability of two electron events. Radical yields go down, because of recombination, and the product yields via two one-electron reduction should decrease. The molecular yield via o5 and o6, Figure 3.1, should increase.

3.9 Discussion

3.9.1 Performance of the model

Based on the data presented in Chapter 2, the model predicts up to 200 kGy, damage to the protein in the crystals consists of one-electron reductions and one-electron oxidations. With the exceptions of Glu and Asp, these are small (negligible) structural perturbations. Above 200 kGy, damage due to multiple tracks grows in linearly with dose (at low doses the dependence is quadratic).

Changes in the observed electron density for lysozyme and XI as a function of absorbed dose were compared to the estimates of radical yield. While lysozyme data was not collected to a high enough dose to show all of the characteristics of damage predicted by the model, multi-track damage was observed for the disulfide bonds (the intended study, Chapter 2). For XI, the sum of the total absorbed dose was 5.56 times the total absorbed dose for lysozyme. Damage observed was consistent with the multi-track

model proposed. Radical accumulation around the sulfur atom of Met was observed and the Asp and Glu residues showed early signs of decarboxylation via an increase in negative electron density surrounding the carboxyl group. Similarly the saturation of the ring carbons was observed for Tyr, indicated by an increase in positive density surrounding these atoms.

However, while the qualitative predictions from the model were consistent with the experimental results, the estimations of the radical yield for Asp, Glu, Tyr, Met and Cys are higher than would be expected based on analysis of the electron density. The yields of individual amino acids at room temperature determined in solution at the natural pH of the free amino acid (Hatano, 1962) have been used to estimate the radical yields. Yields at cryotemperatures have not been used, either because they are not available or because, where they are, they were not measured under conditions similar to those used for crystallization and cryogenic studies. Radiation chemistry predicts that the radical processes will be chemistry dependent. The pH, residue environment and temperature are all experimental variables that will affect the radical yield. The pH of the crystal may also play a role in the susceptibility of radiation-induced damage. For example, large differences in the effect of pH on carbonyl yields from pepsin and gelatin solutions have been observed with gelatin ranging from G(>C=O) of 0.87-1.04 for pH 1.3-9.0, and pepsin ranging from 1.34-2.21 over the same pH range (Garrison & Weeks, 1962). Interestingly, with increasing pH the reactivity of the aqueous electron with the amino acids is always decreased (Braams, 1966). Based on this result, both crystals received the same absorbed dose; lysozyme would be expected to be less susceptible

to damage as it was crystallized at pH 4.6, than XI which was crystallized at pH 7.7. At cryotemperatures aqueous electrons are the most damaging radical species. Improvements in the model are needed.

3.9.2 Improving the model

The estimation of radical yields in the protein crystal is based on a room temperature, solution radiation damage study. The radical chemistry differs at these cryotemperatures. Hydroxyl radicals are immobile at 100 K, altering the solvent chemistry that occurs. In order to improve the accuracy of these estimations, cryogenic data for amino acid radical yields is needed.

While lysozyme and XI were used to show the damage predicted by the model, the model is not specific for these two proteins. The probability that a residue will be oxidized, or reduced, through an interaction with free radicals is a residue specific physical property. This probability will be the same for all proteins, neglecting the influence of the immediate residue environment. The current model predicts damage equally to all residues but that is clearly not the case experimentally. Active sites appear to be more sensitive to damage than regions more distant from them. The current model can be extended to take into account the influence of the protein structure. Within a macromolecule, the amino acids are in close proximity to each other and have a tertiary structure. Surrounding residues may influence the probability of specific residues to radicalization. Support for this comes from Braams *et al.* (Braams & Ebert, 1967) who

compared the rate constants of folded and unfolded proteins. The rate constant for the unfolded protein, gelatin, was about equal to the sum of the rate constants of the individual side chains. However, the rate constants for the folded proteins, ribonuclease and lysozyme, were lower than the simple sum of the rate constants of the sum of the rate constants for the side chains. Although quantitative detail was not given in this study, the authors suggested that the folded protein provided some protection for the reactive disulfide bonds, by shielding them with unreactive amino acids. This prevents the hydrated electron from reacting with these sites. For ribonuclease, an increase in temperature, inducing unfolding of the protein, gave a higher rate constant, due to the exposed disulfide bridges. To some extent a molecular dynamics approach is possible, but it will need more experimental evidence for model validation.

The model illustrates both the forward processes and the recombination events. The estimations of radical yields and probability do not take the backward processes into account. Recombination competes with radical formation (two reductions, or two oxidations), bringing the hole and electron back together. These recombination reactions are the dominant reaction. The rate of recombination (k_b) occurs at a rate that is an order of magnitude faster than the radical formation (k_f) as calculated for elastase in Chapter 2. The rate at which radical formation and radical recombination reach equilibrium is known as the saturation level. We determined the saturation dose was 0.2 MGy for the disulfide bond in lysozyme crystals, in Chapter 2. In order to improve the model, all radiation chemistry effects need to be taken into account at cryotemperatures.

3.9.3 Context in terms of the Garman limit

For XI, at an absorbed dose of approximately 5 MGy, 100 % of the Tyr residues and 25 % of the Asp and Glu residues are predicted to have been oxidized by two one-electron oxidations. This is significant, considering the 30 MGy experimental dose limit (Owen *et al.*, 2006a) used for developing a data collection strategy. The 30 MGy experimental dose limit was developed through 1) accurately measuring the absorbed dose and 2) a structural study of perturbations from radiation chemistry. The model presented here suggests a dose at a fraction of the 30 MGy limit. This also suggests that the G values used may overestimate the damage by including the OH radical processes at room temperature which is not present at 100 K.

3.9.4 Summary

The data presented here provide the first steps towards the development of a generalized comprehensive and predictive model for X-ray induced damage to macromolecules. It is not complete. The radical yields for amino acids at cryotemperatures need to be determined; the influence of pH on the radical yield and the influence of the protein structure on radical yield also need to be investigated. However, with these data, one could determine the expected radiation induced radical effects and the structural response, based on the absorbed dose received by the crystal, for any protein.

4. Xylose Isomerase: A case study for X-ray induced structural perturbations in metalloproteins

4.1 *Introduction to Xylose Isomerase mechanism*

Xylose isomerase (XI) is used industrially to catalyze the reversible isomerization of D-xylose and D-glucose to D-xylulose and D-fructose in the manufacture of high fructose corn syrup. This enzyme is one of the three highest tonnage enzymes used industrially. XI is stable, does not require any cofactor molecules, can withstand high temperatures (optimum temperature range: 60-80°C) and has a shelf life of two years. In addition to its use in the manufacture of high fructose corn syrup, it is used in the biofuels industry to ferment xylose to ethanol in yeast strains (ethanolic fermentation of lignocellulosic biomass). Understanding its mechanism and how, if possible, to improve that mechanism is of industrial interest with the potential for significant economic impact.

Carrell *et al.* (1984) reported the first structure of XI from *Streptomyces rubiginosus*, the sample used in this study. Its mechanism involves four sequential steps:

1. sugar binding,
2. ring opening,
3. extension of the linear substrate to an open chain conformation,
4. isomerization including a hydride shift.

The sugar binding step is well defined, but questions about the exact mechanism of the subsequent three steps remain unanswered. Firstly, there is uncertainty surrounding the role lysine plays in deprotonating the substrate oxygen to initiate the ring opening step. Secondly, the identity of the linear intermediate in the extension step is ambiguous. Thirdly, the role and identity of the catalytic water species in the active site during isomerization, is still unclear. Finally, related to all of these, is the mobility of the catalytic metal ion. In this chapter the XI mechanism is described, with particular focus on these aspects. XI is studied as a function of radiation dose; structural changes caused by radiation chemistry effects are noted. These changes are discussed in the context of the uncertainties in the biological mechanism to determine if radiation chemistry could explain these uncertainties to clarify the exact enzymatic mechanism.

4.2 XI mechanism

XI is a tetrameric enzyme with a bridged bimetallic system. This system acts as an electrophilic center to promote hydride transfer during catalysis. Although XI does not require an organic cofactor for activity, it does require a divalent cation such as Mg^{2+}, Co^{2+} or Mn^{2+} (Carrell *et al.*, 1984). Two mechanisms were proposed to explain the stereospecific hydrogen transfer, one proceeding through an ene-diol intermediate (Rose *et al.*, 1969, Rose, 1975) known for other sugar isomerases, (Rose, 1981), and the other involving a shift of a hydride ion, termed the hydride shift mechanism (Collyer *et al.*, 1990, Rose, 1981). The four steps making up the mechanism are described below in detail.

4.2.1 Sugar binding

Water molecules serve as a template for substrate binding. In the sugar binding step (Figure 4.1), O3 and O4 of the cyclic form of α-D-xylose, Figure 4.2(a), interact with M1, the structural metal site with Lys182 stabilizing the substrate for formation of a hydrogen bond in the next step. The role of M1 in the binding the cyclic form of xylose was determined by Carrell *et al.* (1989), who solved the structure complexed with a mechanism-based inhibitor, 3-deoxy-C3-fluoro-methylene-D-glucose, DMFG, Figure 4.2(b). DMFG is a five-membered ring glucose (as seen in Figure 4.2c) analog that mimics binding, but is not acted on by the enzyme (XI also performs the reversible isomerization of glucose to fructose). The structural study showed that the reactive end of the substrate, O1 and O2, bind through structured water molecules in close proximity to Thr89. Collyer *et al.* (1990) subsequently published a complex with 5-thio-α-D-glucose (TGP), an inhibitor that contains sulfur (Figure 4.2d). The sulfur was well defined in the structure showing that M1 binds to O3 and O4. Other studies confirmed these results; cyclic xylose binds to the active site through side chain interactions with O1 and O2 and the interaction of M1 with O3 and O4 (Kovalevsky *et al.*, 2010, Whitlow *et al.*, 1991, Collyer *et al.*, 1990, Fenn *et al.*, 2004).

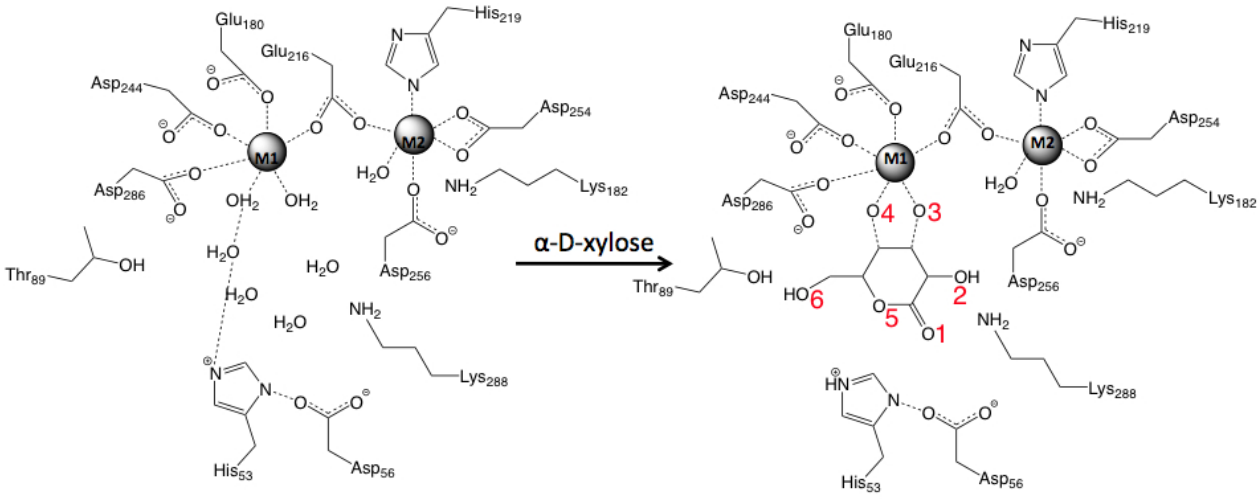

Figure 4.1: XI (A) without and (B) with the substrate, α-D-xylose, bound. In A, the water molecules serve as a template for binding the substrate. In B, the substrate binds with O3 and O4 coordinated to M1, the structural metal site. O5 interacts with His53. No structural rearrangements of the active site residues or conformational changes occur upon substrate binding.

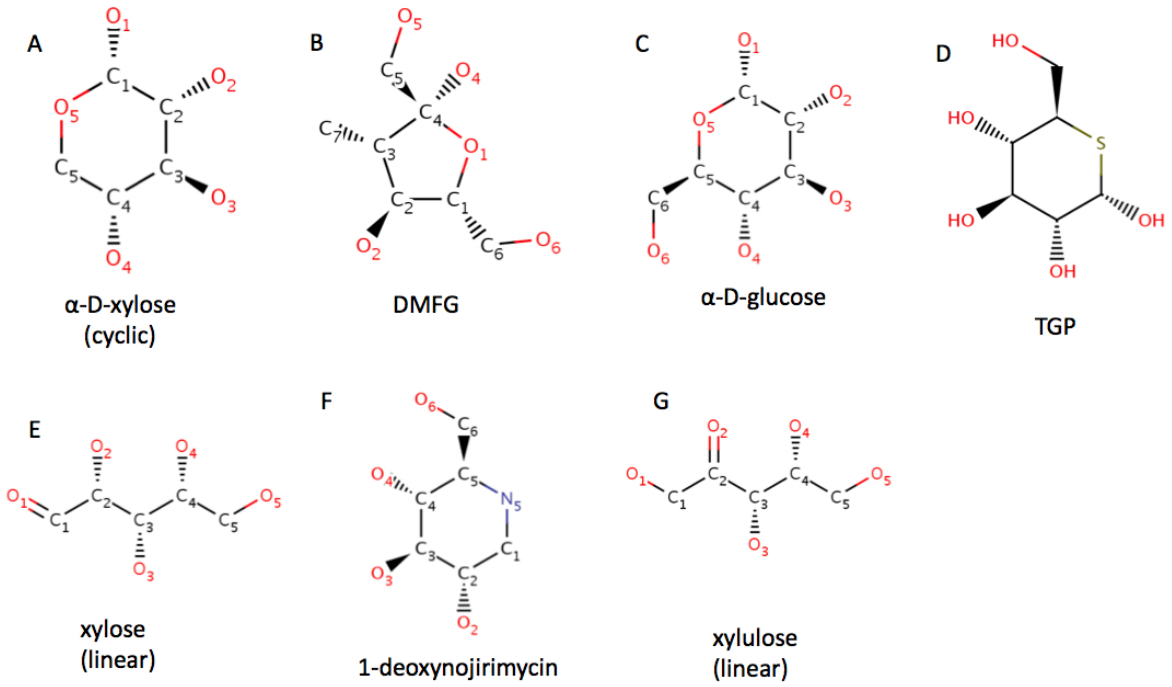

Figure 4.2: Substrates and inhibitors used in mechanistic studies of XI. (A) cyclic α-D-xylose, (B) 3-deoxy-C3-fluoro-methylene-D-glucose,linear xylose, (C) α-D-glucose, (D) 5-thio-α-D-glucose, (E) linear xylose, (F) 1-deoxynojirimycin and (G) linear xylulose.

4.2.2 Ring Opening

The ring opens via His53 and Asp56 acting as an acid-base pair to linearize the substrate through a hydrogen bond between His53 and O5 of the cyclic substrate, breaking the C1-O5 endocyclic bond, Figure 4.3. The reaction is stereospecific, the C1 proton of xylose is abstracted from the pro-R position. Structural evidence for the cis-ene-diol mechanism based on complexes of XI and the cyclic inhibitor and linear xylose suggested hydrogen abstraction through C1 (Carrell *et al.*, 1994). The hydrogen atom is abstracted from the substrate and transferred to His53, forming a hydrogen bond between His53 and the substrate. His53 acts as the base catalyst in the acid-base pair, while an active site water molecule near O1 and O2 acts as the acid catalyst to form the cis-ene-diol intermediate.

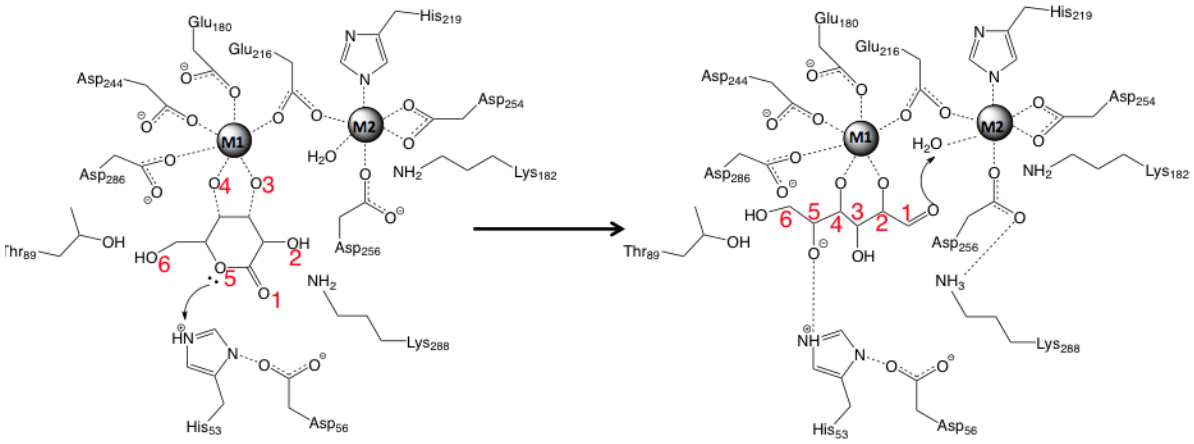

Figure 4.3: Following the binding of xylose, His53 and Asp56 act as an acid-base pair to linearize the substrate. (A) Negatively charged Asp56 interacts with the solvent and positively charged His53 interacts with the substrate, by forming a hydrogen bond with O5. (B) After ring opening occurs, the linear substrate is bonded at O5 to His53, O2 and O4 are coordinated to M1 and the active end of the substrate, C1, is positioned toward M2.

Unlike other sugar isomerases XI requires a divalent metal ion for activity (Whitlow et al., 1991). Early studies proposed a hydride shift mechanism where Asp56 acts as the catalytic acid, instead of an active site water molecule, in conjunction with His53 as an acid-base pair to bind the cyclic substrate and catalyze ring opening (Collyer et al., 1990). The C1 and C2 of the linear substrate have no base residue nearby, a requirement for the ene-diol mechanism. The role of the His53-Asp56 pair in the ring-opening step of the reaction was revised by a high-resolution X-ray diffraction study (Fenn et al., 2004). Asp56 abstracts a proton from a water molecule in close proximity and transfers it to His53 on ND1, since His53 is already protonated at NE2. His53, which is initially neutral, becomes charged and functions with the hydroxyl anion to donate a proton to O5 of the substrate and to pull a proton from the O1 hydroxyl. Kovalevsky et al. (2010) support this; using neutron diffraction they located the hydrogen atoms (or the isotope deuterium) and demonstrated that before substrate binding, the His53-Asp56 pair donates a deuterium in a hydrogen bond to a water molecule in the active site. This water molecule serves as a template for the substrate and is displaced upon cyclic substrate binding. The substrate O5 occupies the position of the active-site water and accepts a deuterium in a hydrogen bond with NE2 of the His53-Asp56 pair.

The combination of X-ray and neutron structural information led to modifications of the hydride shift mechanism, suggesting that His53 transiently donates its proton to O5 to initiate ring opening and accepts it back after the C1-O5 endocylic bond is broken (Kovalevsky *et al.*, 2010). Two lysine residues, Lys182 and Lys288 were suggested to

stabilize the substrate during the ring opening step. As the ring opens, the reactive end of the substrate, O1, is stabilized by Lys182 through a hydrogen bond and is protonated before ring opening and becomes deprotonated during the ring opening step. Similarly, Lys288 binds through a water molecule to O1 during the sugar binding step and becomes protonated during ring opening when the bond with the water molecule is broken, allowing the substrate to extend into the linear form (Kovalevsky *et al.*, 2010). Uncertainty remains surrounding the role of Lys182 and Lys288 in deprotonating the substrate oxygen to initiate the ring opening step.

4.2.3. Extension of the linear substrate

During the extension of the linear substrate step xylose moves further into the active site, losing coordination with M1 and binding to M2. M2 shifts to a new position M2b, closer to M1, to form the bond with the substrate. The shift in position of M2 causes a change in its coordination, breaking the bond with His219 and forming a bond with Asp256 in a bidentate manner. During the extension Lys182 and His219 stabilize both the active site environment and the substrate, and prepare the substrate for the next step of the reaction, isomerization (Fenn *et al.*, 2004).

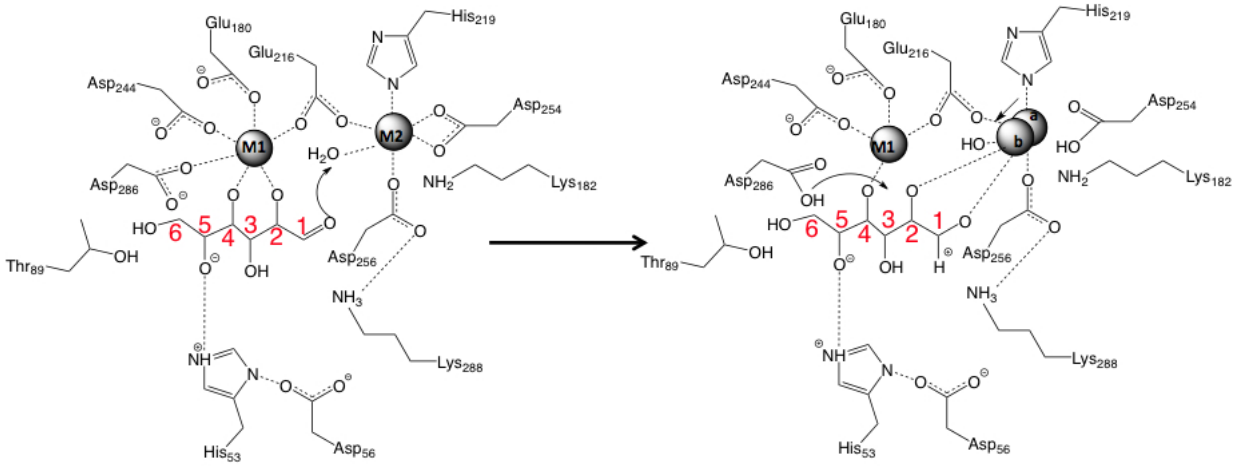

A B

Figure 4.4: (A) The linear substrate bound to M1, through interactions with O2 and O4. (B) M2 shifts to a new position to interact with the active end of the linear substrate, O1 and O2, through a hydrogen bonding interaction. Lys182 stabilizes the active end of the substrate. Asp254 is no longer coordinated to M2.

The dynamic extension of the substrate is difficult to visualize using X-ray crystallography, and the identity of the linear intermediate is still unclear due to uncertainty in the protonation state of the intermediate and surrounding water species. Rose *et al.* (1969) suggested XI had a *cis*-ene-diol transition state with protonation of C1 or C2 from the same side of the *cis*-ene-diol intermediate the same for as for the other Mn-dependent aldose isomerases.

The cis-ene-diol transition state was the accepted intermediate until Carrell *et al.* (1994) determined the structures of XI with bound substrates and inhibitors. The improved resolution (1.6-1.9 Å) of these structures aided the identification of possible catalytic groups in the proposed mechanisms. Originally, Carrell *et al.* (1989) suggested His53 acted as a catalytic base that abstracted a proton from the substrate, according to the cis-ene-diol mechanism. Whitlow *et al.* (1991) suggested that this could not be possible since His53 is not in an environment where a transferred proton could be protected from solvent exchange. Instead His53 acts as an acid base catalyst extracting a proton from Asp56. His53 can then shuttle a proton between the substrate O1 hydroxyl group and O5 of xylose, as explained in the ring opening step. More recent data, shown in Section 4.2.5, suggests His53-Asp56 serves to stabilize the oxyanion at O5. The metal-mediated hydride shift, where a proton of xylose moves to the *pro*-R position on C1 to give D-xylulose by a 1,2-hydride shift, was proposed because there was no base nearby for proton abstraction and there is no indication of solvent exchange.

In the hydride shift mechanism, the active-site metal atoms stabilize the substrate. M1 is initially bound to O2 and O4 until the substrate extends into the active site and M2 binds to O2. Lys182 aids in this stabilization (Whitlow *et al.*, 1991, Collyer *et al.*, 1990, Whitaker *et al.*, 1995), positioning the substrate in the proper orientation for isomerization. Similarly, His219 maintains the structure and coordination around the M2 site when the extended form of the substrate is present (Whitaker *et al.*, 1995). Evidence for these stabilizing events comes from the mutation of Lys182 to methionine, which changes the metal coordination and inactivates the enzyme (Whitaker *et al.*, 1995). Mutating His219 to serine inactivates the protein; this is due to the ability of serine's smaller side chain to stabilize M2.

When the substrate binds to Lys182 and is extended, xylose moves further into the active site, away from M1 and towards M2. M2 changes its coordination state; it is no longer bound to His219, and forms a new bond with Asp256 in a bidentate manner. The metal position, M2, shifts to position M2b with extension of the substrate and the change in coordination (Fenn *et al.*, 2004). The substrate-bound, high-resolution structure of XI, reported by Fenn *et al*. (2004), shows three positions for M2. The third position of M2 has been suggested to be the reason for the low turnover rate for XI. The identity of the linear intermediate between this step and isomerization remains unclear. There is no substrate present in the structures reported below. Therefore, any metal movement observed as a function of dose is due to X-ray induced structural perturbation in the active site and not enzymatic turnover. X-ray induced metal movement observed here indicates that the three positions of M2 may be an artifact of

the data collection technique; the proposed enzymatic mechanism could be based upon an experimentally altered structure.

4.2.4 Isomerization

Xylose isomerization proceeds via a 1,2 hydride shift promoted by electrophilic catalysis, as explained in the previous section. This is initiated by the metal ions, M1 and M2. Both of the metal ions act to lower the pKa of the sugar O2, aiding in its deprotonation. The deprotonated hydroxyl causes the metal ions to move closer together to establish the correct geometry for the hydride transfer. Then the C-O1 and C-O2 bonds of the substrate are polarized by the close approach of the M2 cation, assisted by the coordination of O2 to M1 and O1 to Lys182. Hydride transfer from C2 to C1 occurs, Figure 4.5. Isomerization is complete during the ring closure step, the reverse of the ring opening step.

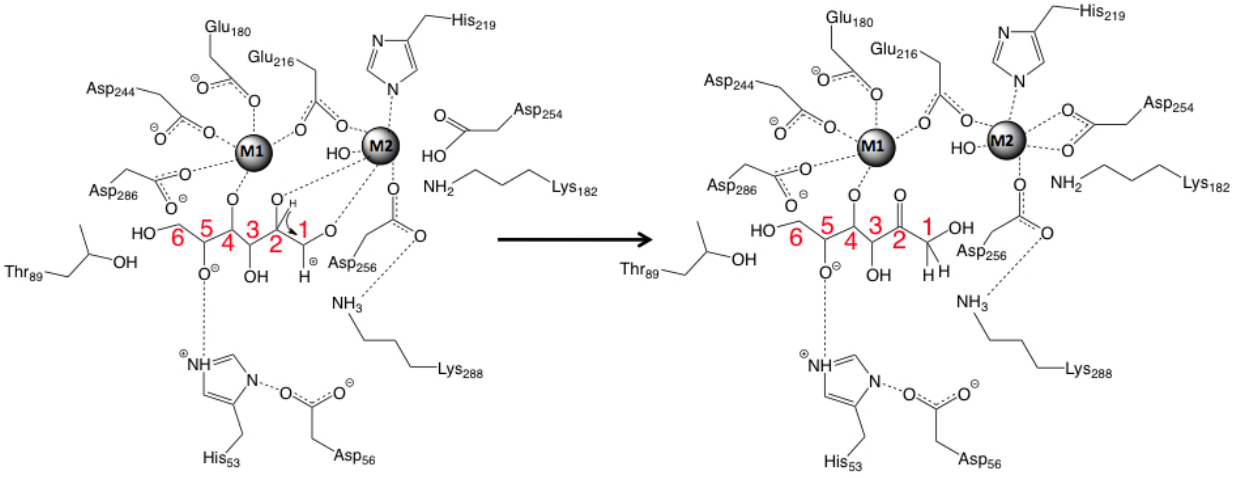

Figure 4.5: (A) The carbonyl end of the substrate extends further into the active site. O2 is negatively charged and the hydrogen on C2 is transferred to C1. (B) The linear product is in the active site before the isomerization reaction is complete. Isomerization is complete with the ring closure step, the reverse of the ring opening step. (Ring closure step is not shown).

4.2.5 Hydride shift versus the cis-ene-diol mechanism

As indicated above the cis-ene-diol based mechanism was initially proposed as the enzymatic mechanism for XI. Proton transfer from C2 to C1 was investigated with three manganese-dependent isomerases: L-arabinose isomerase, L-fucose isomerase and D-XI (Rose *et al.*, 1969). Tritiated substrates were incorporated for L-arabinose and L-fucose, but not for D-xylose (Rose *et al.*, 1969), separating XI from the other isomerases where solvent exchange does occur. Allen *et al.* (1994) supported this through a similar observation. This data suggested that proton transfer to a solvent exchangeable base could not be involved in XI isomerization, disproving the cis-ene-diol mechanism.

In contrast, instead of proton transfer to a solvent exchangeable base, the hydride shift mechanism involves intramolecular transfer of hydrogen from C2 to C1 of the substrate. The absence of solvent exchange is consistent with hydride transfer. The divalent metal ion stabilizes the formation of a carbocation at the carbonyl carbon before the transfer of hydrogen occurs. The metal ion was also suggested to play a conformational role by stabilizing the orientation at the reactive end of the substrate, again favoring the hydride shift mechanism.

Using this mechanism, XI isomerization proceeds via a hydride shift promoted by electrophilic catalysis. This is initiated by the metal ions, M1 and M2, both required for activity (Allen *et al.*, 1994), which function to lower the pKa of the sugar O2, aiding in its

deprotonation. The deprotonated hydroxyl reduces the separation between the metal ions establishing the correct geometry for the hydride transfer (Lavie *et al.*, 1994). The C-O1 and C-O2 bonds of the substrate are polarized by the close approach of the M2 cation assisted by the coordination of O2 to M1 and O1 to Lys182 (Collyer *et al.*, 1990).

Deprotonation of the substrate O2 is initiated by either a catalytic hydroxide ion (Fenn *et al.*, 2004) or a catalytic water species (Kovalevsky *et al.*, 2010) bound to M2. Fenn *et al*. (2004) proposed that the hydroxide ion is necessary for the initiation of the hydride shift step, extracting a proton from the bound linear sugar as M2 shifts to an alternate position, closer to the reactive end of the substrate to coordinate with O1 and O2. Hydrogen transfer occurs from O2 to O1 by a native metal-activated hydroxide ion. Kovalevsky *et al.* (2010) disagreed with this, proposing instead that M2 bound a catalytic water which protonates O1 of the linear form of the sugar to produce a carbocation with the positive charge located on C1. The O2 hydroxyl, which is coordinated to both M1 and M2, would then become acidic and could be deprotonated by the nearest carboxylate, Asp286, moving the proton into the bulk solvent through the water molecule network. The hydride transfer from C2 to C1 would occur after, or at the same time, as O2 deprotonation.

The identity of the catalytic water species remains unclear; the precise mechanism of the hydride shift from C2 to C1 is undetermined. It is unclear whether the transferred hydrogen is provided as a hydride ion (H^-) in a simple hydride shift or as a hydrogen ion

(H^+) through hyperconjugation. In the latter case, the electrons in the C-C sigma bond interact with the adjacent orbital, to give an extended molecular orbital to increase the stability of the carbocation. This results in the C1-C2 bond achieving double bond character and the positive charge on C1 shifting to the H on C2 and weakening the C2-H bond (Kovalevsky *et al.*, 2010).

4.2.6 Metal motion

Of interest for the studies presented in this thesis is the metal motion seen in the enzyme mechanism. Lavie *et al.* (1994) observed elliptically shaped density for M2, differing from the spherical density observed in the substrate-free structure, and attributed this to M2 mobility in active site. This was interpreted as a shift of M2 upon substrate binding from the site occupied in the native structure, to a site closer to M1 and the substrate. M2 occupied two alternate positions, separated by a distance of 1.8 Å. Kovalevsky *et al.* (2010) observed a similar shift in the position of M2 of 1.9 Å. Fenn *et al.* (2004), in a high resolution study of both the inhibitor-bound (0.95 Å) and substrate-bound complex (0.98 Å) modeled three metal positions for M2 (a, b and c) with the inhibitor-bound (Figure 4.6) and one position for M2 in the substrate-bound complex. In the first configuration, M2a is coordinated in a distorted octahedron by Glu216, His219, Asp254, Asp256 and the catalytic hydroxyl ion. The hydroxyl ion is 2.41 Å from the metal, suggesting it is likely to be a water molecule. When the metal moves to position M2b, the hydroxyl ion is 1.89 Å away and is consistent with an OH^- assignment. M2b is coordinated by Asp256, which also adopts a second conformation.

M2c, which is located 1.53 Å and 1.88 Å from M2a and M2b respectively, is no longer coordinated with Asp256, but binds to the xylitol. M2c is the only conformation where the metal ion is bound to the ligand, suggesting that this conformation is the only catalytically competent position. The multiple conformations suggested that the metal site was disordered and provided a possible explanation for the low rate of turnover for the enzyme. M2a, M2b and M2c had occupancies of 0.30, 0.31 and 0.06, respectively. Analysis of the anisotropic ellipsoids indicated that M2c had a high degree of anisotropy, suggesting a high degree of disorder. This may be due to the loss of the coordination of M2 to active-site residue Asp256. The metal shift from M2a to M2c of 1.88 Å is consistent with the shift of 1.8 Å observed by Lavie *et al.* (1994) and 1.9 Å shift seen by Kovalevsky *et al.* (2010).

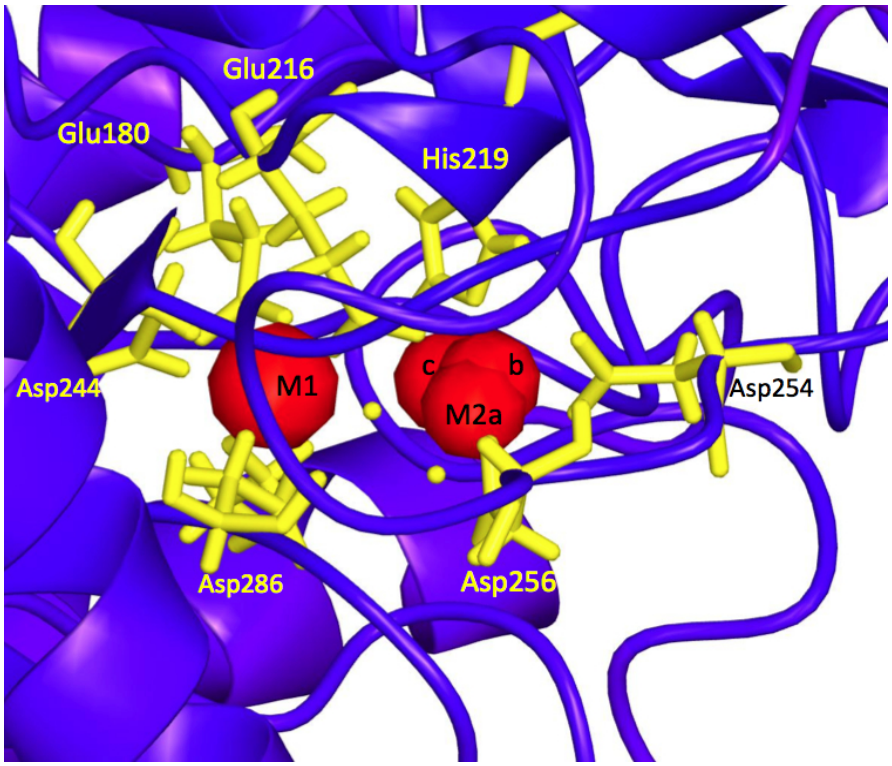

Figure 4.6: Active site of XI showing M1 occupied by magnesium and manganese and three distinct positions of M2. Active site residues coordinating M2 are shown in yellow.

4.3 The influence of radiation chemistry on XI structure

After four decades of research, there are still uncertainties and inconstancies in the precise details describing the chemical mechanism of XI. Given the effects that radiation chemistry drives presented in chapter 1, damage to disulfide residues in chapter 2 and the general model presented in chapter 3 it may well be that these uncertainties are a result of these radiation chemistry effects on the system. To probe this, substrate free XI was structurally studied with increasing absorbed doses of X-ray radiation.

4.3.1 Crystal preparation

XI from *Strepomyces rubiginosus* was obtained from Genencor (Palo Alto, CA). The commercially prepared XI was purified by gel-filtration chromatography using a Superdex 200 HiLoad 16/60 column (GE Healthcare). The purification buffer contained 50 mM sodium phosphate pH 7.7, 100 mM sodium chloride and 0.02% sodium azide. The concentrated protein was first dialyzed against distilled water at room temperature and then dialyzed in 50 mM magnesium sulfate. As described in section 4.2, the two metal binding sites in XI contain magnesium and/or manganese. Dialyzing the protein in magnesium sulfate provides a stable buffer condition and ensures that the metal is not lost from the protein. The enzyme is stable at ambient temperatures, but unstable at low temperatures and once purified was stored at 22 °C as a dilute solution (~3 mg/ml). The protein was concentrated to 100 mg/ml shortly before crystallization experiments were set up.

The protein was transported to the synchrotron (Stanford Synchrotron Radiation Lightsource - SSRL) where crystals were grown using the hanging drop vapor diffusion crystallization method. A total of 5 uL of protein (100 mg/ml) was added to a 5 uL drop of precipitant solution containing 8% (v/v) 2-propanol (as a precipitant), 25% (v/v) ethylene glycol (as a cryoprotectant), 50 mM HEPES pH 7.0 and 50 mM magnesium chloride. The reservoir in the crystallization plate contained 1 mL of the precipitant solution. Crystals (0.3 x 0.3 x 0.3 mm) grew in 1 day at room temperature. Crystals were extracted using Cryo-Loops (Hampton Research, CA) and flash cooled at 100 K directly in the cryostream for data collection.

4.3.2 X-ray data collection and processing

X-ray data were collected on beamline 11-1 of SSRL using an ADSC Quantum 315 CCD detector. Radiation damage occurs at all resolutions. A medium-resolution data set was collected first, using short exposures (to avoid overloading the detector) coupled with large angular ranges. A complete medium-resolution data set can be collected in the same time as a few frames of the high-resolution data. The complete 90 degree low-resolution dataset was collected at a wavelength of 0.954 Å, with a crystal to detector distance of 100 mm and 0.5° oscillation with 2 second exposure time per image. The total absorbed dose for this dataset was 0.35 MGy. A high-resolution 10 degree swathe was collected between each medium-resolution data set at a wavelength of 0.855 Å with a crystal to detector distance of 100 mm and 0.5° oscillation with 30 second exposures. This was used to monitor the decay of high-resolution reflections.

The total dose absorbed for the high-resolution swathes was 0.47 MGy. A dose of 0.82 MGy was absorbed for each of the seven datasets, for a total absorbed dose of 5.6 MGy, Table 4.1. The dose was calculated from the measured flux, using RADDOSE (Murray *et al.*, 2004b, Paithankar & Garman, 2010, Paithankar *et al.*, 2009a). The flux was calculated from an ion chamber reading. The data were integrated using Mosflm (Powell, 1999, Rossmann & van Beek, 1999) and reduced with Scala (Evans, 2006) in the CCP4 suite (Winn *et al.*, 2011). Only the medium-resolution data set was used for subsequent structural studies.

Table 4.1 Data collection dose.

Data set	Dose (MGy)	Accumulated dose (MGy)	Data set	Dose (MGy)	Accumulated dose (MGy)
1*	0.35	0.35	5	0.35	3.63
1(a)**	0.47	0.82	5(a)	0.47	4.10
2	0.35	1.17	6	0.35	4.45
2(a)	0.47	1.64	6(a)	0.47	4.92
3	0.35	1.99	7	0.35	5.27
3(a)	0.47	2.46	7(a)	0.47	5.74
4	0.35	2.81			
4(a)	0.47	3.28			

* Medium-resolution data set

** High-resolution swathe

4.3.3 Modeling of the structures at each radiation dose

ARP w/ARP (Perrakis *et al.*, 2001) was used for molecular replacement with PDB entry 1MUW as the initial search model (a 0.86 Å structure of XI from *streptomyces olivochromogenes* with 95% sequence identity (Fenn *et al.*, 2004)). All metal ions and water molecules were removed from the search model. Each of the seven datasets were processed and refined independently initially with REFMAC5 (Vagin *et al.*, 2004) and later with Phenix (Adams *et al.*, 2010a) for occupancy and anisotropic refinement. Riding hydrogens were incorporated in the refinement to aid the correct conformer positioning of residues. In-between refinement steps, the model was built iteratively using COOT (Emsley & Cowtan, 2004, Emsley *et al.*, 2010) and checked with Molprobity (Otwinowski, 1997, Luft *et al.*, 2003).

Isomorphous difference Fourier maps, Fo_n-Fo_1 (Rould & Carter, 2003), were calculated, using the observed amplitudes from each dataset and the phases from the structure at a dose of 0.8 MGy – the lowest dose dataset. These difference maps provide a sensitive means to identify subtle structural changes while having little sensitivity to the initial phase set used for their calculation (Rould & Carter, 2003).

4.4 Results

4.4.1 Global indicators of radiation damage

Simple observation of the raw diffraction images indicated a progressive decrease in diffracting resolution, Figure 4.7. A reflection highlighted at 1.2 Å rapidly diminishes as dose increases, vanishing to the eye at 5.27 MGy.

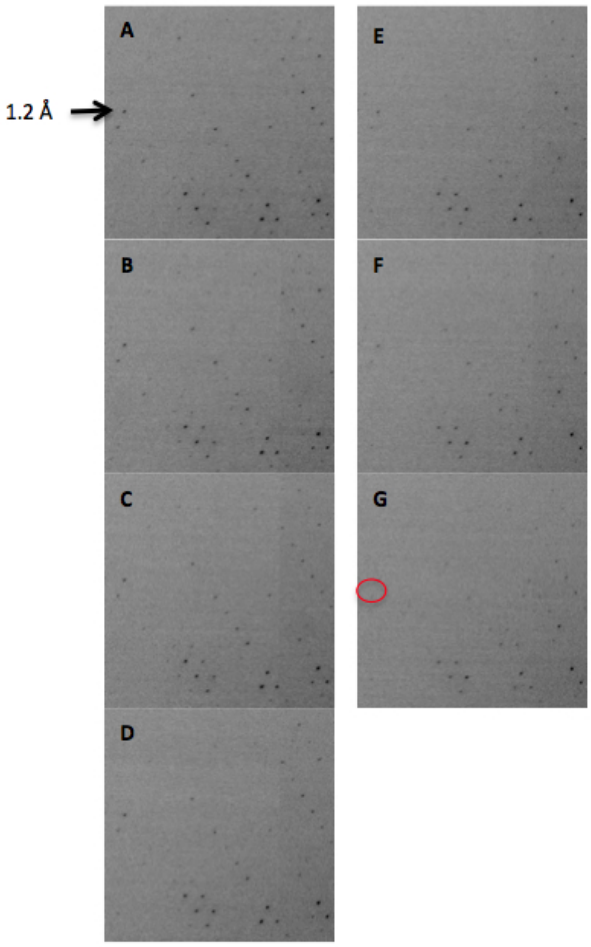

Figure 4.7: Decrease in reflection intensity of the high-resolution region of the diffraction image. The same area of the first image of each dataset is shown for datasets 1(A)-7(G). The arrow points to a reflection in panel A, which decreases in intensity over the course of the data collection. The red circle on the last data set shows where the reflection should be.

Global indicators in the refinement showed systematic changes, Table 4.2. With the exception of the a axis length which increased by 0.1 Å after 1.17 MGy of absorbed dose, the unit cell parameters remained constant. The signal-to-noise ratio, (I/σ(I)), in the highest resolution shell (1.21-1.19 Å) decreases linearly with dose. By the last dataset, I/σ(I) in the highest resolution shell has decreased by 52%. Overall the R_{sym}[2], does not significantly increase, however, a substantial increase is seen in the highest resolution shell. This is also reflected in the completeness with a drop from 86 to 78% in the highest shell. A sigma cutoff of 2.0 was used to determine completeness. The reflections are still recorded, but the intensity of the reflection has diminished to where it can no longer be distinguished from the background, so that reflection is not used in the data. There is a slight increase in the observed mosaicity. The Wilson B factor, or overall B factor, was calculated using the program *TRUNCATE* (French, 1978) after the final merging and scaling of the data. It increased linearly by 20% from 9.05 to 10.94 Å^2 over the total absorbed dose of 5.27 MGy.

$$R_{sym} = \frac{\sum_{hkl}\sum_{i=1}^{n}\left|I_i(hkl) - I_i(\overline{hkl})\right|}{\sum_{hkl}\sum_{i=1}^{n} I_i(hkl)} \quad (1)$$

$$R_{work} = \frac{\sum_{h}\left|F_{obs} - F_{calc}\right|}{\sum_{h} F_{obs}} \quad (2)$$

Table 4.2: Global indicators from integration, scaling and merging statistics for seven consecutive datasets collected on a single crystal of XI.

Dataset	1	2	3	4	5	6	7
Dose (MGy)	0.35	1.17	1.99	2.81	3.62	4.45	5.74
Cell Parameters							
a (Å)	92.27	92.37	92.37	92.37	92.37	92.37	92.37
b (Å)	97.31	97.31	97.31	97.31	97.31	97.31	97.31
c (Å)	102.30	102.30	102.30	102.30	102.30	102.30	102.30
I/σ(I)	17.83 (4.58)	17.85 (4.19)	17.75 (3.92)	17.71 (3.54)	17.58 (3.16)	17.49 (2.76)	17.39 (2.39)
R_{sym} (%)	7.4 (24.4)	7.4 (27.3)	7.6 (29.7)	7.5 (32.3)	7.8 (36.3)	7.8 (41.1)	7.7 (45.9)
Completeness (%)	99 (86)	99 (86)	99 (87)	99 (83)	99 (82)	99 (79)	99 (78)
Mosaicity (°)	0.134	0.133	0.132	0.132	0.132	0.134	0.138
Wilson B factor ($Å^2$)	9.05	9.58	9.78	10.18	10.49	10.94	11.34

4.4.2 Specific damage

Specific damage effects are shown in Table 4.3. The isotropic B factor increased linearly by 16% from 13.19 $Å^2$ in the first dataset to 15.3 $Å^2$ over the total dose of 5.6 MGy. The working R-factor (R_{work}[1]) increased linearly from 11.42% to 12.64% with the exception of dataset 4, which showed a slight decrease from dataset 3. The root-mean-squared deviation (RMSD) in bond length remained constant for all datasets. However, the RMSD bond angle varied over the seven datasets, ranging from 1.264 to 1.303°, with no obvious trends. The number of protein atoms varied due to the number of alternate conformations that were modeled in each dataset. There was no correlation between number of alternate conformations and absorbed dose. The number of water molecules modeled decreased with increased dose, varying from 533 in the first dataset to 460 in the last dataset.

Table 4.3: Specific damage statistics for seven consecutive datasets collected on a single crystal of XI.

Dataset	1	2	3	4	5	6	7
Dose (MGy)	0.35	1.17	1.99	2.81	3.62	4.45	5.74
Average Isotropic B factor ($Å^2$)	13.13	13.44	13.9	14.12	14.48	15.05	15.33
R_{work} (%)	11.42	11.8	11.94	11.89	12.14	12.38	12.64
RMSD bond length (Å)	0.008	0.008	0.008	0.008	0.008	0.008	0.008
RMSD bond angle (°)	1.303	1.271	1.287	1.295	1.297	1.274	1.264
Protein atoms	3215	3219	3207	3178	3187	3212	3213
Water	533	504	477	501	476	478	460
# of Alternate conformations	16	14	13	13	13	16	17

The program $B_{average}$ from the CCP4 suite (Winn *et al.*, 2011) was used to calculate the differences in atomic B factor between datasets. There was an increase in both average and specific atomic B factors for all of the residues. This is illustrated in Figure 4.8 where the residues are divided as a function of their properties, i.e. charged, polar uncharged, hydrophobic and special cases. The B factor increased for all residues with a difference, of about 1 $Å^2$, between the largest increase (lysine) and the smallest increase (tyrosine). From the first (0.35 MGy) to the last (5.74 MGy) dataset there were no significant differences in atomic positions (displacement was less than the coordinate error estimate) or occupancies for amino acid residues having an alternate conformation (16 residues).

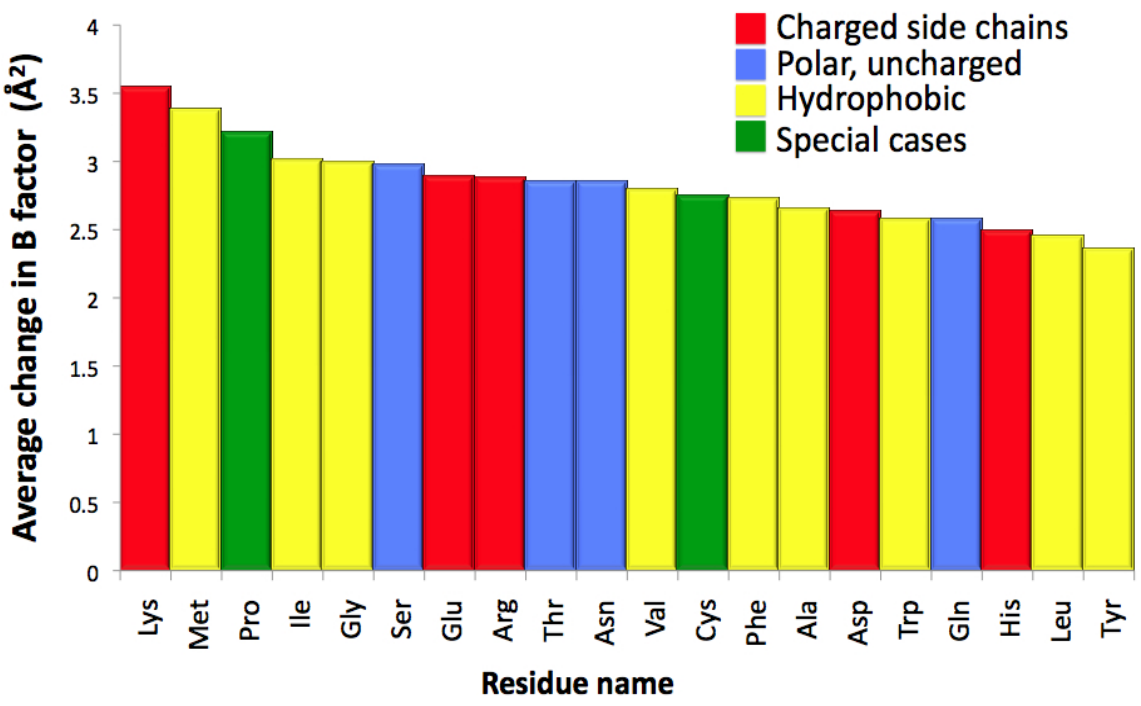

Figure 4.8: Average change in side chain B factor from the first dataset to the seventh dataset, plotted for each residue and colored by residue properties.

The solvent accessibility was calculated for each residue *Areaimol* (CCP4) (Winn *et al.*, 2011). The top 10 solvent accessible residues, consisting of Phe, Arg, Trp, Phe and Asp residues had solvent accessibilities ranging from 146.2 to 197.3 $Å^2$. Ten residues with zero solvent accessibility were chosen to compare to the residues with high solvent accessibility. All 20 residues were analyzed using $B_{average}$ to plot the change in average main chain B, side chain B and overall B factor, Figure 4.9. The change in B factor, an indicator of the loss of electron scattering power and therefore radiation damage, was similar for both the residues with high solvent accessibility and the residues with zero solvent accessibility. In this case there was no significant trend between the solvent accessibility and the change in B factor.

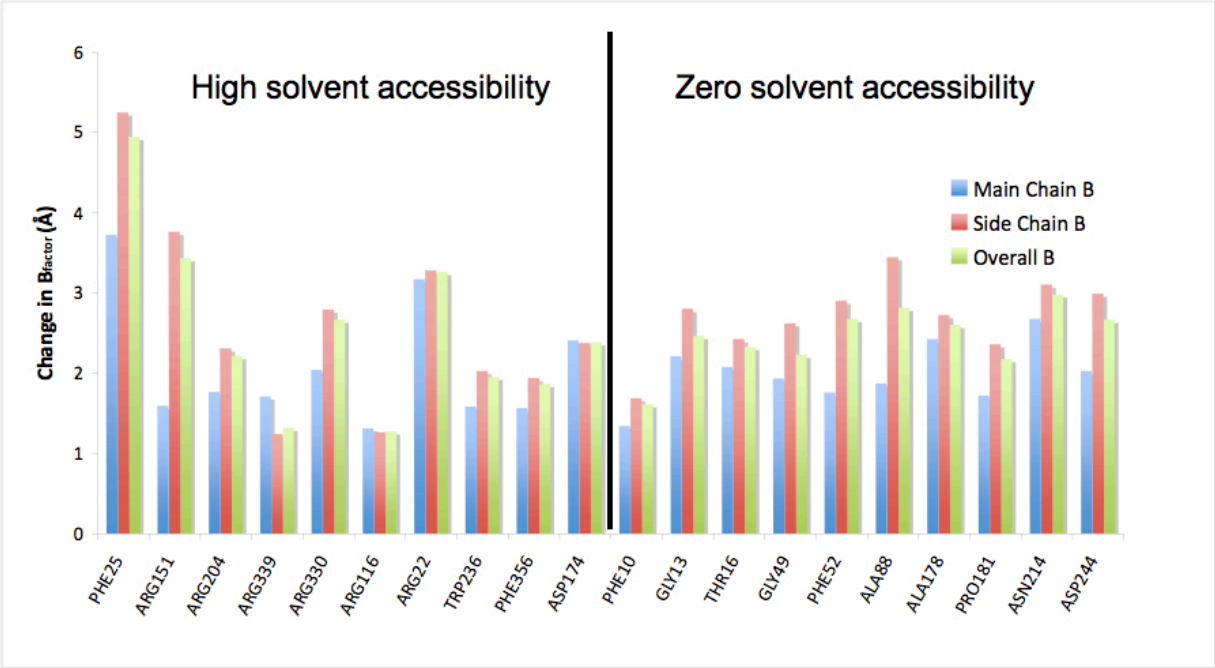

Figure 4.9: Change in main chain, side chain and overall B factor from the first dataset to the seventh dataset, plotted for 10 solvent accessible residues (to the left of the line) and 10 residues with zero solvent accessibility (to the right of the line).

The structure from the first dataset was superimposed on the structure from the seventh dataset using *Superpose* (CCP4) (Winn *et al.*, 2011). The overall root-mean-squared deviation (RMSD) for the two structures was 0.056 Å, indicating no large scale radiation driven conformational changes. However, 21 residues had a RMSD of 0.1 Å or higher (Table 4.4). Of these, three were polar uncharged, three were charged, 13 were hydrophobic and two were special cases (proline).

Although there was no significant trend observed with solvent accessibility and B factor, the position of residues having more hydrophobicity changed more than any other type. This included hydrophobic stretches of residues: Val134, Ala135 and Trp136, which are in close proximity to the active site. Glu220 and Gln221 are also close to the active site, bound to active site residue His219. One of the active site residues is also in this category of significant positional change, Asp254.

Residue	RMSD
Ser 1	0.10
Thr 89	0.10
Gly 101	0.10
Val 134	**0.10**
Gly 146	0.10
Asn 249	0.10
Gly 262	0.10
Ala 267	0.10
Pro 289	0.10
Asp 100	**0.11**
Gly 145	0.11
Gln 221	**0.11**
Glu 220	**0.12**
Tyr 253	0.12
Asp 254	**0.12**
Gly 141	0.13
Pro 24	0.14
Ala 135	**0.14**
Trp 136	**0.14**
Ala 266	0.14
Lys 252	0.33

Table 4.4: RMSD values from the superposition of the first and seventh dataset. Only values > 0.1Å are reported. Colors represent residue properties: blue= polar uncharged residues, orange= hydrophobic residues, green= special cases, red= charged side chains. Residues shown in bold (Val134, Ala135, Trp136, Gln221, Glu220 and Asp254) are in close proximity to the active site.

4.4.3 Progressive structural damage

Isomophous difference density maps (Fo_n-Fo_1) were used to highlight the structural differences between the structures calculated for each subsequent absorbed dose compared to the lowest dose. Positive density (green) indicates where the electron density in dataset 1 is greater than in dataset n, and negative density (red) peaks indicates where the electron density in dataset 1 is less than in dataset n.

A detailed analysis of the Fo_n-Fo_1 map (Figure 4.10) shows a decrease in electron density between the first and second dataset for the sulfur containing residues (Met157, Cys305, Met369, Met379) and carboxyl groups of acidic side chains (Asp100, Glu140, Glu185, Glu263, Glu372). Contoured at 5σ, the difference densities are present only at protein residues or the metal site, but not present in the solvent regions. Thr118 and Asp100 are solvent exposed residues and are not close to the enzyme's active site.

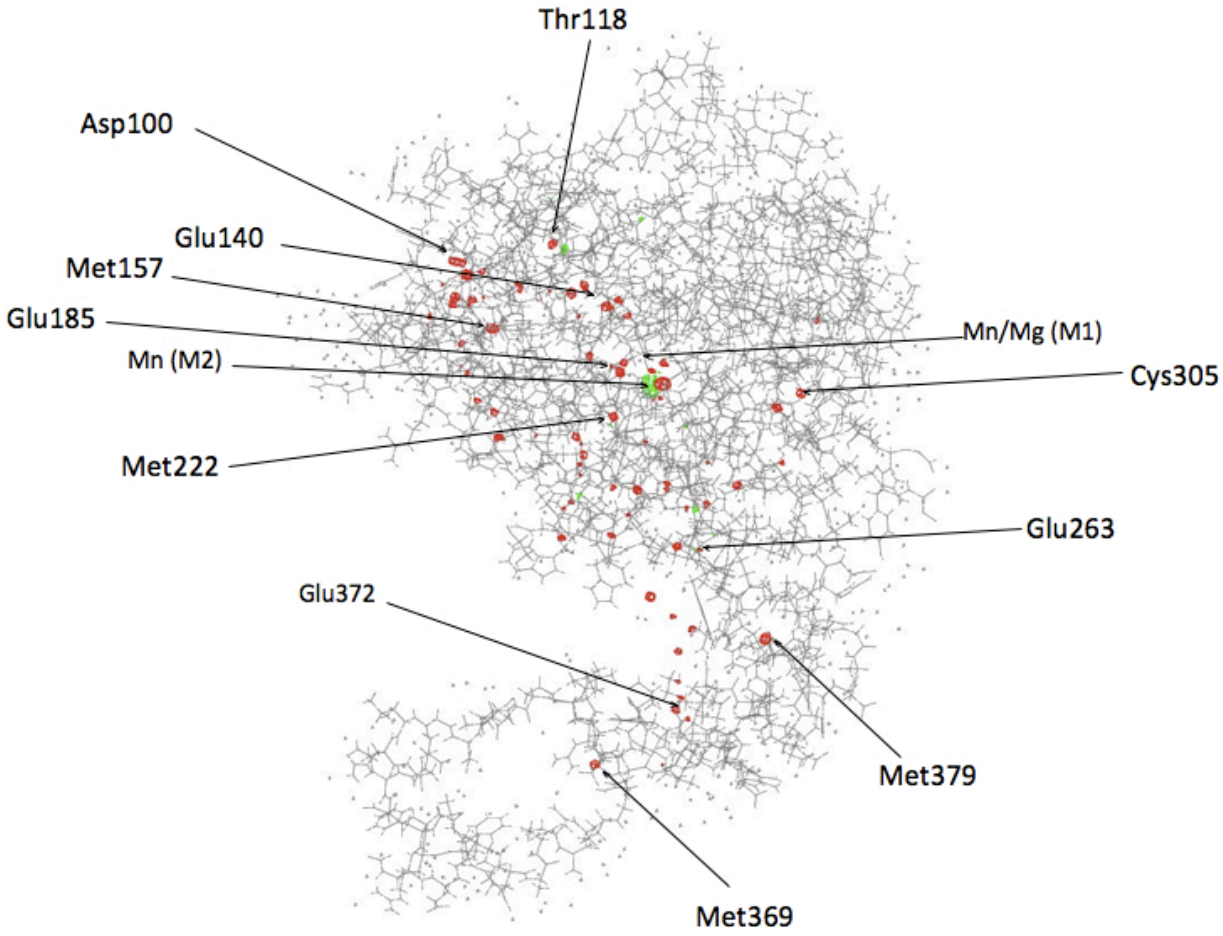

*Figure 4.10: Experimental electron density maps Fo_2-Fo_1, contoured at 3 **σ** (green) and -3 **σ** (red) showing specific damage at the metal ions and the sulfur containing residues.*

The progression of structural perturbations were visualized through consecutive Fo_n-Fo_1 maps, Figure 4.11. The Fo_7-Fo_1 map was used to determine the effects of X-ray induced radiation the highest dose collected, 5.74 MGy. This dose is within the range commonly used for crystallographic X-ray data collection and is below the 30 MGy Garman limit (Owen *et al.*, 2006a), the point where structural damage is guaranteed to have occurred. The active site metal, M2, showed the largest negative density peak in the Fo_7-Fo_1 maps (-40 σ). Three of the seven methionine residues have the next highest difference in density, Met222, Met157 and Met379 at the sulfur atom, above -15 σ. Following the methionine residues, the successive set of most negative peaks are associated with the carboxyl groups of aspartic acid and glutamic acid residues, as observed by others and predicted by the model presented in chapter 3.

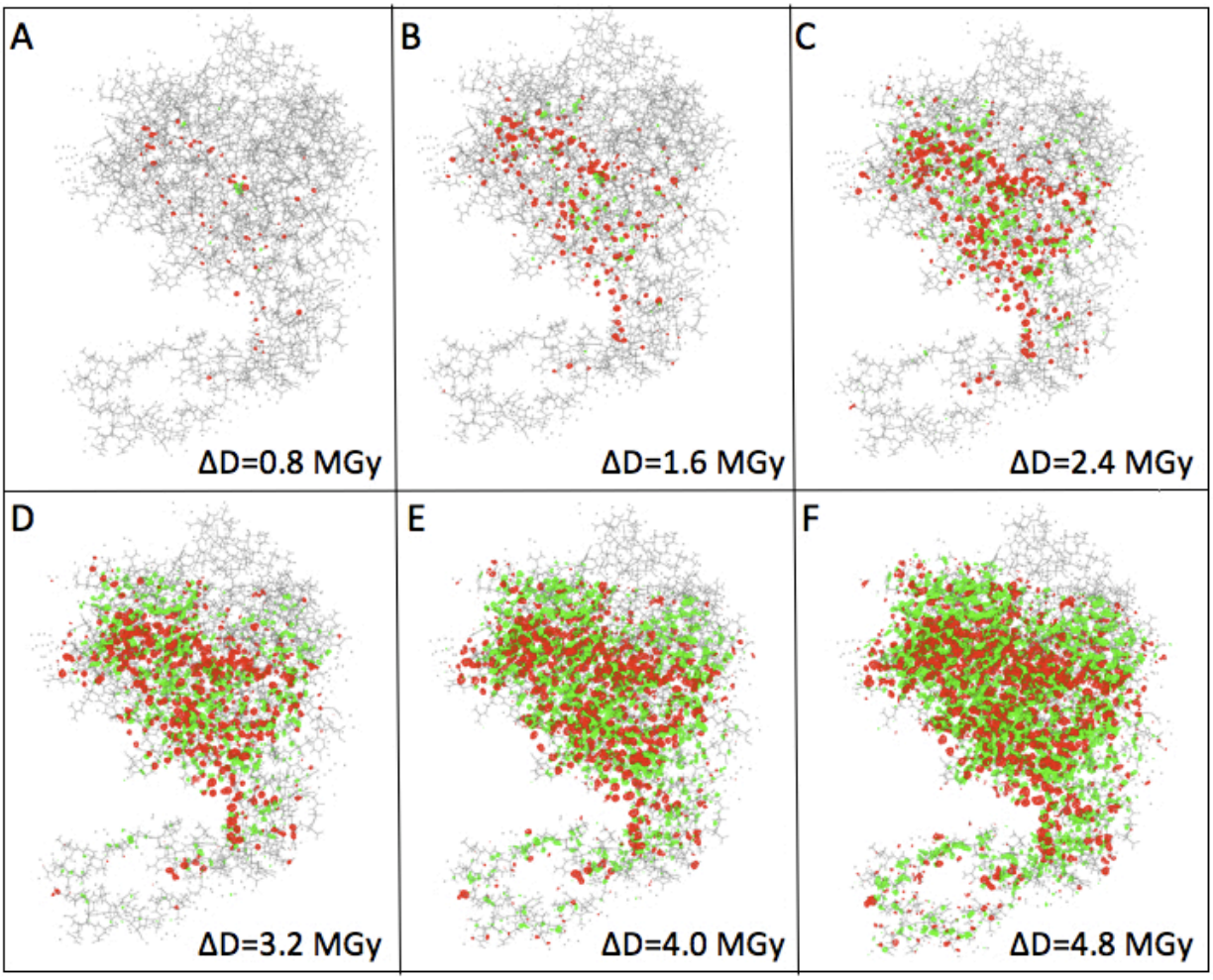

Figure 4.11: Progression of the damage over consecutive data collection Fo_n-Fo_1, where n=2 (A) through n=7 (F). ΔD is equal to the difference in dose, calculated from the cumulative absorbed dose in dataset n minus the absorbed dose for dataset 1.

In addition to the effects seen on the active site residues coordinating the metal atoms, the residues directly involved in the XI mechanism showed a decrease in electron density with increasing absorbed dose. Glu180, essential for isomerization (as described in Section 4.2.4), had an electron density difference of -11 σ. Lys288 and Lys182, essential for proton shuttling and stabilization of the linear substrate (as described in Section 4.2.3), also show signs of damage with Fo_7-Fo_1 map peaks of -7.61 σ and -8.68 σ, respectively.

4.4.4 Active site- Metal movement

The positions of the three configurations of M2 differ in the seven structures of XI. A detailed view of the active site of the structure resulting from the first dataset with an absorbed dose of 0.35 MGy is shown in Figure 4.6, including both M1 and M2 and the coordinating residues. The residues coordinating the manganese ion, M2; Asp254, Asp256, Glu216, His219 and coordinated water are highlighted in yellow. Changes in position of the active site residues as well as the metal atoms were visualized by the superposition of the structure from the last dataset with the structure from the first dataset. The catalytic active site, M2 is shown in Figure 4.12. All three conformations of M2 do not align in the active site. From the first dataset (0.35 MGy) to the last dataset (5.74 MGy) each of the three conformations of M2 shifted in position. M2a, M2b and M2c shifted 0.42, 0.17 and 0.56 Å respectively. The water molecules are also in different positions in both datasets, experiencing shifts of 0.13 and 0.94 Å. However, the active site residues do not experience the same shift.

The position of the metal M2 differed as a function of dose. In Figure 4.12 the structural results for the first (0.35 MGy) and last (5.74 MGy) are shown. The 5.74 MGy structure is shown with bright colors while the 0.35 MGy structure is shown muted. The positions of the three configurations of M2 in the first structure do not superimpose with the configurations of M2 in the seventh structure. While the position of one of the active-site water molecules remains the same, the position of the second active-site water molecule changes with increased dose. The positions of the residues coordinating the metal ion are comparable in both structures. Lys182, adjacent to the residues coordinating the metal atom, does experience an X-ray induced shift.

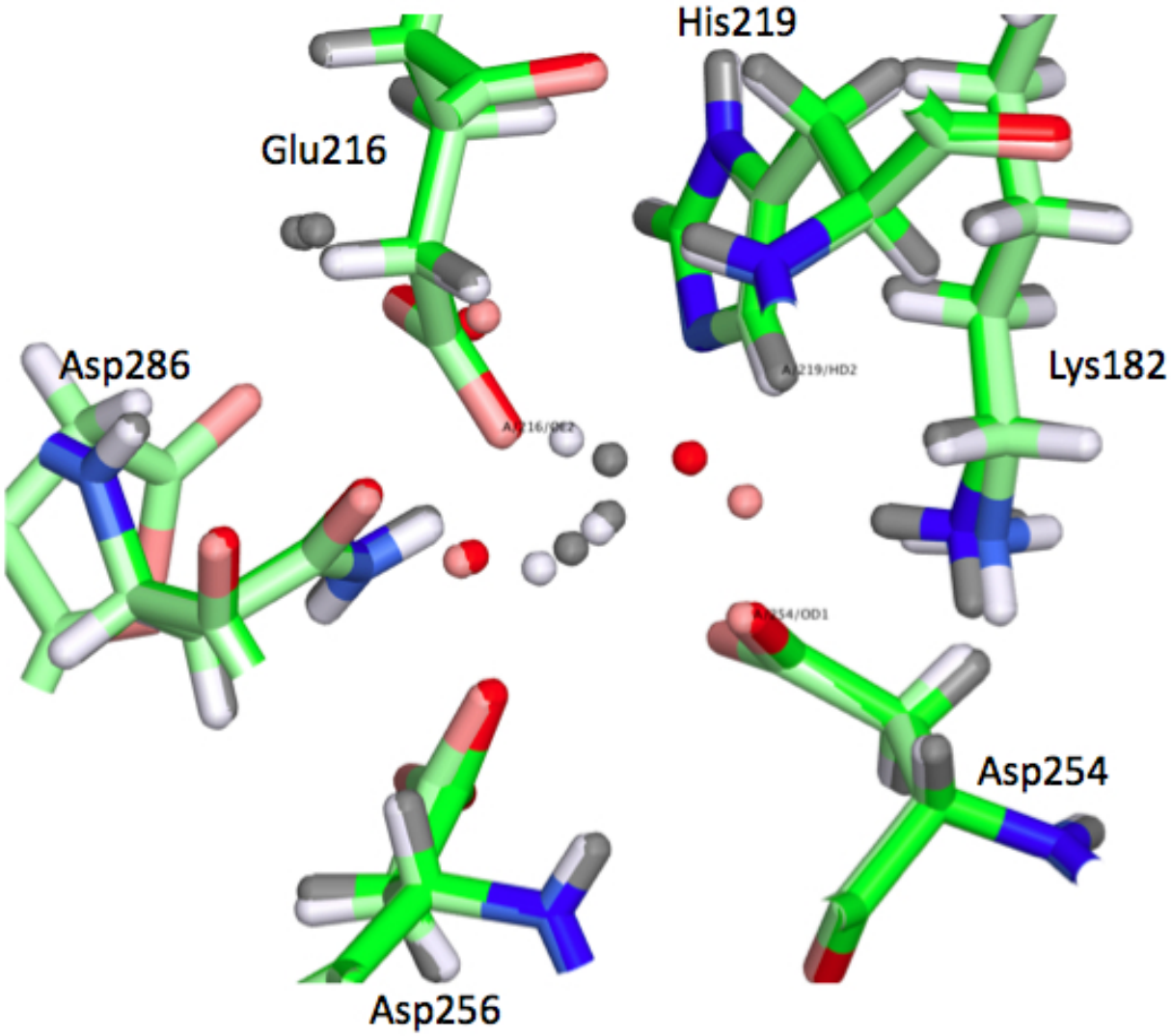

Figure 4.12: Superposition of the active site of the first (dull colors) and seventh (bright colors) datasets.

The experimental electron density maps of the active site with 2Fo-Fc electron density are shown for the first and the seventh datasets in Figure 4.13. The active site showed three alternate manganese positions at M2. The structural metal site, M1, was modeled as occupied partially by manganese (42%) and partially by magnesium 58%) which provided the best agreement with the X-ray data. The difference in metal position in these structures suggests movement in the active site of the manganese atoms. The position of M2c and the active site water vary in each dataset, whereas the positions of M2a and M2b seem to remain consistent. Analysis of the Fo7-Fo1 maps of the active site Figure 4.13, show specific changes in the active site are evident, even from the first dataset to the second dataset, at relatively low doses. This is readily observed as positive and negative density surrounding the M2 site, and a small negative density hole surrounding M1 in Figure 4.14a. A difference of 0.8 MGy (between dataset 1 and 2) causes a decrease in the electron density at both of the metal sites. By the third dataset (Figure 4.14b) there are both positive density peaks and negative density holes surrounding the M2 site, which both increase in magnitude with increasing dose. Electron density decreases surrounding M2, and increases close to His219. This suggests that the metal position changes from the initial position (where the negative density in red develops) to a new position (where the positive density in green develops) with increasing absorbed dose. The His219 residue acts as an electron sink, attracting the electrons generated in the active site.

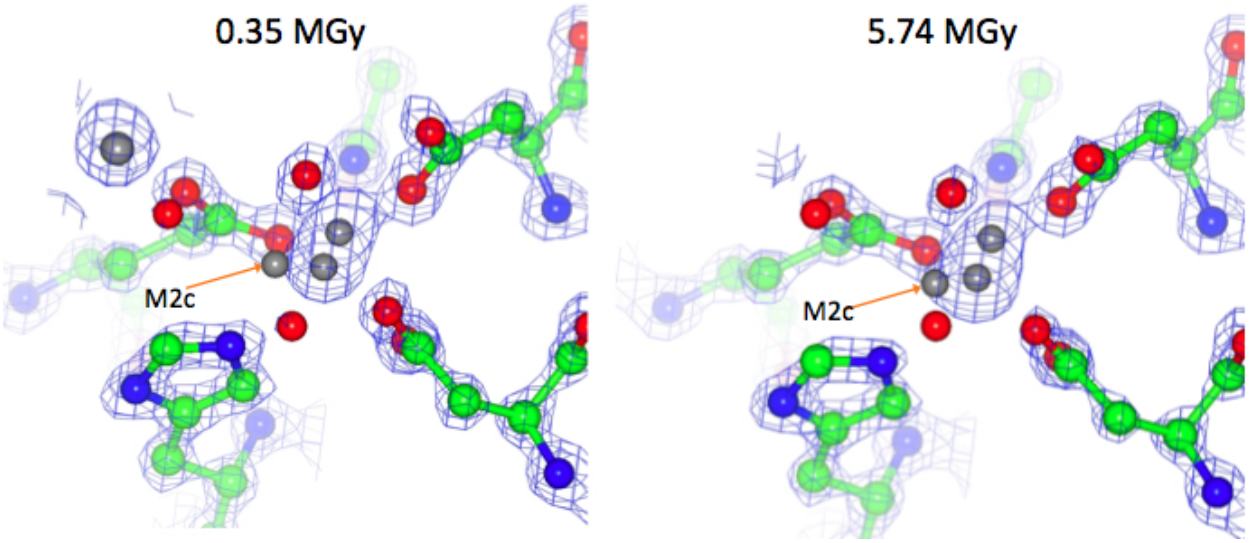

*Figure 4.13: 2Fo-Fc electron density maps of the active site (contoured at 1 **σ**) for Dataset 1 and Dataset 7 with absorbed doses of 0.35 and 5.74 MGy, respectively. The orange arrow points to the third conformation of M2, M2c. M2c and the water molecule in the active site occupy slightly different positions in each of the seven datasets.*

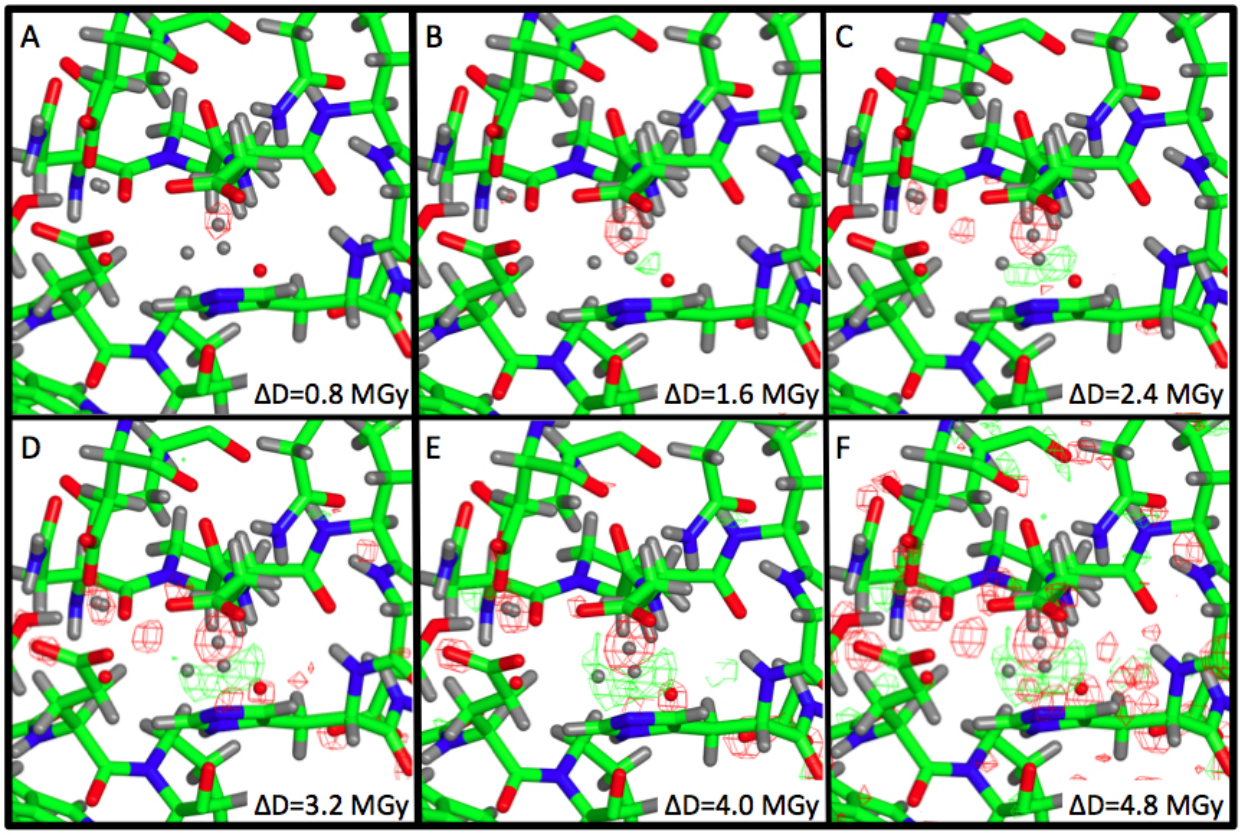

Figure 4.14: Experimental electron difference density maps Fo_n-Fo_1 of the active site, contoured at 0.25e-/Å^3 (green) and -0.25 e-/Å^3 (red). This view is similar to Figure 4.13, with His219 rotated down slightly below M2 for clarity. (a) Fo_2-Fo_1 shows negative density around both the M1 and M2 sites, with a small amount of positive density indicating a change in occupancy. (b) Fo_3-Fo_1, negative difference density on the carboxyl groups of Asp and Glu in the active site indicating decarboxylation of these residues (c) Fo_4-Fo_1 (d) Fo_5-Fo_1 (e) Fo_6-Fo_1 (f) Fo_7-Fo_1.

To visualize the change in position of the M2 metal atom, the coordinates were plotted in three dimensions (Figure 4.15). M2a transitions to M2b. M2c continues along a similar trajectory but then veers to the left towards His219.

The residues coordinating the M2 site: His219, Asp256, Asp254, Glu216 and a coordinated water molecule also show Fo_7-Fo_1 peaks in the range of -13 to -5 σ (Table 4.5), mostly on the active-site carbonyls, but also on the nitrogen of His219 and on the active-site water molecule. The density loss on the active-site carbonyls is an indication that X-ray induced decarboxylation has occurred, causing a change in the active site geometry. The decarboxylated acidic side chains do not appear to be bound to M2, which could lead to a misinterpretation of the metal's coordination state. Further analysis of the bond lengths of M2 and the surrounding residues is provided in Table 4.7.

M1 has a similar environment to M2, coordinated by acidic side chains; Glu180, Glu216, Asp244 and Asp286. The peak height is less for M1 than for M2. The decrease in M1 density (-8.27 σ) between the first two datasets resembles the decrease of the active-site residues (i.e. Asp244 -4.01 σ, His219 -5.33 σ), whereas M2 has a more dramatic decrease (-21.14 σ). This may be due to the uncertainty in position and occupancy of M2, compared to M1.

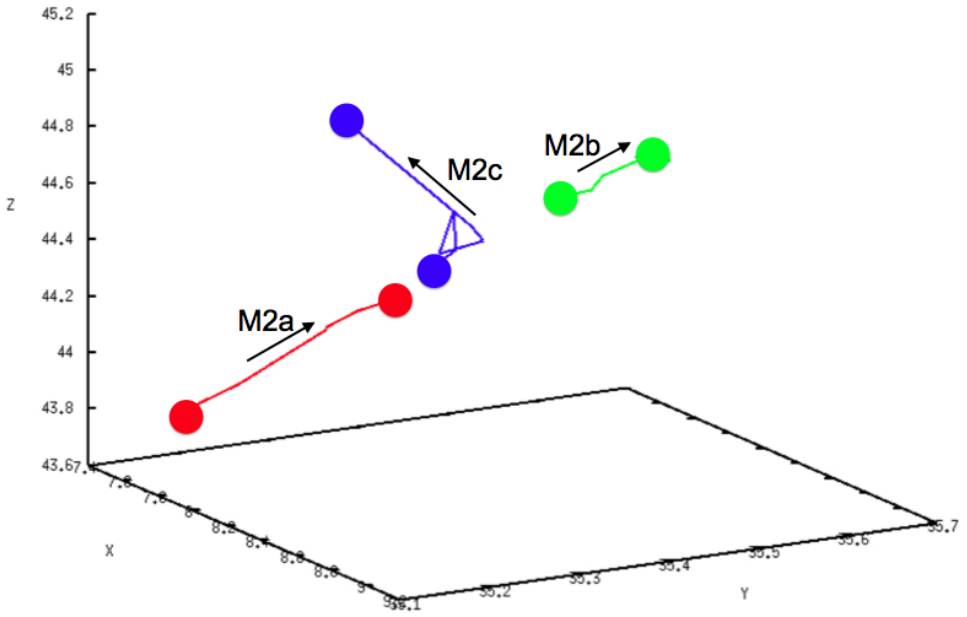

Figure 4.15: The coordinates of the three configurations of M2 are plotted in three dimensions. The trajectories indicate that M2a shifts towards M2b. The position of M2c initially follows the same trajectory and then veers to the left. The shift of M2a to M2b is similar to the change in position of M2 during the extension of the linear substrate step of the XI mechanism.

Table 4.5: Sigma values for negative density differences from the isomorphous difference density maps, comparing the difference between the first and second dataset and the first and seventh dataset.

Residue	Fo_2-Fo_1	Fo_7-Fo_1
M1	-8.27	-13.75
Glu180	-5.05	-11.48
Asp244	-4.01	-7.45
Asp286	-3.80	-8.88
M2	-21.14	-40.44
Glu216	-5.00	-6.90
His219	-5.33	-10.33
Asp254	-4.91	-9.80
Asp256	-4.94	-9.90
H_2O	-8.27	-12.56

The occupancies of the M1 and M2 were refined (Figure 4.16). The occupancy of M1 remains relatively stable with approximately 60% occupancy for Mg and approximately 40% occupancy for Mn throughout. The occupancies of M2a and M2b are correlated, with M2a increasing and M2b decreasing with increased absorbed dose. The occupancy of M2c fluctuates. Starting with occupancies of 48%, 40% and 12% for M2a, M2b and M2c respectively, in the first dataset, M2a ranges from 48% to 69%, M2b ranges from 28% to 47% and M2c ranges from 0 to 14%. These results show occupancy and position of the metal ion within the same crystal can change during the data collection process. An X-ray induced metal shift occurs, mimicking the mechanistic M2 shift during the extension step of the XI mechanism.

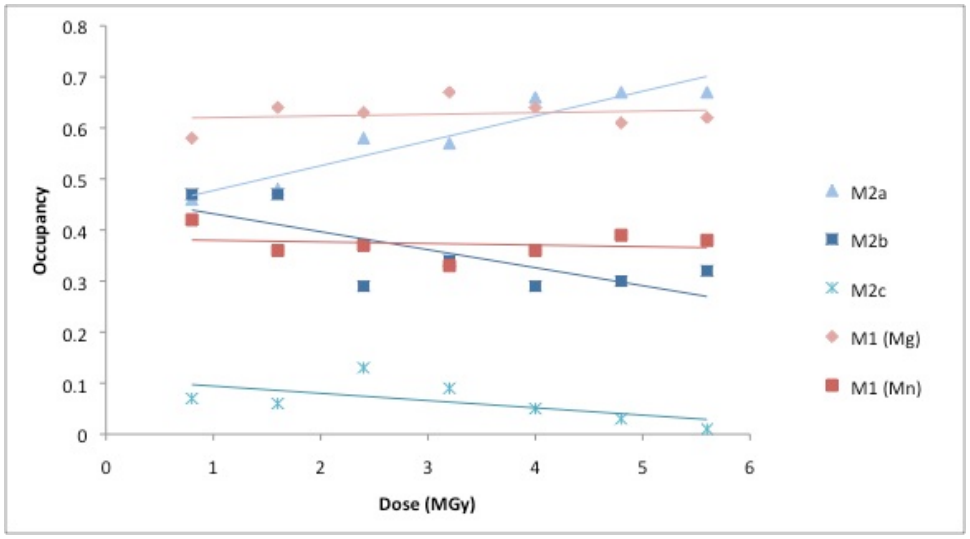

Figure 4.16: Change in metal site occupancies with dose. M1 remains constant. M2a increases, M2b decreases and M2c slightly decreases. Linear trend lines were fit to the data points.

Occupancy and B factor are closely related, but can be refined independently at this resolution. To check that this was indeed the case, the occupancy of the active site residues was restrained to 1.0 and the B factors were refined. The B factor of M2a and M2b increased with dose. The B factor of M2c fluctuates from 1.27 to 15.10 $Å^2$ and does not follow a trend with increased dose.

Table 4.6: Positional coordinates and B factors for M1 and M2.

	D1	D2	D3	D4	D5	D6	D7
Coordinates							
	12.191	12.225	12.245	12.298	12.218	12.211	12.219
	34.421	34.406	34.210	34.300	34.393	34.389	34.389
M1 (Mg)	43.031	43.039	42.975	42.887	43.025	43.026	43.010
	12.255	12.246	12.221	12.172	12.267	12.295	12.291
	34.240	34.244	34.374	34.327	34.219	34.212	34.195
M1 (Mn)	42.966	42.961	43.020	43.108	42.965	42.929	42.922
	7.574	7.584	7.600	7.648	7.647	7.660	7.662
	35.173	35.188	35.229	35.316	35.319	35.350	35.394
M2a	43.788	43.831	35.245	44.044	44.055	44.103	44.130
	7.783	7.806	7.797	7.829	7.820	7.814	7.866
	35.561	35.583	35.598	35.635	35.659	35.670	35.620
M2b	44.447	44.464	44.502	44.554	44.533	44.530	44.580
	9.006	9.024	8.763	9.072	9.042	8.953	8.700
	35.170	35.197	35.245	35.169	35.224	35.229	35.137
M2c	44.688	44.750	44.795	44.763	44.776	44.802	45.150
B factor							
M1 (Mg)	5.21	5.72	15.80	10.24	5.94	6.54	8.07
M1 (Mn)	11.52	11.64	6.54	7.26	16.57	17.72	14.07
M2a	6.60	7.40	9.61	11.44	12.31	13.59	13.53
M2b	5.52	6.92	6.32	10.39	10.23	11.49	12.84
M2c	8.14	1.27	8.65	2.14	1.57	1.92	15.10

Mn binds to the carboxyl groups of Asp and Glu with a target bond distance of 2.15 Å and to the nitrogen atom of His with a target bond distance of 2.21 Å, Table 4.7. In the first two datasets M1 (Mn) is coordinated by Glu216, Asp286, Asp244, Glu180 and a cryoprotectant molecule, ethylene glycol (EDO). In the third dataset, M1 (Mn) appears to lose coordination with EDO. The coordination remains the same for the fourth dataset, but for the remaining three datasets, the coordination with EDO is restored and the bond length to Glu216 increases, causing a loss of coordination. M2 is the catalytic metal and the position and coordination of M2 is essential in determining the biologically relevant enzymatic mechanism. X-ray induced changes in the bond lengths from M2 to the coordinating residues occur, indicating the active site is sensitive to radiation damage. These changes in bond length do not indicate a change in the coordination of the metal. M2a remains within typical bond distances to Glu216, Asp256 and an active-site water molecule. Glu216 and Asp254 coordinate M2b, while M2c is bound to His219 and an active-site water molecule.

Table 4.7: Bond distances for active site metal atoms, M1 and M2. Shaded distances are within the accepted Mn-O bond distance of 2.17 Å.

	D1	D2	D3	D4	D5	D6	D7
Mg-E216 OE1	2.01	2.04	2.18	2.17	2.03	2.03	2.03
Mg-D286 OD2	2.10	2.13	2.00	2.06	2.12	2.12	2.11
Mg-D244 OD2	2.04	2.03	2.02	1.91	2.05	2.06	2.05
Mg-E180 OE2	2.02	2.02	2.16	2.14	2.04	2.04	2.04
Mg-EDO	2.29	2.27	2.13	2.19	2.28	2.29	2.29
Mg-H2O	2.37	2.41	2.43	2.54	2.42	2.40	2.42
Mn-E216 OE1	2.17	2.16	2.01	2.06	2.18	2.21	2.21
Mn-D286 OD2	2.00	2.01	2.11	2.08	2.01	2.02	2.00
Mn-D244 OD2	1.99	2.00	2.03	2.15	2.01	1.98	1.99
Mn-E180 OE2	2.13	2.15	2.05	2.03	2.14	2.16	2.17
Mn-EDO	2.12	2.15	2.26	2.23	2.13	2.13	2.13
Mn-H20	2.41	2.45	2.42	2.30	2.44	2.47	2.47
M2a-H219 NE2	3.16	3.12	3.06	2.89	2.89	2.84	2.80
M2a-E216 OE2	2.02	2.01	2.01	1.98	1.98	1.98	1.96
M2a-H2O	1.98	1.98	1.99	2.03	2.04	2.05	2.09
M2a-D256 OD1	1.75	1.81	1.84	1.99	1.99	2.03	2.04
M2a-D254 OD2	2.35	2.33	2.34	2.26	2.29	2.28	2.30
M2a-D254 OD1	2.68	2.67	2.64	2.55	2.56	2.55	2.52
M2b-H219 NE2	2.43	2.40	2.38	2.32	2.33	2.33	2.30
M2b-E216 OE2	2.02	1.99	2.03	2.02	1.99	1.98	2.01
M2b-H2O	2.31	2.32	2.33	2.35	2.36	2.36	2.30
M2b-D256 OD1	2.46	2.47	2.48	2.54	2.51	2.51	2.55
M2b-D254 OD2	2.01	2.03	2.04	2.05	2.10	2.11	2.12
M2b-D254 OD1	2.35	2.36	2.34	2.34	2.33	2.34	2.40
M2c-H219 NE2	1.92	1.91	1.93	1.95	1.91	1.92	1.91
M2c-E216 OE2	2.24	2.26	2.25	2.29	2.25	2.25	2.55
M2c-H2O	2.00	2.04	2.03	2.00	2.03	2.01	2.02
M2c-D256 OD1	3.47	3.56	2.31	3.53	3.50	3.45	3.47
M2c-D254 OD2	2.81	2.80	2.58	2.88	2.87	2.79	2.43
M2c-D254 OD1	3.54	3.53	3.29	3.60	3.55	3.49	3.31

The *CCP4* program *SFall* (Winn *et al.*, 2011) was used to record the calculated amplitudes (F calc) of the structure. Subsequently, the M2 metal atoms were removed, and the amplitudes were recalculated. By determining the reflections that had maximal differences between the two calculated sets, a series of reflections that the metal strongly contributed to were selected. The change in intensity of these reflections, having a strong metal contribution, was compared to the change in intensity for a group of reflections having little, or no, metal contribution with increased absorbed dose. There was no clear difference, or trends observed in the change in intensity between these two groups of reflections.

4.4.4 Damage to residues involved in XI mechanism

Radiation induced structural changes to residues involved in the enzyme's mechanism were observed. Lys182, responsible for stabilization of the ring form of xylose and stabilization of M2 during isomerization, develops an X-ray induced alternate conformation, as shown in the Fo_7-Fo_1 maps in Figure 4.17. The X-ray induced conformation is shifted 0.31 Å from the initial conformation of Lys182 and the distance between Lys182 and M2 becomes shorter with increased absorbed dose. The Lys182-M2 distance is even shorter in the substrate free structure determined by Fenn *et al.* (2004), indicating their structure has the X-ray induced conformation of Lys182.

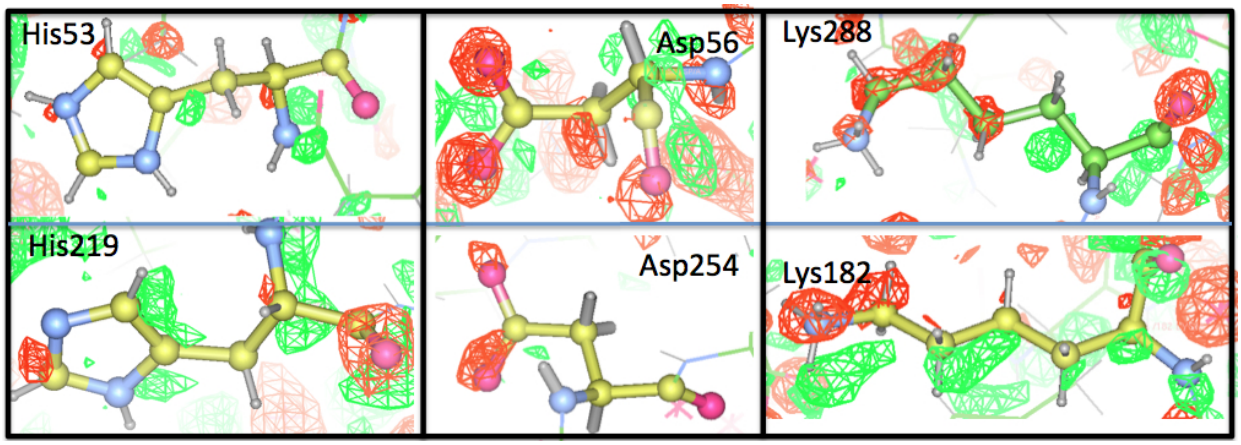

Figure 4.17: Experimental electron difference density maps Fo_n-Fo_1 of active site residues involved in the enzyme mechanism, contoured to 0.25 e-/Å^3 (green) and -0.25 e-/Å^3 (red), ΔD= 4.8 MGy. His53 and Asp56 are involved in the sugar binding step. Lys182 is involved in stabilization of the ring form. Thr89 and Lys288 bind to substrate through water molecules. His219 maintains structure and coordination of M2 during linear extension. Asp254 changes the metal coordination during the reaction.

His219 and Asp254 are two of the six residues that coordinate M2. These active-site residues show decarboxylation of Asp254 and a decrease in electron density of His219 with increasing absorbed dose. These changes mimic the extension of the linear substrate step in the XI mechanism. During this step, M2 shifts to a new position, M2b, loses coordination with Asp254 and His219 and forms a new bond with Asp256 in a bidentate manner. The decarboxylation and development of an alternate conformation induced by increased absorbed dose could be interpreted as a change in the coordination of M2.

The acid/base pair, His53/Asp56, is responsible for binding the ring form of the sugar as it displaces active-site water molecules. In this structure no sugar is bound. Although His53 does not show any signs of damage (a shift in position or decrease in electron density), Asp56 does show evidence of radiation-induced decarboxylation and a possible alternate conformation. The decarboxylation does not mimic any step in the XI mechanism; it is an artifact of damage.

The observed X-ray induced conformational changes; development of the alternate conformation of Lys182, decarboxylation of Asp254 and decrease in electron density of His219 mimic the progression of XI isomerization (sugar binding, ring opening, extension of the linear substrate or isomerization). In this case, the substrate is not present in the structure; biochemically-induced structural changes are not possible. The structural changes observed here are solely due to radiation chemistry effects.

4.5 Discussion

4.5.1 Global indicators of damage

The analysis of the global indicators of damage during scaling and refinement showed a decrease in reflection intensity at high resolution, with a corresponding linear decrease in the signal-to-noise as a function of dose. Mosaicity also increased with dose. Global damage occurs due to X-ray induced damage. The global damage observed is entirely consistent with the observations of others; intensity decay (Ravelli & McSweeney, 2000a, Ravelli *et al.*, 2002, Murray & Garman, 2002), increase in Wilson B factor ((Murray & Garman, 2002, Ravelli & McSweeney, 2000a, Ravelli *et al.*, 2002), increase in R_{sym} (Ravelli & McSweeney, 2000a, Murray & Garman, 2002) increase in mosaicity (Muller *et al.*, 2002, Murray & Garman, 2002, Ravelli *et al.*, 2002) and decrease in completeness (Leiros *et al.*, 2001). Here the focus is on the specific structural perturbations, caused by the experimental technique, that relate to proposed structural changes that could influence the interpretation of the enzymatic mechanism.

4.5.2. Specific Damage

Specific damage was detected through the analysis of radiation damage metrics after refinement- average isotropic B factor, R_{work}, RMSD bond lengths and angles and the number of protein and solvent atoms. An increase in average isotropic B factor with increased dose was expected, due to the increased movement of the protein molecules in the unit cell, disordered side chains and creeping non-isomorphism. A linear increase in isotropic B factors led to analysis of the change in residue specific B factor. Although

there was no correlation between solvent accessibility and change in average B factor for each side chain, the superposition of the first and seventh structure revealed that 21 residues had a RMSD greater than or equal to 0.1 Å. Of the 21 residues, 13 were hydrophobic in nature. This is the opposite of what would be expected due to hydrophobic residues being closer to the interior of the protein with less room for movement. However, a hydrophobic 3 residue stretch (Val134, Ala135 and Trp136) close to the active site and a hydrophobic 2 residue stretch (Glu220 and Gln221) bound to active-site residue His219 had RMSDs ranging from 0.1 Å to 0.14 Å. X-ray induced changes in the active site cause the surrounding residues to change in position.

An increase in R_{work} is observed with increasing dose, as expected. R_{work} depends on the mean value of $| F_{obs}| - |F_{calc}|$. This value can only be small if the intensities have been measured accurately, to give suitable observed amplitudes, and successful refinement has given good estimates of the calculated amplitudes. As the protein suffers from radiation damage, the model becomes less accurate for the data. This leads to an increase in $R_{work.}$

In the isomorphous difference maps, large negative difference density peaks indicated damage to a residue. There was a progression of specific damage, with the metal ions being the most susceptible to damage, followed by cleavage of the carbon sulfur bond in methionine, the decarboxylation of acidic side chains, reduction of cysteine residues and the loss of the hydroxyl group on tyrosine as predicted in chapter 3.

Fo_7-Fo_1 maps highlighted damage at Glu180, which is especially of interest with a hole of -11 σ, because of its essential role for isomerization in concert with M1, which was postulated by Allen and coworkers (Allen *et al.*, 1994). The distance between Glu180 and M1 increases from 2.02 Å to 2.04 Å, which is still within the bond distance for Mn-O. The Fo-Fc maps for the first and the seventh dataset do not show any peaks or holes at 3 σ, indicating that the loss of electron density induced by radiation may go undetected without the use of Fo-Fo maps.

Kovalevsky et al. postulated that Lys182 changes conformation in order to move closer to the active site (Kovalevsky *et al.*, 2010). We have observed an X-ray induced change in conformation for Lys182, with the new conformation positioned closer to M2. This mimics the extension step of the mechanism of XI. In addition, Lys288 and Lys182, essential for proton shuttling and stabilization of the linear substrate (Collyer *et al.*, 1990, Carrell *et al.*, 1989, Carrell *et al.*, 1994, Fenn *et al.*, 2004, Kovalevsky *et al.*, 2010) show signs of damage with Fo_7-Fo_1 map peaks at NZ and O.

4.5.3 Active site damage

An accurate structural depiction of the active-site and its surrounding residue environment are often key to fully understand enzymatic mechanisms. Metalloproteins contain a metal atom typically having a large photoabsorption cross section, presenting an area where radical formation occurs. This likely makes these regions in the protein the most susceptible to X-ray induced damage. In this study, we analyzed the damaging

effects of X-rays on the structure of the active site of *Strepomyces rubiginosus* XI. A decrease in electron density was observed for Asp254 and His219, two active-site residues coordinating M2. This mimics the extension of the linear substrate step in the mechanism, where the substrate moves further into the active site and M2 changes position. The change in position of M2 causes a change in its coordination, no longer coordinated to His219 and Asp254, it bonds to Asp256 in a bidentate manner. M2 plays a role in every step of the reaction; therefore accurate position and occupancy information is necessary to determine the correct mechanism. The position of M2a and M2b change in a systematic manner, shifting towards Lys182 and Asp254, with increased absorbed dose. The occupancy of M2a and M2b also reflect this shift, with M2a increasing in occupancy and M2b decreasing in occupancy. M2c does not follow any systematic trends correlated with M2a, M2b or any of the surrounding active-site residues.

The results from the analysis of Electron Paramagnetic Resonance (EPR) spectra from XI conflict with the results of X-ray crystallographic analysis. The EPR technique is described in detail in chapter 2. The dipole interaction between the metal sites occupied with paramagnetic metal ions, provides spectroscopic evidence for M2 movement. The EPR spectra for substrate-free XI containing 8 moles of Mn^{2+} per tetramer and mixed metal substituted XI (Mn^{2+} at M1 and Co^{2+} at M2) was in agreement with the proposed metal-mediated hydride shift mechanism. These spectra showed a largely symmetric coordination environment of both metal sites, with a octahedral coordination at both sites. When xylose or cyclic substrate analogs were added, the EPR spectra indicated

metal movement of M2 (Bogumil *et al.*, 1997). Since this spectral change occurred in the presence of the competitive inhibitor 5-thio-α-D-glucose and ring opening cannot occur, the metal movement is directly induced by binding of the cyclic substrate. Bogumil *et al.* (Bogumil *et al.*, 1997) suggested the binding of the substrate causes structural rearrangement due to the substrate O3 and O4 hydroxyls binding to the M1 site mediated by the bridging Glu216 to M2, causing M2 to move to a new position. This correlated binding and disturbance of the ligand environment of M1, along with other steric or electronic changes, could be the trigger for metal movement. This is where the EPR and the X-ray analysis deviate from one another.

According to the X-ray analysis by groups investigating the structure of XI with ligand, metal movement was thought to follow the ring-opening step and occurs when the linear extended form is bound. Metal movement does occur during XI turnover, based EPR studies that confirmed two positions for M2. We have driven the metal movement of M2 through X-ray induced radiation without the presence of the substrate and observed three positions for M2. The driving force for metal movement remains unclear. In chapter 5, the influence of X-rays on metal position and redox state is covered in detail.

Lavie and Fenn postulate that metal movement at M2 in the active site of XI upon catalysis may be the reason for low turnover of the enzyme (Lavie *et al.*, 1994, Fenn *et al.*, 2004). We have observed this same movement, induced by X-ray radiation. Other studies have shown that X-rays can induce these positional changes of active site metal

ions (Borshchevskiy *et al.*, 2011, Yano *et al.*, 2005, Takeda *et al.*, 2004, Schlichting *et al.*, 2000, Corbett *et al.*, 2007, Berglund *et al.*, 2002). We have observed three positions for M2, with M2a transitioning to M2b with increased absorbed dose. M2c does not follow a trajectory in position, or a trend in occupancy or B factor with increased dose. M2c is likely to be an artifact of radiation damage.

Metal motion is induced due the photoreduction of the manganese and magnesium atoms by secondary electrons. The photoreduction causes a change in the coordination of these ions resulting in a shift in position of the metal. The exact position is not easily determined because the process does not simultaneously take place among all of the protein molecules that make up the crystal. The metal atoms in the active site act as a target for the X-rays, attracting excess electrons to the active site. This causes peripheral damage to the residues coordinating the metal atoms. For XI, the acidic side chains coordinating the metals appear to be decarboxylated due to a reduction in electron density. This can be interpreted as a loss of coordination to the metal ions.

In the Fenn et *al.* study (2004), the M2 site has multiple conformations with occupancies of a) 0.48, (b) 0.69 and (c) 0.16, having a combined occupancy of 1.33, - over-explaining the experimental electron density. There are two possible explanations for the additional occupancy. The first explanation involves an over-fit active site, meaning something other than the metal ion could be built into the density in the active site, perhaps water. The second explanation involves excess electron build up at the active

site due to the absorption of electrons at the active site. This causes an inflated value in the occupancy of the manganese atom.

In looking at the other 109 structures of XI from different bacterial species in the Protein Data Bank, only seven are solved to atomic resolution (< 1 Å). Of the seven structures on the atomic scale, three structures have refined three positions for the M2 site. In the structures with only one position for M2, there is evidence of three partial occupancy sites, indicating there is some uncertainty in position for M2. Over the course of the consecutive data collection in this study, we have induced this uncertainty in metal position and observed a change in occupancy of the M2 site (not the M1 site). Fenn *et al.* (2004), who solved the structures with the substrate and the inhibitor (xylitol), and attributed the low enzyme turnover to the movement of M2. The X-ray data collected for these structures was collected at the Advanced Photon Source, a third generation synchrotron. The intense X-rays generated by the synchrotron enable the collection of high-resolution data. The absorbed dose is directly related to the incident flux on the sample. Fenn *et al.* (2004) did not report an absorbed dose or even exposure time, but, given that the data was collected at the APS on BioCARS beamline 14-BMC with a flux of ~ $6x10^{11}$ photons s^{-1} and, the resolution was higher 0.95 Å vs. 1.2 Å, the absorbed dose is equal or probably higher to that used in this study. Therefore, the structures are susceptible to the same X-ray induced structural changes. The structure reported by Fenn *et al.* (2004) was used to propose a mechanism for XI turnover. Although our structure did not contain the substrate and therefore catalysis cannot occur, it provided structural evidence similar to turnover. The structural changes observed here are solely

due to radiation chemistry effects. X-ray induced photoreduction of M2 shows the same characteristics of the proposed mechanism-based movement.

4.5.4. Radiation damage in metalloproteins

Radiation induced structural changes can emulate structural changes during enzyme catalysis including: changes in metal coordination, changes in metal position and changes in position of residues involved in the mechanism. The residues involved in the proposed enzyme mechanism are affected by radiation damage through decarboxylation (Asp56 and Asp254), development of alternate conformations (His53, His219, Lys182 and Lys288) and free radical damage (M2).

The position of M2 is of central importance to the XI mechanism. There is some discrepancy in the number of positions M2 occupies throughout the reaction. High-resolution X-ray crystallographic data shows three positions for M2. EPR data shows evidence for only two positions for M2. Our X-ray crystallographic data shows three positions for M2, with the positions and occupancies of M2a and M2b related. The B factor for both M2a and M2b increases linearly with dose. M2a transitions to M2b and the occupancy of M2a increases while M2b occupancy decreases. The third position for M2 does not follow a trajectory, the occupancy does not follow a trend and the occupancy fluctuates with increased dose. Due to these observations, it is probable that the third position of M2 is an artifact of radiation damage and the mechanism based on three positions of M2 should be reevaluated.

4.6 Conclusions

Structural changes in XI are seen as predicted by the radiation damage model presented in chapter 3. Specific X-ray induced structural perturbations mimic steps of the proposed mechanism for XI. This may be the reason for the uncertainties that still remain: the role of Lys182 in deprotonating the substrate during ring opening, the identity of the linear intermediate, the role of the catalytic water species during isomerization and the mobility of M2. We have observed mobility of M2 that was not induced by catalysis, but induced strictly by X-ray radiation. The radiation-induced positional change of M2 mimics the change in position previously used to explain the low turnover rate of the enzyme.

XI was used as a model protein to demonstrate the radiation chemistry that was suggested by our radiation damage model. Radiation damage is not a problem that is unique to XI. Other metalloproteins, which account for 30% of reported structures in the PDB, will experience a similar progression of damage with increased absorbed dose. The active-site metal atom acts as a large target for X-rays. The metal and the surrounding amino acid environment will experience a buildup of free radicals, making it more susceptible to damage than the rest of the protein. The effect of different metals and the surrounding amino acid environment is presented in chapter 5.

5. Understanding the effect of radiation on the active site of metalloproteins with different metal targets and surrounding amino acid environment.

5.1 Introduction

In Chapter 4 motion of the metal atom involved in the enzymatic mechanism of XI was observed as a function of X-ray dose. The position of M2 shifts to position M2b mimicking the substrate extension step of the mechanism. Metal ions are found in ~30% of all proteins and are involved in many key biological processes, including DNA synthesis, metabolism, photosynthesis and detoxification. A bioinformatic study of 1,371 three-dimensional protein structures estimated that 47% required metals (Andreini, 2008), with 41% containing metal at their catalytic centers (Lieberman, 2005). Compared to the lower atomic number elements commonly making up a biological structure, metals have a significantly larger X-ray cross-section. X-ray radiation causes changes in the redox state of these metals and their positions, potentially masking the interpretation of key structural features and sometimes mechanism. The nature of the metal and its surrounding environment play a role in the extent of the damage, but the extent of each contribution is unknown. In this chapter, to address this question, the metal in XI was exchanged and structural studies were carried out as a function of both the metal and dose. Following this a similar study was performed on superoxide dismutase, selected to determine the influence of the active site environment, due to its free radical scavenging activity. SOD actively scavenges free radicals, including the

damaging radicals created by the ionizing X-rays. Due to this native activity, SOD can be expected to be less susceptible to X-ray induced damage than XI. The active site of XI contains acidic side chain residues, which are susceptible to X-ray induced damage as predicted by the model in Chapter 3, that coordinate the metal atom. In contrast, histidine residues acting as electron sinks, coordinate the active site metal atom in SOD. The environment of the two proteins differs and comparison of the damage susceptibility provides some insight into the influence of the active site environment.

5.2 The influence of the active site metal and the surrounding amino acid environment

XI suffers from radiation damage and an X-ray induced shift in the position of the active site metal atom (Chapter 4). Both XI and SOD are well-characterized proteins that diffract to high resolution (~1.2 Å). XI natively contains manganese and magnesium in its active site, both of which can be removed or exchanged, affecting its activity. Acidic residues, Asp and Glu, coordinate the active site metals. XI does not contain any disulfide bonds. SOD contains copper and zinc, coordinated by histidine residues and actively scavenges free radicals. It contains two disulfide bonds, one in each subunit of the dimer.

5.3 Experimentally determining the damage at metal sites

5.3.1 Xylose Isomerase

XI from *Strepomyces rubiginosus* was prepared as described in Chapter 4, section 4.3.1. EDTA dialysis was used to remove the native metals. XI was dialyzed in 50 mM EDTA for two hours, exchanging the EDTA solution 3 times. EDTA is a chelating agent, forming soluble, complex molecules with metal ions to remove the metal ion from the protein.

After dialysis, the protein was concentrated and purified using gel filtration chromatography at 4°C using a Superdex 200 HiLoad 16/60 column (GE Healthcare) to remove the metal-EDTA complexes. The purified protein was concentrated to 50 mg/ml and submitted to the HWI crystallization screening service which samples 1536 different biochemical conditions using the microbatch-under-oil method (Luft *et al.*, 2003). The experiments were imaged to identify promising conditions for further experimental optimization (hits). Several of these were obtained and the cocktails used were noted as metal containing or non-metal. A hit from the non-metal category was selected to optimize conditions for crystal growth. Large crystals (>0.3 x 0.3 x 0.3 mm) grew in about 1 week from the condition containing 0.1 M sodium bromide, 0.1 M sodium citrate pH 4.2 and 30% (w/v) PEG 20,000. To verify that the protein was metal free a complete room temperature X-ray dataset was collected on the home source, MicroMax 007 (Rigaku). Data were processed using Mosflm (Powell, 1999), CCP4 (Winn *et al.*, 2011), Refmac (Vagin *et al.*, 2004) and Phenix (Adams *et al.*, 2010a), with iterative model building using COOT (Emsley *et al.*, 2010). The active site was examined for the presence of metal.

Crystallization conditions containing a metal were selected for optimization. Initial hits from two conditions, (1) 0.01 M copper chloride, 0.1 M MES pH 6.5, 1.8 M ammonium sulfate and (2) 0.01 M zinc sulfate heptahydrate, 0.1M MES pH 6.5 and 25% polyethylene glycol 550 monomethyl ether, were used as starting points for optimization. The metal salt was replaced with other metal containing salts to introduce other metals. These included cadmium, manganese, cobalt, nickel, copper, and zinc. The crystals were optimized from the original hit using the batch under oil crystallization method again. Crystallization conditions are summarized in Table 5.1. A drop containing 2 µL of protein concentrated to 225 mg/mL was added to 2 µL of a precipitant solution, except for the conditions containing cadmium (2 µL protein: 3.5 µL cocktail) and copper (1.5 µL protein: 2 µL cocktail). For each metal replaced XI condition, two identical crystallization plates were set up; one plate was incubated at 14 °C and the other at 23 °C, to determine optimal temperature for each condition. The crystal quality was assessed based on size, dimensionality, singularity and absence of skin on the crystallization drop. The absence of skin on the drop leads to less crystal manipulation while mounting the crystals. The conditions that produced crystals of the highest quality based on these criteria for each metal complex were selected for diffraction. Since the effect of using a cryoprotectant had not been determined, about half of the crystals sent for remote data collection were cryoprotected using 20% glycerol. It was not clear if the addition of the cryoprotectant was needed, as the crystal froze clear without it. The crystal screening process determined the best crystals for data collection, based on low crystal mosaicity, diffraction limit and diffraction quality.

Table 5.1: Crystallization conditions for the metal replaced XI crystals used for diffraction studies.

Metal replaced XI	Crystallization temperature	Crystallization condition	cryoprotectant
XI-Cd	14 °C	0.01 M Cadmium chloride, 0.1 M MES pH 6.5, 1.8 M Ammonium sulfate	20% (v/v) glycerol
XI-Mn	23 °C	0.01 M Manganese chloride tetrahydrate, 0.1 M MES pH 6.5, 1.78 M ammonium sulfate	none
XI-Co	14 °C	0.01 M Cobalt chloride hexahydrate, 0.1 M MES pH 6.5, 1.82 M ammonium sulfate	20% (v/v) glycerol
XI-Ni	14 °C	0.01 M Nickel chloride hexahydrate, 0.1 M MES pH 6.5, 1.85 M ammonium sulfate	none
XI-Cu	14 °C	0.01 M Copper chloride, 0.1 M MES pH 6.5, 1.8 M ammonium sulfate	none
XI-Zn	23 °C	0.01 M Zinc sulfate heptahydrate, 0.1 M MES pH 6.5, 25% PEG 550 MME	none

Crystals were harvested using a nylon loop and cooled by plunging in liquid nitrogen. They were shipped to Stanford Synchrotron Radiation Laboratory (SSRL, Palo Alto, CA) where X-ray diffraction data were collected remotely on beamline 9-2 at 12.7 keV using an MAR325 CCD detector. Data for each crystal were collected in eight consecutive sets, exposing the same volume of the crystal for each dataset. The cross section of the beam (0.2 x 0.2 mm) matched the crystal dimensions, Table 5.2. The data collection settings for each metal metal replaced XI crystal are shown below in Table 5.2.

The strategy program BEST (Campbell, Bunn*, et al.*, 2006) was used to determine the optimum oscillation angle, exposure time, detector distance and coverage to obtain a full dataset with maximum completeness while minimizing the absorbed dose for each crystal. However, due to the different metals in the active site, it was problematic to achieve the same absorbed dose per dataset for each metal. Each metal has a different photoelectric cross section. A larger photoelectric cross section leads to an increased absorbed dose. The crystals differ only in the active site metal, but required a difference in absorbed dose of several orders of magnitude depending on the metal present and the amount of data needed for a complete dataset. The dose per dataset and corresponding cumulative absorbed dose for each crystal are shown in Table 5.3.

Table 5.2: X-ray data collection strategy for each metal replaced crystal of XI.

	Cadmium	Manganese	Cobalt	Nickel	Copper	Zinc
Crystal size (mm)	0.25 x 0.25 x 0.15	0.40 x 0.35 x 0.30	0.25 x 0.20 x 0.15	0.25 x 0.15 x 0.10	0.30 x 0.30 x 0.25	0.30 x 0.25 x 0.20
Detector Distance (mm)	150.0	138.8	236.2	218.9	150.0	150.0
Oscillation (°)	1	1	0.75	0.55	0.45	0.65
Exposure time (s)	2.00	2.00	2.00	2.17	2.00	2.00
# Images	83	66	147	126	167	104
Coverage (°)	83.00	66.00	110.25	69.30	75.15	67.60
Dose (MGy)	0.730	0.006	0.060	0.800	0.170	0.014
Dose rate (Gy/s)	4403	43	404	2907	494	66

Table 5.3: Resolution and absorbed doses (given to three significant figures) for each metal replaced crystal.

	Resolution (Å)	Dose per dataset (kGy)	Cumulative dose (kGy)
Cadmium	1.20	731	5848
Manganese	1.13	5.75	46
Cobalt	1.64	59.4	475
Nickel	1.56	800	6400
Copper	1.18	165	1320
Zinc	1.19	13.7	109

The flux on the beamline was calculated from an ion chamber reading before the crystal in the beam path. The dose was then calculated using this flux with RADDOSE (Murray *et al.*, 2005, Paithankar & Garman, 2010). Data were integrated with HKL2000 (Otwinowski, 1997) and reduced with Scala (Winn *et al.*, 2011) from the CCP4 suite.

ARP w/ARP (Perrakis *et al.*, 2001) was used for molecular replacement with PDB entry 1MUW as an initial search model (metal and water molecules removed). This model is the native 0.86 Å structure of XI from *streptomyces olivochromogenes* solved by Fenn et al. (Fenn *et al.*, 2004). The first and the eighth datasets were processed and structurally refined independently. The refinement was carried out using the PHENIX suite (Adams *et al.*, 2010a). The model was built iteratively using COOT (Emsley *et al.*, 2010) with anisotropic refinement following each build. The majority of the crystals diffracted to at least 1.2 Å resolution with the exception of XI-Co and XI-Ni, which diffracted to 1.64 and 1.56 Å, respectively. Studies with XI-Co were carried out to investigate whether or not radiation damage could be detected at this range of resolution. All the crystals were in the I222 spacegroup except the Xi-Ni. Because XI-Ni diffracted to a lower resolution and crystallized in a different spacegroup $P2_12_12$, it was excluded from the analysis. Different crystal contacts would have introduced another variable in the analysis of the data.

Isomorphous difference density maps Fo_8-Fo_1 were calculated and the difference density peaks were analyzed for each metal replaced structure. The ten most negative

peak values, in addition to the metal peak values, were determined and scaled to absorbed dose.

5.3.2 Superoxide Dismutase

Bovine superoxide dismutase was obtained from Sigma as a lyophilized powder (Catalog number S7571). The protein was reconstituted to 10 mg/ml in a 0.1 M MOPS pH 6.0 buffer. SDS-PAGE was run to verify the purity of the protein. The protein was submitted to the HWI crystallization screening laboratory (Luft *et al.*, 2003) for crystallization. The crystallization cocktail containing 0.1 M potassium carbonate, 0.1 M MES pH 6.0, 40 % (w/v) PEG 20,000 and 2.5 % (v/v) ethylene glycol produced the largest crystals (0.3 x 0.3 x 0.2 mm). These were scaled up using the batch under oil crystallization method with paraffin oil and 4 uL of protein to 2 uL of cocktail with no further optimization. Crystals were harvested using a nylon loop and cooled by plunging in liquid nitrogen. They were shipped to Stanford Synchrotron Radiation Laboratory (SSRL, Palo Alto, CA) where X-ray diffraction data were collected remotely on beamline 9-2 at 12.7 keV using an MAR325 CCD detector. Data for each crystal were collected in five consecutive sets, exposing the same area of the crystal for each dataset. Each dataset was collected at a wavelength of 0.954 Å, with a crystal to detector distance of 150 mm and 0.5° oscillation with a 2 second exposure time per image. The total absorbed dose for the full datasets was 120 MGy (24 MGy/dataset). Each dataset contained 360 images for a total of 180 degrees of data.

ARP w/ARP (Perrakis *et al.*, 2001) was used for molecular replacement with PDB entry 1Q0E, a 1.15 Å structure of copper-Zinc superoxide dismutase from *bos taurus* (Hough & Hasnain, 2003), as an initial search model. Before running molecular replacement, the metal ions and the water molecules were removed from the search model. Each dataset was processed and anisotropically refined independently using the PHENIX suite with riding hydrogens (Adams *et al.*, 2010a). The protein is a dimer in the asymmetric unit. The model was built iteratively using COOT (Emsley *et al.*, 2010).

5.4 Results

5.4.1 Global indicators of damage for XI

The data collected on XI-Cd experienced a 60% decrease in the overall signal-to-noise ratio (I/σ(I)) from the first dataset (0.73 MGy) to the last dataset (5.84 MGy). In the high resolution shell the decrease of 73% of I/σ(I) indicates the high resolution reflections were preferentially susceptible to damage, Table 5.4. The decrease in completeness in the high resolution shell from 90% to 66% also indicates the loss of high resolution data throughout data collection. The loss in completeness was not as extreme for any of the other crystals with completeness changing by -1%, 4%, 1%, and 3% for XI-Mn, Xi-Co, XI-Cu and XI-Zn, respectively. The decrease in overall I/σ(I) for the other crystals was 5, 9, 9 and 15%, for Mn, Cu, Zn and Co respectively. The decrease in I/σ(I) for the high resolution shell was 3, 5, 41 and 61% for Mn, Co, Cu and Zn, respectively. An overall increase in Wilson B factor for each crystal indicates that global damage is occurring, through global disorder, decreased diffraction intensity or increased noise in the

diffraction. With the exception of the cobalt containing XI, all data was collected to ~1.2 Å (Table 5.2). The structures were refined anisotropically, providing directional information for the fluctuations in atomic positions. The overall secondary and tertiary structure remained unchanged. The root-mean-squared displacements for the first versus the last datasets were insignificant (XI-Cd=0.057 Å, XI-Co=0.034 Å, XI-Cu=0.088 Å, XI-Mn=0.036 Å and XI-Zn=0.040 Å). Any damage present appears not to have caused large-scale structural changes.

Table 5.4: Data processing statistics for XI crystals containing different active site metal ions. The data shown is from the first and the eighth data sets for each metal replaced XI structure. Although the absorbed doses are different, each metal replaced XI shows similar global indicators of radiation damage; decrease in I/σ(I), increase in Wilson B factor, and increase in mosaicity.

	Cadmium		Manganese		Cobalt		Copper		Zinc	
Absorbed dose (MGy)	0.730	5.84	0.006	0.046	0.059	0.475	0.165	1.32	0.014	0.104
I/σ(I)	26.96 (6.09)	10.68 (1.63)	9.70 (1.63)	9.24 (1.38)	13.75 (8.09)	11.70 (7.69)	13.24 (5.02)	14.47 (2.95)	30.27 (15.18)	27.43 (5.90)
Compl. (%)	99 (90)	97 (66)	92 (59)	91 (58)	94 (87)	93 (91)	97 (76)	97 (77)	94 (94)	98 (97)
R_{sym} (%)	3.5 (19.9)	3.3 (35.8)	3.6 (39.0)	3.6 (51.8)	7.2 (16.7)	8.9 (20.0)	3.0 (9.38)	2.5 (19.1)	2.9 (13.5)	3.0 (16.4)
Average redund.	3.3	3.2	2.3	2.6	4.0	4.3	2.7	2.7	2.3	2.7
Wilson B ($Å^2$)	9.70	9.94	9.37	9.99	15.16	13.49	8.28	10.53	8.88	11.11
Average B ($Å^2$)	13.30	14.02	13.57	14.39	21.74	20.97	11.57	14.84	13.34	15.97
Mosaicity (°)	0.300	0.300	0.144	0.145	0.938	0.876	0.106	0.106	0.133	0.271

5.4.2 Specific damage in metal replaced XI crystals

Isomorphous Difference Density Maps (Fo_n-Fo_1) were used to visualize damage over the course of the collection of the consecutive datasets, as described in Chapter 4. The highest positive and negative 10 peaks from the Fo-Fo maps were recorded for each metal replaced XI structure and normalized to absorbed dose, shown in Table 5.5. The highest negative peak heights grow as a function of dose. The metal is either losing electrons (likely being oxidized) or being structurally displaced causing a reduction in scattering. In the case of Thr118, a large positive peak is observed, presumably from a gain of electrons or radicalization. Radical cations are trapped at 77 K (Swenson & Moulton, 1973). A systematic increase in scattering may be due to visualization of a trapped radical cation.

For each metal replaced structure, with the exception of XI-Co, the metal atom has one of the top 10 negative electron density peaks in the Fo-Fo map. XI-Co has negative density at -6.3 sigma at the metal site, the 27th most negative peak. The lower resolution of this structure (1.64 compared 1.2 Å) makes visualization of specific changes more difficult.

Table 5.5: Fo_8-Fo_1 peaks for metal positions and the remaining top ten peak heights scaled to absorbed dose present in each of the metal replaced XI structures. XI-Mn, XI-Zn, XI-Cu and XI-Cd are all of comparable resolution ~1.2 Å. XI-Co was collected to a lower resolution (1.6 Å).

	Mn	Zn	Cu	Cd	Co
Total absorbed dose (MGy)	0.05	0.10	1.32	5.84	0.47
Metal-387(A)	-120.00	-52.21	-55.21	-10.82	-13.43
Metal-387(B)	-	-84.71	-8.71	-	-
Metal-388	-264.60	-174.52	-27.33	-9.06	9.79
Average	-192.30	-137.15	-30.42	-9.94	-1.82
Standard deviation	102.25	73.73	23.40	1.24	16.41
Thr-118	347.60	121.54	6.85	2.47	28.74
Met-157 SD	-259.20	-338.65	-15.44	-2.27	-12.89
Met-369 SD	-407.20	-227.88	-13.20	-3.04	-22.40
Met-379 SD	-374.60	-185.77	-12.24	-2.80	-16.60
Asp-100 OD2	-333.80	-168.94	-10.38	-2.76	-18.00
Asp-100 OD1	-327.80	-161.83	-13.05	-2.89	-22.72
Glu-140 OE2	-278.00	-159.04	-11.10	-2.59	-18.28
Lys-148 NZ	-287.00	-122.12	-10.17	-2.30	-17.89
Asn-121 ND2	-163.00	-83.85	-5.63	-1.43	-17.45
Glu-372 OE2	-252.20	-113.46	-9.83	-2.25	-15.81
Ala-261 O	-225.60	-113.17	-7.97	-1.81	-15.70
Average	-290.84	-167.47	-10.90	-2.41	-17.77
Standard deviation	72.30	73.26	2.80	0.51	2.98

In addition to the specific damage of the metal atoms, the sulfur atoms of methionine residues are preferentially damaged compared to the non-sulfur containing residues. Met369 and Met379, in particular, exhibit a decrease in electron density with increased absorbed dose in all of the metal-replaced structures. Asp100 and Thr118 also displayed a loss of density in the native XI structure. This observation of characteristics of radiation damage for residues that are not involved in the enzyme's mechanism, are not located in the active site and are not labile residues can be explained. Chapter 3 suggests that Asp is susceptible to multi-track damage and Thr residues are less susceptible than acidic side chains, sulfur containing residues and Tyr residues. Both Asp100 and Thr118 are solvent accessible making them more susceptible to solvent radical species than residues that are not accessible to the solvent. Thr118 is ~8 Å away from Thr89, which is involved in stabilizing the ring form of the substrate during the ring binding step of the XI mechanism. Although the electron difference density peak heights differ for each metal replaced XI crystal, the damage is localized in similar locations; on the Met, Asp and Glu residues. Unfortunately it is not possible to quantitatively or accurately compare the damage between different metals as a function of dose with the data presented here. There is a difference in both the single data set and cumulative absorbed dose for each sample. There is an overlap in absorbed dose between the different metals, Table 5.6, could provide some information, but in hindsight, the ideal experiment was not performed. Ideally, the same absorbed dose for each metal replaced sample would allow a quantitative assessment of the radiation damage as a function of dose.

Table 5.6: Datasets with comparable approximate absorbed doses that could be used to compare the damage.

Approx. absorbed Dose (kGy)		
10	Zn (D1)	Mn (D2)
25	Zn (D2)	Mn (D5)
40	Zn (D3)	Mn (D7)
50	Co (D1)	Mn (D8)
55	Co (D1)	Zn (D4)
150	Cu (D1)	Co (D2)
150	Co (D2)	Zn (D8)
300	Cu (D2)	Co (D5)
500	Co (D8)	Cu (D3)
700	Cd (D1)	Cu (D4)

5.4.3 Active site damage in metal replaced XI crystals

The metal replaced structures differ only in the composition of metal in the active site. Native XI contains Mn and Mg at M1 and Mn at M2. The native XI M2 metal has three configurations, or metal positions. In the metal replaced structures, M2 has a varying number of configurations (3 for XI-Cu and XI-Zn, 2 for XI-Cd and 1 for XI-Co and XI-Mn). XI-Co, with a resolution of 1.64 Å, does not show enough detail to determine if there is an alternate configuration for M2. For the other metal replaced structures, at ~1.2 Å resolution, there is a good fit to the density and no unexplained regions. The active site residues do not display alternate conformations. The position of the metal atoms and active site water molecules do fluctuate with increased dose. This shift in position of active site metal atoms and water molecules is similar to that observed for the native XI data.

Observations of the Fo-Fo maps (Figure 1-6) show that the active site damage is localized to the metal atoms and the carboxyl groups of the acidic active site residues. Changes in the position, occupancy, B factor of the metal atom, and binding distances also occur. Given identical doses, these values would be compared and a quantitative assessment of damage associated with each metal could be made. While the differences in absorbed doses prevent this, there is a clear trend of increased negative peak height in the Fo_8-Fo_1 map with increased absorbed dose. A qualitative assessment of damage for each metal replaced structure is described in detail below.

XI containing cadmium

The cadmium dataset experienced the highest cumulative absorbed dose of the 5 metal replaced structures, 5.85 MGy. In the first dataset, cadmium occupies M1 and M2 (in two configurations). In the last dataset, there is only one configuration of M2, which lies between the positions of the two configurations in the first dataset, Figure 5.1. The increased absorbed dose may induce a shift of M2 towards the single position in the last dataset. There are four changes in bond distances to M2 because of this listed in Table 5.6. These are M1-M2a (0.18 Å), M2a-His219 (-0.19 Å), M2a-Asp256 (0.16 Å) and M2a-Asp254 (-0.18 Å).

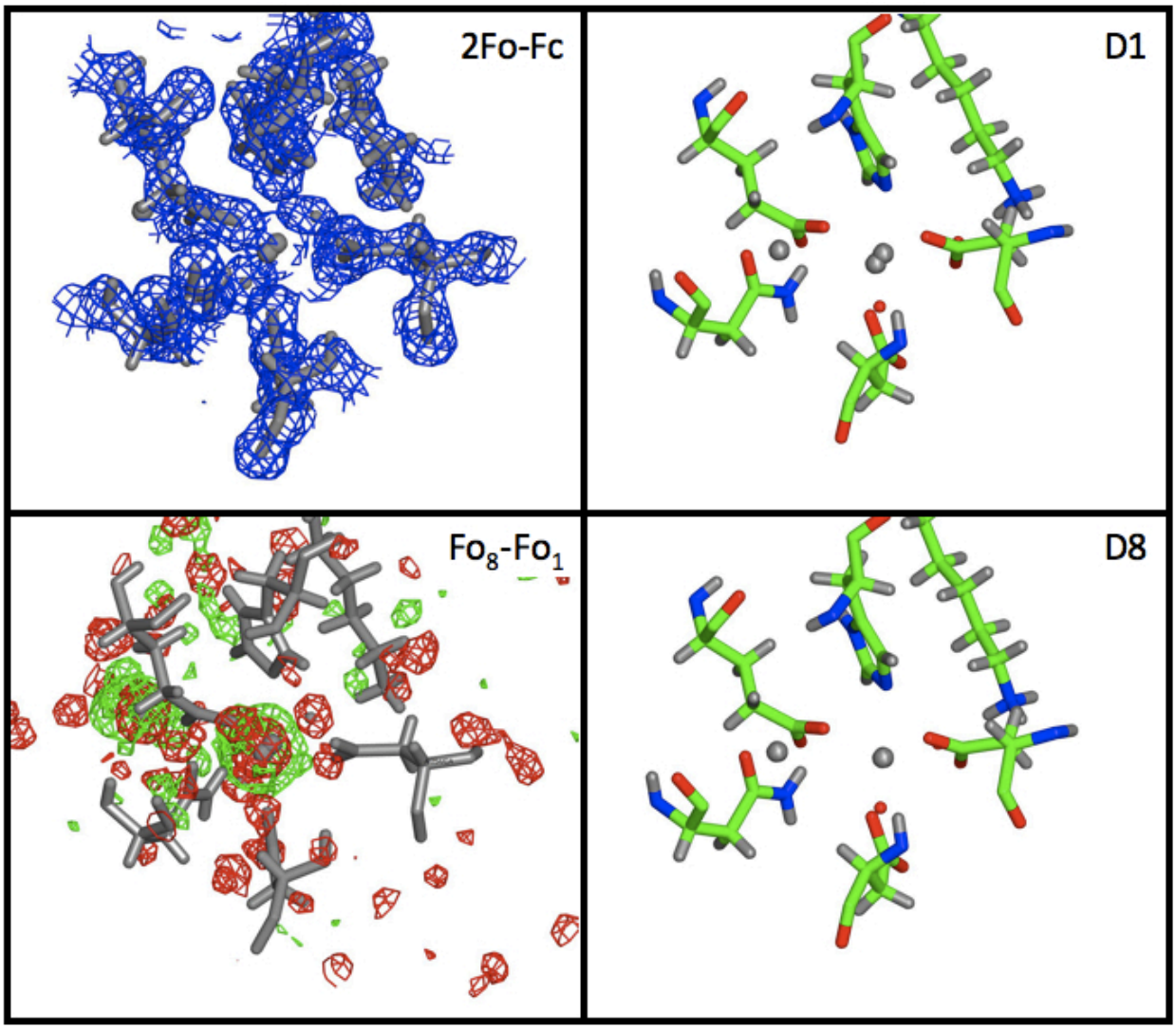

Figure 5.1: The active site of XI containing cadmium. 2Fo-Fc maps contoured at 1 sigma indicate that the active site density is well modeled. Specific active site damage is shown in the Fo_8-Fo_1map contoured at +/- 5 sigma. The second column represents the structures from the first (0.73 MGy) and last dataset (5.84 MGy). In the first dataset there are two configurations of M2, in the eighth dataset there is only one configuration of M2.

XI containing manganese

The manganese dataset experienced the lowest cumulative absorbed dose of the 5 metal replaced structures, 0.05 MGy. XI-Mn showed little change over the course of the data collection. There are no significant (>0.15 Å) differences in binding distances, amino acid positions or metal position for XI-Mn. The Fo-Fo maps show a decrease of 3.2 to 6.0 sigma in the electron density on the carboxyl groups of the acidic side chains.

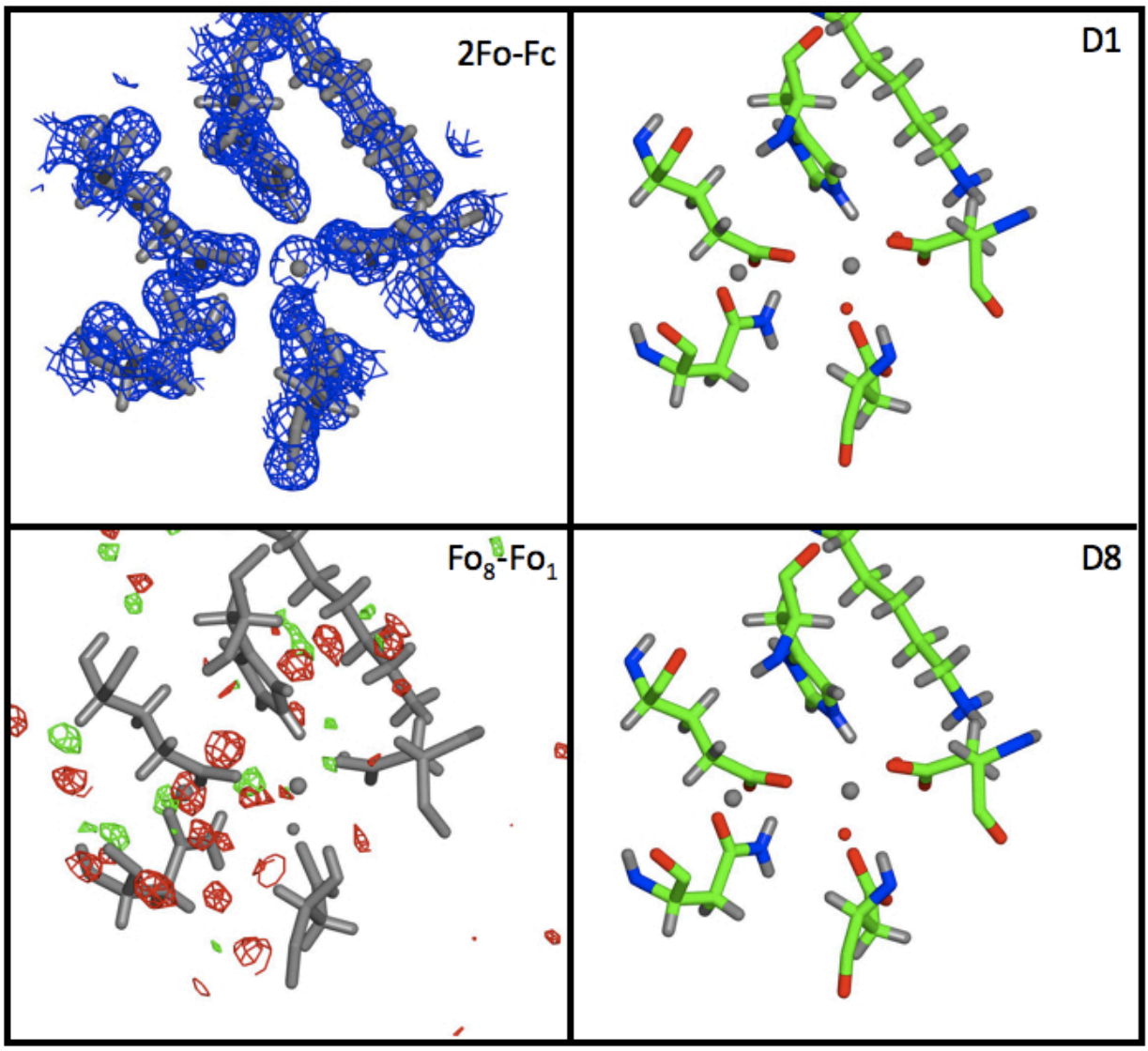

Figure 5.2: The active site of XI containing magnanese. 2Fo-Fc maps contoured at 1 sigma indicate that the active site density is well modeled. Specific active site damage is shown in the Fo_8-Fo_1map contoured at +/- 5 sigma. The second column represents the structures from the first (0.006 MGy) and last dataset (0.046 MGy). In both datasets there is a single position for M2.

XI containing cobalt

The active site structure of XI-Co showed little change with increased absorbed dose up to 0.0475 MGy. The position of the active site water, near M1 in XI-Co is the only obvious structural change in this data. The binding distance of the active site water to M1 decreases from 3.58 to 2.26 Å, placing it in closer proximity to M1. Other than this water, the bond lengths of the residues coordinating the metal ions remain stable (±0.03 Å). This agrees with the Fo_8-Fo_1 map for XI-Co, showing little difference between the datasets.

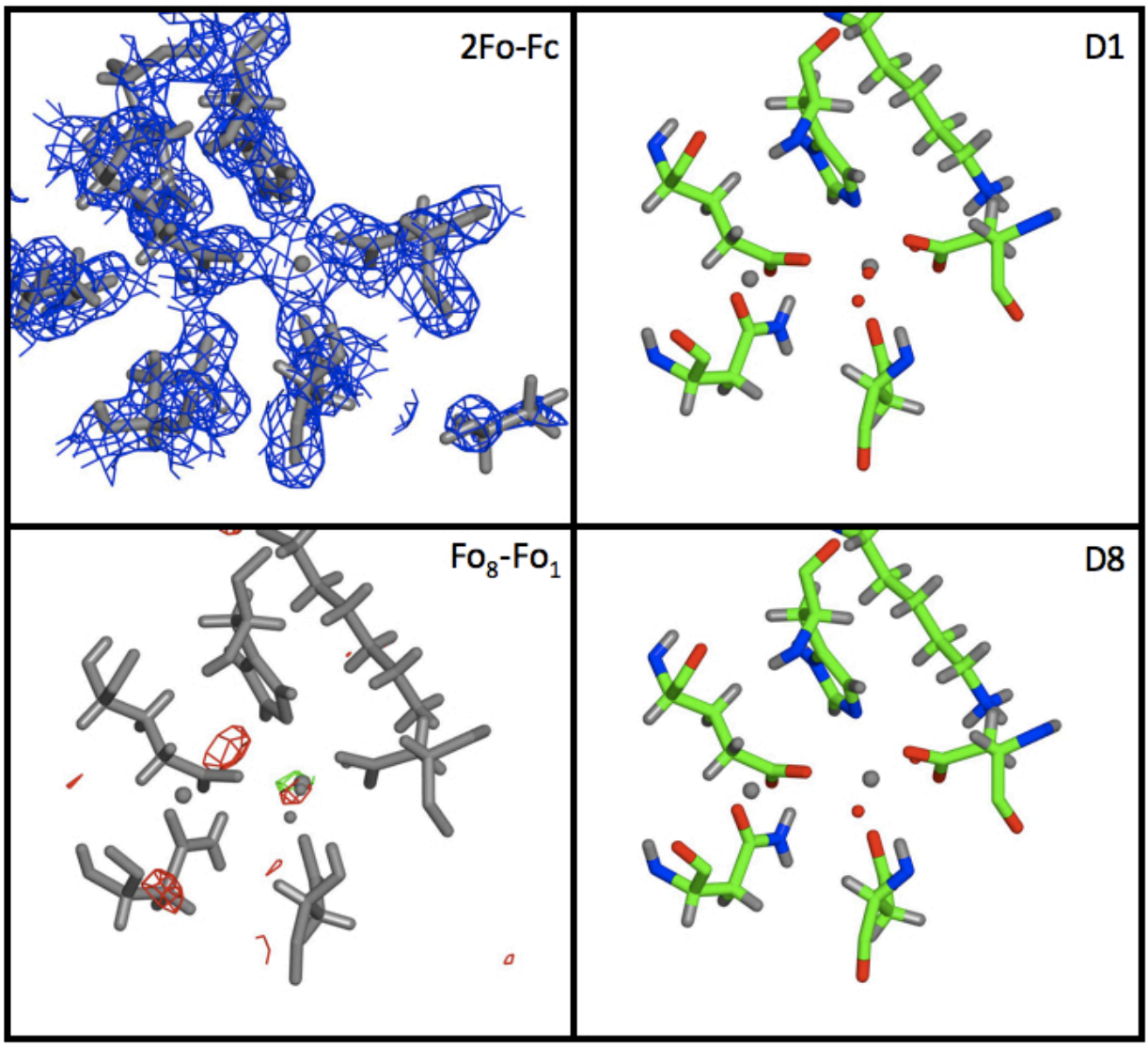

Figure 5.3: The active site of XI containing cobalt. 2Fo-Fc maps contoured at 1 sigma indicate that the active site density is well explained. Specific active site damage is shown in the Fo_8-Fo_1map contoured at +/- 5 sigma. The second column represents the structures from the first (0.059 MGy) and last dataset (0.475 MGy). In both datasets there is a single position for M2.

XI containing copper

XI-Cu retains the same number of configurations of M1 (2) and M2 (3) in the first and eighth datasets, this metal replaced structure has the most changes in binding distances to M1 and M2, with 19 metal-side chain bond lengths differing over 0.3 Å in the first dataset versus the eighth dataset. This represents the greatest number of changes in M1 and M2 binding distances of any other metal replaced structure in this study. XI-Cu has the highest increase in B factor for both M1 (+97% for Mg and +149 % for Cu) and M2 (M2a +204%, M2b -67% and M2c +96%). With a cumulative absorbed dose of 1.32 MGy, this is the second highest absorbed dose, only second to XI-Cd (5.85 MGy). The Fo_8-Fo_1 map for XI-Cu contains the most difference density, compared to the other Fo_8-Fo_1 maps (contoured at 5 sigma) calculated for the other metal replaced structures, indicating XI-Cu experiences the most radiation-induced changes. The radiation-induced changes in M2 position, occupancy and B factor for XI-Cu are similar to the radiation-induced changes in native XI (5.6 MGy cumulative absorbed dose). The photoelectric cross sections at 12 keV for manganese in native XI is 91.5 cm^2/gm compared to copper at 134.4 cm^2/g. The damage is comparable for XI-Cu with a lower absorbed dose and a larger photoelectric cross section to XI with the higher absorbed dose and smaller photoelectric cross section. While a very qualitative result, reduction chemistry aside, this suggests that radiation chemistry effects on the metal and surrounding environment are predictable, based on the metal atom contained in the active site.

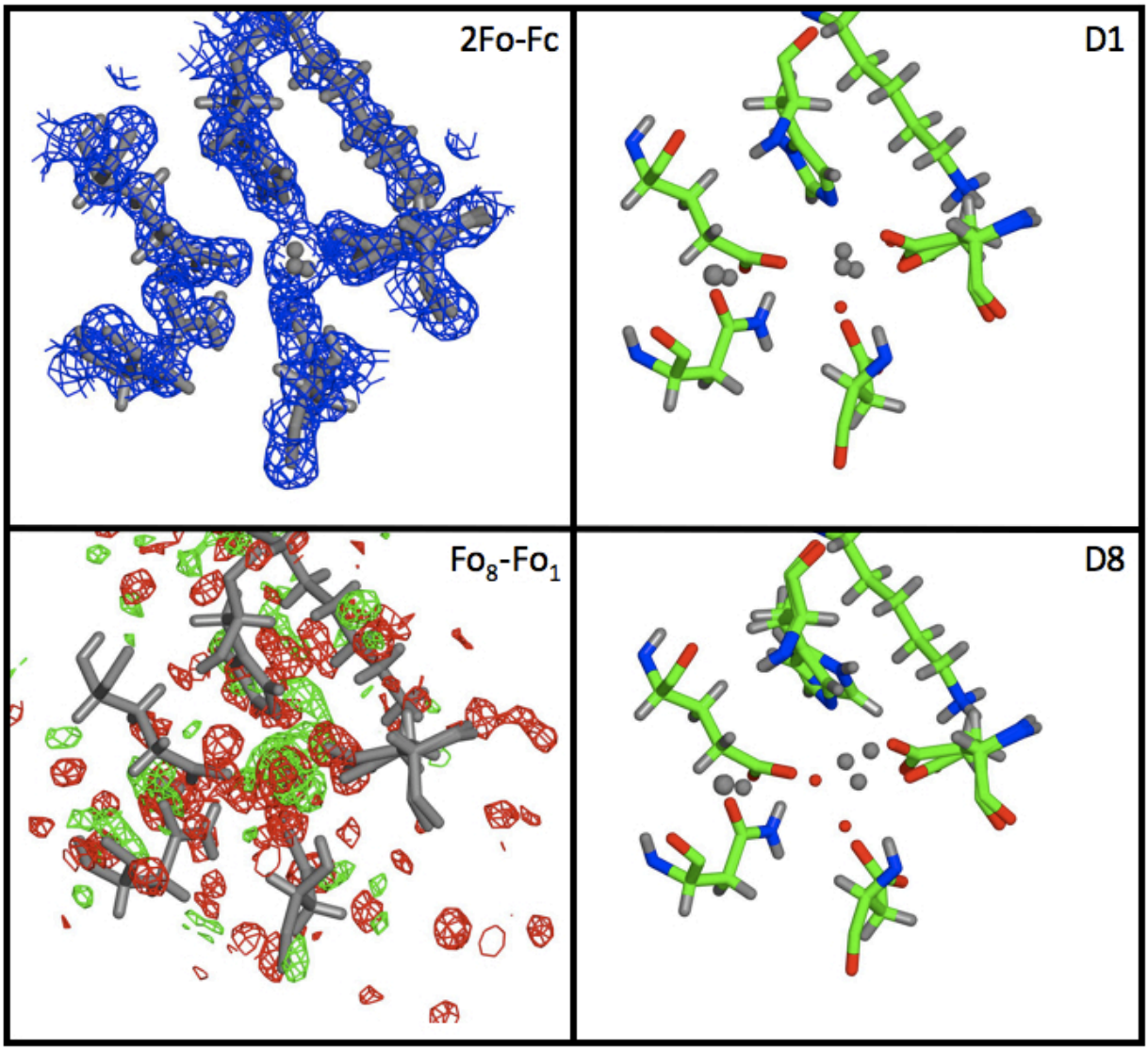

Figure 5.4: The active site of XI containing copper. 2Fo-Fc maps contoured at 1 sigma indicate that the active site density is well explained. Specific active site damage is shown in the Fo_8-Fo_1map contoured at +/- 5 sigma. The second column represents the structures from the first (0.165 MGy) and last dataset (1.32 MGy). In both datasets there are three configurations for M2.

XI containing zinc

Analysis of the metal sites in XI-Zn shows an increase in B factor for both M1 and M2, with average increases of 5.80 and 4.02 $Å^2$, respectively. M2 changes in position, shifting closer to His219 and Asp256, which in turn affects the corresponding binding distances, occupancy and B factor. In the first dataset (0.014 MGy) the occupancies of M2a, M2b and M2c are 38, 44 and 17 %, respectively. By the eighth dataset (0.104 MGy) the occupancies are 39, 41, and 21%, indicating a shift toward M2c. The B factors also increase, by 29, 37 and 63% of M2a, M2b and M2c respectively, when compared to the first dataset. With the shift in position and occupancy, M2c bonds to His219 in a shorter bond (2.23 vs. 1.59 Å). Asp256 develops closer binding distances with both M2a and M2b in the eighth dataset. M2b loses coordination with Glu216 with bond length increasing to 2.23 Å from 1.93 Å.

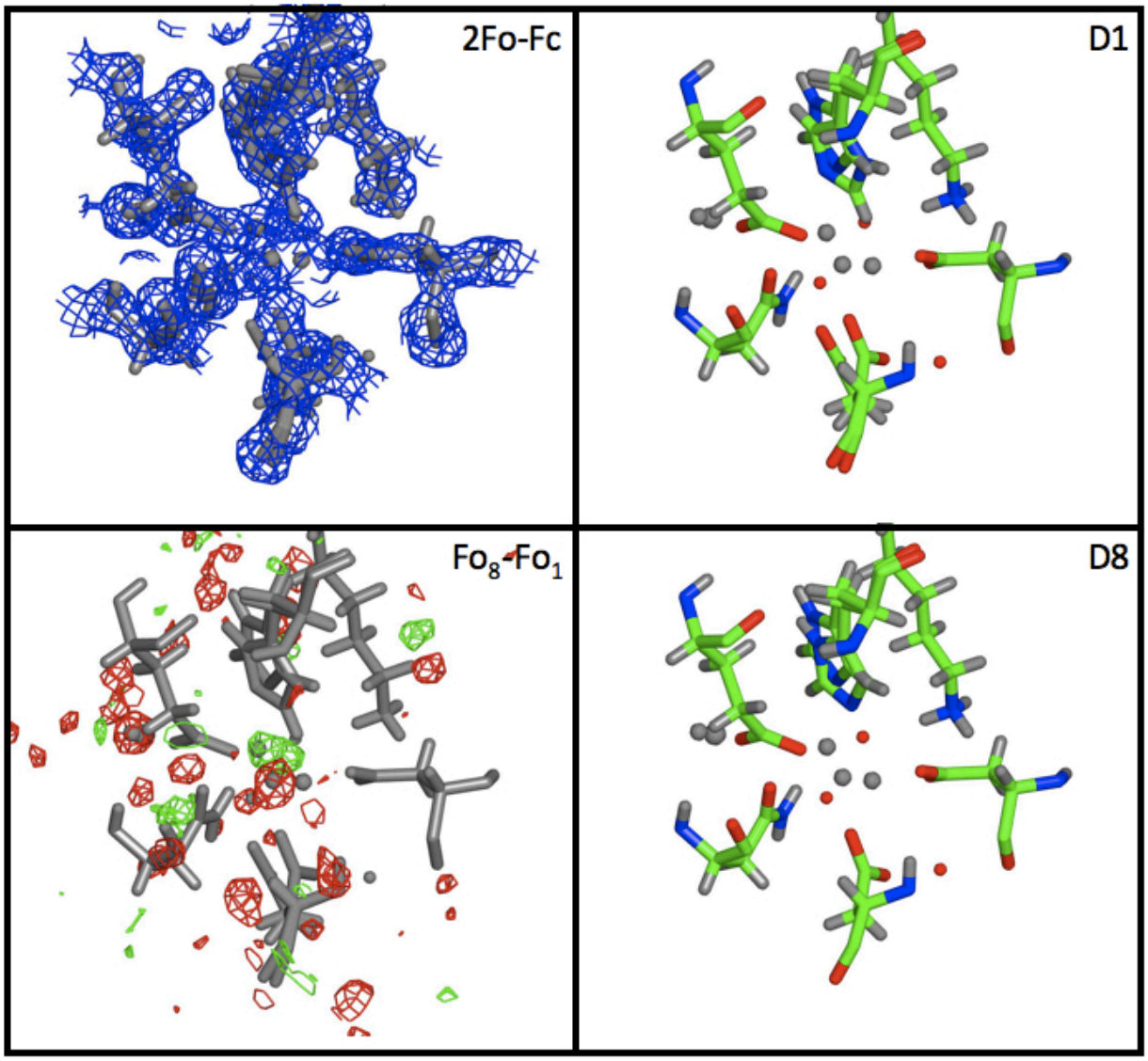

Figure 5.5: The active site of XI containing zinc. 2Fo-Fc maps contoured at 1 sigma indicate that the active site density is well explained. Specific active site damage is shown in the Fo_8-Fo_1map contoured at +/- 5 sigma. The second column represents the structures from the first (0.014 MGy) and last dataset (0.109 MGy). In both datasets there are three configurations for M2.

The position, B factor, occupancy, and binding distances for metals were tabulated for the first and the last dataset (Tables 5.7-5.9). The structure of the active site, labeled with residues is shown in Chapter 4.

Table 5.7: Metal properties (coordinates, B factor and occupancy) and binding distances to M1 & M2 for XI-Co and XI-Mn for the first and last dataset. These structures contain a single configuration of both M1 and M2. Changes in distance larger than 0.15 Å are shaded.

	Co 1	Co 8	Change in distance (Å)	Mn 1	Mn 8	Change in distance (Å)
M1 xyz	12.23 35.01 -8.14	12.23 35.03 -8.13		12.16 34.96 -8.05	12.19 34.99 -8.06	
M1 B factor	17.55	16.58		8.58	9.90	
M1 occ	0.63	0.60		0.87	0.88	
M1-GLU 216 OE1	2.18	2.18	0.00	2.12	2.13	0.01
M1-ASP 286 OD2	2.13	2.10	-0.03	2.11	2.11	0.00
M1-ASP 244 OD2	2.22	2.22	0.00	2.16	2.15	-0.01
M1-GLU 180 OE2	2.21	2.21	0.00	2.13	2.13	0.00
M1-EDO O1	2.36	2.37	0.01	2.29	2.27	-0.02
M1-H2O 520	3.58	2.26	-1.32	3.92	3.91	-0.01
(M1)-(M2)	5.09	5.09	0.00	4.87	4.90	0.03
M2 xyz	7.56 36.46 -6.71	7.57 36.47 -6.70		7.65 36.26 -6.75	7.65 36.28 -6.73	
M2 B factor	16.12	15.07		9.57	10.53	
M2 occ	1.00	1.00		0.61	0.62	
M2-HIS 219 NE2	2.24	2.25	0.01	2.53	2.56	0.03
M2-GLU 216 OE2	2.07	2.07	0.00	2.04	2.05	0.01
M2-H2O	2.14	2.11	-0.03	2.18	2.18	0.00
M2-ASP 256 OD1	2.09	2.08	-0.01	2.28	2.28	0.00
M2-ASP 254 OD2	2.10	2.09	-0.01	2.27	2.26	-0.01
M2-ASP 254 OD1	2.17	2.16	-0.01	2.27	2.27	0.00

Table 5.8: Metal properties (coordinates, B factor and occupancy) and binding distances to M1 & M2 for XI-Cd for the first and last dataset. M1 is occupied by cadmium in both datasets, M2 is occupied by 2 configurations of cadmium in the first dataset and a single configuration of cadmium in the eighth dataset. Changes in bond length greater than 0.15 Å are shaded.

	Cd 1	Cd 8	Change in Å
M1-Cd (xyz)	-11.99 -34.98 -8.13	-12.04 -35.02 -8.12	
M1-Cd B factor	7.32	8.61	
M1-Cd occupancy	0.89	0.81	
Cd-E216 OE1	2.27	2.27	0
Cd-D286 OD2	2.27	2.25	-0.02
Cd-D244 OD2	2.23	2.24	0.01
Cd-E180 OE2	2.26	2.22	-0.04
Cd-EDO	2.4	2.41	0.01
Cd-H20	3.91	3.93	0.02
M1(Cd)-M2a	4.39	4.57	0.18
M1(Cd)-M2b	4.58		
M2a (xyz)	-50.83	-50.72	
M2b (xyz)		-7.8 -36.16 -6.72	
M2a B factor	5.5	8.33	
M2b B factor	7.77		
M2a occupancy	0.28	0.86	
M2b occupancy	0.72		
M2a-H219 NE2	2.6	2.41	-0.19
M2a-E216 OE2	2.27	2.27	0
M2a-H2O	2.15	2.29	0.14
M2a-D256 OD1	2.18	2.34	0.16
M2a-D254 OD2	2.52	2.4	-0.12
M2a-D254 OD1	2.63	2.45	-0.18
M2b-H219 NE2	2.3		
M2b-E216 OE2	2.29		
M2b-H2O	2.4		
M2b-D256 OD1	2.42		
M2b-D254 OD2	2.3		
M2b-D254 OD1	2.37		

Table 5.9: Metal properties (coordinates, B factor and occupancy) and binding distances to M1 for XI-Cu and XI-Zn for the first and last dataset. In both cases, magnesium and either copper or zinc occupies M1. Changes in bond length greater than 0.15 Å are shaded. XI-Cu and XI-Zn both have similar active site geometry to native XI, with magnesium and copper or zinc at M1 and three configurations of copper or zinc at M2.

	Cu 1	Cu 8	Change in distance (Å)	Zn 1	Zn 8	Change in distance (Å)
M1-Mg (xyz)	12.24 35.50 -8.62	12.31 35.62 -8.67		-12.30 -34.69 -8.18	-12.37 -34.06 -7.65	
M1-X (xyz)	12.34 34.91 -8.14	12.40 34.85 -8.01		-12.24 -35.60 -8.54	-12.27 -34.90 -8.44	
M1-Mg B factor	9.44	18.62		14.28	20.39	
M1-X B factor	7.96	19.79		9.50	14.98	
M1-Mg	0.66	0.59		0.59	0.56	
M1-X	0.34	0.41		0.41	0.44	
Mg-E216 OE1	1.80	1.74	-0.06	2.50	2.50	0.00
Mg-D286 OD2	2.30	2.38	0.08	1.95	1.94	-0.01
Mg-D244 OD2	1.98	2.00	0.02	2.65	2.81	0.16
Mg-E180 OE2	2.16	2.50	0.34	1.92	1.95	0.03
Mg-EDO	3.03	3.08	0.05	-	-	0.00
Mg-H2O	4.12	3.11	-1.01	3.00	3.03	0.03
X-E216 OE1	2.19	2.30	0.11	1.94	1.95	0.01
X-D286 OD2	2.03	2.05	0.02	2.18	2.15	-0.03
X-D244 OD2	2.30	2.46	0.16	2.00	2.03	0.03
X-E180 OE2	2.04	2.13	0.09	2.15	2.14	-0.01
X-EDO	3.86	2.18	-1.68	-	-	0.00
X-H20	3.45	2.32	-1.13	3.78	3.74	-0.04
M1(Mg)-M2a	5.03	5.36	0.33	5.43	5.35	-0.08
M1(Mg)-M2b	5.18	4.27	-0.91	4.85	4.78	-0.07
M1(Mg)-M2c	4.42	5.05	0.63	3.84	3.79	-0.05
M1(X)-M2a	5.10	5.96	0.86	5.58	5.58	0.00
M1(X)-M2b	5.18	4.38	-0.80	4.84	4.64	-0.20
M1(X)-M2c	4.32	4.86	0.54	3.97	3.99	0.02

Table 5.10: Metal properties (coordinates, B factor and occupancy) and binding distances to M2 for XI-Cu and XI-Zn for the first and last dataset. In both cases, M2 is occupied by three configurations of the metal. Changes in bond length greater than 0.15 Å are shaded.

Mn2a (xyz)	7.62 36.49 -6.89	7.33 36.51 -6.88		-7.18 -35.48 -6.25	-7.18 -35.47 -6.26	
Mn2b (xyz)	7.52 36.13 -6.58	8.87 36.04 -6.17		-7.69 -35.83 -7.09	-7.72 -35.85 -7.03	
Mn2c (xyz)	8.66 35.96 -6.08	8.49 36.00 - 5.38		-8.21 -35.70 -6.49	-8.91 -35.71 -6.49	
Mn2a B factor	6.82	20.72		9.43	12.13	
Mn2b B factor	41.41	13.61		13.38	18.29	
Mn2c B factor	14.33	28.09		7.10	11.56	
M2a occupancy	0.52	0.48		0.38	0.39	
M2b occupancy	0.27	0.17		0.44	0.41	
M2c occupancy	0.21	0.35		0.17	0.21	
M2a-H219 NE2	2.25	3.01	0.76	3.17	3.22	0.05
M2a-E216 OE2	1.94	2.16	0.22	2.91	2.91	0.00
M2a-H2O	2.36	2.40	0.04	2.14	2.12	-0.02
M2a-D256 OD1	2.11	2.21	0.10	3.04	2.20	-0.84
M2a-D254 OD2	1.94	1.54	-0.4	1.83	1.84	0.01
M2a-D254 OD1	2.43	2.24	-0.19	2.27	2.26	-0.01
M2b-H219 NE2	2.33	1.89	-0.44	3.03	3.02	-0.01
M2b-E216 OE2	2.38	2.38	0.00	1.93	2.23	0.30
M2b-H2O	2.13	2.07	-0.06	2.07	2.18	0.11
M2b-D256 OD1	2.21	3.65	1.44	2.43	1.93	-0.50
M2b-D254 OD2	1.59	2.55	0.96	2.86	2.85	-0.01
M2b-D254 OD1	2.36	3.74	1.38	2.67	2.66	-0.01
M2c-H219 NE2	1.68	1.95	0.27	2.03	1.59	-0.44
M2c-E216 OE2	2.54	3.12	0.58	2.16	2.12	-0.04
M2c-H2O	1.86	2.55	0.69	1.85	1.97	0.12
M2c-D256 OD1	3.33	3.96	0.63	3.23	3.21	-0.02
M2c-D254 OD2	2.37	2.15	-0.22	3.29	3.27	-0.02
M2c-D254 OD1	-	-		3.59	3.57	-0.02

X-ray crystallographic data cannot give direct information for metal coordination, however the binding distances of the metals to the surrounding residues can be compared to a database of known metal-donor atom target distances (Harding, 2006) and the coordination can be inferred. A residue is considered to be coordinated to a metal atom if its bond length is within the target distance. These distances are described below. For all XI crystals studied, based on the bond distances of active site residues to the metal atoms, M1 did not appear to change coordination state over the course of the data collection. However, based on bond lengths, the coordination of M2 did appear to change for XI-Cd, XI-Cu and XI-Zn, but not for XI-Co and XI-Mn. The active site geometry of XI-Cd changed more than any other metal replaced XI. M2 had two configurations of Cd in the first dataset and only one in the eighth dataset. With the loss of the second position for Cd in the eighth dataset, the Asp256-Cd bond length increases from 2.18 Å to 2.34 Å, indicating it has undergone a change in coordination. The Cd-O bond length is expected to be between 2.25-2.29 Å. M1 in XI-Cu was initially bound to Glu216, Asp244 and Glu180. The bond length for M1-E180 increased by 0.34 Å with increased absorbed dose breaking that bond. M2b and M2c (XI-Cu) also had increases in bond lengths for Asp254 (0.96 Å) and the active site water molecule (0.69 Å), respectively. This increase in bond length exceeds the target distance for Cu-O of 1.99-2.13 Å indicating that these atoms are likely no longer coordinated to the copper atom. XI-Zn had an increase in bond length of 0.3 Å for M2b-E216, indicating that this residue is likely no longer coordinated to the Zn atom.

XI-Cu had three configurations of M2 in both datasets, however, the bond lengths from M2 to Glu216, Asp256 and the active site water increased in the eighth dataset by a distance of more than 2.00 Å, the target distance for Cu-O. A decrease in bond length indicating tighter bonding occurred for Asp254 and His219. This was similar to the shift in position for M2 in native XI with M2a moving towards M2b and the resulting changes in bond lengths. Similarly, XI-Zn changes coordination with M2b losing a binding partner His219 and binding more tightly with Asp256 and His219. Both XI-Cu and XI-Zn with three positions for M2 show an X-ray induced shift in position for M2, similar to the shift shown in the previous chapter. Binding distances alone cannot give the coordination and redox state of the metal atom, but can provide a comparative assessment. In this case they imply changes in coordination with increased absorbed dose.

The active site amino acid residues remain stable in position with absorbed dose. The position of the M2 site varies between structures. This could be due to the influence of the metal properties: ionic radius, possible coordination state and metal bond distances, Table 5.11. Each of the metal atoms in the data presented appears to be coordinated by four residues. The damage to the metal in the active site appears to be dependent on total absorbed dose, with the exception of XI-Co, which does not follow the same dose dependent reduction in apparent electron density loss. This may be due to the lower resolution of the XI-Co data. The reduced resolution may be insufficient to visualize the reduction in apparent electron density. We would expect it to behave in the same dose dependent manner as the other metal replaced XI structures, with data at a comparable resolution. The protein residues behave as expected (decarboxylation of acidic side

chains, loss of the hydroxyl group on tyrosine, carbon-sulfur bond cleavage in methionine) and the affects, like that to the metal, is also dose dependent.

Table 5.11: Metal properties that may influence position of M2.

	Cadmium	Manganese	Cobalt	Copper	Zinc
atomic radius (Å)	1.49	1.27	1.25	1.28	1.34
possible coordination number	4, 6, 8,12	4, 6, 8	4, 6, 8	4, 6	4, 6, 8
metal bond distance (Å)	2.25-2.29	2.15-2.21	2.05-2.14	1.99-2.13	1.99-2.09

Some of the dose points overlap and allow a structural comparison. The active site superposition of the first dataset of XI-Cu (0.165 MGy) with the eighth dataset of XI-Zn (0.110 MGy), Figure 5.6, shows the active site residues aligning well, with the exception of His219 and Asp254 as mentioned in the previous section. The three positions of the metal atom do not align well. This may be due to the difference in ionic radii. The superposition of the first dataset of XI-Co (0.059 MGy) with the eighth dataset of XI-Mn (0.046 MGy) shows a better alignment of both active site residues and the single position for M2.

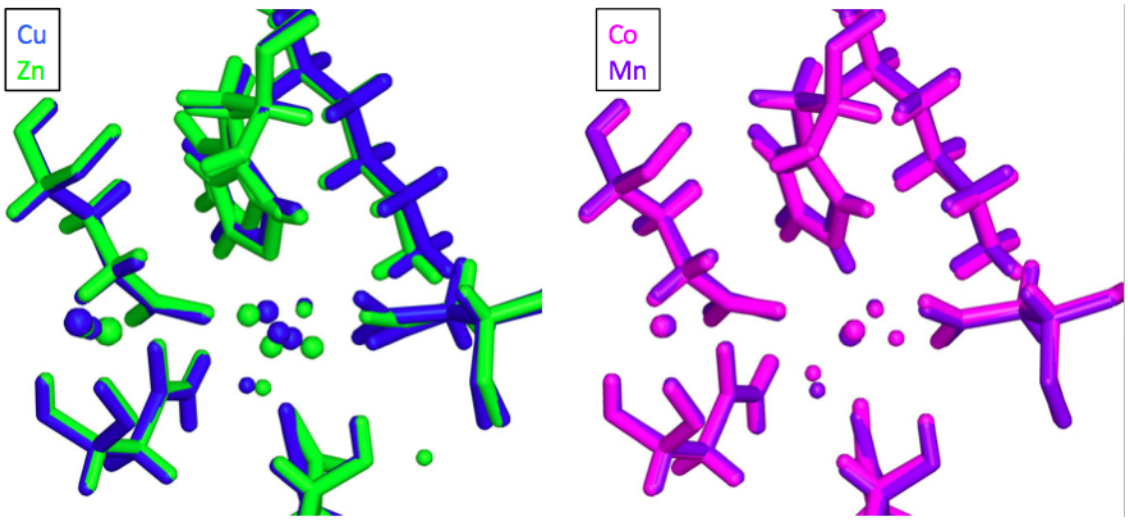

Figure 5.6: Active site superposition for metal replaced XI structures with comparable absorbed doses. Dataset 1 for XI-Cu (in blue) with D=0.165 MGy, superpositioned on to the structure of dataset 8 of XI-Zn (in green) with D=0.110 MGy. Dataset 1 of XI-Co (in pink) with D= 0.059 MGy, superpositioned on to the structure of XI-Mn (in purple) with D= 0.046 MGy.

Comparing the superposition of first dataset of XI-Cu (0.165 MGy) and the eighth dataset of XI-Zn (0.109 MGy) with the eighth dataset of XI-Cu (1.32 MGy), a ten-fold increase in absorbed dose, we observed a change in position for His219, Asp254 and M2, Figure 5.7. M2c shifts towards His219, His219 moves away from the active site, while Asp254 is closer to M2a, M2b and M2c. This could be interpreted as a change in coordination, due to the increase in bond length of M2a to His219 of 0.76 Å. The other active site residues superpose well.

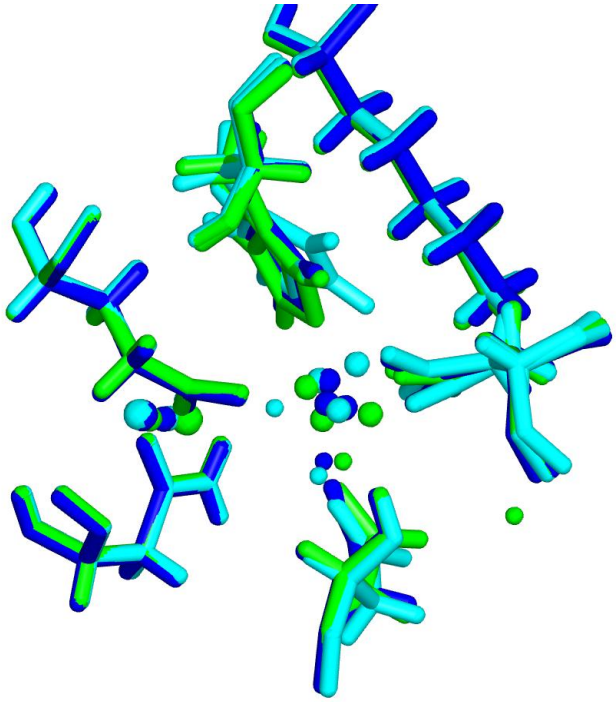

Figure 5.7: Active site superposition for metal replaced XI structures. Dataset 1 for XI-Cu (in blue) with D=0.165 MGy, superpositioned on to the structure of dataset 8 of XI-Zn (in green) with D=0.110 MGy and dataset 8 of XI-Cu with D=1.32 MGy (in cyan). Increase in absorbed dose changes the coordination of M2 and alters the position of His219 and Asp254.

The beamline used for data collection was equipped with an energy sensitive fluorescence detector. This allows for online fluorescence scans to be conducted. With appropriate instrumentation this can be used to detect a change in the metal's redox state. While fluorescence correctly identified the metals present, the energy discrimination was not sensitive enough to detect changes to their redox state. An example of one of these scans is shown in Figure 5.8. In addition to the metal present in the active site, other trace metals were also present in the crystal, at a much lower concentration than the active site metal. The trace metal content differed for each metal replaced crystal. Metals observed were copper, iron and zinc. This could be due to trace metals in the protein, crystallization cocktail or the cryoprotectant. The iron signal is likely due to some scattering from the steel pin used to hold the sample loop.

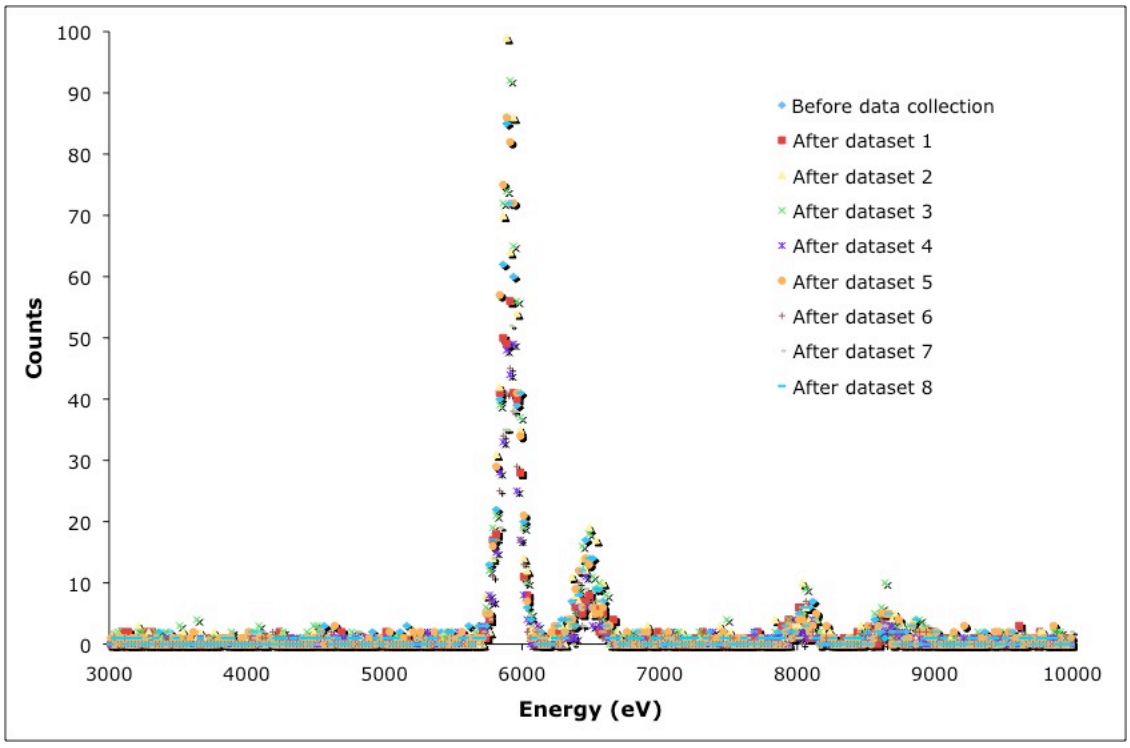

Figure 5.8: Enlarged excitation scan of XI-Mn, showing a fluorescence peak at 5899 eV, confirming the presence of manganese. A minor peak is also observed at 6403 eV for iron.

5.4.4 Global indicators of damage in superoxide dismutase

The data collected for SOD ranges in dose from 24-120 MGy. The absorbed dose of the first dataset (24 MGy) is approaching the Garman limit of 30 MGy. These doses are much higher than the doses used for XI. The overall data statistics for the structures at 1.22 Å (Table 5.12) are still acceptable even at the highest absorbed dose (120 MGy). The overall signal-to-noise ratio (I/σ(I)) remains stable, but in the highest resolution shell it does decrease from 4.84 in the first dataset (20 MGy) to 2.14 in the fifth dataset (120 MGy). This decay does not cause the completeness or redundancy to decrease. The Wilson B factor, average isotropic B factor and mosaicity do increase, by 22, 21 and 2%, respectively. The individual datasets, even up to the final dose, are respectable in terms of structural data collection.

Table 5.12: Data collection statistics for five consecutive datasets collected on a single SOD crystal.

Dataset	1	2	3	4	5
Dose (MGy)	24	48	72	96	120
Resolution (Å)	29.81-1.22 (1.23-1.22)	29.81-1.22 (1.23-1.22)	29.81-1.22 (1.23-1.22)	29.81-1.22 (1.23-1.22)	29.81-1.22 (1.23-1.22)
I/σ(I)	19.29 (4.84)	23.30 (4.18)	22.74 (3.49)	22.53 (2.72)	22.85 (2.14)
Completeness (%)	100 (96)	100 (99)	100 (97)	100 (97)	100 (97)
Rsym (%)	7.4 (43.5)	6.6 (50.3)	6.7 (59.6)	6.8 (73.9)	6.8 (87.4)
Redundancy	3.8 (3.5)	3.8 (3.6)	3.8 (3.6)	3.8 (3.4)	3.8 (3.4)
Wilson B factor (Å)	10.48	10.90	11.41	12.09	12.79
Mean B value ($Å^2$)	13.10	14.20	14.31	14.96	15.90
Mosaicity (°)	0.325	0.324	0.326	0.331	0.332

The root-mean-squared-displacement between the first and the fifth dataset was 0.063 Å, comparable to the RMSD values for the metal replaced XI structures (0.034-0.088 Å), indicating large scale global damage did not occur.

5.4.5 Specific damage in superoxide dismutase

Analysis of specific damage was carried out using the same tools as for the native and the metal replaced XI structures. Isomorphous Difference Density Maps (Fo_n-Fo_1) were used to visualize specific damage over the course of the collection of the consecutive datasets, Figure 5.9. The density of the first dataset (20 MGy) was subtracted from the last dataset (120 MGy), using the phases from the first dataset. SOD is a dimer in the asymmetric unit. The damage was compared for each monomer. The top 10 negative and positive peaks from the Fo_5-Fo_1 maps were recorded and are shown in Table 5.13.

Table 5.13: Top 10 difference density peaks for each monomer in the Fo5-Fo1 map for SOD. Positive peaks are shown in bold.

Monomer A			Monomer B	
Sigma level	Peak location		Sigma level	Peak location
-40.1	Cys55 SG		**41.79**	**Cu152a**
31.13	**Zn153**		-39.98	Cys55 SG
30.83	**Cu152a**		**29.35**	**Zn153**
15.67	**Cys144 SG**		-23.08	Cys144 SG
-14.63	Cu152b		-12.5	Met115 SD
-11.74	Lys151 O		-12.14	Cys6 S
-11.55	Cys6 S		-11.96	Lys151 O
9.54	**Arg141 O**		-9.09	Glu75 OE1
9.53	**Ser140 O**		-8.82	Lys151 OXT
8.83	**Val116 O**		-8.76	Asp99 OD2

Of these 20 electron density differences, the metals represent five of the top 20 density differences, cysteines involved in disulfide bridges represent 4 of the differences and the sulfur atom of a methionine residue also is represented by a negative density peak. In some cases, there is a negative value for sigma in the Fo-Fo map. This means the apparent electron density surrounding the sulfur decreases with increased absorbed dose and the bond is likely elongated or cleaved as described in Chapter 2.

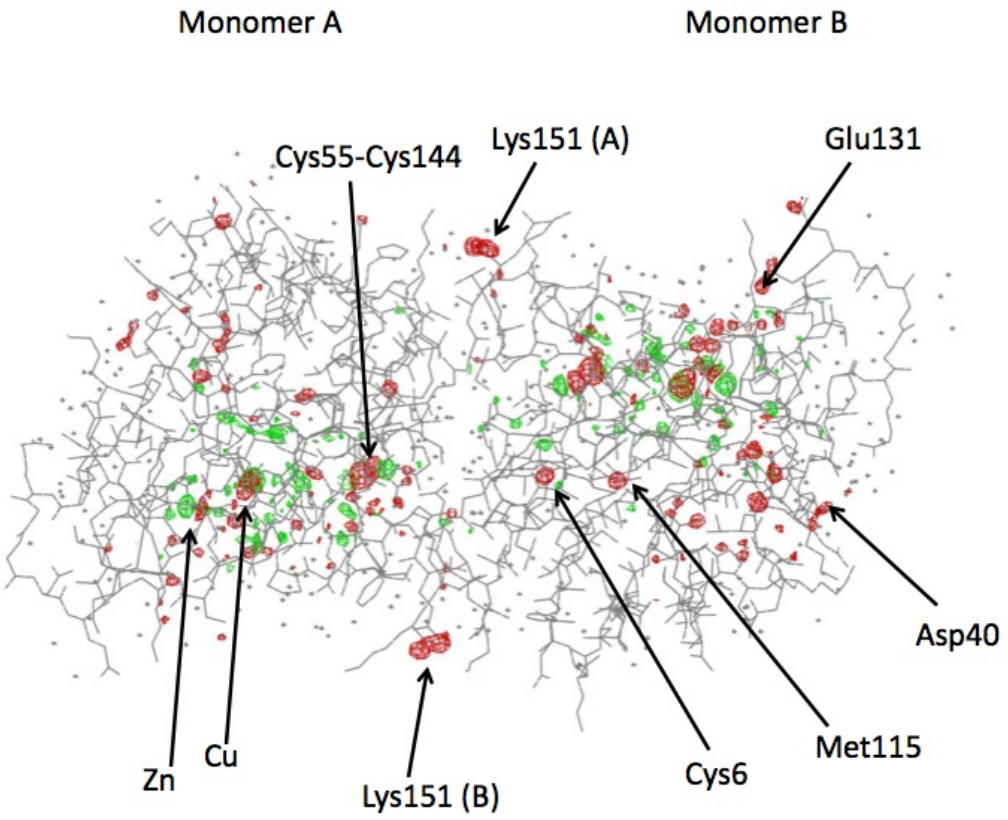

Figure 5.9: Fo5-Fo1 map for superoxide dismutase contoured at +/- 5 sigma. SOD is a dimer in the asymmetric unit.

The SOD structure has an asymmetry between the two copper sites. Others have observed one monomer occupied by the five coordinate conformation, consistent with Cu(II). The other monomer occupied a three coordinate state, consistent with Cu(I). We observe the three coordinate conformation in both monomers, as observed in PDB IB 1Q0E. SOD contains two disulfide bonds, one in each monomer with a length of 2.03 Å. These bonds are radicalized in the first dataset with elongation taking place, Table 5.14. The bonds are then broken by the completion of the second dataset, Table 5.14. The radiation damage process for disulfide bonds is covered in detail in Chapter 2 and it appears that the process is similar for SOD, an unsurprising observation given that it is based on the physical chemistry of the system rather than any specific structural feature. Evidence for disulfide bond breakage is visible in the Fo-Fc maps for the first dataset (Figure 5.10).

Table 5.14: Disulfide bond lengths for Cys55-Cys144 in each monomer.

Dose (MGy)	24	48	72	96	120
Cys55-Cys144 (A) Å	2.09	3.06	3.27	3.34	3.37
Cys55-Cys144 (B) Å	2.11	3.06	3.26	3.32	3.33

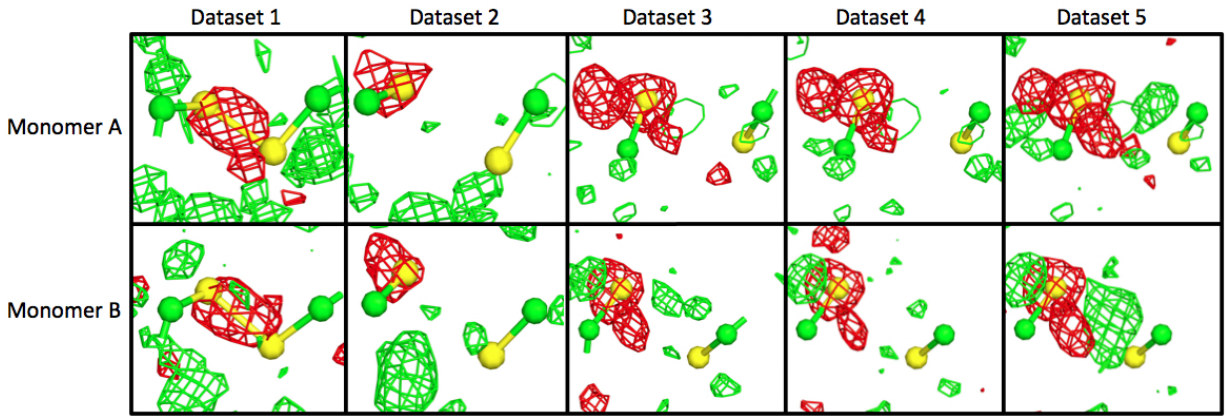

Figure 5.10: Breakage of the Cys55-Cys144 disulfide bond in SOD. Fo-Fc maps for each dataset contoured at 3 sigma (green) and -3 sigma red).

5.4.6 Superoxide dismutase active site damage

The active site of SOD contains histidine residues coordinating the copper and zinc atoms, Figure 5.11. There are no detectable conformational changes in the active site residues and no Fo-Fo peaks associated with these residues, indicating that the histidine residues do not seem to be damaged to the extent of the acidic side chains in the active site of XI. The model in Chapter 3 predicts this, that histidine is not as susceptible as other residues to X-ray induced damage.

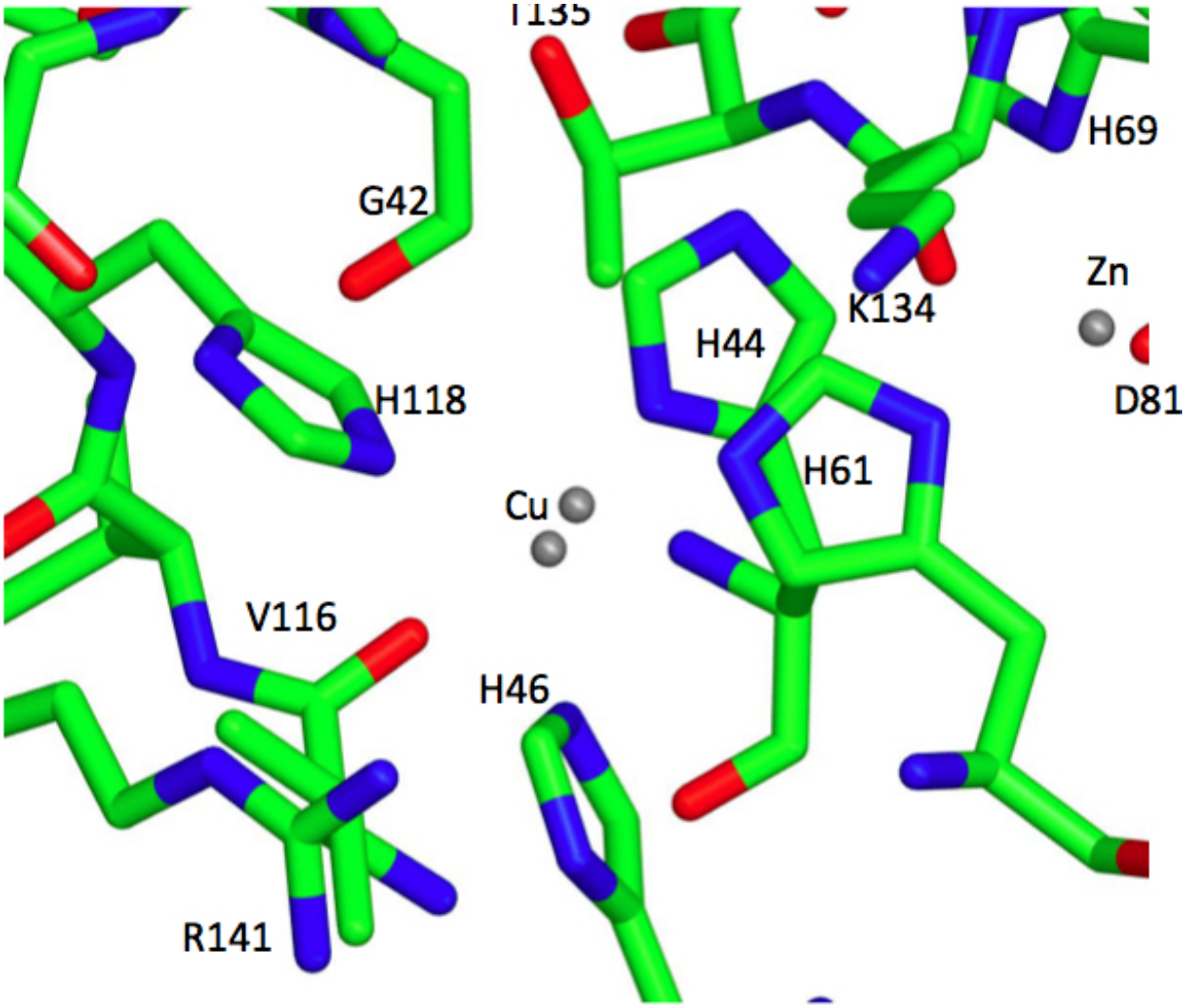

Figure 5.11: Active site of SOD. Copper and Zinc ions are coordinated by surrounding histidine residues.

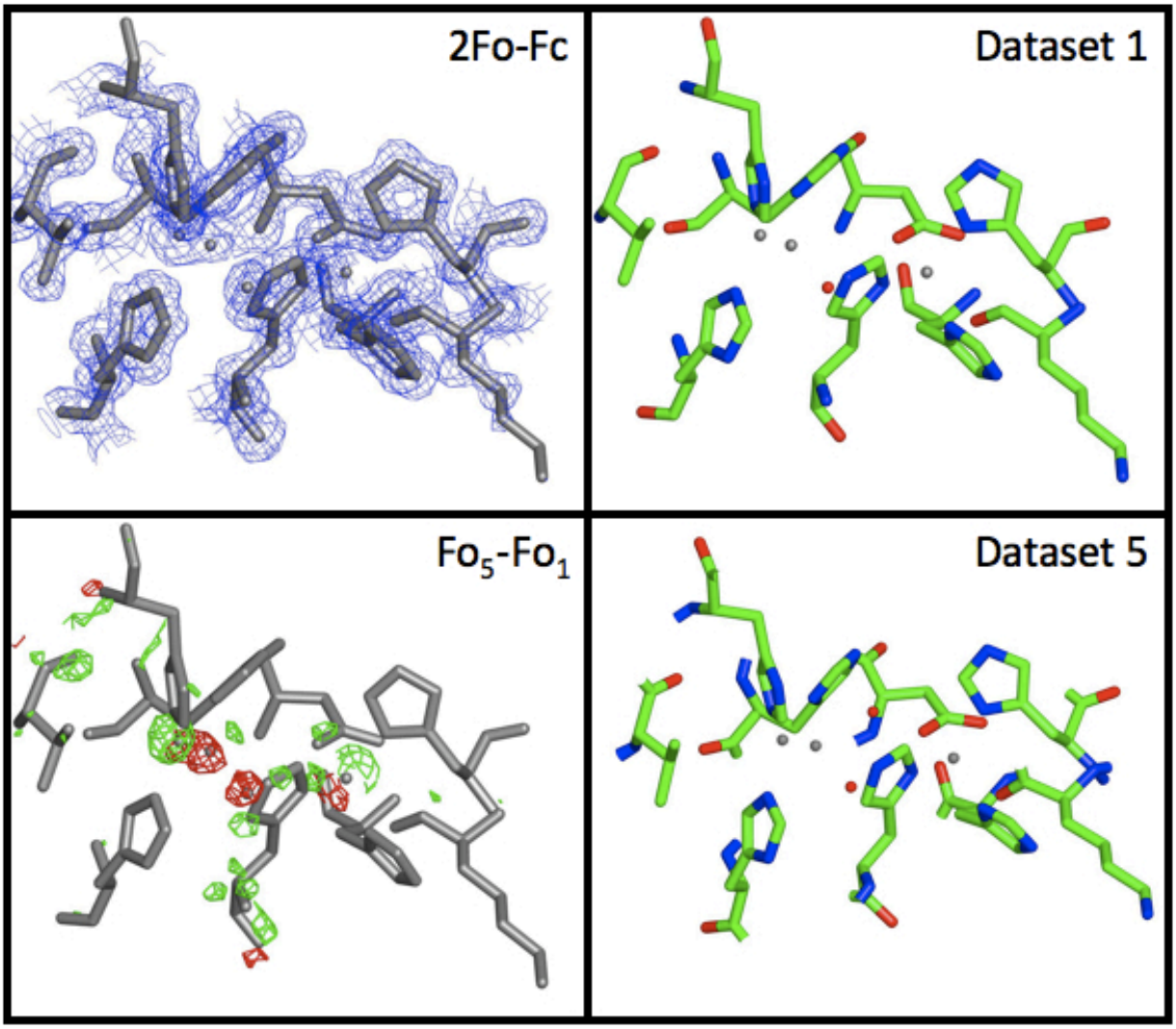

Figure 5.12: Images of the active site for each monomer of SOD. 2Fo-Fc map contoured at 1 sigma shows that the active site density is well-explained at 1.2 Å. The Fo_5-Fo_1 maps show that the largest changes occur near the copper and zinc atoms. The active site structure from dataset 1(20MGy) and dataset 5 (120 MGy) are shown for comparison, with some variation of the metal atoms.

The Fo_5-Fo_1 maps of the active site showed a decrease in density at M2 and an adjacent increase in density, which could be caused by a change in position of the metal atom. A change in metal position also affects the surrounding residues by altering the metal-side chain bond distances. The zinc and copper occupancies, B factors and bond distances were tabulated in Table 5.15 for dataset 1 and dataset 5 to show the differences in the active site structure. All metal atoms have an increased B factor in the fifth dataset. Copper has two configurations in each monomer. The occupancy of Cu(b) increases with increasing dose. The shift in the metal position causes some changes in bond lengths for the residues coordinating the two copper positions. Specifically, the Cu(a)-His61 bond length with an increased absorbed dose (0.18 and 0.16 Å for monomer A and B respectively). The Cu(b)-His46 distance also increases by 0.08 and 0.9 Å for monomer A and B, respectively. In contrast, the bond lengths for the residues coordinating the zinc atom remain relatively stable.

Table 5.15: Metal properties and bond lengths for each monomer in the first and fifth dataset for SOD.

	Dataset 1		Dataset 5	
Monomer A				
Zn B factor	8.45		10.35	
Cu(a) B factor	8.18		8.69	
Cu(b) B factor	10.75		28.90	
Cu(a) occupancy	0.79		0.71	
Cu(b) occupancy	0.21		0.29	
Monomer B				
Zn B factor	8.10		10.02	
Cu(a) B factor	6.94		7.96	
Cu(b) B factor	13.11		27.83	
Cu(a) occupancy	0.69		0.65	
Cu(b) occupancy	0.31		0.35	
	Monomer A	**Monomer B**	**Monomer A**	**Monomer B**
Zn-Asp81	2.04	2.05	2.02	2.02
Zn-His61	2.05	2.05	2.05	2.07
Zn-His78	2.08	2.09	2.08	2.09
Zn-His69	2.11	2.11	2.10	2.09
Cu(a)-His46	2.03	2.05	2.03	2.05
Cu(a)-His118	2.08	2.08	2.08	2.09
Cu(a)-His44	2.14	2.12	2.13	2.14
Cu(a)-His61	3.20	3.18	3.38	3.34
Cu(b)-His46	2.41	2.30	2.49	2.39
Cu(b)-His118	2.33	2.32	2.33	2.35
Cu(b)-His44	2.21	2.20	2.30	2.19
Cu(b)-His61	2.24	2.29	2.33	2.36

The absorbed dose for the first dataset in this study, 24 MGy, is approaching the Garman limit of 30 MGy. Beyond this limit, the biological information extracted from a resulting structure is thought to be compromised. It appears that SOD is more stable than predicted by this limit with the active site remaining relatively stable at this dose. Superposition of dataset 1 with PDB ID 1QOE (Hough 2003 Structure), Figure 5.13, shows that the structures align well (RMSD (302 residues)=0.36 Å). The positions of the metal ions are the only noticeable differences at this resolution (1.15-1.2 Å). The absorbed dose for 1QOE was not reported, but the data was collected at Daresbury SRS beamline 9.6 which has a flux of ~ $1x10^{13}$ ph/s. Similarly, the exposure time was not reported, but the comparable resolution indicates that the absorbed dose was probably comparable to the data presented here. This structure was the first atomic resolution structure (higher than 1.2 Å) of SOD, allowing a more detailed examination of the metal center environment and the associated water network in the active site. The authors did mention they noticed radiation damage to the disulfide bonds in the protein, with a S-S bond distance of 2.9 Å. This elongation agrees with our second dataset (48 MGy) with a S-S distance of 3.06 Å.

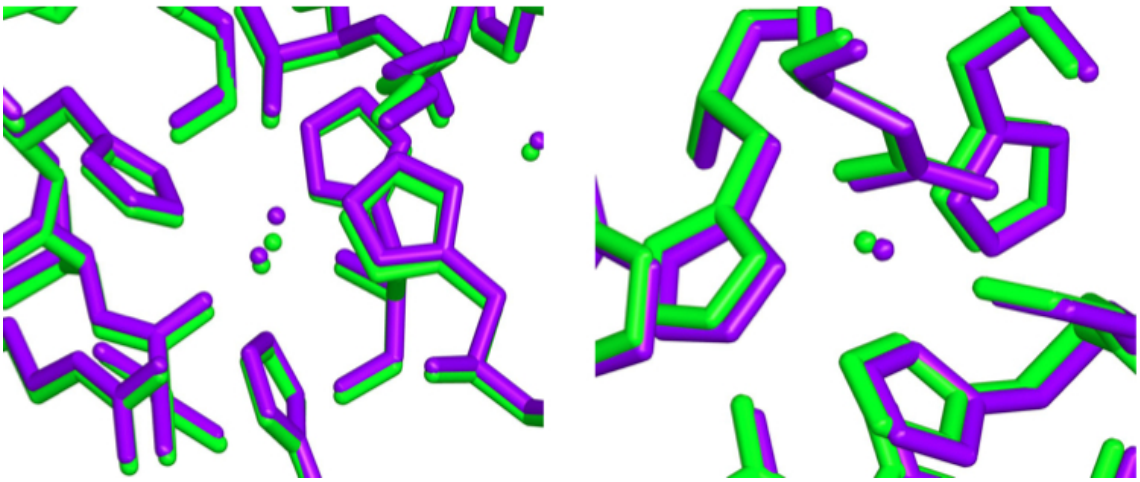

Figure 5.13: Superposition of the first dataset of SOD (green) and PDB ID 1QOE (purple). RMSD for all 302 residues of SOD is 0.36 Å.

5.4.7 Comparison of XI and SOD

The five metal replaced structures of XI showed similar damage characteristics. A change in the metal position was observed for all of the metal replaced structures with increasing dose. The change in position was also reflected by an increase in the metal B factor and a change in occupancy for alternate configurations of the metal site. Increased dose caused specific damage to XI-Cu and XI-Zn reflecting mechanistic changes that were observed in the native XI, shown in Chapter 4. The other metal replaced structures; XI-Cd, XI-Mn and XI-Co did not show the mechanistic shift. The structures of XI-Cu and XI-Zn were the only metal replaced structures with three configurations of M2. The absorbed doses for XI-Cu, 0.012-1.32 MGy, overlap with the absorbed dose for XI native (0.35 MGy-5.74 MGy).

The SOD diffraction data was collected with a much higher absorbed dose, 24-120 MGy, than the XI data. SOD contains two disulfide bonds, one in each monomer. The bonds elongated in the first dataset and were broken in the second dataset. Also, the copper atom in the active site changed position by 0.02 Å with increasing dose, leading to changes in bond lengths in the active site. This is much less than the shift in native XI from M2a to M2b of 1.8 Å.

5.5 Discussion

The initial aim out of the work in this Chapter was to determine the influence of the amino acid environment and the metal on the observed radiation damage. Using two model proteins, one that is known to be prone to radiation damage and the other having a protective free radical scavenging environment and the ability to exchange metals, a systematic study of the influence of the metal and its environment should have been possible. Unfortunately there were variables that were not controlled for including the absorbed dose and multiple positions of the metal.

Different data collection strategies were selected for each crystal based on the crystal properties in order to give the most complete dataset with the lowest absorbed dose. Because of this the eight datasets for each metal replaced XI crystal did not have comparable doses due to the different X-ray cross sections, Table 5.14. There was some overlap Figure 5.14, allowing for the comparison of the active site structures of these datasets, but not enough to do a complete comparison. The ideal experiment would compare data with the same absorbed dose. We hypothesized that proteins containing metals with a larger photoelectric cross section would be more susceptible to damage.

Table 5.16: Photoelectric cross sections (at 12 keV) for the elements used in this study.

Element	**Photoelectric Cross Section at 12 keV**
Manganese	91.5
Cobalt	112.5
Nickel	128.4
Copper	134.4
Zinc	145.6
Cadmium	73.8

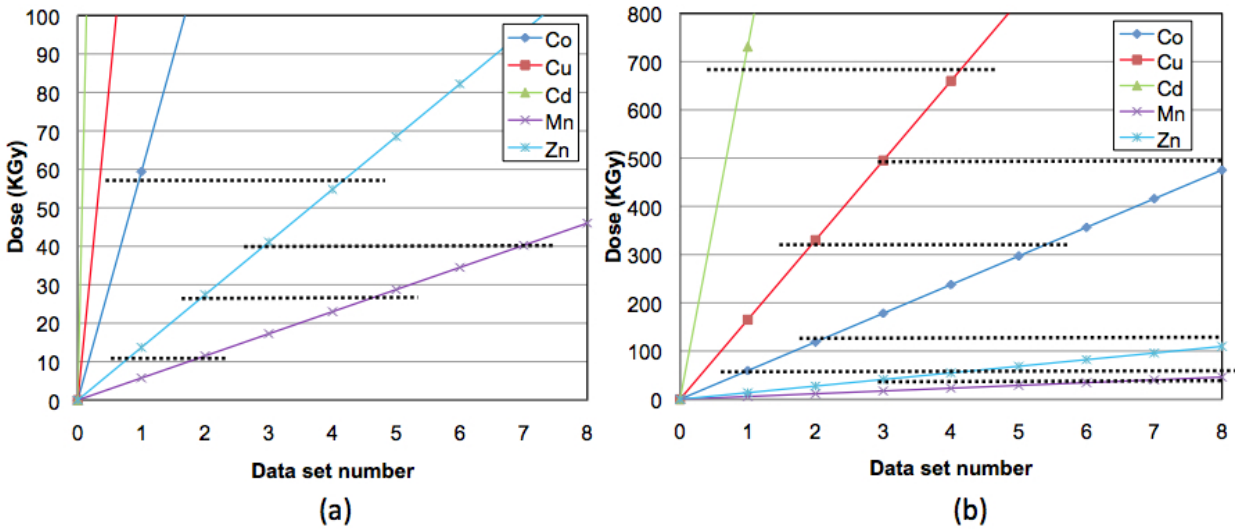

Figure 5.14: Absorbed doses for each metal replaced crystal plotted against dataset number. Overlap in dose is shown by the dotted lines. (a) low dose plot and (b) higher dose range. Dataset 1 of XI-Zn and dataset 2 of XI-Mn have a similar total absorbed dose of ~10 kGy. Dataset 1 of XI-Co and dataset 4 of XI-Zn have a similar total absorbed dose of ~55 kGy.

The difference in number of positions for M2 in the metal replaced structures of XI was unexpected. This also makes the comparison of the active site challenging. To detect active site damage, the bond lengths and B factor$_s$ were analyzed; especially for M2c the X-ray induced metal position. However, XI-Mn, XI-Cd and XI-Co did not have a position M2c in the structure. XI-Mn and XI-Co only had one position for M2. The comparison of dataset 1 of XI-Cu (0.165 MGy) with dataset 8 of XI-Zn (0.110 MGy) and dataset 8 of XI-Cu (1.32 MGy), gave the most promising results. The active sites of the two structures, at approximately the same dose, superimpose very well with a RMSD value of 0.12 Å. The structural differences between the lower dose structures (~0.14 MGy) and the higher dose (1.32 MGy) structure of XI-Cu include a change in position for His219, Asp 254 and M2. His219 and Asp254 of the first dataset (0.35 MGy) and the seventh dataset (5.8 MGy) of the native structure lay in between the 0.14 MGy and 1.32 MGy metal replaced structures. The metal positions for copper, zinc and manganese in are all in the same vicinity, but not one conformation overlays perfectly.

The experiments to determine the effects of the environment on the susceptibility to radiation damage have not been concluded. The general model for radiation damage in Chapter 2 is applicable. The Fo_8-Fo_1 maps showed a relationship between absorbed dose and apparent damage when the negative peaks were normalized to absorbed dose. The decrease in electron density surrounding the metals in the active site of each metal replaced XI structure was greater for the lowest dose data (XI-Mn) and the least for the highest dose data (XI-Cd). The residues followed the same trend. Every

indication would show that it is possible to develop a model for radiation damage that includes the influence of the active site metal target and its surrounding environment.

5.6 Conclusion

Understanding the effect of the metal in the active site and its surrounding amino acid environment is key to developing a generalized model for radiation damage. We have observed dose dependent damage to the active site metal M2 and Met, Asp, Glu residues. This damage causes a change in position for M2 in metal replaced XI structures, XI-Cu and XI-Zn, which contain three positions for M2. The other metal replaced structures do not exhibit the same change in position and have only one (XI-Mn and XI-Co) position or two positions for M2 that converges into one position with increased dose (XI-Cd). The effect of the free radical scavenging environment of SOD was analyzed with increased absorbed dose. The active site of SOD does not experience the same changes in bond length and changes in metal position as XI, even at a much higher absorbed dose (120 MGy). This indicates the free radical scavenging environment of SOD may play a protective role against X-ray induced structural perturbation. The metal plays a role and so does the environment of that metal in the radiation chemistry response to X-rays.

6. Discussion and Future Work

6.1 Discussion

Radiation chemistry has had a significant impact on X-ray crystallography. In this work, a study of the process has been made in order to further the understanding of it and develop means to predict, identify, and perhaps calculate the native state. The state of the field is summarized in Chapter 1 and in Chapter 2 the most common structural observation, the cleavage of disulfide bonds, is explored. Damage to disulfides is seen in many structures and mechanisms for this process have been proposed. By combining X-ray crystallography with Electron Paramagnetic Resonance (EPR) and microspectrophotometry the damage has been visualized, quantitated through in situ observation, and followed at doses typical at synchrotron sources. The process is a result of multi-track radiation chemistry. One electron addition to the disulfide bond causes elongation and another electron addition is required for bond cleavage. Both the online microspectrophotometry and the EPR provided a saturation dose of 0.2 MGy, where radical production occurs at the same rate as radical recombination. Repair process take place with the secondary damage (but not primary damage).

There is a rich literature on multi-track radiation chemistry. With knowledge that the process in X-ray crystallography is a multi-track process, Chapter 3 explores reaction schemes for residues most likely to be damaged. These are examined with a light on what would produce a noticeable structural change and the predictions compared to lysozyme data recorded for the disulfide study in Chapter 2 and higher dose studies on

Xylose Isomerase in Chapter 4. The results are in agreement with the model but there is limited information available on radical yield for amino acids at conditions where X-ray crystallography takes place, i.e. in crystals usually flash cooled to 100K.

The damage process was observed in crystals of lysozyme in Chapter 2. While a mechanism for disulfide bond cleavage exists (Carpentier 2010), our studies combining the complementary techniques of X-ray crystallography, Electron Paramagnetic Resonance (EPR), and microspectrophotometry allowed us to propose a new model in which disulfide bond cleavage is a result of multi-track radiation chemistry. One electron addition to the disulfide bond causes elongation and another electron addition is required for bond cleavage. Both the online microspectrophotometry and the EPR provided a saturation dose of 0.2 MGy, where radical production occurs at the same rate as radical recombination. Using EPR, we were also able to quantitate the total free radical production and the disulfide radical production and their associated rates of formation. This was the first time this kind of data was collected on a single protein crystal. This data is typically collected on aqueous or dry samples.

Lysozyme is a non-metal containing enzyme; approximately 30% of proteins contain a metal site, which is often involved in the mechanism. Metals have a significantly larger X-ray cross section than the atoms typically found in biological macromolecules and could be expected to exert a larger influence on the damage that does take place. In Chapter 4 this is studied with XI examined as a function of absorbed dose. XI is well

characterized but its exact mechanism is still unclear. The specific X-ray induced damage mimics the steps of the proposed reaction mechanism for XI. Mobility of the manganese atom in the metal site is observed as well as the development of alternate positions of residues involved in the mechanism, induced by X-ray radiation. According to a proposed mechanism for XI, the metal in the active site occupied three different positions throughout the steps of the reaction. The third position was suggested to be the reason for low enzymatic turnover. From the data in Chapter 3, the third position for the metal is likely an artifact of X-ray induced damage. While the first two positions follow the trajectory suggested by the mechanism, the third position is uncertain and fluctuates in position and occupancy. Significant structural changes can occur at metal sites, which may have significant implications for the interpretation of mechanism if this is not taken into account.

Knowing that a multi-track model has the potential to explain radiation damage and that metal motion can be induced by X-ray radiation, the next question posed was the influence of the metal and the site in which it sat. In chapter 5 the enzymatic metal in XI was replaced with several others and a similar radiation damage study undertaken. In parallel, Superoxide Dismutase (SOD) was studied in a similar manner. Damage was known to occur in XI from the previous chapters and SOD natively operates as a free radical scavenger. It was expected that damage to SOD would be less than that to XI and indeed that proved to be the case. Dose dependent damage to Met, Asp, and Glu residues was observed. XI containing copper and XI containing zinc contained three positions for the active site metal atom and experienced a dose-induced shift in position

similar to native XI. The other metal replaced structures did not experience the same change in position and only have one (XI containing manganese and XI containing cobalt) position or two positions for the active site metal that converge into one with increased dose (XI containing cadmium). Although we were able to obtain quality diffraction data to ~1.2 Å for several metal replaced structures, we were unable to quantify the effect of the metal target on the damage that occurs. The active site of superoxide dismustase does not experience the same changes in bond length and changes in metal position as XI. The absorbed dose in the XI experiment (5.6 MGy) is much lower than for SOD (120 MGy). Even so, radiation-induced metal position changes as evidenced in XI were not observed for SOD. This suggests active site environment of SOD may play a protective role against X-ray induced damage. The absorbed dose differs for each metal replaced crystal. It was difficult to quantitate the effect of different metals (and their associated X-ray cross sections) due to difficulties with keeping the absorbed dose comparable. A similar data collection scheme was used for all and given the different cross sections of the metals involved, which resulted in very different dose sampling.

Chapters 2 to 4 present key information to lay the groundwork for a general predictive model for radiation damage. While the influence of the active site metal and its environment still need a quantitative assessment, the multi-track model for radiation damage based on radiation chemistry demonstrates how susceptible residues will be affected by radiation-induced damage, either through oxidation or reduction reactions. The residue type has an influence, the metal if present and the environment. It will not

be a simple process but the results indicate that it is possible. This has significant implications. With a model of the radiation damage process and recording of the absorbed dose it should be possible to predict radiation damaged residues. Understanding the scheme associated with that damage would allow calculation of the native state. This could be done for future structural studies but also used in a retroactive manner to examine structures where biochemical results did not agree completely with structural explanations of mechanism. It enables a better understanding of mechanism.

6.2. Future work

A complete radiation damage model has not been produced. There are several key components that are still needed. The radical yield for each amino acid needs to be determined as a function of typical crystallization conditions. There is evidence that the yield can vary as a function of concentration and pH among a few of the many biophysical parameters. For an accurate model this needs to be tabulated through calculation, a more extensive literature review, new measurements, or combinations of all three.

The metalloprotein study showed the practical problems of this kind of experiment. With hindsight, the absorbed dose should be kept as near as constant for each dataset as possible. Unfortunately absorbed dose is different from the transmitted dose. A greatly increased absorbed dose results from the crystal content rather than the illumination

used and, for example, a ten-fold increase in absorbed dose does not translate to significant diffraction resolution. The study is constrained by the need for structural detail over the requirement for orders of magnitude differences in exposure time. The absorbed dose is also calculated based on the protein contents. While a metal site greatly increases the overall absorbed dose the radicals have a short lifetime and travel distance. The dose close to the metal site may be much higher but the rest of the protein probably receives a dose similar to those without the metal. This suggests a combination of studies, the examination of the same protein with and without metal and artificial dose construction with multiple crystals used instead of a single one.

Metal coordination was inferred from bond lengths, however it would be useful to know the actual metal coordination throughout the diffraction experiment. This can be done for proteins with an absorbing metal cofactor, such as cobalt. However, manganese is optically silent and cannot be observed spectroscopically. Ideally, Extended X-ray absorption Fine Structure (EXAFS) would be collected to assign metal coordination states. This technique is sensitive enough to determine the difference between Mn (II) and Mn (III). The data analysis is not trivial. Information about the coordination of the metal and how it changes with increased absorbed doses for many different metals would provide valuable information for the development of the general model for radiation damage.

Finally we see a difference in damage due to the metal site. This implies that tertiary structure has an influence. A comprehensive model would involve the build-up of information on the individual amino acid components, the metal type/s if present, and the overall environment of the component. A molecular dynamics or similar approach would be required to integrate all the measurements into a theoretical model. Despite this, there does not appear to be any practical limitation of achieving this. A full model of the damage process is possible and this thesis presents key steps in the path of achieving this.

References and Literature Cited

Adam, V., Royant, A., Niviere, V., Molina-Heredia, F. P. & Bourgeois, D. (2004). *Structure* **12**, 1729-1740.

Adams, P. D., Afonine, P. V., Bunkoczi, G., Chen, V. B., Davis, I. W., Echols, N., Headd, J. J., Hung, L. W., Kapral, G. J., Grosse-Kunstleve, R. W., McCoy, A. J., Moriarty, N. W., Oeffner, R., Read, R. J., Richardson, D. C., Richardson, J. S., Terwilliger, T. C. & Zwart, P. H. (2010a). *Acta Crystallogr D Biol Crystallogr* **66**, 213-221.

Adams, P. D., Afonine, P. V., Bunkoczi, G., Chen, V. B., Davis, I. W., Echols, N., Headd, J. J., Hung, L. W., Kapral, G. J., Grosse-Kunstleve, R. W., McCoy, A. J., Moriarty, N. W., Oeffner, R., Read, R. J., Richardson, D. C., Richardson, J. S., Terwilliger, T. C. & Zwart, P. H. (2010b). *Acta Crystallographica Section D-Biological Crystallography* **66**, 213-221.

Agre, P. (2003). Aquaporin Water Channels, The Nobel Prizes 2003, Stockholm: The Nobel Foundation.

Allen, K. N., Lavie, A., Glasfeld, A., Tanada, T. N., Gerrity, D. P., Carlson, S. C., Farber, G. K., Petsko, G. A. & Ringe, D. (1994). *Biochemistry* **33**, 1488-1494.

Alphey, M. S., Gabrielsen, M., Micossi, E., Leonard, G. A., McSweeney, S. M., Ravelli, R. B., Tetaud, E., Fairlamb, A. H., Bond, C. S. & Hunter, W. N. (2003). *The Journal of biological chemistry* **278**, 25919-25925.

Andreini, C., Bertini, I., Cavallaro, G., Holliday, G.L. and Thornton, J.M. (2008). *J. Biol. Inorg. Chem.* **13**, 1205-1218.

Asmus, K.-D., Bahnemanann, D. & Bonifacic, D. M. (1977). *Faraday Discuss. Chem. Soc.* **63**, 213-225.

Barker, A. I., Southworth-Davies, R. J., Paithankar, K. S., Carmichael, I. & Garman, E. F. (2009). *Journal of synchrotron radiation* **16**, 205-216.

Barton, J. P. & Packer, J. E. (1970). *International Journal for Radiation Physics and Chemistry* **2**, 159-166.

Bednarek, J., Plonka, A., Hallbrucker, A. & Mayer, E. (1998). *Journal of Physical Chemistry A* **102**, 9091-9094.

Beitlich, T., Kuhnel, K., Schulze-Briese, C., Shoeman, R. L. & Schlichting, I. (2007). *Journal of synchrotron radiation* **14**, 11-23.

Berglund, G. I., Carlsson, G. H., Smith, A. T., Szoke, H., Henriksen, A. & Hajdu, J. (2002). *Nature* **417**, 463-468.

Berman, H. M., Westbrook, J., Feng, Z., Gilliland, G., Bhat, T. N., Weissig, H., Shindyalov, I. N. & Bourne, P. E. (2000). *Nucleic acids research* **28**, 235-242.

Bernhard, W. A. & Fouse, G. W. (1989). *Journal of Magnetic Resonance* **82**, 156-162.

Black, P. J. & Bernhard, W. A. (2011). *J Phys Chem B* **115**, 8009-8013.

Black, P. J. & Swarts, S. G. *Health Phys* **98**, 301-308.

Blake, C. C. F., Phillips, D.C. (1962). *Vienna International Atomic Energy Agency*, 183-191.

Bogumil, R., Kappl, R., Huttermann, J. & Witzel, H. (1997). *Biochemistry* **36**, 2345-2352.

Borshchevskiy, V. I., Round, E. S., Popov, A. N., Buldt, G. & Gordeliy, V. I. (2011). *Journal of molecular biology* **409**, 813-825.

Box, H. C. (1998). *Foundations of Modern EPR*, edited by S. S. E. a. K. M. S. Gareth R. Eaton. Singapore: World Scientific Publishing Co. Pte. Ltd.
Braams, R. (1966). *Radiat Res* **27**, 319-329.
Braams, R. & Ebert, M. (1967). *Int J Radiat Biol Relat Stud Phys Chem Med* **13**, 195-197.
Burmeister, W. P. (2000a). *Acta Cryst D Biological Crystallography* **56**, 328-341.
Burmeister, W. P. (2000b). *Acta Crystallogr D Biol Crystallogr* **56**, 328-341.
Campbell, D. I., Bunn, J. E., Weaver, L. T., Harding, M., Coward, W. A. & Thomas, J. E. (2006). *Clinical infectious diseases : an official publication of the Infectious Diseases Society of America* **43**, 1040-1042.
Campbell, K. S., Foster, A. J., Dillon, C. T. & Harding, M. M. (2006). *Journal of inorganic biochemistry* **100**, 1194-1198.
Carpentier, P., Royant, A., Weik, M. & Bourgeois, D. (2010). *Structure* **18**, 1410-1419.
Carrell, H. L., Glusker, J. P., Burger, V., Manfre, F., Tritsch, D. & Biellmann, J. F. (1989). *Proceedings of the National Academy of Sciences of the United States of America* **86**, 4440-4444.
Carrell, H. L., Hoier, H. & Glusker, J. P. (1994). *Acta Crystallogr D Biol Crystallogr* **50**, 113-123.
Carrell, H. L., Rubin, B. H., Hurley, T. J. & Glusker, J. P. (1984). *The Journal of biological chemistry* **259**, 3230-3236.
Carugo, O. & Djinovic Carugo, K. (2005). *Trends in biochemical sciences* **30**, 213-219.
Chan, P. J. & Bielski, B. H. J. (1973). *J. Am. Chem. Soc.* **95**, 5504-5508.
Chinte, U., Shah, B., Chen, Y. S., Pinkerton, A. A., Schall, C. A. & Hanson, B. L. (2007). *Acta Crystallogr D Biol Crystallogr* **63**, 486-492.
Collyer, C. A., Henrick, K. & Blow, D. M. (1990). *Journal of molecular biology* **212**, 211-235.
Corbett, M. C., Latimer, M. J., Poulos, T. L., Sevrioukova, I. F., Hodgson, K. O. & Hedman, B. (2007). *Acta Crystallogr D Biol Crystallogr* **63**, 951-960.
Crick, F. (1962). On the Genetic Code, Vol. Medicine, Nobel Lectures, Amsterdam: Elsevier Publishing Company
Davis, R. J., Pesah, Y. I., Harding, M., Paylor, R. & Mardon, G. (2006). *Genesis* **44**, 84-92.
Deisenhofer, J. (1988). The Photosynthetic Reaction Centre from the Purple Bacterium *Rhodopseudomonas Viridis*, Vol. Chemistry 1981-1990, Nobel Lectures, Singapore: World Scientific Publishing Co.
Dubnovitsky, A. P., Ravelli, R. B., Popov, A. N. & Papageorgiou, A. C. (2005). *Protein Sci* **14**, 1498-1507.
Emsley, P. & Cowtan, K. (2004). *Acta Crystallogr D Biol Crystallogr* **60**, 2126-2132.
Emsley, P., Lohkamp, B., Scott, W. G. & Cowtan, K. (2010). *Acta Crystallogr D Biol Crystallogr* **66**, 486-501.
Evans, P. (2006). *Acta Crystallogr D Biol Crystallogr* **62**, 72-82.
Fenn, T. D., Ringe, D. & Petsko, G. A. (2004). *Biochemistry* **43**, 6464-6474.
Fioravanti, E., Vellieux, F. M., Amara, P., Madern, D. & Weik, M. (2007). *Journal of synchrotron radiation* **14**, 84-91.
Fletterick, R. J., Sygusch, J., Murray, N., Madsen, N.B., Johnson, L.N. (1976). *Journal of Molecular Biology* **103**, 1-13.

French, G. S., Wilson, K.S. (1978). *Acta Crystallographica* **A34**, 517.
Garman, E. F. (1999). *Acta Crystallographica* **D55**, 1641-1653.
Garman, E. F. & Doublie, S. (2003). *Methods in enzymology* **368**, 188-216.
Garman, E. F. & Nave, C. (2009). *Journal of synchrotron radiation* **16**, 129-132.
Garman, E. F. & Owen, R. L. (2006). *Acta Crystallogr D Biol Crystallogr* **62**, 32-47.
Garrison, W. M. & Weeks, B. M. (1962). *Radiat Res* **17**, 341-352.
Gizatullin, F., Yao, Y., Kung, V., Harding, M. W., Loda, M. & Shapiro, G. I. (2006). *Cancer research* **66**, 7668-7677.
Gonzalez, A., Denny, R. & Nave, C. (1994). *Acta Crystallogr D Biol Crystallogr* **50**, 276-282.
Gonzalez, A., Moorhead, P., McPhillips, S. E., Song, J., Sharp, K., Taylor, J. R., Adams, P. D., Sauter, N. K. & Soltis, S. M. (2008). *Journal of Applied Crystallography* **41**, 176-184.
Gonzalez, A. & Nave, C. (1994). *Acta Crystallogr D Biol Crystallogr* **50**, 874-877.
Haas, D. J., Rossmann, M.G. (1970). *Acta Crystallographica Section B* **26**, 998-1004.
Harding, M. M. (2006). *Acta Crystallogr D Biol Crystallogr* **62**, 678-682.
Hatano, H., Ganno, S., Ohara, A. (1962). *The Proceedings of the 5th Symposium on Radiation Chemistry of the Chemical Society of Japan*, pp. 61-70.
Helliwell, J. R. (1988). *Journal of Crystal Growth* **90**, 259-272.
Hendrickson, W. A. (1976). *Journal of Molecular Biology* **106**, 889-893.
Holton, J. M. (2007). *Journal of synchrotron radiation* **14**, 51-72.
Homer, C., Cooper, L. & Gonzalez, A. (2011). *J Synchrotron Radiat* **18**, 338-345.
Hope, H. (1988). *Acta Crystallographica* **B44**, 22-26.
Hough, M. A., Antonyuk, S. V., Strange, R. W., Eady, R. R. & Hasnain, S. S. (2008). *Journal of molecular biology* **378**, 353-361.
Hough, M. A. & Hasnain, S. S. (2003). *Structure* **11**, 937-946.
Huber, R. (1988). A Stuctural Basis of Light Energy and Electron Transfer in Biology, Vol. Chemistry 1981-1990, Nobel Lectures, Singapore: World Scientific Publishing Co.
Hutchinson, F. (1958). *Radiation Research* **9**, 13-23.
Inglis, S. R., McGann, M. J., Price, W. S. & Harding, M. M. (2006). *FEBS letters* **580**, 3911-3915.
Johari, G. P., Hallbrucker, A. and Mayer, E. (1987). *Nature* **330**, 552-553.
Johnson, J. E. & Moulton, G. C. (1978). *J. Chem. Phys.* **69**, 3108-3111.
Kauffmann, B., Weiss, M. S., Lamzin, V. S. & Schmidt, A. (2006). *Structure* **14**, 1099-1105.
Kendrew, J. C. (1962). Myoglobin and the structure of proteins, Vol. Chemistry, Nobel Lectures, pp. 676-698. Amsterdam: Elsevier Publishing Company.
Kmetko, J., Husseini, N. S., Naides, M., Kalinin, Y. & Thorne, R. E. (2006). *Acta Crystallogr D Biol Crystallogr* **62**, 1030-1038.
Kovalevsky, A. Y., Hanson, L., Fisher, S. Z., Mustyakimov, M., Mason, S. A., Forsyth, V. T., Blakeley, M. P., Keen, D. A., Wagner, T., Carrell, H. L., Katz, A. K., Glusker, J. P. & Langan, P. (2010). *Structure* **18**, 688-699.
Krivokapic, A., Ohman, K. T., Munthe, M., Nelson, W. H., Hole, E. O. & Sagstuen, E. (2010). *Radiat Res* **173**, 689-702.
Lavie, A., Allen, K. N., Petsko, G. A. & Ringe, D. (1994). *Biochemistry* **33**, 5469-5480.

Lawrence, C. C., Bennati, M., Obias, H. V., Bar, G., Griffin, R. G. & Stubbe, J. (1999). *Proc. Natl. Acad. Sci. USA* **96**, 8979–8984.
Leiros, H. K., McSweeney, S. M. & Smalas, A. O. (2001). *Acta Crystallogr D Biol Crystallogr* **57**, 488-497.
Leiros, H. K., Timmins, J., Ravelli, R. B. & McSweeney, S. M. (2006). *Acta Crystallogr D Biol Crystallogr* **62**, 125-132.
Lieberman, R. L. R., A.C. (2005). *Nature* **434**, 177-182.
Luft, J. R., Collins, R. J., Fehrman, N. A., Lauricella, A. M., Veatch, C. K. & DeTitta, G. T. (2003). *Journal of structural biology* **142**, 170-179.
Macedo, S., Pechlaner, M., Schmid, W., Weik, M., Sato, K., Dennison, C. & Djinovic-Carugo, K. (2009). *Journal of synchrotron radiation* **16**, 191-204.
MacKinnon, R. (2003). Potassium Channels and the Atomic Basis of Selective Ion Conduction, The Nobel Prizes 2003, Stockholm: The Nobel Foundation.
Matsui, Y., Sakai, K., Murakami, M., Shiro, Y., Adachi, S., Okumura, H. & Kouyama, T. (2002). *Journal of molecular biology* **324**, 469-481.
Matsuki, K., Nelson, W.H., Hadley, J.H. (1981). *J Chem Phys* **75**, 5587-5593.
Matthews, B. W. (1968). *Journal of Molecular Biology* **33**, 491-497.
McGeehan, J., Ravelli, R. B., Murray, J. W., Owen, R. L., Cipriani, F., McSweeney, S., Weik, M. & Garman, E. F. (2009). *Journal of synchrotron radiation* **16**, 163-172.
McNicholas, S., Potterton, E., Wilson, K. S. & Noble, M. E. (2011). *Acta Crystallogr D Biol Crystallogr* **67**, 386-394.
McPhillips, T. M., McPhillips, S. E., Chiu, H. J., Cohen, A. E., Deacon, A. M., Ellis, P. J., Garman, E., Gonzalez, A., Sauter, C., Phizackerley, R. P., Soltis, S. M. & Kuhn, P. (2002). *J. Synchrotron Radiation* **9**, 401-406.
Meents, A., Gutmann, S., Wagner, A. & Schulze-Briese, C. (2010). *Proceedings of the National Academy of Sciences of the United States of America* **107**, 1094-1099.
Meents, A., Wagner, A., Schneider, R., Pradervand, C., Pohl, E. & Schulze-Briese, C. (2007). *Acta Crystallogr D Biol Crystallogr* **63**, 302-309.
Michel, H. (1988). The Photosynthetic Reaction Centre from the Purple Bacterium *Rhodopseudomonas Viridis*, Vol. Chemistry 1981-1990, Nobel Lectures, Singapore: World Scientific Publishing Co.
Muller, R., Weckert, E., Zellner, J. & Drakopoulos, M. (2002). *Journal of synchrotron radiation* **9**, 368-374.
Murray, J. & Garman, E. (2002). *Journal of synchrotron radiation* **9**, 347-354.
Murray, J. W., Garman, E. F. & Ravelli, R. B. G. (2004a). *Journal of Applied Crystallography* **37**, 513-522.
Murray, J. W., Garman, E. F. & Ravelli, R. B. G. (2004b). *Journal of Applied Crystallography* **37**, 513-522.
Murray, J. W., Rudino-Pinera, E., Owen, R. L., Grininger, M., Ravelli, R. B. & Garman, E. F. (2005). *Journal of synchrotron radiation* **12**, 268-275.
Niroomand-Rad, A., Blackwell, C. R., Coursey, B. M., Gall, K. P., Galvin, J. M., McLaughlin, W. L., Meigooni, A. S., Nath, R., Rodgers, J. E. & Soares, C. G. (1998). *Medical Physics* **25**, 2093-2115.
Northrop, J. H. (1946). The Preparation of Pure Enzymes and Virus Proteins, Vol. Chemistry, Nobel Lectures, pp. 124-134. Amsterdam: Elservier Publishing Company.

Nowak, E., Brzuszkiewicz, A., Dauter, M., Dauter, Z. & Rosenbaum, G. (2009). *Acta Crystallogr D Biol Crystallogr* **65**, 1004-1006.
O'Neill, P., Stevens, D.L, Garman, E.F. (2002). *Journal of synchrotron radiation* **9**, 329-332.
Otwinowski, Z. & Minor, W. (1997). *Methods in Enzymology*, edited by C. W. Carter Jr. & R. M. Sweet, pp. 307-326. New York: Academic Press.
Otwinowski, Z., Minor, W. (1997). *Macromolecular Crystallography*, edited by C. W. Carter, Jr. & Sweet, R. M.`, pp. 307-326. New York: Academic Press.
Owen, R. L., Rudino-Pinera, E. & Garman, E. F. (2006a). *Proceedings of the National Academy of Sciences of the United States of America* **103**, 4912-4917.
Owen, R. L., Rudino-Pinera, E. & Garman, E. F. (2006b). *Proceedings of the National Academy of Sciences of the United States of America* **103**, 4912-4917.
Owen, R. L., Yorke, B. A., Gowdy, J. A. & Pearson, A. R. (2011). *J Synchrotron Radiat* **18**, 367-373.
Paithankar, K. S. & Garman, E. F. (2010). *Acta Crystallogr D Biol Crystallogr* **66**, 381-388.
Paithankar, K. S., Owen, R. L. & Garman, E. F. (2009a). *Journal of synchrotron radiation* **16**, 152-162.
Paithankar, K. S., Owen, R. L. & Garman, E. F. (2009b). *Journal of Synchrotron Radiation* **16**, 152-162.
Pearson, A. R., Pahl, R., Kovaleva, E. G., Davidson, V. L. & Wilmot, C. M. (2007). *Journal of synchrotron radiation* **14**, 92-98.
Perrakis, A., Harkiolaki, M., Wilson, K. S. & Lamzin, V. S. (2001). *Acta Crystallogr D Biol Crystallogr* **57**, 1445-1450.
Perutz, M. F. (1962). X-ray Analysis of Haemoglobin, Vol. Chemistry, Nobel Lectures, pp. 653-673. Amsterdam: Elsevier Publishing Company.
Petrova, T., Ginell, S., Mitschler, A., Kim, Y., Lunin, V. Y., Joachimiak, G., Cousido-Siah, A., Hazemann, I., Podjarny, A., Lazarski, K. & Joachimiak, A. (2011). *Acta Crystallogr D Biol Crystallogr* **66**, 1075-1091.
Powell, H. R. (1999). *Acta Crystallogr D Biol Crystallogr* **55**, 1690-1695.
Purkayastha, S. & Bernhard, W. A. (2004). *J. Phys. Chem. B* **108**, 18377-18382.
Purkayastha, S., Milligan, J. R. & Bernhard, W. A. (2007). *Radiat Res* **168**, 357-366.
Ramakrishnan, V. (2009). Unraveling the Structure of the Ribosome, The Nobel Prizes 2009, Stockholm: The Nobel Foundation.
Rao, D. N. R., Symons, M. C. R. & Stephenson, J. M. (1983a). *J. Chem. Soc., Perkin Trans. 2*, 727-730.
Rao, D. N. R., Symons, M. C. R. & Stephenson, J. M. (1983b). *Journal of the Chemical Society, Perkin Transactions 2: Physical Organic Chemistry*, 727-730.
Ravelli, R. B. & Garman, E. F. (2006). *Current opinion in structural biology* **16**, 624-629.
Ravelli, R. B. & McSweeney, S. M. (2000a). *Structure* **8**, 315-328.
Ravelli, R. B., Theveneau, P., McSweeney, S. & Caffrey, M. (2002). *Journal of synchrotron radiation* **9**, 355-360.
Ravelli, R. B. G. & McSweeney, S. M. (2000b). *Structure* **8**, 315-328.
Rodgers, M. A., Sokol, H.A., Garrison, W.M. (1968). *Journal of the American Chemical Society* **90**, 795-796.
Rose, I. A. (1975). *Adv Enzymol Relat Areas Mol Biol* **43**, 491-517.

Rose, I. A. (1981). *Philos Trans R Soc Lond B Biol Sci* **293**, 131-143.
Rose, I. A., O'Connell, E. L. & Mortlock, R. P. (1969). *Biochim Biophys Acta* **178**, 376-379.
Rossmann, M. G. & van Beek, C. G. (1999). *Acta Crystallogr D Biol Crystallogr* **55**, 1631-1640.
Rould, M. A. & Carter, C. W., Jr. (2003). *Methods in enzymology* **374**, 145-163.
Sato, M., Shibata, N., Morimoto, Y., Takayama, Y., Ozawa, K., Akutsu, H., Higuchi, Y. & Yasuoka, N. (2004). *Journal of synchrotron radiation* **11**, 113-116.
Schlichting, I., Berendzen, J., Chu, K., Stock, A. M., Maves, S. A., Benson, D. E., Sweet, R. M., Ringe, D., Petsko, G. A. & Sligar, S. G. (2000). *Science (New York, N.Y* **287**, 1615-1622.
Sevilla, M. D., D'Arcy, J.B., Morehouse, K.M. (1979a). *J Phys Chem* **83**, 2887-2892.
Sevilla, M. D., D'Arcy, J.B., Morehouse, K.M. (1979b). *J Phys Chem* **83**, 2893-2897.
Sharma, K. K., Swarts, S.G., Bernhard, W.A. (2011). *J Phys Chem B* **115**, 4843-4855.
Shimizu, N., Hirata, K., Hasegawa, K., Ueno, G. & Yamamoto, M. (2007). *Journal of Synchrotron Radiation* **14**, 4-10.
Sliz, P., Harrison, S. C. & Rosenbaum, G. (2003). *Structure* **11**, 13-19.
Southworth-Davies, R. J. & Garman, E. F. (2007). *Journal of synchrotron radiation* **14**, 73-83.
Spinks, J. W. T. a. W., R.J. (1990). *Introduction to Radiation Chemistry*, Third Edition ed. New York, NY: John Wiley and Sons Inc.
Swarts, S. G., Gilbert, D. C., Sharma, K. K., Razskazovskiy, Y., Purkayastha, S., Naumenko, K. A. & Bernhard, W. A. (2007a). *Radiat Res* **168**, 367-381.
Swarts, S. G., Gilbert, D. C., Sharma, K. K., Razskazovskiy, Y., Purkayastha, S., Naumenko, K. A. & Bernhard, W. A. (2007b). *Radiation Research* **168**, 367-381.
Swenson, H. & Moulton, G. C. (1973). *Radiat Res* **53**, 366-375.
Sygusch, J., Allaire, M. (1988). *Acta Crystallographica* **A44**, 443-448.
Takeda, K., Matsui, Y., Kamiya, N., Adachi, S., Okumura, H. & Kouyama, T. (2004). *Journal of molecular biology* **341**, 1023-1037.
Teng, T. Y. & Moffat, K. (2000). *Journal of synchrotron radiation* **7**, 313-317.
Teng, T. Y. & Moffat, K. (2002). *Journal of synchrotron radiation* **9**, 198-201.
Thomas, J. K. & Hart, E. J. (1962). *Radiation Research* **17**, 408-418.
Utschig, L. M., Chemerisov, S. D., Tiede, D. M. & Poluektov, O. G. (2008). *Biochemistry* **47**, 9251-9257.
Vagin, A. & Teplyakov, A. *Acta Crystallogr D Biol Crystallogr* **66**, 22-25.
Vagin, A. A., Steiner, R. A., Lebedev, A. A., Potterton, L., McNicholas, S., Long, F. & Murshudov, G. N. (2004). *Acta Crystallogr D Biol Crystallogr* **60**, 2184-2195.
von Sonntag, C., Schuuchmann, H.-P. (1994). *Methods in enzymology* **233**, 3-20.
Weik, M., Berges, J., Raves, M. L., Gros, P., McSweeney, S., Silman, I., Sussman, J. L., Houee-Levin, C. & Ravelli, R. B. (2002a). *Journal of synchrotron radiation* **9**, 342-346.
Weik, M., Berges, J., Raves, M. L., Gros, P., McSweeney, S., Silman, I., Sussman, J. L., Houee-Levin, C. & Ravelli, R. B. G. (2002b). *Journal of Synchrotron Radiation* **9**, 342-346.
Weik, M. & Colletier, J. P. (2010). *Acta Crystallogr D Biol Crystallogr* **66**, 437-446.

Weik, M., Ravelli, R. B., Kryger, G., McSweeney, S., Raves, M. L., Harel, M., Gros, P., Silman, I., Kroon, J. & Sussman, J. L. (2000a). *Proceedings of the National Academy of Sciences of the United States of America* **97**, 623-628.
Weik, M., Ravelli, R. B., Silman, I., Sussman, J. L., Gros, P. & Kroon, J. (2001). *Protein Sci* **10**, 1953-1961.
Weik, M., Ravelli, R. B. G., Kryger, G., McSweeney, S., Raves, M. L., Harel, M., Gros, P., Silman, I., Kroon, J. & Sussman, J. L. (2000b). *Proceedings of the National Academy of Sciences of the United States of America* **97**, 623-628.
Weiss, M. S., Panjikar, S., Mueller-Dieckmann, C. & Tucker, P. A. (2005). *Journal of Synchrotron Radiation* **12**, 304-309.
Whitaker, R. D., Cho, Y., Cha, J., Carrell, H. L., Glusker, J. P., Karplus, P. A. & Batt, C. A. (1995). *The Journal of biological chemistry* **270**, 22895-22906.
Whitlow, M., Howard, A. J., Finzel, B. C., Poulos, T. L., Winborne, E. & Gilliland, G. L. (1991). *Proteins* **9**, 153-173.
Wilkins, M. (1962). The Molecular Configuration of Nucleic Acids, Vol. Medicine, Nobel Lectures, pp. 754-782. Amsterdam: Elsevier Publishing Company.
Wilson, J. H., Paturzo, F. X., Johnson, L. K., Carreiro, M. P., Hixson, D. C., Mennone, A., Boyer, J. L., Pober, J. S. & Harding, M. J. (2006). *Xenotransplantation* **13**, 53-62.
Winn, M. D. (2003). *J Synchrotron Radiat* **10**, 23-25.
Winn, M. D., Ballard, C. C., Cowtan, K. D., Dodson, E. J., Emsley, P., Evans, P. R., Keegan, R. M., Krissinel, E. B., Leslie, A. G., McCoy, A., McNicholas, S. J., Murshudov, G. N., Pannu, N. S., Potterton, E. A., Powell, H. R., Read, R. J., Vagin, A. & Wilson, K. S. (2011). *Acta Crystallogr D Biol Crystallogr* **67**, 235-242.
Yano, J., Kern, J., Irrgang, K. D., Latimer, M. J., Bergmann, U., Glatzel, P., Pushkar, Y., Biesiadka, J., Loll, B., Sauer, K., Messinger, J., Zouni, A. & Yachandra, V. K. (2005). *Proceedings of the National Academy of Sciences of the United States of America* **102**, 12047-12052.
Zhou, Y. & Nelson, W. H. (2010). *J Phys Chem B* **114**, 5567-5582.

VITA

Kristin Amy Sutton, daughter of Dale Thomas and Cindy Ann Wunsch (maiden name Zimmerman), was born in Buffalo, New York on April 6, 1984. After completing her degree at Sweet Home Senior High School in Amherst, New York in 2002, she enrolled at Syracuse University in Syracuse, New York, the following fall. During the summers of 2005 and 2006 she participated in the Summer Apprentice Program at the Hauptman-Woodward Medical Research Institute. She graduated from Syracuse in May 2006, receiving the degree of Bachelor of Science in Bioengineering. She entered graduate school at the University at Buffalo, The State University of New York, in August 2006. She was formally accepted into the laboratory of Dr. Edward Snell in the Structural Biology department, housed at the Hautpman-Woodward Medical Research Institute in August 2007. During her graduate career, she authored and coauthored papers in the field of biological macromolecular crystallography. She also presented her work at various conferences. This document constitutes partial fulfillment of the requirements for the degree of Doctor of Philosophy (PhD.) in Structural Biology, awarded by the University at Buffalo, The State University of New York; January 9, 2013.

This dissertation was typed entirely by the author.